DISSERTATION

DEVELOPING HYPERPOLARIZED KRYPTON-83 FOR NUCLEAR MAGNETIC RESONANCE SPECTROSCOPY AND MAGNETIC RESONANCE IMAGING

Submitted by

Zackary I. Cleveland

Department of Chemistry

In partial fulfillment of the requirements

For the Degree of Doctor of Philosophy

Colorado State University

Fort Collins, Colorado

Summer 2008

COLORADO STATE UNIVERSITY

April 25, 2008

WE HERBY RECOMMEND THAT THE DISSERTATION PREPARED UNDER OUR SUPERVISION BY ZACKARY I CLEVELAND ENTITLED DEVELOPING HYPERPOLARIZED KRYPTON-83 FOR NUCLEAR MAGNETIC RESONANCE SPECTROSCOPY AND MAGNETIC RESONANCE IMAGING BE ACCEPTED AS FULFILLING IN PART REQUIREMENTS FOR THE DEGREE OF DOCTOR OF PHILOSOPHY.

Committee on Graduate Work

Prof. David S. Dandy

Prof. Nancy E. Levinger

Prof. Grzegorz Szamel

Prof. Alan Van Orden

Adviser Prof. Thomas Meersmann

Department Head Prof. Anthony K. Rappe

ABSTRACT OF DISSERTATION

DEVELOPMENTING HYPERPOLARIZED KRYPTON-83 FOR NUCLEAR MAGNETIC RESONANCE SPECTROSCOPY AND MAGNETIC RESONANCE IMAGING

This dissertation discusses the production of highly nonequilibrium nuclear spin polarization, referred to as hyperpolarization or hp, in the nuclear spin I = 9/2 noble gas isotope krypton-83 using spin exchange optical pumping (SEOP). This nonequilibrium polarization yields nuclear magnetic resonance (NMR) signals that are enhanced three or more orders of magnitude above those of thermally polarized krypton and enables experiments that would otherwise be impossible. Krypton-83 possesses a nuclear electric quadrupole moment that dominates the longitudinal (T_1) relaxation due to coupling of the quadrupole moment to fluctuating electric field gradients generated by distortions to the spherical symmetry of the electronic environment. Relaxation slows polarization buildup and limits the maximum signal intensity but makes krypton-83 a sensitive probe of its environment.

The gas-phase krypton-83 longitudinal relaxation rate increases linearly with total gas density due to binary collisions. Density independent relaxation, caused by the formation of krypton-krypton van der Waals molecules and surface adsorption, also contributes to the observed rate. Buffer gases suppress van der Waals molecule mediated relaxation by breaking apart the weakly bound krypton dimers. Surface relaxation is gas composition independent and therefore more difficult to suppress. However, this

relaxation mechanism makes hp krypton-83 sensitive to important surface properties including surface-to-volume ratio, surface chemistry, and surface temperature. The presence of surfaces with high krypton adsorption affinities (i.e. hydrophobic surfaces) accelerates the relaxation times and can produce T_1 contrast in hp krypton-83 magnetic resonance imaging (MRI). Tobacco smoke deposited on surfaces generates strong T_1 contrast allowing the observation of smoke deposition with spatial resolution. Conversely, water adsorption on surfaces significantly lengths the T_1 times due competitive surface adsorption.

Finally, this work demonstrates that hp krypton-83 MRI of intact, excised lungs is feasible. No attempts have been made to observe pathology specific contrast, but this work represents the first steps in developing hp krypton into a useful biomedical tool. Although the signal must be improved for biomedical applications, additional enhancements of up to 180 times greater than the currently obtained signal are possible through improved SEOP, and another order of magnitude increase can be obtained through isotopic enrichment.

Zackary Ian Cleveland
Department of Chemistry
Colorado State University
Fort Collins, Colorado 80523
Summer 2008

Bad enough! The same old story! When one has finished building one's house, one suddenly realizes that in the process one has learned something that one really needed to know in the worst way—before one began. The eternal distasteful "Too late!"

The melancholy of everything finished!

- Friedrich Nietzsche,

from Beyond Good and Evil

ACKNOWLEDGEMENTS

Accomplishing any long-term goal, whether personal or professional, rarely results from the effort or ingenuity of one individual alone. The work presented in the following dissertation pages certainly represents no exception to this rule. Many people contributed both directly and indirectly to my development as a scientist and, thus, to the research I performed while at CSU. I lack both the eloquence and the space needed to fully express the gratitude I feel toward these individuals, but I find myself compelled to at least make an imperfect attempt.

First of all, I must thank my adviser Professor Thomas Meersmann. I benefited greatly over the past four and a half years from his creativity, his support, and his enthusiasm. I am extremely fortunate to have found myself in the unique position of

being his first Ph.D. student and to have experienced all of the excitements, joys, and occasional frustrations that go along with being the first. I also wish to thank the past and present members of the Meersmann group: Karl Stupic and Dr. Galina Pavlovskaya, Charlene Horton-Garcia, Satya Anala, Catherine F. LeNoir, Ramon Saavedra, and Markus Seitz. Karl and Galina in particular made important contributions to most of the work discussed in this dissertation. Karl has also been an excellent companion and friend on this difficult journey through the world of graduate school. My work has benefited greatly from the contributions of our collaborators: Prof. John E. Repine, Dr. Jan Wooten, Nancy Elkins, and Prof. Randall Basaraba. Several aspects of my research were also improved by conversations with Prof. Fred Salsbury, Dr. Michael Barlow, Prof. Susan Kraft, and Prof. David Grainger.

I also owe thanks to a number of people within the Chemistry Department at CSU. Prof. Gary Maciel and the members of his group have always being willing to lend equipment, reference materials, and provide their expertise. In particular I would like to thank Dr. Joseph DiVerdi, who showed me a number of useful tricks about NMR equipment and proper machining methods that do not appear in textbooks. Of course, even with a handful of useful machining tricks, I could never have performed my work as an experimentalist without the patient and skilled assistance of Thom Frederick, Elden Burk, and Michael Olsen.

I would be remiss if I did make special mention of Michael Olsen. I have long believed that the great scientific discoveries of late nineteen and early twentieth centuries, which provided the foundations for all modern research, occurred in large part because the master artisans living at that time possessed the talent and knowledge needed to construct

the necessary experimental apparatus. Mike, more than any person I have ever known, has carried this noble and important tradition into the modern era. On a more personal note, my conversations with Mike touching on topics ranging from existentialism to cinema have helped to prevent those portions of my mind, not totally devoted to science, from atrophying. That any portion of my sanity has survived graduate school is due largely to his influence and friendship.

Though I have learned much while at CSU, my journey into the world of science did not begin here. In my youth, I was fortunately enough to attend a small rural school in Shepherd, Montana where the teachers still held the archaic notion that "boring" topics like grammar and mathematics are important subjects. I will be forever grateful to these passionate educators. I especially wish to thank Jeff Greenfield, who helped to set me on this path many years ago. I am also greatly indebted to my chemistry professors from my years as and undergraduate at The University of Montana. I owe special thanks to Prof. Richard Field who introduced me to physical chemistry. I also wish to express the deep gratitude that I feel toward Jack Stanford, Bonnie K. Ellis, Art McKee, and Richard J. Field. Their well considered advice, heartfelt encouragement, and the example they set reminded me why I wanted to be a scientist — at a time when I needed to be reminded.

Finally, I wish to thank my parents Mary and Barry Cleveland and my brother Shawn Cleveland. Although my work has CSU kept me far more distant from their lives than I would have liked, they never failed to provide me with both support and encouragement. I could never have made it to this point without them.

DEDICATION

I dedicate this work to the memory of my grandparents. From Lois and Albert Cleveland, I inherited a fairly intense stubborn streak. Although this particular personality trait has not always kept me out of trouble, I would never have survived graduate school without it. From my maternal grandfather Harold "Ike" Schulz, who had one of the keenest intellects I have ever encountered, I learned the meaning of work hard. If he had been born in a different place and at a different time, he would have been a truly remarkable scientist.

TABLE OF CONTENTS

CHAPTER 1

AN INTRODUCTION TO NMR, MRI, AND SPIN EXCHANGE OPTICAL PUMPING WITH EMPHASIS ON KRYPTON-83

1.1 Background and Motivation

Nuclear magnetic resonance (NMR) was first observed in 1945 by the research groups of Edward M. Purcell at Harvard University and Felix Bloch at Stanford University. During the six decades since its discovery, NMR and the related technique magnetic resonance imaging (MRI) have been applied to almost every area of laboratory science. Chemical structure determination by NMR spectroscopy is now indispensable in modern synthetic chemistry, and NMR is used increasingly for the determination of the tertiary and quaternary structure of biological macromolecules [1]. Pulsed field gradient (PFG) NMR methods yield detailed information about the diffusion, dispersion, and flow in fluids [2]. MRI has become a dominant clinical technique for non-invasively examining soft tissues in both the clinical and biomedical applications [2].

Despite the rapid development and broad usefulness of MR based techniques, they are often severely limited by their insensitivity compared to other analytical methods (See Section 1.2.1.) and typically require on the order of 10^{14} nuclei to yield a detectable signal. However, the past decade several novel technologies have been developed that create highly nonequilibrium nuclear spin polarization, commonly called hyperpolarization (hp), which can partially overcome the low sensitivity associated with conventional MR methods. For instance, in solids it is possible to irradiate a coupled electron-nuclear spin system with microwave radiation having a frequency near that of the electron Larmor frequency. Through this method, called dynamic nuclear polarization (DNP), polarization can be transferred from the irradiated electron to the nucleus of the atom of interest. Under optimal conditions, DNP can enhance sensitivity by several orders of magnitude [3] over those obtained from thermally polarized samples. In ^{1}H NMR, it is possible to make use of

the high spin order of parahydrogen to obtain signal intensities that are about three orders of magnitude greater than are achieved using conventional ^{1}H NMR [4, 5]. Hp ^{129}Xe can be generated by "brute force" techniques in which high equilibrium polarization is produced using strong magnetic fields and millikelvin temperatures. Following polarization, the xenon is heated to room temperature quickly enough to avoid relaxation thus producing high, nonequilibrium polarization [6]. Additionally, non-equilibrium polarization in ^{3}He can be produced by electronic excitation of a metastable helium atom using circularly polarized light [7]. This technique increases the observed MR signal by up to five orders of magnitude.

Another method of producing highly polarized noble gases is alkali metal vapor spin exchange optical pumping (SEOP) [8], but this method, unlike optical pumping with metastable atoms, is applicable to any of the NMR active noble gas isotopes. By removing the highly reactive alkali metal vapor of the SEOP process [9-11] many intriguing experiments as well as practical MR applications become possible. In SEOP, angular momentum is transferred from circularly polarized photons, to the valence electron of an alkali metal vapor, and then to noble gas nuclei through alkali metal-noble gas interactions. SEOP of the noble gases has been studied extensively with a variety of experimental methods using a wide range of gas mixtures and pressures, temperatures, magnetic field strengths, and light illumination powers [8, 12, 13]. The details of the SEOP process change considerably under these differing conditions, but the fundamental processes are similar. A more complete discussion of these processes is presented in Section 1.3.

Although ^{3}He has no appreciable chemical shift, it has received a great deal of attention due to its large range of potential applications, which range from the production of high efficiency neutron spin filters [14] to biomedical imaging [15]. This widespread use is largely due to the high gyromagnetic ratio and long T_1 times of this isotope, which can reach hundreds of hours in the absence of paramagnetic species [16, 17]. Together these ^{3}He characteristics yield extremely high nonequilibrium nuclear spin polarizations. Hp ^{3}He MRI allows direct, spatially resolved observation of ventilation distribution and dynamics in both healthy and diseased lungs [18]. Apparent diffusion constant (ADC) measurements and ACD weighted MRI are sensitive to hp ^{3}He confinement within pores and thus provide information about changes in alveolar size resulting from normal aging [19, 20] and chronic obstructive pulmonary disease progression (COPD) [21-23]. Finally, the high gyromagnetic ratio of ^{3}He makes the longitudinal (T_1) relaxation of this isotope extremely sensitive to the presence of paramagnetic species such as molecular oxygen [24]. Although the T_1 of hp ^{3}He is typically reduced to 10 to 20 s in the presence of a breathable oxygen mixture [25], this sensitivity makes hp ^{3}He a useful probe of regional O_2 partial pressure in lungs [26-29].

Hp ^{129}Xe provides lower signal intensities than does hp ^{3}He, but this isotope is of interest because of its large ^{129}Xe chemical shift range of ~300 ppm [30, 31]. The potential utility of ^{129}Xe NMR was first pointed out in studies of nanoporous media [32] and clathrates [33] conducted in the early 80's, and ^{129}Xe NMR has subsequently found wide-spread used in materials science (See refs. [34-40] for reviews.). Further, ^{129}Xe chemical shift anisotropy (CSA) can be used to probe void space geometries, pore dimensions, guest molecule loading, and gas dynamics within nanoporous materials [41-45]. Information about

the permeability, porosity, and tortuosity of porous materials [46-51] can be obtained through hp ^{129}Xe diffusion measurements, and information about the surface-to-volume ratios of soft porous materials can be obtained through xenon exchange experiments [52]. There has also been interest in transferring the high, nonequilibrium spin polarization of hp ^{129}Xe to other atoms of interest [40, 53].

Biomedical interest in hp ^{129}Xe began when pulmonary, gas-phase MRI was first reported [54] . The Oswald solubility of xenon in tissues is ~10% [55], and has a T_1 time of tens of seconds in biological fluids [31]. The large ^{129}Xe chemical shift range provides information about structure and gas dynamics in both healthy and injured lungs [56-59], and hp ^{129}Xe ADC measurements can detect pathological changes in lung morphology [60]. *In vivo* hp ^{129}Xe NMR studies have also been extended beyond the lungs to other tissues and organ systems including the blood [61], kidneys [62], and brain [62-64], where tissue specific chemical shifts can be observed [65]. Additionally, hp ^{129}Xe in conjunction with functionalized cryptophane biosensors may be useful as a molecular imaging contrast agent [66, 67].

Table 1.1: NMR Parameters for Nuclear Spin $I > 0$ Noble Gas Isotopes [a]

Noble Gas Isotope	^{3}He	^{21}Ne	^{83}Kr	^{129}Xe	^{131}Xe
Nuclear Spin (K)	½	3/2	9/2	1/2	3/2
Gyromagnetic Ratio (γ) /10^7 rad T^{-1} s^{-1}	-20.38	-2.113	-1.033	-7.452	2.209
Frequency Factor $\left|\gamma/\gamma_{^1H}\right|\cdot$100%	76.18%	7.89%	3.85%	27.81%	8.24%
Natural Abundance	1.37×10^{-4} [b]	0.27%	11.49%	26.44%	21.18%
Nuclear Quadrupole Moment (Q) /10^{-28} m^2	---	10.16	25.9	---	-11.4

[a] All values were obtained from ref. [68]

[b] ^{3}He can be obtained from the radioactive decay of ^{3}H.

The majority of the following dissertation is concerned with the development of a third hp noble gas isotope, ^{83}Kr, for NMR and MRI applications. The ^{83}Kr isotope possesses a nuclear spin of I = 9/2 and thus a nuclear electric quadrupole that is not available with either ^{129}Xe or ^{3}He and that is a far more sensitive 'sensor' of the surrounding environment than the ^{129}Xe chemical shift. (See Table 1.1 for a more complete comparison of the relevant parameters for NMR active noble gas isotopes.) In the presence of an anisotropic environment, the spherical electronic symmetry of the krypton atom becomes distorted, and an electric field gradient (EFG) is produced that interacts with the nuclear electric quadruple moment. These 'quadrupolar interactions' can lead to rapid longitudinal relaxation, homogeneous broadening of the ^{83}Kr lineshape (i.e. T_2 relaxation), and inhomogeneous broadening (i.e. a quadrupolar powder pattern) [69].

1.2 Principles of NMR Spectroscopy and MR Imaging

1.2.1 Polarization and Signal Intensity in Nuclear Magnetic Resonance

Any nucleus having a non-zero nuclear spin possess a nuclear magnetic moment, μ, which is given by $\mu = \gamma I$. In this expression, γ and I represent the gyromagnetic ratio of the nucleus and the nuclear spin respectively. In the presence of an external magnetic field, the nuclear magnetic moments of the individual molecules align along the z-axis, which is, by convention, defined as being in the direction of the applied magnetic field. Thus, a collection of spins within a magnetic field will produce a net nuclear magnetization M_z. In the simplest case of a spin I = 1/2 isotope, the observed nuclear

magnetic resonance signal is proportional to M_z, and thus depends on the spin states of the observed nuclei. The more complicated case of spin $I > 1/2$ is discussed in Chapter 7.

NMR spectroscopy, like most other forms of spectroscopy, involves detecting transitions between the energy levels of the system, and is therefore best thought of in quantum mechanical terms. For NMR, the relevant Hamiltonian operator, which allows the nuclear energy levels to be calculated, is

$$\hat{H} = -\gamma\hbar\mathbf{B}\cdot\hat{\mathbf{I}} = -\gamma\hbar B_0\hat{I}_z, \tag{1.2.1}$$

where, $\mathbf{B}$ is the applied magnetic field, B_0 is the strength of that field, and I_z, which can take on the eigenvalues $m = -I, -I+1, ..I-1, I$, is the projection of $\mathbf{I}$ along the z-axis. Note that the quantity γB_0 has special significance in NMR, because it describes the frequency at which the nuclear magnetization vector precesses about the axis of the external magnetic field. This frequency, typically referred to as the Larmor frequency, is denoted $\omega_0 = \gamma B_0$.

From the Hamiltonian in Eq. 1.2.1, it is possible express the population, p_m, having a given value of m as

$$p_m = \frac{e^{m\gamma\hbar B_0/k_BT}}{\sum_{m=-I}^{I} e^{-\gamma m\hbar B_0/k_BT}}. \tag{1.2.2}$$

Because the signal intensity depends on the ability to excite transitions in the system by a $\Delta m = 1$ selection rule, it is necessary to discuss the difference in populations of adjacent energy levels. This is done most conveniently by defining a positive quantity called the spin polarization, P. For the general case of spin $I \geq 1/2$ nuclei with a Boltzmann population distribution, the polarization can be written as

$$P = \frac{\gamma}{|\gamma|} \frac{\sum_{m=-I}^{m=(I-1)} \left(e^{-(m+1)\gamma\hbar B_0 / k_B T} - e^{-m\gamma\hbar B_0 / k_B T} \right)}{\sum_{m=-I}^{I} e^{-\gamma m\hbar B_0 / k_B T}}, \tag{1.2.3}$$

where $\gamma/|\gamma|$ has been included to account for the sign of γ. For spin I = 1/2 nuclei, Eq. 1.2.3 simplifies to

$$P = \frac{\gamma}{|\gamma|} \frac{e^{\gamma\hbar B_0 / 2k_B T} - e^{-\gamma\hbar B_0 / 2k_B T}}{e^{\gamma\hbar B_0 / 2k_B T} + e^{-\gamma\hbar B_0 / 2k_B T}}. \tag{1.2.4}$$

If the system is at thermal equilibrium and at high temperature (i.e. $k_B T >> |\gamma|\hbar B_0$), Eq. 1.2.4 can be approximated by the well-known expression

$$P = \frac{|\gamma|\hbar B_0}{2k_B T}. \tag{1.2.5}$$

In the high temperature limit, the total equilibrium magnetization M_0 is related to P by

$$M_0 = \frac{1}{2} N_s \gamma\hbar P, \tag{1.2.6}$$

and the observed signal intensity is proportional to the spin polarization. Because $\gamma\hbar B_0$, and thus the spacing between energy levels, is exceedingly small at any reasonable field strength, the thermal polarization is a small number except at temperatures well below 1 K. For instance, a collection of protons at 300 K in a 9.4 T magnetic field, has a polarization of $P \approx 3.3\times10^{-5}$. This low polarization at the temperatures required for most practical experimental situations is the origin of the insensitivity commonly associated with MR based techniques.

1.2.2 Relaxation in Magnetic Resonance

The nuclear magnetization can be conceptually divided into two components. The component of the total magnetization aligned along the applied magnetic field (i.e. in the z direction), is referred to as the longitudinal magnetization or M_z. Magnetization that lies in the x,y plane is referred to be transverse magnetization (denoted $M_{x,y}$). While the value of M_z determines the magnitude of the observed signal, transverse magnetization is actually detected in NMR. Applying an RF pulse with a frequency on or nearly on resonance with the Larmor frequency rotates magnetization away from the z-axis producing transverse magnetization along the x-axis were it can be detected. Following an RF pulse, the transverse magnetization relaxes with a characteristic rate constant T_2 and is described by the differential equation (i.e. one of the Bloch Equations).

$$\frac{dM_{x,y}(t)}{dt} = \frac{-M_{x,y}(t)}{T_2}. \tag{1.2.7}$$

Because no transverse magnetization exists at equilibrium, the solution to the differential equation shown in Eq. 1.2.7 is simply

$$M_{x,y}(t) = M_{x,y}(0)\exp(-t/T_2), \tag{1.2.8}$$

where $M_{x,y}(0)$ is the transverse magnetization produced by the RF pulse at time $t = 0$.

In the work described in the subsequent chapters, the time dependent longitudinal magnetization $M_z(t)$ is of primary importance. The time needed for the system to reach equilibrium longitudinal magnetization is described by the Bloch equation

$$\frac{dM_z(t)}{dt} = \frac{-\left(M_z(t) - M_0\right)}{T_1}, \tag{1.2.9}$$

where T_1 is the relevant rate constant for longitudinal relaxation. The most general solution to Eq. 1.2.9 is

$$M_z(t) = \left(M_z(0) - M_0\right)e^{-t/T_1} + M_0. \tag{1.2.10}$$

where $M_z(0)$ is the initial value of the longitudinal magnetization. Commonly, the magnetization at time t = 0 can be taken to be zero, and Eq. 1.2.10 reduces to

$$M_z(t) = M_0\left(1 - \exp(-t/T_1)\right). \tag{1.2.11}$$

However, for most of the situations discussed throughout this work, the initial magnetization is highly nonequilibrium (i.e. $M_z(0) >> M_0$), and Eq. 1.2.10 simplifies to

$$M_z(t) \approx M_z(0)\exp(-t/T_1) \tag{1.2.12}$$

On the quantum mechanical level, relaxation is caused by transitions between the energy states of the system due to fluctuations in the local magnetic environment. Because the differences between nuclear energy levels are small compared to the k_BT, fluctuations in the transverse local magnetization $B_x(t)$ caused by molecular motion provide sufficient energy to induce transitions between the energy levels and thus cause relaxation. For most situations in NMR, especially where liquids and gases are concerned, the fluctuations are both rapid and random. Therefore, even at relatively short times, the average value of these fluctuations is $\langle B_x(t)\rangle = 0$.

Although the fluctuations average to zero, it is the average of the squared fluctuations that is responsible for relaxation, and $\langle B_x^2(t)\rangle \neq 0$. To discuss how rapidly the field fluctuates in time, it is necessary to introduce an autocorrelation function for the fluctuations, which is assumed to be independent of the origin in time. The autocorrelation function is defined as

$$G(\tau) = \langle B_x(t)B_x(t+\tau)\rangle, \tag{1.2.13}$$

where τ is a time increment, and for $\tau = 0$, $G(0) = \langle B_x^2(t)\rangle$.

The value of $G(\tau)$ tends to be large if τ is short and small if τ is large. Thus, it is typically assumed that the correlation decays exponentially and can be written as

$$G(\tau) = \langle B_x^2\rangle \exp(-|\tau|/\tau_c), \tag{1.2.14}$$

where τ_c is the correlation time of the fluctuations. The observed relaxation rate depends on the Fourier transform of the autocorrelation function, and the resulting function, known as the spectral density function $\boldsymbol{J}(\omega)$, is given by

$$\boldsymbol{J}(\omega) = \int_{-\infty}^{\infty} G(\tau)\exp^{(-i\omega\tau)}\, d\tau = 2\langle B_x^2\rangle \frac{\tau_c}{1+\omega^2\tau_c^2}. \tag{1.2.15}$$

Rather than discussing the complete expression for the $\boldsymbol{J}(\omega)$, it is common to discuss only the normalized spectral density function $J(\omega)$, which is given by

$$J(\omega) = \frac{\tau_c}{1+\omega^2\tau_c^2}. \tag{1.2.16}$$

The actual functional dependence of the longitudinal relaxation rate on $\boldsymbol{J}(\omega)$, depends on the nature of the interaction responsible for the magnetic field fluctuations. For instance, in the case of chemical shift anisotropy (CSA), which is discussed in the following section, the longitudinal relaxation is related to the spectral density by

$$\frac{1}{T_1} = \gamma^2\langle B_x^2\rangle J(\omega_0) = \gamma^2\langle B_x^2\rangle \frac{\tau_c}{1+\omega_0^2\tau_c^2}. \tag{1.2.17}$$

Thus, the magnitude of the longitudinal relaxation is strongly influenced by the value of τ_c. In most situations, the local magnetic field fluctuations are extremely rapid making τ_c

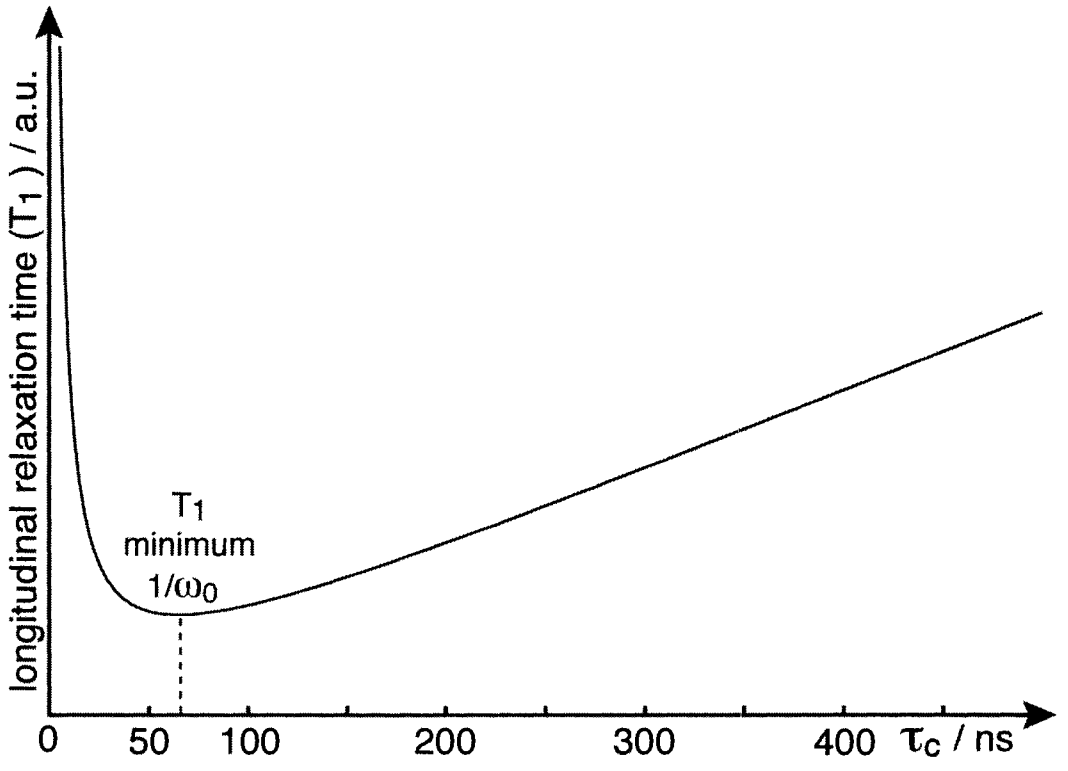

Figure 1.1: Longitudinal relaxation time of ^{83}Kr as a function of correlation time. The T_1 curve was calculated assuming that the sample relaxes within a homogeneous, 9.4 T magnetic field where the ^{83}Kr Larmor frequency is ω_0 = 15.4 MHz. The T_1 time is presented in arbitrary units so that it is not necessary to evoke as specific relaxation mechanism. Due the functional dependence of the relaxation time on the correlations time shown in Eq. 1.2.17, T_1 decreases with increasing values of τ_c until reaching the minimum value at $\tau_c = 1/\omega_0$ = 6.49 × 10^{-8} s. At longer correlation times, the value of T_1 increases.

small (i.e. $1 >> \omega^2\tau_c^2$), and the relationship $1/T_1 \propto \tau_c$ is a good usually a good approximation.

1.2.3 Relaxation Mechanisms in the Gas-Phase

One relaxation mechanism that is extremely important for gases and, to a lesser extent for small molecules in inviscid fluids, results from molecular rotations. When molecules rotate, the motion of the molecule's electrons produces a magnetic field. This magnetic field is proportional to the rotational angular momentum of the molecule and couples rotational angular momentum to the nuclear spin. The spin-rotation interaction can be described in terms of the spin-rotation Hamiltonian

$$H_{SR} = \hbar \mathbf{I} \cdot \mathbf{C} \cdot \mathbf{J}, \tag{1.2.18}$$

where $\mathbf{J}$ is the angular momentum operator for the molecular rotation. $\mathbf{C}$ is the spin rotation tensor and takes the form

$$\mathbf{C} = \begin{bmatrix} c_{xx} & c_{yx} & c_{zx} \\ c_{xy} & c_{yy} & c_{zy} \\ c_{xz} & c_{yz} & c_{zz} \end{bmatrix}. \tag{1.2.19}$$

The elements of $\mathbf{C}$ are empirically determined constants that are most conveniently described in terms of the principle axis coordinates appropriate for the given molecular geometry.

In general, the relationship between spin-rotation coupling and longitudinal relaxation is complex and depends on parameters such as the sample temperature, the molecular geometry, and fluid viscosity in the case of liquids. However, in gases this situation is simplified because the molecules are isolated, and the fluctuations are rapid.

For instance in linear molecules, the relaxation rate due to spin rotation interaction in the limit of rapid fluctuations is given by

$$\frac{1}{T_1} = \frac{1}{T_2} = \frac{4k_B T I_0 C_\perp^2 \tau_c}{3\hbar^2}, \tag{1.2.20}$$

where I_0 is the moment of inertia about a line through the center and perpendicular the molecule. For linear molecules, $C_\perp = C_{xx} = C_{yy}$. In the case of molecular gases, the correlation time is the time between binary collisions that randomize the magnitude or the direction of the rotational angular momentum vector.

As mentioned in Section 1.2.2, chemical shift anisotropy is also a powerful relaxation mechanism. The Hamiltonian describing the chemical shift is given by

$$H_{CS} = -\gamma \mathbf{I} \cdot \boldsymbol{\Sigma} \cdot \mathbf{B}, \tag{1.2.21}$$

where $\boldsymbol{\Sigma}$ is a second rank tensor describing the spatial dependence of the chemical shift and has elements σ_{ij}, with i and j taking on the values x, y, or z. Note that the isotropic shielding commonly discussed in the context of solution NMR is given by $\sigma_{iso} = (\sigma_{xx} + \sigma_{yy} + \sigma_{zz})/3$. As was the case for spin-rotation interaction, the relaxation due to CSA is, in general, complex. However in the limit of rapid fluctuations, the longitudinal relaxation due to CSA for a linear molecule can be expressed rather simply as

$$\frac{1}{T_1} = \frac{I_0 (\gamma B_0)^2 (\sigma_\parallel - \sigma_\perp)^2}{45 k_B T} \tau_c, \tag{1.2.22}$$

where $(\sigma_\parallel - \sigma_\perp)$ describes the anisotropy of the shielding.

When two nuclear spins interact, there can be a coupling between their magnetic dipole moments. The Hamiltonian operator for intermolecular dipole coupling between two unlike nuclei is

$$H_{DP} = \frac{\mu_0 \gamma_1 \gamma_2 \hbar^2}{4\pi} \mathbf{I}_1 \cdot \mathbf{D} \cdot \mathbf{I}_2, \tag{1.2.23}$$

where μ_0 is the Bohr magneton, and $\mathbf{D}$ is the dipolar tensor having elements d_{ij}. The two interacting nuclei, denoted by the subscripts **1** and **2**, have spin operators $\mathbf{I}_1$ and $\mathbf{I}_2$ and gyromagnetic ratios γ_1 and γ_2 respectively. In the limit of rapid fluctuations, the relaxation rate is given by

$$\frac{1}{T_1} = \frac{4}{3} \gamma_1^2 \gamma_2^2 \hbar^2 I_2 (I_2 + 1) \tau_c \sum_i r_i^{-6}, \tag{1.2.24}$$

where the r_i values are distances between the nucleus of interest and the neighboring spins that contribute to relaxation. Provided that intramolecular interactions do not contribute, relaxation due to interactions with paramagnetic species can be viewed as a special case of intermolecular dipolar relaxation in which the second spin is an unpaired electron or a collection of unpaired electrons.

For the purposes of this work, relaxation due to quadrupolar interactions will be of primary concern. These interactions arise because spin $I > 1/2$ nuclei possesses nonspherical charge distributions and therefore a nonzero nuclear quadrupole moment. This quadrupole moment will couple strongly to the electric field gradients produced by deviations from spherical symmetry in the electronic environment experienced by the nucleus. The quadrupolar Hamiltonian can be expressed as

$$H_Q = \mathbf{I} \cdot \mathbf{Q} \cdot \mathbf{I}, \tag{1.2.25}$$

where the magnitude of the quadrupolar interaction is described by the tensor $\mathbf{Q}$, which is given by

$$\mathbf{Q} = \frac{eQ}{2I(2I-1)\hbar}\mathbf{V}. \tag{1.2.26}$$

In the above expression, Q is the nuclear electric quadrupole moment. The spatial dependence of the electric field gradient responsible for quadrupolar relaxation is described by the second rank tensor $\mathbf{V}$ with elements V_{ij}.

Within the fast fluctuation limit, the longitudinal relaxation due to quadrupolar interactions can be expressed as

$$\frac{1}{T_1} = \frac{3}{40}\left(1+\eta_a^2/3\right)\frac{2I+3}{I^2(2I-1)}\left(\frac{eQq}{\hbar}\right)^2\tau_c, \tag{1.2.27}$$

where q is the electric field gradient at the location of the nucleus. The term $eQq/\hbar$ is collectively referred to as the quadrupole coupling constant. In Eq. 1.2.27, η_a is the asymmetry parameter defined by

$$\eta_a = \frac{V_{xx}-V_{yy}}{V_{zz}}, \tag{1.2.28}$$

where the axes have been chosen such that $|V_{zz}| \geq |V_{xx}| \geq |V_{yy}|$. The V_{ij} terms in Eq. 1.2.28 represent the second derivatives of the electric potential (i.e. $V_{xx} = d^2V/dx^2$). Note that for an isotropic sample, η_a vanishes.

1.2.4 Magnetic Resonance Imaging

In most conventional spectroscopic applications of nuclear magnetic resonance, especially high-resolution solution NMR, obtaining the narrowest spectral linewidths possible is of great importance. Thus, great emphasis is placed on producing highly homogeneous magnetic fields. However, if a magnetic field gradient is intentionally

applied across the sample region, the Larmor frequency becomes a function of the location of the nucleus within in the field gradient. The spatial dependence of the Larmor frequency in a magnetic field gradient can be expressed as

$$\omega(\mathbf{r}) = \gamma B_0 + \gamma \mathbf{G} \cdot \mathbf{r}, \tag{1.2.29}$$

where $\gamma B_0 = \omega_0$ is the Larmor frequency of the nuclei in the presence of a homogeneous magnetic field, $\mathbf{G}$ is the magnetic field gradient applied along the z-axis, and $\mathbf{r}$ is the vector describing the spatial coordinates of the nuclear spin.

Typically a linear field gradient is applied, and a simple 1-D spectrum in the presence of such a gradient becomes a 1-D image of the spin density of the sample. Acquiring many 1-D images with different orientations and then employing one of a variety of reconstruction algorithms can provide 2-D and 3-D information about the sample. Rather than using somewhat laborious projection reconstruction methods to produced MR images, a method known as phase encoding is more commonly employed. In this technique, an additional incremented gradient (or gradients) imparts a phase modulation on the MR signal. This phase modulation is, like the Larmor frequency, is function of location within the gradient. Thus phase modulation provides a second approach by which spatial information about a sample may be obtained.

1.3 Alkali Metal Vapor Spin Exchange Optical Pumping

1.3.1 Polarization of the Alkali Metal

SEOP is typically performed in a glass cell containing a low density, alkali metal vapor and at noble gas a pressures of a few kPa (See Fig. 1.2.). Spin orbit coupling (fine

splitting) causes the electron P level to split into $^2P_{1/2}$ and $^2P_{3/2}$ terms with total angular momentum $S = 1/2$, having corresponding z components m_S = -1/2 and +1/2, and $J = 3/2$, having z components m_J = -3/2, -1/2, +1/2, and +3/2. For an isolated alkali metal atom (i.e. in the time interval during which the metal is not interacting with other atoms, molecules, or photons), the evolution of the of spin wave function, $|\psi\rangle$, can be described by the time dependent Schrödinger equation

$$i\hbar\frac{d}{dt}|\psi\rangle = H|\psi\rangle. \tag{1.3.1}$$

For the $^2S_{1/2}$ electronic ground state, the relevant Hamiltonian operator is [70]

$$H = A_g\mathbf{I}\cdot\mathbf{S} + g_s\mu_B\mathbf{S}\cdot\mathbf{B} + g_I\mu_B\mathbf{I}\cdot\mathbf{B}, \tag{1.3.2}$$

where $A_g\mathbf{I}\cdot\mathbf{S}$ describes the hyperfine coupling between the alkali metal nuclear spin $\mathbf{I}$ and the valence electron spin $\mathbf{S}$ with A_g being the isotropic magnetic dipole coupling coefficient. The other terms in Eq. 1.3.2 describe the Zeeman interactions of the electronic and the nuclear spins with the applied magnetic field $\mathbf{B}$ having strength of B_0. In the Zeeman terms g_s = 2.00232 is the electron g factor, $\mu_B = 9.274 \times 10^{-24}$ J·T^{-1} is the Bohr magneton, and g_I is the g factor of the alkali metal nucleus. Note that the value of A_g changes as a result of interactions with a noble gas atom and produces pressure dependent shifts in the alkali metal EPR spectrum [71].

If left-handed circularly polarized (σ^+) light is adsorbed, the conservation of angular momentum dictates the selection rule Δm = 1, whereas σ^- light yields Δm = -1 (See Fig. 1.2.). Thus the adsorption of σ^+ light resonant with the alkali metal D_1 transition excites the alkali metal valence electron from the spin-down sublevel of the $^2S_{1/2}$ ground

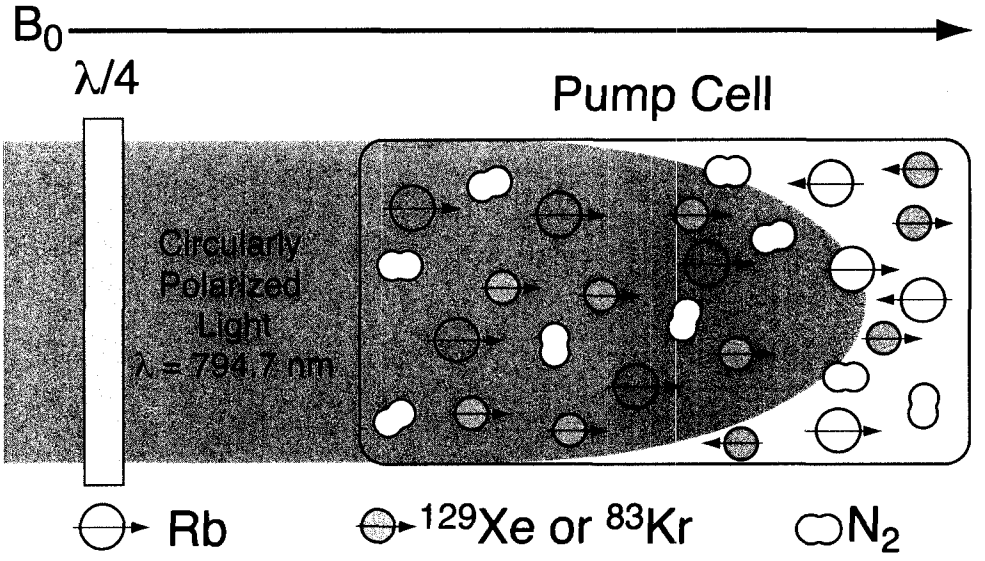

Figure 1.2: Diagram of a spin exchange optical pumping cell. Linearly polarized laser light parallel to the applied magnetic field, B_0, and having a wavelength resonant with the Rb D_1 transition passes through a quarter-wave plate becoming left-hand (σ^+) circularly polarized. Within the region of illumination, the circularly polarized light creates nonequilibrium polarization in the rubidium valence electrons and orients the spin angular momentum along the z-axis of the cell. Subsequent interactions with the noble gas atoms transfer polarization to the noble gas nuclear spins. The arrows on the atoms indicate the orientation of either the alkali metal electron or the noble gas nuclear spin angular momentum with respect to the applied magnetic field. The diatomic molecule N_2 is present to nonradiatively quench the electronic excited state of rubidium preventing radiation trapping. In an optically thick or poorly aligned cell, some areas will be unilluminated. In these regions of 'dark rubidium', the alkali metal is effectively unpolarized with the angular moment being aligned either parallel or antiparallel to the z-axis. Interactions between the polarized noble gas and unpolarized rubidium atoms in these regions can produce substantial noble gas depolarization.

state (m_S = -1/2) to the spin-up sublevel of the $^2P_{1/2}$ excited-state (m_J = +1/2). In $^2P_{1/2}$ state, the analogous excited-state spin Hamiltonian

$$H_e = A_e \mathbf{I} \cdot \mathbf{J} + g_s \mu_B \mathbf{J} \cdot \mathbf{B} + g_I \mu_B \mathbf{I} \cdot \mathbf{B} \tag{1.3.3}$$

applies, where $\mathbf{J}$ denotes the spin of the excited electron and A_e is the relevant excited-state coupling coefficient.

For a discussion of practical SEOP, H_e can be neglected because of the exceedingly short lifetime of the excited-state. At the densities common in SEOP, gas-phase collisions rapidly mix the populations of the $^2P_{1/2}$ sublevels eliminating excited-state spin polarization. Subsequently, either radiative or non-radiative transitions from the excited-state to the ground state repopulate both sublevels with equal probability. Because only the electrons in the m_S = -1/2 sublevel are excited during SEOP with σ^+ light, an alkali metal atom can be said to have -1/2 units of spin angular momentum prior to photon absorption. Because both of the m_S sublevels are repopulated with equal probability, there will be, on average, 0 units of electron-spin angular momentum associated with the alkali metal after it is returned to the ground state. Thus, each absorbed photon provides 1/2 unit of spin angular momentum with the remainder of the momentum being converted into translational motion.

SEOP achieves nonequilibrium alkali metal polarization because any electron returned to the $^2S_{-1/2}$ sublevel can be re-excited resulting in a depletion of the m_S = -1/2 population. In contrast, the population of the m_S = 1/2 sublevel increases because the $^2S_{1/2}$ sublevel cannot be excited by σ^+ light. Additionally, collisional mixing of the m_S = 1/2 and -1/2 sublevels is slow compared to other relaxation processes because of the zero

orbital angular momentum of the S-term. Under optimal conditions, the alkali metal polarization in the pump cell and approaches 100% [72]. A diagram of the alkali metal electronic transitions involved in SEOP is presented in Fig. 1.3.

1.3.2 Alkali Metal-Noble Gas Interactions

When the alkali metal interacts with noble gas atom, the relevant wave function for the alkali metal vapor electron at the noble gas nucleus can be written as [73]

$$|\psi(R)\rangle = \eta|\phi(R)\rangle, \tag{1.3.4}$$

where R is the internuclear separation of the alkali metal-noble gas pair and $|\phi(R)\rangle$ is the alkali metal valence electron wave function in the absence of the noble gas. The constant η accounts for the enhancement produced by the kinetic energy gained when the alkali metal electron scatters in the core-potential of the noble gas. In general the relationship η>>1 holds for all alkali metal noble gas interactions.

Additional terms must be included in the spin Hamiltonian to properly account for the evolution of the system when the alkali metal valence electron interacts with a noble gas. The relevant Hamiltonian is [70]

$$H = A_g \mathbf{I}\cdot\mathbf{S} + \gamma(R)\mathbf{N}\cdot\mathbf{S} + \alpha(R)\mathbf{K}\cdot\mathbf{S} + \ldots, \tag{1.3.5}$$

where $\gamma(R)\mathbf{N}\cdot\mathbf{S}$ describes the spin-rotation interaction between electron spin and the rotational angular momentum of metal-noble gas pair $\mathbf{N}$ and $\alpha(R)\mathbf{K}\cdot\mathbf{S}$ accounts for Fermi contact between the alkali metal electron and the noble gas nuclear spin $\mathbf{K}$. The value of the spin rotation coupling constant is given by [74]

$$\gamma(R) = \frac{-m_e G}{\mu R} \frac{d|\phi(R)|^2}{dR}, \tag{1.3.6}$$

where m_e is the mass of the electron, μ is the reduced mass of the alkali metal-noble gas pair, and G is a noble gas specific constant that depends on the spin-orbit coupling for that isotope. The magnetic dipole coupling constant is given by [73]

$$\alpha(R) = \frac{8\pi}{3} \frac{\mu_B \mu_K}{K} |\psi(R)|^2, \tag{1.3.7}$$

where μ_B is the Bohr magneton and μ_K is the magnetic moment of the noble gas nucleus. The function $|\psi(R)|^2$ can be approximated by the Kronecker delta function, $\delta(R)$, which equals 1 if the electron is at the location of the nucleus and equals 0 otherwise.

Although $\gamma \mathbf{N} \cdot \mathbf{S}$ is responsible for the majority of the spin relaxation in the metal [74], $\alpha \mathbf{K} \cdot \mathbf{S}$ is of primary interest for this discussion because Fermi contact transfers angular momentum to the noble gas producing non-equilibrium nuclear spin polarization. The Fermi contact interaction term can be rewritten using the raising and lowering operators as

$$\mathbf{K} \cdot \mathbf{S} = \hat{K}_z \hat{S}_z + \frac{1}{2}\left(\hat{K}^+ \hat{S}^- + \hat{K}^- \hat{S}^+\right), \tag{1.3.8}$$

where the 'flip-flop' operators $\hat{K}^+ \hat{S}^-$ and $\hat{K}^- \hat{S}^+$ transfer angular momentum between the electron spin and the noble gas nucleus. It should be noted that not every collision leads to spin exchange for instance when a 'polarized' alkali metal atom collides with a polarized noble gas atom. While such collisions can cause electron depolarization through spin rotation interaction, these events do not lead to significant noble gas depolarization since the Fermi contact operator does not contain the double quantum terms $\hat{K}^+ \hat{S}^+$ or $\hat{K}^- \hat{S}^-$.

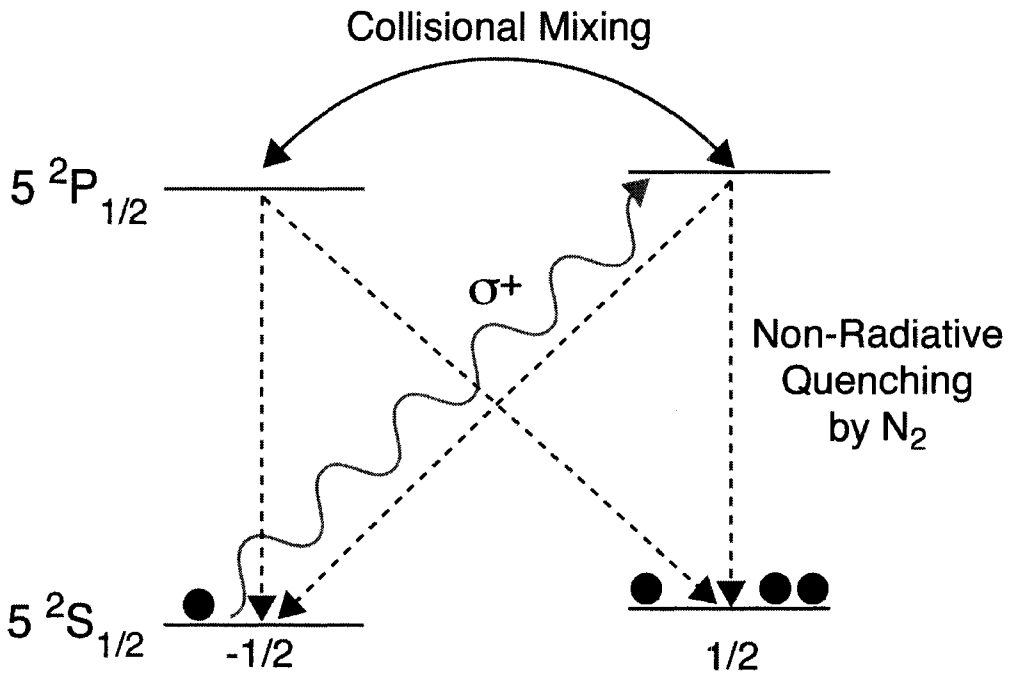

Figure 1.3: Schematic diagram of the alkali metal electronic transitions. Hyperfine splitting has been neglected, and, in any case, is unresolved under practical SEOP conditions due to pressure broadening. The Zeeman splitting of electronic sublevels has been exaggerated in this diagram. Circularly polarized (σ^+) light excites the alkali metal valence electron from the spin-down sublevel of the $^2S_{1/2}$ ground-state (m_S = -1/2) to the spin-up sublevel of the $^2P_{1/2}$ excited-state (m_J = +1/2) following a Δm = 1 selection rule. Collisional mixing rapidly equalizes the populations of the $^2P_{1/2}$ sublevels, and subsequently radiative or non-radiative transitions repopulate both ground-state sublevels with equal probability. Collisions of the excited rubidium atoms with diatomic molecule N_2 nonradiatively quench the electronic excited state of preventing radiation trapping. Ultimately high nonequilibrium alkali metal polarization is achieved because electrons returned to the $^2S_{-1/2}$ sublevel can be re-excited resulting in a depleted m_S = -1/2 population but a highly populated m_S = 1/2 sublevel.

However, interactions between unpolarized alkali metal atoms and polarized noble gas atoms can lead to angular momentum transfer from the noble gas to the alkali metal. This mechanism of noble gas relaxation can be especially problematic if some regions of the pump cell are not illuminated by circularly polarized light. In these regions of 'dark' alkali metal, the only source of nonequilibrium alkali metal spin polarization is diffusion from illuminated regions of the cell. Thus, the relatively high densities of unpolarized alkali metals in these regions can be a substantial source of polarization loss for the noble gases. Two types of alkali metal-noble gas interactions are of interest for SEOP (See Fig. 1.4.). The first of these is binary collision, which are sudden with respect to the nuclear polarization. Thus, the hyperfine coupling to the alkali metal nucleus, which is comparatively slow, can be ignored during the collision, and the Fermi contact interaction with the noble gas nucleus dominates. The rate relaxation of the alkali metal for this interaction is given by [75]

$$\frac{1}{2}\frac{1}{T_{K'}}\left(\frac{\alpha\tau'}{\hbar}\right)^2 = [AM]\langle v\sigma\rangle, \tag{1.3.9}$$

where $1/T_{K'}$ is the binary collision rate per noble gas atom, τ' is the duration of the collision, $[AM]$ is the number density of the alkali metal, and $\langle v\sigma\rangle$ is the velocity averaged spin exchange cross-section for alkali metal-noble gas binary collisions.

In addition to two-body collisions, spin exchange can occur as a result of the formation of comparatively long-lived van der Waals molecules. For a gas-phase van der Waals complex to form, a three-body collision between an alkali metal, a noble gas atom, and a third body must occur. This third body, which can be either another noble gas atom of interest or a buffer gas component of the gas (typically He or N_2), transfers translational

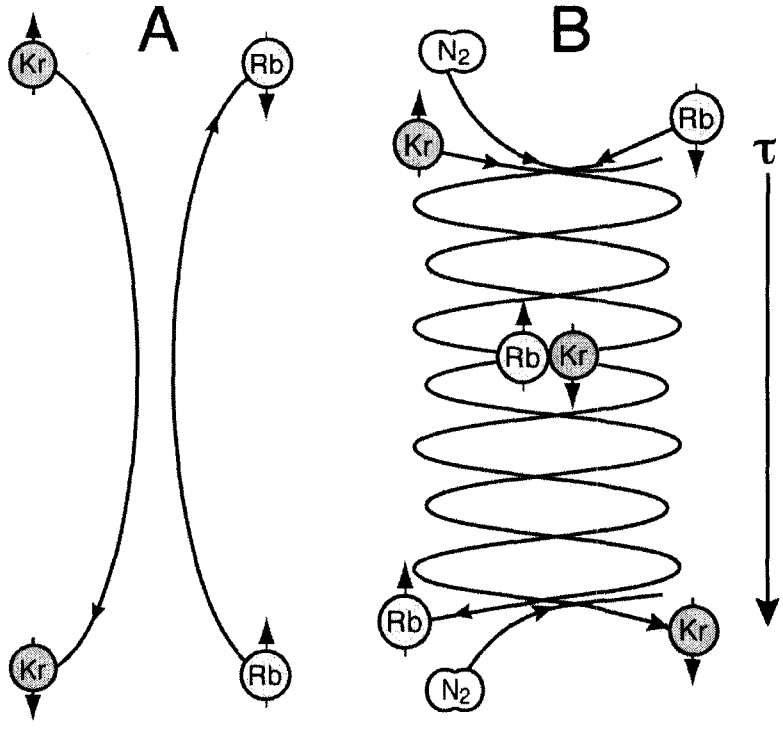

Figure 1.3: Spin exchange mechanisms. **(A)** Binary collisions: Binary collisions are interactions between the alkali metal and the noble gas, which are sudden with respect to the nuclear polarization of the alkali metal. Therefore hyperfine coupling to the alkali metal nucleus is negligible, and the interaction is dominated Fermi contact between the alkali metal valence electron and noble gas nucleus. Fermi contact can produce a spin flip transition in which the alkali metal is depolarized and the noble gas nucleus is polarized. **(B)** Van der Waals molecules. Van der Waals complexes result from three-body collisions between an alkali metal, a noble gas atom, and a third body, which transfers translational energy away from the alkali metal-noble gas pair producing a sticking collision. This third body, though depicted as N_2, can any component of the gas mixture. The van der Waals pair remains bound for some lifetime τ, during which polarization can be transferred between the alkali metal valence electron to the noble gas nucleus by Fermi contact, until broken apart by a subsequent collision.

energy away from the alkali metal-noble gas atom pair allowing a sticking collision to occur. The pair remains bound as a van der Waals molecule until the complex is broken apart by a subsequent collision. Because neither the nuclear nor the electron spin polarization are expected to influence the thermodynamics gas-phase processes, molecular formation is at equilibrium. The chemical equilibrium constant for molecular formation, κ, is given by

$$\kappa = \frac{[AM-NG]}{[AM][NG]}, \tag{1.3.10}$$

where $[AM-NG]$ is the number density of the van der Waals complex and $[NG]$ is the number density of the noble gas. At equilibrium, the molecular formation rate equals the molecular breakup rate. Thus it is possible for a gas mixture consisting only of the alkali metal and the noble gas to write the equality [70]

$$\frac{[AM-NG]}{\tau} = \frac{[NG]}{T_K} = \frac{[AM]}{T_F}, \tag{1.3.11}$$

where $1/T_F$ is the rate of van der Waals molecule formation per alkali metal atom, $1/T_K$ is therate of molecular breakup, and τ is the molecular lifetime. From Eqs. 1.3.10 and 1.3.11, it follows that

$$\frac{1}{T_F} = \frac{[NG]\kappa}{\tau}. \tag{1.3.12}$$

Inspection of Eq. 1.3.12 indicates that τ must depend on the number density of the noble gas (i.e. the pressure present during SEOP).

In gas mixtures, collisions with gases other than the noble gas of interest also break up van der Waals molecules. Thus the molecular breakup rate in the presence of buffer gases can be written as

$$\frac{1}{\tau} = \left(\frac{1}{\tau}\right)_{NG} + \sum_j \left(\frac{1}{\tau}\right)_{BGj}, \tag{1.3.13}$$

where $(1/\tau)_{NG}$ is the breakup rate due to collisions with the noble gas of interest and $(1/\tau)_{BGj}$ is the breakup rate due to collisions with the *jth* buffer gas in the mixture. It should be noted that different buffer gases differ in their ability to breakup van der Waals molecules. Thus both gas pressure and the composition during SEOP will strongly influence the lifetime of the van der Waals molecule and thus influence the spin exchange rate.

The differing effects of buffer gases on the molecular lifetime are typically accounted for by defining the so-called characteristic pressure P_0 at which the molecular breakup rate is equal to the spin-rotation frequency $\gamma N/h$. (Note that $\gamma N/h$ originally appeared in Eq. 1.3.5.) The lifetime of the van der Waals molecule at a given pressure, P, is related to the characteristic pressure by the equation [70]

$$\tau = \frac{\hbar}{\gamma N}\frac{P_0}{P}. \tag{1.3.14}$$

In gas mixtures, it is necessary to consider the characteristic pressure for noble gas, $P_0(NG)$, and the *jth* buffer gas, $P_0(BG_j)$, which are defined in the limit that only the noble gas or the *jth* buffer gas is responsible for molecule breakup.

It is now possible to define the parameter $b_j = P_0(NG)/P_0(BG_j)$, which accounts for the ability of the *jth* buffer gas to break up a van der Waals molecule relative to the noble gas of interest. Additionally, the pressures of the noble gas and the buffer gases can be accounted for by defining the parameter $r_j = P(BG_j)/P(NG)$, where $P(BG_j)$ is the pressure of the *jth* buffer gas and $P(NG)$ is the pressure of the noble gas. Using the

above definitions, if follows from Eq. 1.3.14 that the molecular breakup rate in a multicomponent mixture is given by [70]

$$\frac{1}{\tau} = \frac{\gamma N}{\hbar}\left(\frac{P(NG)}{P_0(NG)} + \sum_j \frac{P(BG_j)}{P_0(BG_j)}\right) = \frac{\gamma N}{\hbar}\frac{P(NG)}{P_0(NG)}\left(1 + \sum_j b_j r_i\right). \tag{1.3.15}$$

Multiplying both sides of Eq. 1.3.12 by $(\alpha\tau/\hbar)^2$ and substituting the definition of $1/\tau$ from Eq. 1.3.15 yields

$$\frac{1}{T_F}\left(\frac{\alpha\tau}{\hbar}\right)^2 = [NG]\kappa\frac{\hbar}{\gamma N}\frac{P_0(NG)}{P(NG)}\left(1 + \sum_j b_j\right)^{-1}\left(\frac{\alpha}{\hbar}\right)^2. \tag{1.3.16}$$

Defining the parameter

$$\gamma_M = \lim_{\sum_j P(BG_j)\to 0} \frac{1}{T_F}\left(\frac{\alpha\tau}{\hbar}\right)^2 \tag{1.3.17}$$

and assuming ideal gas behavior (i.e. $P(NG) = [NG]k_BT$) yields

$$\gamma_M = \frac{\kappa\hbar N P_0(NG)}{\gamma N k_B T}\left(\frac{\alpha}{\hbar}\right)^2, \tag{1.3.18}$$

which is a pressure independent constant for a given noble gas-alkali metal pair. As will be seen in the following section of this chapter, the spin exchange rate due to alkali metal-noble gas van der Waals molecules is proportional to γ_M. Thus under many practical SEOP conditions, the noble gas polarization as a function of SEOP time depends strongly on the value of γ_M.

1.3.3 Spin Exchange Rates and Noble Gas Polarization

At the relatively low B_0 commonly used in optical pumping, the magnitude of the Zeeman interactions is much less than that of the hyperfine interaction. Thus the total

angular momentum of the alkali metal, $\mathbf{F} = \mathbf{I} + \mathbf{S}$, is a good quantum number, i.e. the eigenstates of the ground-state spin Hamiltonian are also eigenstates of $\mathbf{F}$ as well as its projection along the direction of the applied magnetic field F_z. For NMR applications of SEOP, the observable of interest is the average value of the z component of the noble gas spin angular momentum, $\langle K_z \rangle$. The instantaneous rate at which $\langle K_z \rangle$ changes during SEOP has been shown be [70]

$$\frac{d\langle K_z \rangle}{dt} = \frac{1}{T_K} \sum_i f_i \left(\frac{\alpha\tau}{(2I_i+1)\hbar} \right)^2 \left[\left\langle \hat{K}^2 - K_z^2 \right\rangle \langle F_{iz} \rangle - \left\langle \hat{F}_i^2 - F_{iz}^2 \right\rangle \langle K_z \rangle \right] + \frac{1}{T_{K'}} \left(\frac{\alpha\tau'}{\hbar} \right)^2 \left[\langle S_z \rangle \left\langle \hat{K}^2 - K_z^2 \right\rangle - \langle K_z \rangle \right] - \Gamma \langle K_z \rangle, \tag{1.3.19}$$

where I_i is the spin of the *ith* alkali metal isotope, f_i is the fraction of the *ith* alkali metal isotope, $\hat{F}^2 = \mathbf{F} \cdot \mathbf{F}$, $\hat{K}^2 = \mathbf{K} \cdot \mathbf{K}$, and Γ is the longitudinal relaxation rate of the noble gas in the absence of the alkali metal. The longitudinal relaxation rate of hp noble gases results from a combination of interactions with surfaces [76-78], binary collisions with other gas-phase species [79-81], gas diffusion through magnetic field gradients that are transverse to $\mathbf{B}$ [82, 83], and the formation of noble gas-noble gas van der Waals molecules [84, 85]. Eq. 1.3.19 is rather complex, but the discussion can be greatly simplified by defining a number of composite parameters. The first of these will be the alkali metal specific parameter

$$\zeta_M = \sum_i f_i \frac{\left\langle \hat{F}_i^2 - F_{iz}^2 \right\rangle}{(2I_i+1)^2}, \tag{1.3.20}$$

which was obtained from algebraic rearrangement of Eq. 1.3.19.

The remainder of this discussion will focus on rubidium because it is the most commonly used alkali metal in SEOP, and it is the only alkali metal used in the experimental work described in the subsequent chapters. Rubidium is favored because it has a substantial vapor pressure at reasonably low temperatures [86, 87] providing high rubidium number densities. Additionally, the rubidium D_1 line absorbs at 794.7 nm, which is a wavelength readily produced at high powers using light sources such as Ti-sapphire, dye, and diode array lasers. The two rubidium isotopes ^{85}Rb (I = 5/2) and ^{87}Rb (I = 5/2) have isotopic fractions $f_i = 0.7215$ and $f_i = 0.2785$ respectively. Because ζ_M depends on the total rubidium spin angular momentum, it is a function of the rubidium polarization. While ζ_M necessarily depends upon the SEOP conditions, it is possible to discuss several limiting values. Under optimal SEOP conditions rubidium polarization approaches 100%, and $\left\langle \hat{F}_i^2 - F_{iz}^2 \right\rangle = I_i + 1/2$. Thus, for rubidium at very high levels of polarizations, ζ_M = 0.095. Under conditions such as low laser power or high noble gas densities, the rubidium polarization approaches zero, and $\left\langle \hat{F}_i^2 - F_{iz}^2 \right\rangle = (2/3)I_i(I_i + 1) + 1/2$ leading to ζ_M = 0.1791.

Polarization transfer is largely determined by the spin exchange rate, γ_{SE}, which is given by [75, 88]

$$\gamma_{SE} = [Rb]\left(\frac{\gamma_M \zeta_{Rb}}{[NG] + \sum_i b_i [BG]_i} + \langle \sigma v \rangle \right), \tag{1.3.21}$$

where number density of rubidium $[Rb]$ is now used rather than the more general $[AM]$. For NMR and MRI applications, the objective is to use spin exchange optical pumping to

improve the observed noble gas signal intensity, which is proportional to the nuclear spin polarization for K= 1/2 isotopes under all conditions and also proportional to the polarization of the K > 1/2 isotopes at low polarization levels. (For additional details see the discussion in Chapter 7.) In addition to the terms stated in Eq. 1.3.19, the polarization of the noble gas, which will be denoted P_{NG}, is affected the destruction of the rubidium spin polarization by binary collisions with components of the gas mixture. The rate of spin destruction, γ_{sd}, can be expressed as [89]

$$\gamma_{sd} = \sum_j \kappa_{sd}^j [M_j], \tag{1.3.22}$$

where κ_{sd}^j is the spin destruction rate constant for the *jth* component of the gas and $[M_j]$ is the number density of that component. Assuming uniform illumination, the polarization of the rubidium, $P_{Rb}(z)$, as a function of position along the pump cell z-axis of the is [90]

$$P_{Rb}(z) = \frac{\gamma_{op}(z)}{\gamma_{op}(z) + \gamma_{sd}}, \tag{1.3.23}$$

where $\gamma_{op}(z)$ is the optical pumping rate per rubidium atom. The value of $\gamma_{op}(z)$ depends on position in the pump cell, z, due to reduced laser intensity along the optically thick beam path [91]. In addition to the magnitude of the achievable polarization, the time needed to achieve this polarization is of concern. The polarization of the noble gas as a function of polarization time, t_p, is given by [89]

$$P_{NG}(t_p) = \frac{\gamma_{se}}{\gamma_{se} + |\Gamma|} \cdot \frac{\gamma_{op}(z)}{\gamma_{op}(z) + \sum_i \kappa_{sd}^i [M_i]} \left(1 - e^{-(\gamma_{se}+\Gamma)t_p}\right), \tag{1.3.24}$$

where $\gamma_{SE} > 0$ during optical pumping and $\Gamma < 0$.

Under a number of conditions important for many practical applications of SEOP, Eq. 1.3.24 can be simplified considerably. For most NMR applications, hyperpolarized gas is separated from the pump cell, and considerable effort is often exerted to ensure that the observed signal intensity is constant. Under these steady-state conditions, the positional dependence of the optical pumping rate can be ignored, and $\gamma_{op}(z)$ can be replaced with the mean pumping rate $\bar{\gamma}_{op}$ [92]. In the case of ^{129}Xe spin exchange optical pumping, the spin destruction rate due to collisions with xenon atoms, κ_{sd}^{Xe}, is approximately 5.2×10^{-15} cm^3 s^{-1} [89] while the spin destruction due to collisions with N_2, κ_{sd}^{N2} and He, κ_{sd}^{He} [72] have much smaller values of 9×10^{-18} cm^3 s^{-1} and 2×10^{-18} cm^3 s^{-1} respectively. These orders of magnitude smaller terms can, therefore, also be disregarded. Finally, in the case of ^{129}Xe or ^{3}He, the self-relaxation is extremely small compared to the spin exchange rate [89], so Γ can also be omitted. Thus for ^{129}Xe optical pumping, Eq. 1.4.24 reduces to

$$P_{129Xe}(t_p) = \frac{\bar{\gamma}_{op}}{\bar{\gamma}_{op} + \kappa_{sd}^{Xe}[Xe]}\left(1 - e^{-\gamma_{se} t_p}\right). \tag{1.3.25}$$

Note that the first simplification discussed above may not be possible for noble gases lighter than xenon, because they will produce smaller κ_{sd} values. Additionally, the second simplification is probably not possible for the spin $K > 1/2$ isotopes where longitudinal relaxation is much faster than that of ^{129}Xe. It is instructive to examine the dependence of Eqs. 1.3.21, 1.3.24, and 1.3.25 on the number density of the noble gas. Eq. 1.3.21 shows that the spin exchange rate must decrease as $[NG]$ increases. The magnitude of the noble gas polarization in Eqs. 1.3.24, and 1.3.25 also suffer from higher numbers of

spin destroying collisions at higher noble gas densities. Finally, as mentioned before, high noble gas densities will lead to increased values of Γ.

1.3.4 Practical Spin Exchange Optical Pumping Considerations

Alkali atoms in the excited-state will can undergo radiative relaxation with no net preference between $\Delta m_J = +1$ or $\Delta m_J = -1$ transitions, thus leading to the emission of σ^+ and σ^- photons. This process represents a significant source of spin-depolarization through radiation trapping caused by elastic scattering of photons emitted having an opposite polarization to that of the circularly polarized pumping light. A diatomic molecule (usually N_2) is often added to the SEOP gas mixture at concentrations of a few percent to non-radiatively quench the fluorescence of alkali metal by transferring the energy of the excitation to rotational and vibrational excited modes of the diatomic [12].

For most NMR and MRI applications of SEOP, including those described in this work, solid-state diode array lasers are chosen as a light source for their high power output and relatively lost cost. However, these lasers are not an optimal light source due to their broad line widths (typically around 2 nm) that cannot be fully absorbed by the rubidium vapor. A substantial concentration of ^{4}He (nuclear spin K = 0), which yields very little rubidium depolarization, is often added to the optical pumping gas mixture to pressure broaden the rubidium absorption line allowing for more efficient use of the optical pumping beam [89]. Alternatively, external cavity laser line narrowing devices can be used to allow improved light absorption and thus allow more efficient use of the laser power [93].

The high polarization produced by ^{129}Xe SEOP is most effectively exploited by slowly flowing a low density xenon mixture through the spin exchange cell, which

maximizes the ^{129}Xe polarization. Upon exiting the SEOP cell, the gas mixture is cooled to near-room temperature to freeze out the rubidium vapor. The hp ^{129}Xe is then separated from the optical pumping gas mixture by freezing the xenon in a liquid nitrogen cold finger within a strong (greater than 500 G) magnetic field [89, 94]. Under these conditions the solid-state longitudinal relaxation time of ^{129}Xe is on the order of 2 h [95]. This process removes the buffer gases and concentrates the hp ^{129}Xe while destroying little of the non-equilibrium polarization. The hp ^{129}Xe can then be returned to the gas-phase having both high concentration and high spin polarization. However, this approach will likely not be possible with hp ^{83}Kr, which has longitudinal relaxation times of less than 10 s at liquid nitrogen temperatures [96].

1.4 Previous NMR and SEOP Work with Krypton-83

1.4.1 Thermally Polarized ^{83}Kr

Historically ^{83}Kr has been more difficult to work with than ^{129}Xe, because its lower natural abundance and lower gyromagnetic ratio (See Table 1.1.) yield a sensitivity that is only 3.8% that of ^{129}Xe. The problem of lower sensitivity may be compounded in solution NMR because of lower krypton solubility in some liquids [97]. Additionally, the smaller and less polarizable krypton electron cloud produces a smaller ^{83}Kr chemical shift range than is observed from ^{129}Xe [98]. Despite these difficulties, a body of ^{83}Kr NMR work exists that dates back to the 1960s. Initial investigations dealt theoretically [99] with solid-state ^{83}Kr chemical shifts and then experimentally with ^{83}Kr chemical shifts in solid, liquid, and high-pressure gas samples [100]. Additionally, ^{83}Kr NMR was used in the determination of the ^{83}Kr magnetic moment [101].

More detailed studies in the 1970s examined the ^{83}Kr solid-state chemical shift and longitudinal relaxation at temperatures between 40 K and the triple point of krypton (115.78 K) and the liquid-state chemical shifts between the triple point and the critical point (209.4 K) [102]. Relaxation times in the solid-state were found to be short due to the quadrupolar nature of the ^{83}Kr isotope. The relaxation rates in the solid state were observed to increase by a maximum of 20% in samples deliberately contaminated by molecular oxygen providing early evidence of the insensitivity of ^{83}Kr relaxation to paramagnetic species. Later Brinkmann and Kuhn [103] studied the density dependence of gas-phase ^{83}Kr longitudinal relaxation at room temperature. Using densities that were assumed to be high enough to exclude wall contributions, they found that the relaxation rate was empirically well described by

$$\frac{1}{T_1} = [Kr](2.13 \pm 0.05) \times 10^{-3} \text{ amagat}^{-1} \text{ s}^{-1}, \tag{1.4.1}$$

where an amagat is the number density of an ideal gas at 1 atm and 273.15 K. 1 amagat = 2.69×10^{25} m^{-3}. The limitations of this assumption will be discussed in Chapter 4.

Using pulsed field gradient NMR techniques, Cowgill and Norberg studied krypton self-diffusion in liquid and solid-phase, [96] and found the diffusion behavior to be well described by Arrhenius type behavior. Also discussed in this work where the spin-spin relaxation processes and line shapes. The decay of transverse magnetization was found be multiexponential with one rate constant describing dipolar interactions and another describing quadrupolar interactions. Further, solid-state investigations by Madaras and Norberg explored a number of features including relaxation processes, defect

structures, and spectral diffusion using both natural abundance and isotopically enriched krypton [104, 105].

The first NMR investigations of ^{83}Kr in more complex systems were of krypton dissolved in a variety of polar and non-polar solvents [98]. This work examined the chemical shift and longitudinal relaxation of ^{83}Kr in a variety of different solvents as well as the temperature dependence of these variables. Since then, through both experiment and computation, researchers have explored the longitudinal relaxation of ^{83}Kr dissolved in isotropic liquids that differ greatly in their electrostatic properties [106], the temperature dependence of longitudinal relaxation and diffusion in non-aqueous solvents [107], and quadrupolar relaxation in acetonitrile using molecular dynamics simulations [108]. Perhaps more interesting are studies of krypton dissolved in various nematic liquid crystals [97, 109, 110] where, because of the net alignment of the liquid crystal anisotropy, quadrupolar effects can be directly observed through splitting of the ^{83}Kr NMR spectrum. NMR studies of ^{83}Kr and other noble gases in solution have been previously reviewed in detail [111, 112] and therefore will not be discussed further here.

Though krypton in zeolites has been studied indirectly in xenon/krypton mixtures through ^{129}Xe NMR [113], only one study has used ^{83}Kr NMR spectroscopy to probe nanoporous materials [114]. Despite the low sensitivity of natural abundance ^{83}Kr, meaningful ^{83}Kr NMR measurements in zeolites were accomplished in this work within a few hours at both 9.4 T and 14.1 T. Due to quadrupolar interactions, the ^{83}Kr lineshape and chemical shift were found to differ significantly in different zeolite structures. The lineshape depended strongly on cage structure and cation charge inside the zeolite framework. In some Ca^{2+} exchanged zeolites, a field dependence of the ^{83}Kr lineshape

was observed that was attributed to long-range disorder. Interestingly, the ^{83}Kr chemical shift did not reflect in all cases the behavior of the ^{129}Xe chemical shift in the same materials, a phenomenon that remains unexplained thus far and warrants further study.

1.4.2 Spin Exchange Optical Pumping of ^{83}Kr

Although the ability to use the quadrupolar nature of thermally polarized krypton gas to probe porous materials shows promise, it will likely be limited to high surface area, nanoporous materials like zeolites where fast ^{83}Kr longitudinal relaxation times of ~1 ms [114] will allow rapid signal averaging and high gas densities will provide reasonably high signal intensities. Meaningful studies of materials with void spaces on the order of 100 μm will require much higher signal intensities. Fortunately, like ^{129}Xe, the nuclear polarization of ^{83}Kr can be dramatically enhanced by spin exchange with optically pumped alkali metal vapor. To date, much less work has been done to examine the spin exchange physics of ^{83}Kr optical pumping compared to ^{129}Xe or ^{3}He. This may be due partially to rapid krypton relaxation on pump cell walls that can complicate experiments [115]. Also, the small Kr-Rb spin exchange cross-section requires the use higher temperatures leading to high rubidium vapor concentrations that hindered the use of optical detection methods [70] prior to the existence of high power diode array lasers.

In early work, the spin relaxation of rubidium in the presence of krypton gas was studies both experimentally [116] and theoretically [117]. It was concluded that the dominant alkali metal relaxation mechanisms were 'sudden' binary collisions and formation of relatively long-lived Rb-Kr van der Waals molecules. To simplify the theoretical treatment, it was assumed that the rubidium was interacting with a nuclear spin $K = 0$

isotope, so no mention was made of ^{83}Kr nuclear polarization. Some of the results of these works and the works described in the remainder of this section, which are relevant to the spin exchange rate, are presented in Table 1.2.

Table 1.2: Spin Exchange Parameters for ^{83}Kr and with ^{129}Xe Rubidium

Parameter	^{83}Kr	Ref.	^{129}Xe	Ref.
$\langle v\sigma \rangle$	$(2.1\pm0.5)\times10^{-24}$ m^3 s^{-1}	70	10×10^{-22} m^3 s^{-1}	87
			$(3.7\pm0.15\pm0.55)^{-22}$ m^3 s^{-1} [a]	75
			2.8×10^{-21} m^3 s^{-1} [b]	118
			7.4×10^{-21} m^3 s^{-1} [c]	118
			6×10^{-22} m^3 s^{-1}	119
γ_M	63±12 s^{-1}	70	$(1.02\pm0.08)\times10^5$ s^{-1}	87
			$(2.92\pm0.18\pm0.41)\times10^4$ s^{-1} [a]	75
$P_0(NG)$	1280±53 Pa	116	$(3.80\pm0.60)\times10^3$ Pa	75
$P_0(N_2)$	680±40 Pa	70	1.37×10^3 Pa [c]	75
α/h	2.77±0.27 MHz	70	33 MHz	120
	1.8 MHz	120	38±6 MHz [d]	120
$\gamma N/h$	26.85±0.78 MHz	116	65 MHz	120
	21 MHz	120	121±14MHz	74
κ	170	120	310	120
	110±9 Å^3	116	244±44 Å^3	120
η	35	121	-50	121

The data presented for ^{83}Kr represent, to the best of our knowledge, all the available literature data. Spin exchange with ^{129}Xe, however, has been much more extensively studied, and only representative subset of the available literature data is presented.

[a] The first quoted error was due to scatter in the data and the second was systematic error due to temperature variations across the pump cell.

[b] Conducted at a xenon pressure of 60 kPa.

[c] Conducted at a xenon pressure of 200 kPa.

[c] Calculated using the experimental data of and [122]

[d] Calculated using the experimental data of refs. [74] and [122]

Non-equilibrium ^{83}Kr nuclear polarization was first observed by Grover [123] using isotopically enriched samples (72% ^{83}Kr) at low krypton pressures (~1 Torr). This work studied the noble gas polarization by means of a rubidium magnetometer, where the rubidium was mixed the noble gas, and the ^{83}Kr polarization was estimated to be less than 1%. Estimates ^{83}Kr-Rb spin exchange parameters, obtained both from theory and

extrapolated from literature data, were first provided by Walker [120]. Subsequently, Happer and coworkers [70] performed a systematic study of ^{83}Kr spin exchange by measuring the EPR shift of Rb vapor in an optical pumping cells. (See Table 1.2.) In this work, it was also demonstrated that at high pressures, the spin exchange process is dominated by binary collisions.

Additional work by Grover and coworkers [115] investigated the transverse relaxation of spin-polarized ^{83}Kr within cylindrical optical pumping cells. It was found that the relaxation rate and precession frequency depended strongly on the orientation of the cells with respect to the applied magnetic field. In these experiments the rubidium did not completely coat the surface of the cell, and it was found the location of the Rb reservoir influenced the relaxation behavior at a given cell angle. The influence of the Rb location was attributed to different surface krypton adsorption characteristic for the metal and the glass. Also noted was the fact that the cell volume contributed strongly to the relaxation behavior. Together, these results were taken to indicate that the transverse relaxational processes were dominated by quadrupolar interactions resulting from krypton surface adsorption. Using optically detected magnetic resonance in the presence of rubidium vapor, Mehring and coworkers studies the frequency shifts and transverse relaxation of hp ^{83}Kr as a function of pump cell temperature and geometry [124]. Using these data, they were able to measure the absolute value of quadrupolar coupling constant of ^{83}Kr on borosilicate gas, which was found to be 5.61±0.70 MHz. It was also determined that the activation energy E_A for desorption of krypton bound to the borosilicate glass pump cell walls E_A = 0.095±0.005 eV.

References:

1. Levitt, M. H., *Spin Dynamics: Basics of Nuclear Magnetic Resonance*. John Wiley & Sons, LTD: West Sussex, UK, 2001.

2. Callaghan, P. T., *Principles of Nuclear Magnetic Resonance Microscopy*. Oxford University press: New York, 1991.

3. Wind, R. A.; Lewis, R.; Lock, H.; Maciel, G. E., Solid Materials Research with Nmr and Dynamic Nuclear-Polarization Spectroscopy. *Advances in Chemistry Series* **1993**, (229), 45-63.

4. Natterer, J.; Bargon, J., Parahydrogen induced polarization. *Progress in Nuclear Magnetic Resonance Spectroscopy* **1997,** 31, 293-315.

5. Duckett, S. B.; Sleigh, C. J., Applications of the parahydrogen phenomenon: A chemical perspective. *Progress in Nuclear Magnetic Resonance Spectroscopy* **1999,** 34, (1), 71-92.

6. Krjukov, E. V.; O'Neill, J. D.; Owers-Bradley, J. R., Brute force polarization of Xe-129. *Journal of Low Temperature Physics* **2005,** 140, (5-6), 397-408.

7. Eckert, G.; Heil, W.; Meyerhoff, M.; Otten, E. W.; Surkau, R.; Werner, M.; Leduc, M.; Nacher, P. J.; Schearer, L. D., A Dense Polarized He-3 Target Based on Compression of Optically Pumped Gas. *Nuclear Instruments & Methods in Physics Research Section A-Accelerators Spectrometers Detectors and Associated Equipment* **1992,** 320, (1-2), 53-65.

8. Walker, T. G.; Happer, W., Spin-exchange optical pumping of noble-gas nuclei. *Review of Modern Physics* **1997,** 69, (2), 629-642.

9. Middlleton, H.; Black, R. D.; Saam, B.; G.D.Cates; Cofer, G. P.; Guenther, R.; Happer, W.; Hedlund, L. W.; Johnson, G. A.; Shattuck, M. D.; Schwartz, J. C., *Magnetic Resonance in Medicine* **1995,** 33, 271-275.

10. Raftery, D.; Long, H.; Meersmann, T.; Grandinetti, P. J.; Reven, L.; Pines, A., High-Field NMR of Adsorbed Xenon Polarized by Laser Pumping. *Physical Review Letters* **1991,** 66, (5), 584-587.

11. Cleveland, Z. I.; Pavlovskaya, G. E.; Stupic, K. F.; LeNoir, C. F.; Meersmann, T., Exploring hyperpolarized 83Kr by remotely detected NMR relaxometry. *Journal of Chemical Physics* **2006,** 124, 044312.

12. Happer, W., Optical-Pumping. *Reviews of Modern Physics* **1972,** 44, (2), 169-&.

13. Appelt, S.; Baranga, A. B.; Erickson, C. J.; Romalis, M. V.; Young, A. R.; Happer, W., Theory of spin-exchange optical pumping of He-3 and Xe-129. *Physical Review A* **1998,** 58, (2), 1412-1439.

14. Gentile, T. R.; Babcock, E.; Borchers, J. A.; Chen, W. C.; Hussey, D.; Jones, G. L.; Lee, W. T.; Majkzrak, C. F.; O'Donovan, K. V.; Snow, W. M.; Tong, X.; Velthuis, S. G. E. T.; Walker, T. G.; Yan, H., Polarized He-3 spin filters in neutron scattering. *Physica B-Condensed Matter* **2005,** 356, (1-4), 96-102.

15. Middleton, H.; Black, R. D.; Saam, B.; Cates, G. D.; Cofer, G. P.; Guenther, R.; Happer, W.; Hedlund, L. W.; Johnson, G. A.; Juvan, K.; Swartz, J., Mr-Imaging with Hyperpolarized He-3 Gas. *Magnetic Resonance in Medicine* **1995,** 33, (2), 271-275.

16. Hsu, M. F.; Cates, G. D.; Kominis, I.; Aksay, I. A.; Dabbs, D. M., Sol-gel coated glass cells for spin-exchange polarized He-3. *Applied Physics Letters* **2000,** 77, (13), 2069-2071.

17. Babcock, E.; Chann, B.; Walker, T. G.; Chen, W. C.; Gentile, T. R., Limits to the polarization for spin-exchange optical pumping of He-3. *Physical Review Letters* **2006,** 96, (8), 083003.

18. Spector, Z. Z.; Emami, K.; Fischer, M. C.; Zhu, J.; Ishii, M.; Yu, J.; Kadlecek, S.; Driehuys, B.; Panettieri, R. A.; Lipson, D. A.; Gefter, W.; Shrager, J.; Rizi, R. R., A small animal model of regional alveolar ventilation using (HPHe)-He-3 MRI. *Academic Radiology* **2004,** 11, (10), 1171-1179.

19. Fain, S. B.; Altes, T. A.; Panth, S. R.; Evans, M. D.; Waters, B.; Mugler, J. P.; Korosec, F. R.; Grist, T. M.; Silverman, M.; Salerno, M.; Owers-Bradley, J., Detection of age-dependent changes in healthy adult lungs with diffusion-weighted He-3 MRI. *Academic Radiology* **2005,** 12, (11), 1385-1393.

20. Altes, T. A.; Mata, J.; de Lange, E. E.; Brookeman, J. R.; Mugler, J. P., Assessment of lung development using hyperpolarized helium-3 diffusion MR imaging. *Journal of Magnetic Resonance Imaging* **2006,** 24, (6), 1277-1283.

21. Ley, S.; Zaporozhan, J.; Morbach, A.; Eberle, B.; Gast, K. K.; Heussel, C. P.; Biedermann, A.; Mayer, E.; Schmiedeskamp, J.; Stepniak, A.; Schreiber, W. G.; Kauczor, H. U., Functional evaluation of emphysema using diffusion-weighted (3)Helium-magnetic resonance imaging, high-resolution computed tomography, and lung function tests. *Investigative Radiology* **2004,** 39, (7), 427-434.

22. Woods, J. C.; Choong, C. K.; Yablonskiy, D. A.; Bentley, J.; Wong, J.; Pierce, J. A.; Cooper, J. D.; Macklem, P. T.; Conradi, M. S.; Hogg, J. C., Hyperpolarized He-3 diffusion MRI and histology in pulmonary emphysema. *Magnetic Resonance in Medicine* **2006,** 56, (6), 1293-1300.

23. Fain, S. B.; Panth, S. R.; Evans, M. D.; Wentland, A. L.; Holmes, J. H.; Korosec, F. R.; O'Brien, M. J.; Fountaine, H.; Grist, T. M., Early emphysematous changes in asymptomatic smokers: Detection with He-3 MR imaging. *Radiology* **2006,** 239, (3), 875-883.

24. Saam, B.; Happer, W.; Middleton, H., Nuclear-Relaxation of He-3 in the Presence of O-2. *Physical Review A* **1995,** 52, (1), 862-865.

25. Moller, H. E.; Chen, X. J.; Saam, B.; Hagspiel, K. D.; Johnson, G. A.; Altes, T. A.; de Lange, E. E.; Kauczor, H. U., MRI of the lungs using hyperpolarized noble gases. *Magnetic Resonance in Medicine* **2002,** 47, (6), 1029-1051.

26. Eberle, B.; Weiler, N.; Markstaller, K.; Kauczor, H. U.; Deninger, A.; Ebert, M.; Grossmann, T.; Heil, W.; Lauer, L. O.; Roberts, T. P. L.; Schreiber, W. G.; Surkau, R.; Dick, W. F.; Otten, E. W.; Thelen, M., Analysis of intrapulmonary O-2 concentration by NIR imaging of inhaled hyperpolarized helium-3. *Journal of Applied Physiology* **1999,** 87, (6), 2043-2052.

27. Fischer, M. C.; Spector, Z. Z.; Ishii, M.; Yu, J.; Emami, K.; Itkin, M.; Rizi, R., Single-acquisition sequence for the measurement of oxygen partial pressure by hyperpolarized gas MRI. *Magnetic Resonance in Medicine* **2004,** 52, (4), 766-773.

28. Fischer, M. C.; Kadlecek, S.; Yu, J. S.; Ishii, M.; Emami, K.; Vahdat, V.; Lipson, D. A.; Rizi, R. R., Measurements of regional alveolar oxygen pressure using hyperpolarized He-3 MRI. *Academic Radiology* **2005,** 12, (11), 1430-1439.

29. Wild, J. M.; Fichele, S.; Woodhouse, N.; Paley, M. N. J.; Kasuboski, L.; van Beek, J. R., 3D volume-localized pO(2), measurement in the human lung with He-3 MRI. *Magnetic Resonance in Medicine* **2005,** 53, (5), 1055-1064.

30. Cherubini, A.; Bifone, A., Hyperpolarised xenon in biology. *Progress in Nuclear Magnetic Resonance Spectroscopy* **2003,** 42, (1-2), 1-30.

31. Goodson, B. M., Nuclear magnetic resonance of laser-polarized noble gases in molecules, materials, and organisms. *Journal of Magnetic Resonance* **2002,** 155, (2), 157-216.

32. Ito, T.; Fraissard, J., Xe-129 NMR-Study of Xenon Adsorbed on Y Zeolites. *Journal of Chemical Physics* **1982,** 76, (11), 5225-5229.

33. Ripmeester, J. A.; Davidson, D. W., Xe-129 Nuclear Magnetic-Resonance in the Clathrate Hydrate of Xenon. *Journal of Molecular Structure* **1981,** 75, (1), 67-72.

34. Dybowski, C.; Bansal, N.; Duncan, T. M., Nmr-Spectroscopy of Xenon in Confined Spaces - Clathrates, Intercalates, and Zeolites. *Annual Review of Physical Chemistry* **1991,** 42, 433-464.

35. Barrie, P. J.; Klinowski, J., 129Xe NMR as a Probe for the study of microporous solids: a critical review. *Progress in NMR Spectroscopy* **1992,** 24, 91-108.

36. Ratcliffe, C. I., Xenon NMR. *Annual Reports on NMR Spectroscopy* **1998,** 36, 123-221.

37. Springuel-Huet, M. A.; Bonardet, J. L.; Gedeon, A.; Fraissard, J., Xe-129 NMR overview of xenon physisorbed in porous solids. *Magnetic Resonance in Chemistry* **1999,** 37, S1-S13.

38. Bonardet, J. L.; Fraissard, J.; Gedeon, A.; Springuel-Huet, M. A., Nuclear magnetic resonance of physisorbed Xe-129 used as a probe to investigate porous solids. *Catalysis Reviews-Science and Engineering* **1999,** 41, (2), 115-225.

39. Bartik, K.; Choquet, P.; Constantinesco, A.; Duhamel, G.; Fraissard, J.; Hyacinthe, J. N.; Jokisaari, J.; Locci, E.; Lowery, T. J.; Luhmer, M.; Meersmann, T.; Moudrakovski, I. L.; Pavlovskaya, G. E.; Pierce, K. L.; Pines, A.; Ripmeester, J. A.; Telkki, V. V.; Veeman, W. S., Xenon NMR as a probe for microporous and mesoporous solids, polymers, liquid crystals, solutions, flames, proteins, imaging. *Actualite Chimique* **2005**, 16-34.

40. Raftery, D., Xenon NMR Spectroscopy. *Annual Reports on NMR Spectroscopy* **2006,** 57, 205-271.

41. Springuel-Huet, M. A.; Fraissard, J., 129Xe NMR of Xenon adsorbed on the molecular sieves ALPO4-11 and SAPO-11 CSA related to the asymmetry of the adsorption zones. *Chemical Physics Letters* **1989,** 154, 299-302.

42. Ripmeester, J. A.; Ratcliffe, C. I., The Anisotropic Chemical Shift of 129Xe in Molecular Sieve: A Dynamic Averaging Mode. *Journal of Chemical Physics* **1995,** 99, 619-622.

43. Meersmann, T.; Logan, J. W.; Simonutti, R.; Caldarelli, S.; Comotti, A.; Sozzani, P.; Kaiser, L. G.; Pines, A., Exploring single-file diffusion in one-dimensional nanochannels by laser-polarized Xe-129 NMR spectroscopy. *Journal of Physical Chemistry A* **2000,** 104, (50), 11665-11670.

44. Jameson, C. J., Calculations of Xe line shapes in model nanochannels: Grand canonical Monte Carlo averaging of the Xe-129 nuclear magnetic resonance chemical shift tensor. *Journal of Chemical Physics* **2002,** 116, (20), 8912-8929.

45. Soldatov, D. V.; Moudrakovski, I. L.; Grachev, E. V.; Ripmeester, J. A., Micropores in crystalline dipeptides as seen from the crystal structure, He pycnometry,

and Xe-129 NMR spectroscopy. *Journal of the American Chemical Society* **2006,** 128, (20), 6737-6744.

46. Mair, R. W.; Wong, G. P.; Hoffmann, D.; Hürlimann, M. D.; Patz, S.; Schwartz, L. M.; Walsworth, R. L., Probing porous media with gas diffusion NMR. *Physical Review Letters* **1999,** 83, 3324-3327.

47. Mair, R. W.; Hurlimann, M. D.; Sen, P. N.; Schwartz, L. M.; Patz, S.; Walsworth, R. L., Tortuosity measurement and the effects of finite pulse widths on xenon gas diffusion NMR studies of porous media. *Magnetic Resonance Imaging* **2001,** 19, (3-4), 345-351.

48. Mair, R. W.; Sen, M. N.; Hurlimann, M. D.; Patz, S.; Cory, D. G.; Walsworth, R. L., The narrow pulse approximation and long length scale determination in xenon gas diffusion NMR studies of model porous media. *Journal of Magnetic Resonance* **2002,** 156, (2), 202-212.

49. Mair, R. W.; Wang, R.; Rosen, M. S.; Candela, D.; Cory, D. G.; Walsworth, R. L., Applications of controlled-flow laser-polarized xenon gas to porous and granular media study. *Magnetic Resonance Imaging* **2003,** 21, (3-4), 287-292.

50. Wang, R.; Mair, R. W.; Rosen, M. S.; Cory, D. G.; Walsworth, R. L., Simultaneous measurement of rock permeability and effective porosity using laser-polarized noble gas NMR. *Physical Review E* **2004,** 70, (2), 026312.

51. Wang, R. P.; Pavlin, T.; Rosen, M. S.; Mair, R. W.; Cory, D. G.; Walsworth, R. L., Xenon NMR measurements of permeability and tortuosity in reservoir rocks. *Magnetic Resonance Imaging* **2005,** 23, (2), 329-331.

52. Butler, J. P.; Mair, R. W.; Hoffmann, D.; Hrovat, M. I.; Rogers, R. A.; Topulos, G. P.; Walsworth, R. L.; Patz, S., Measuring surface-area-to-volume ratios in soft porous materials using laser-polarized xenon interphase exchange nuclear magnetic resonance. *Journal of Physics-Condensed Matter* **2002,** 14, (13), L297-L304.

53. Pietrass, T., NMR of molecules and surfaces using laser-polarized xenon. *Colloids and Surfaces A-Physicochemical and Engineering Aspects* **1999,** 158, (1-2), 51-57.

54. Albert, M. S.; Cates, G. D.; Driehuys, B.; Happer, W.; Saam, B.; Springer, C. S.; Wishnia, A., Biological Magnetic-Resonance-Imaging Using Laser Polarized Xe-129. *Nature* **1994,** 370, (6486), 199-201.

55. Weathersby, P. K.; Homer, L. D., Solubility of Inert Gases in Biological Fluids: a review. *Undersea Biomedical Research* **1980,** 7, (4), 277-297.

56. Mansson, S.; Wolber, J.; Driehuys, B.; Wollmer, P.; Golman, K., Characterization of diffusing capacity and perfusion of the rat lung in a lipopolysaccaride disease model using hyperpolarized Xe-129. *Magnetic Resonance in Medicine* **2003,** 50, (6), 1170-1179.

57. Ruppert, K.; Brookeman, J. R.; Hagspiel, K. D.; Mugler, J. P., Probing lung physiology with xenon polarization transfer contrast (XTC). *Magnetic Resonance in Medicine* **2000,** 44, (3), 349-357.

58. Ruppert, K.; Mata, J. F.; Brookeman, J. R.; Hagspiel, K. D.; Mugler, J. P., Exploring lung function with hyperpolarized Xe-129 nuclear magnetic resonance. *Magnetic Resonance in Medicine* **2004,** 51, (4), 676-687.

59. Driehuys, B.; Cofer, G. P.; Pollaro, J.; Mackel, J. B.; Hedlund, L. W.; Johnson, G. A., Imaging alveolar-capillary gas transfer using hyperpolarized Xe-129 MRI.

Proceedings of the National Academy of Sciences of the United States of America **2006,** 103, (48), 18278-18283.

60. Mata, J. F.; Altes, T. A.; Cai, J.; Ruppert, K.; Mitzner, W.; Hagspiel, K. D.; Patel, B.; Salerno, M.; Brookeman, J. R.; de Lange, E. E.; Tobias, W. A.; Wang, H. T. J.; Cates, G. D.; Mugler, J. P., Evaluation of emphysema severity and progression in a rabbit model: comparison of hyperpolarized He-3 and Xe-129 diffusion MRI with lung morphometry. *Journal of Applied Physiology* **2007,** 102, (3), 1273-1280.

61. Albert, M. S.; Schepkin, V. D.; Budinger, T. F., Measurement of Xe-129 T1 in Blood to Explore the Feasibility of Hyperpolarized Xe-129 Mri. *Journal of Computer Assisted Tomography* **1995,** 19, (6), 975-978.

62. Swanson, S. D.; Rosen, M. S.; Coulter, K. P.; Welsh, R. C.; Chupp, T. E., Distribution and dynamics of laser-polarized Xe-129 magnetization in vivo. *Magnetic Resonance in Medicine* **1999,** 42, (6), 1137-1145.

63. Swanson, S. D.; Rosen, M. S.; Agranoff, B. W.; Coulter, K. P.; Welsh, R. C.; Chupp, T. E., Brain MRI with laser-polarized Xe-129. *Magnetic Resonance in Medicine* **1997,** 38, (5), 695-698.

64. Ziegler, A.; Hyacinthe, J. N.; Choquet, P.; Duhamel, G.; Grillon, E.; Leviel, J. L.; Constantinesco, A., Laser-polarized xenon nuclear magnetic resonance, a potential tool for brain perfusion imaging: Measurement of the xenon T-1 in vivo. *Imaging in Biological Research, Part A* **2004,** 385, 149-165.

65. Nakamura, K.; Kondoh, Y.; Wakai, A.; Kershaw, J.; Wright, D.; Kanno, I., Xe-129 spectra from the heads of rats with and without ligation of the external carotid and pterygopalatine arteries. *Magnetic Resonance in Medicine* **2005,** 53, (3), 528-534.

66. Hilty, C.; Lowery, T. J.; Wemmer, D. E.; Pines, A., Spectrally resolved magnetic resonance imaging of a xenon biosensor. *Angewandte Chemie-International Edition* **2006,** 45, (1), 70-73.

67. Schroder, L.; Lowery, T. J.; Hilty, C.; Wemmer, D. E.; Pines, A., Molecular imaging using a targeted magnetic resonance hyperpolarized biosensor. *Science* **2006,** 314, (5798), 446-449.

68. Harris, R. K.; Becker, E. D.; De Menezes, S. M. C.; Goodfellow, R.; Granger, P., NMR nomenclature. Nuclear spin properties and conventions for chemical shifts - (IUPAC recommendations 2001). *Pure and Applied Chemistry* **2001,** 73, (11), 1795-1818.

69. Abragam, A., *The Principles of Nuclear Magnetism.* Oxford University Press: Oxford, UK, 1961.

70. Schaefer, S. R.; Cates, G. D.; Happer, W., Determination of Spin-Exchange Parameters between Optically Pumped Rubidium and Kr-83. *Physical Review A* **1990,** 41, (11), 6063-6070.

71. Schaefer, S. R.; Cates, G. D.; Chien, T. R.; Gonatas, D.; Happer, W.; Walker, T. G., Frequency-Shifts of the Magnetic-Resonance Spectrum of Mixtures of Nuclear Spin-Polarized Noble-Gases and Vapors of Spin-Polarized Alkali-Metal Atoms. *Physical Review A* **1989,** 39, (11), 5613-5623.

72. Wagshul, M. E.; Chupp, T. E., Laser Optical-Pumping of High-Density Rb in Polarized He-3 Targets. *Physical Review A* **1994,** 49, (5), 3854-3869.

73. Herman, R. M., Theory of Spin Exchange between Optically Pumped Rubidium and Foreign Gas Nuclei. *Physical Review* **1965,** 137, (4A), 1062-1065.

74. Wu, Z.; Walker, T. G.; Happer, W., Spin-Rotation Interaction of Noble-Gas Alkali-Metal Atom Pairs. *Physical Review Letters* **1985,** 54, (17), 1921-1924.

75. Cates, G. D.; Fitzgerald, R. J.; Barton, A. S.; Bogorad, P.; Gatzke, M.; Newbury, N. R.; Saam, B., Rb Xe-129 Spin-Exchange Rates Due to Binary and 3-Body Collisions at High Xe Pressures. *Physical Review A* **1992,** 45, (7), 4631-4639.

76. Fitzsimmons, W. A.; Tankersley, L. L.; Walters, G. K., Nature of Surface-Induced Nuclear-Spin Relaxation of Gaseous He3. *Physical Review* **1969,** 179, (1), 156-165.

77. Driehuys, B.; Cates, G. D.; Happer, W., Surface Relaxation Mechanisms of Laser-Polarized Xe-129. *Physical Review Letters* **1995,** 74, (24), 4943-4946.

78. Jacob, R. E.; Driehuys, B.; Saam, B., Fundamental mechanisms of He-3 relaxation on glass. *Chemical Physics Letters* **2003,** 370, (1-2), 261-267.

79. Hunt, E. R.; Carr, H. Y., Nuclear Magnetic Resonance of Xe129 in Natural Xenon. *Physical Review* **1963,** 130, (6), 2302-2305.

80. Moudrakovski, I. L.; Breeze, S. R.; Simard, B.; Ratcliffe, C. I.; Ripmeester, J. A.; Seideman, T.; Tse, J. S.; Santyr, G., Gas-phase nuclear magnetic relaxation in Xe-129 revisited. *Journal of Chemical Physics* **2001,** 114, (5), 2173-2181.

81. Adrian, F. J., Quadrupolar Relaxation of Xe131 in Xenon Gas. *Physical Review* **1965,** 138, (2A), A403-409.

82. Schearer, L. D.; Walters, G. K., Nuclear Spin-Lattice Relaxation in Presence of Magnetic-Field Gradients. *Physical Review* **1965,** 139, (5A), 1398-1402.

83. Cates, G. D.; Schaefer, S. R.; Happer, W., Relaxation of Spins Due to Field Inhomogeneities in Gaseous Samples at Low Magnetic-Fields and Low-Pressures. *Physical Review A* **1988,** 37, (8), 2877-2885.

84. Chann, B.; Nelson, I. A.; Anderson, L. W.; Driehuys, B.; Walker, T. G., Xe-129-Xe molecular spin relaxation. *Physical Review Letters* **2002,** 88, (11), 113201.

85. Berry-Pusey, B. N.; Anger, B. C.; Laicher, G.; Saam, B., Nuclear spin relaxation of Xe-129 due to persistent xenon dimers. *Physical Review A* **2006,** 74, (6), 063408.

86. Killian, T. J., Thermionic phenomena caused by vapors of rubidium and potassium. *Physical Review* **1926,** 27, (5), 578-587.

87. Shao, W. J.; Wang, G. D.; Hughes, E. W., Measurement of spin-exchange rate constants between Xe-129 and alkali metals. *Physical Review A* **2005,** 72, (2), 022713.

88. Happer, W.; Miron, E.; Schaefer, S.; Schreiber, D.; Vanwijngaarden, W. a.; Zeng, X., Polarization of the Nuclear Spins of Noble-Gas Atoms by Spin Exchange with Optically Pumped Alkali-Metal Atoms. *Physical Review A* **1984,** 29, (6), 3092-3110.

89. Driehuys, B.; Cates, G. D.; Miron, E.; Sauer, K.; Walter, D. K.; Happer, W., High-volume production of laser-polarized Xe-129. *Applied Physics Letters* **1996,** 69, (12), 1668-1670.

90. Happer, W.; Vanwijngaarden, W. A., An Optical-Pumping Primer. *Hyperfine Interactions* **1987,** 38, (1-4), 435-470.

91. Wagshul, M. E.; Chupp, T. E., Optical-Pumping of High-Density Rb with a Broad-Band Dye-Laser and Gaalas Diode-Laser Arrays - Application to He-3 Polarization. *Physical Review A* **1989,** 40, (8), 4447-4454.

92. Mortuza, M. G.; Anala, S.; Pavlovskaya, G. E.; Dieken, T. J.; Meersmann, T., Spin-exchange optical pumping of high-density xenon-129. *Journal of Chemical Physics* **2003,** 118, (4), 1581-1584.

93. Zerger, J. N.; Lim, M. J.; Coulter, K. P.; Chupp, T. E., Polarization of Xe-129 with high power external-cavity laser diode arrays. *Applied Physics Letters* **2000,** 76, (14), 1798-1800.

94. Rosen, M. S.; Chupp, T. E.; Coulter, K. P.; Welsh, R. C.; Swanson, S. D., Polarized Xe-129 optical pumping/spin exchange and delivery system for magnetic resonance spectroscopy and imaging studies. *Review of Scientific Instruments* **1999,** 70, (2), 1546-1552.

95. Gatzke, M.; Cates, G. D.; Driehuys, B.; Fox, D.; Happer, W.; Saam, B., Extraordinarily Slow Nuclear-Spin Relaxation in Frozen Laser-Polarized Xe-129. *Physical Review Letters* **1993,** 70, (5), 690-693.

96. Cowgill, D. F.; Norberg, R. E., Pulsed Nmr-Studies of Self-Diffusion and Defect Structure in Liquid and Solid Krypton. *Physical Review B* **1976,** 13, (7), 2773-2781.

97. Ingman, P.; Jokisaari, J.; Diehl, P., Kr-83 and Xe-131-Nmr of the Noble-Gases Dissolved in Nematic Liquid-Crystals - Determination of Quadrupole Couplings and Electric-Field Gradients. *Journal of Magnetic Resonance* **1991,** 92, (1), 163-169.

98. Mazitov, R. K.; Enikeev, K. M.; Ilyasov, A. V., Magnetic-Resonance and Relaxation of Nuclei of Atomic Krypton in Liquid Solutions. *Zeitschrift Fur Physikalische Chemie Neue Folge* **1987,** 155, 55-68.

99. Lurie, J.; Feldman, J. L.; Horton, G. K., Nuclear Magnetic Resonance Local-Magnetic-Field Shift in Solid Xenon. *Physical Review* **1966,** 150, (1), 180-185.

100. Brinkmann, D., Local Magnetic Field Shift in Natural Krypton. *Physics Letters A* **1967,** A 25, (7), 520-521.

101. Brinkman, D., Nuclear Magnetic Moments of 83Kr and 39K. *Physics Letters A* **1968,** A 27, (8), 466-467.

102. Cowgill, D. F.; Norberg, R. E., Spin-Lattice Relaxation and Chemical-Shift of Kr-83 in Solid and Liquid Krypton. *Physical Review B* **1973,** 8, (11), 4966-4974.

103. Brinkmann, D.; Kuhn, D., Nuclear Magnetic-Relaxation of Kr-83 in Krypton Gas. *Physical Review A* **1980,** 21, (1), 163-167.

104. Madaras, E. I.; Norberg, R. E., Kr-83 in Solid Krypton.1. Defects and Diffusion. *Physical Review B* **1986,** 33, (9), 5999-6014.

105. Madaras, E. I.; Norberg, R. E., Kr-83 in Solid Krypton.2. Rotating-Frame Relaxation and Spectral Diffusion. *Physical Review B* **1986,** 33, (9), 6015-6024.

106. Vaara, J.; Jokisaari, J.; Rantala, T. T.; Lounila, J., Computational and Experimental-Study of Nmr Relaxation of Quadrupolar Noble-Gas Nuclei in Organic-Solvents. *Molecular Physics* **1994,** 82, (1), 13-27.

107. Holz, M.; Haselmeier, R.; Klein, A.; Mazitov, R. K., Temperature-Dependence of Ne-21, Kr-83, and Xe-131 Quadrupole Relaxation and of Xenon Diffusion in Polyatomic Solvents. *Applied Magnetic Resonance* **1995,** 8, (3-4), 501-519.

108. Odelius, M.; Holz, M.; Laaksonen, A., Quadrupolar relaxation of Ne-21, Kr-83, and Xe-131 dissolved in acetonitrile. A molecular dynamics study. *Journal of Physical Chemistry A* **1997,** 101, (49), 9537-9544.

109. Lounila, J. H.; Muenster, O.; Jokisaari, J.; Diehl, P., Temperature-Dependence of Nuclear Shielding and Quadrupolar Coupling of Noble-Gases in Liquid-Crystals. *Journal of Chemical Physics* **1992,** 97, (12), 8977-8985.

110. Jokisaari, J.; Ingman, P.; Lounila, J.; Pukkinen, O.; Diehl, P.; Muenster, O., Electric-Field Gradients Experienced by the Noble-Gas Isotopes Ne-21, Kr-83 and Xe-131 in Thermotropic Liquid-Crystals. *Molecular Physics* **1993,** 78, (1), 41-54.

111. Jokisaari, J., Nmr of Noble-Gases Dissolved in Isotropic and Anisotropic Liquids. *Progress in Nuclear Magnetic Resonance Spectroscopy* **1994,** 26, 1-26.

112. Luhmer, M.; Reisse, J., Quadrupole NMR relaxation of the noble gases dissolved in simple liquids and solutions - A critical review of experimental data in the light of computer simulation results. *Progress in Nuclear Magnetic Resonance Spectroscopy* **1998,** 33, 57-76.

113. Jameson, C. J.; Jameson, A. K.; Lim, H. M., Competitive adsorption of xenon and krypton in zeolite NaA: Xe-129 nuclear magnetic resonance studies and grand canonical Monte Carlo simulations. *Journal of Chemical Physics* **1997,** 107, (11), 4364-4372.

114. Horton-Garcia, C. F.; Pavlovskaya, G. E.; Meersmann, T., Introducing krypton NMR spectroscopy as a probe of void space in solids. *Journal of the American Chemical Society* **2005,** 127, (6), 1958-1962.

115. Volk, C. H.; Mark, J. G.; Grover, B. C., Spin Dephasing of Kr-83. *Physical Review A* **1979,** 20, (6), 2381-2388.

116. Bouchiat, M. A.; Brossel, J.; Pottier, L. C., Evidence for Rb Rare-Gas Molecules from Relaxation of Polarized Rb-Atoms in a Rare-Gas - Experimental Results. *Journal of Chemical Physics* **1972,** 56, (7), 3703-3714.

117. Bouchiat, C. C.; Bouchiat, M. A.; Pottier, L. C. L., Evidence for Rb-Rare-Gas Molecules from Relaxation of Polarized Rb Atoms in a Rare Gas. Theory. *Physical Review* **1969,** 181, (1), 144-165.

118. Augustine, M. P.; Zilm, K. W., Optical pumping magnetic resonance in high magnetic fields: Measurement of high field spin exchange cross sections. *Chemical Physics Letters* **1997,** 280, (1-2), 24-30.

119. Rice, C. V.; Raftery, D., Rubidium-xenon spin exchange and relaxation rates measured at high pressure and high magnetic field. *Journal of Chemical Physics* **2002,** 117, (12), 5632-5641.

120. Walker, T. G., Estimates of Spin-Exchange Parameters for Alkali-Metal Noble-Gas Pairs. *Physical Review A* **1989,** 40, (9), 4959-4963.

121. Walker, T. G.; Bonin, K.; Happer, W., Electron Noble-Gas Spin-Flip Scattering at Low-Energy. *Physical Review A* **1987,** 35, (9), 3749-3752.

122. Zeng, X.; Wu, Z.; Call, T.; Miron, E.; Schreiber, D.; Happer, W., Experimental-Determination of the Rate Constants for Spin Exchange between Optically Pumped K, Rb, and Cs Atoms and Xe-129 Nuclei in Alkali-Metal Noble-Gas van der Waals Molecules. *Physical Review A* **1985,** 31, (1), 260-278.

123. Grover, B. C., Noble-Gas Nmr Detection through Noble-Gas-Rubidium Hyperfine Contact Interaction. *Physical Review Letters* **1978,** 40, (6), 391-392.

124. Butscher, R.; Wäckerle, G.; Mehring, M., Nuclear quadrupole surface interaction of gas phase 83Kr: comparison with 131 Xe. *Chemical Physics Letters* **1996,** 249, 444-450.

CHAPTER 2

THE PRODUCTION OF HYPERPOLARIZED KRYPTON-83 AND ITS BEHAVIOR AT VARIOUS MAGNETIC FIELD STRENGHTS

The majority of the results presented in this dissertation chapter were previously published as the journal article: Zackary I. Cleveland, Galina E. Pavlovskaya, Karl F. Stupic, Catherine F. LeNoir, and Thomas Meersmann, "Exploring Hyperpolarized Krypton-83 by Remotely Detected NMR Relaxometry", *Journal of Chemical Physics.* **2006,** 124 (4): 044312.

Thomas Meersmann and Zackary I. Cleveland wrote the paper mentioned above. Zackary I. Cleveland collected, or along with other individuals was involved in collecting, all of the data discussed in this chapter. Galina E. Pavlovskaya designed and built the ^{83}Kr NMR probe and the probe shuttling system used in the work and provided editorial assistance in writing the manuscript. Karl F. Stupic assisted in conducting the temperature dependent remote detection, magnetic field strength dependent, and the polarization buildup experiments. Catherine F. LeNoir also assisted with the field dependent relaxation measurements.

2.1 Introduction

For more than a decade, hyperpolarized (hp) ^{3}He and hp ^{129}Xe, both having nuclear spin $I = 1/2$, have been used in an increasing number of applications for nuclear magnetic resonance (NMR) and magnetic resonance imaging (MRI) [1, 2]. The high spin polarization obtained through spin exchange optical pumping (SEOP) [3] leads to signal enhancements of many orders of magnitude over that obtained from thermally polarization and allows for experiments that are otherwise not feasible [4-15]. Another NMR active noble gas isotope, ^{83}Kr ($I = 9/2$), possesses a nuclear electric quadrupole moment that typically dominates the longitudinal (spin-lattice) relaxation [16-18]. This relaxation is caused by coupling of the quadrupole moment to fluctuating electric field gradients (EFGs) generated during gas-phase and surface interactions. Quadrupolar interactions in ^{83}Kr and other quadrupolar noble gases ^{21}Ne and ^{131}Xe (both I = 3/2) cause spin relaxation and coherent spin evolution that can probe the shape, size, and symmetry of void spaces as well as the chemical composition of surfaces in porous media [19-28]. Thus the information provided is highly complementary to that obtained from ^{3}He and ^{129}Xe.

This chapter describes the production of hp ^{83}Kr and its subsequent separation from the rubidium vapor used in the SEOP process. Rubidium free hp ^{83}Kr combined with remote NMR detection [10] proved to be a useful method for investigating quadrupolar relaxation over a large range of magnetic field strengths. Also discussed here are the first investigations of the spin exchange optical pumping process of ^{83}Kr at high (> 100 kPa) krypton gas pressures. Using remotely detected hp ^{83}Kr NMR relaxometry, it was demonstrated that krypton–wall interactions at low magnetic field strengths are a

significant source of signal loss and constrain hp ^{83}Kr NMR signal enhancement to about 3 orders of magnitude below the theoretical limit under these conditions.

2.2 Materials and Methods

Experiments were performed on a Chemagnetics CMX II 400 MHz NMR spectrometer in a 9.4 T wide-bore (89 mm) superconducting magnet using a custom-built flow probe tuned to the ^{83}Kr frequency of 15.4 MHz at 9.4 T. SEOP (See Fig. 2.1A.) of research grade krypton (99.995%, natural abundance; Airgas, Radnor, PA) was performed in cylindrical Pyrex cells (length = 125 mm, ID = 24 mm). The pump cell containing 2.5 to 5.0 g of Rb (99.6%; Sigma-Aldrich, Milwaukee, WI) was housed in a quartz and aluminum oven to maintain a constant temperature, typically ~433 K. Light (794.7 nm) from a 60 W Coherent FAP diode-array laser system (line width 2 nm) was directed through a circular polarizer onto the pump cell. The magnetic field needed for SEOP was provided either by two Helmholtz coils (2.0×10^{-3} T) or the fringe field of the superconducting magnet (0.05 T).

In continuous-flow experiments, the gas mixture was recirculated using a Watson-Marlow Bredel peristaltic pump. Gas flow was monitored with a Gilmont direct-reading flow meter and converted for the gas mixture used. In stopped-flow experiments, ^{83}Kr polarization was allowed to build for several minutes in the pump cell. During this time the detection cell was evacuated to less than 0.1 kPa. Following polarization buildup, the hp gas was rapidly transferred from the pump cell to the detection cell by pressure equalization. In all experiments, the pressure in the pump cell was kept above ambient pressure (100–200 kPa) to avoid contamination by atmospheric oxygen and water vapor.

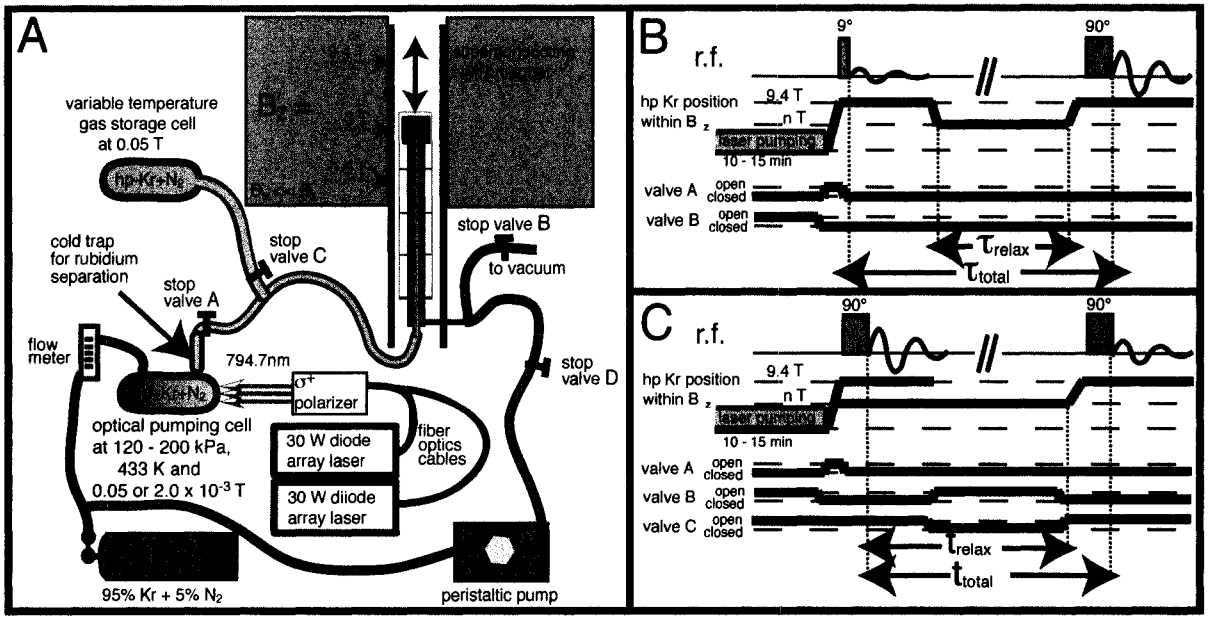

Figure 2.1: Apparatus and procedures used for production and detection of hp ^{83}Kr. **(A)** Experimental setup used for continuous-flow experiments (Valves A & D were permanently open, valves B & C were permanently closed, and the peristaltic pump was operating.); stopped-flow experiments (Valve D was permanently closed. Valve B was open during evacuation but closed during gas transfer and RF pulses.); and remotely detected relaxometry. **(B)** Diagram of stopped-flow experimental procedure used for remotely detected relaxometry with movable probe head. Indicated are the position of ^{83}Kr within the magnetic field, gas valve status, and RF pulse sequence used to obtain field depended T_1 times. **(C)** Diagram of stopped-flow experimental procedure alternately used for remotely detected relaxometry with the gas storage cell at 0.05 T (gas entered and exited through valve C). Indicated are the position of the ^{83}Kr within the magnetic field, gas valve status, and RF pulse sequence.

2.3 Results and Discussion

2.3.1 Hp ^{83}Kr Production under Continuous-flow Conditions

Although SEOP of noble gas isotopes with quadrupolar nuclei had been explored prior to this work [3, 19-22, 29], separation of the hp gas from the paramagnetic and highly reactive alkali metal vapor of optical pumping had never been described for any $I > 1/2$ isotope. The separation process [1, 30, 31] was pivotal for the success of ^{129}Xe and ^{3}He SEOP and is a necessity for any medical and most materials applications. The major obstacle for the production of rubidium free, hp noble gases with $I > 1/2$ is caused by the nuclear electric quadrupole moment, which significantly shortens the longitudinal relaxation (T_1) times of ^{83}Kr. The problem is illustrated by comparing the longitudinal relaxation times of the two NMR active isotopes of the noble gas xenon. ^{129}Xe ($I = 1/2$) has a gas-phase T_1 time on the order of 2 h at near ambient pressures and temperatures [32], but a T_1 relaxation time of only 25 s has been reported for pure gas-phase ^{131}Xe (I = 3/2) at 100 kPa [33, 34]. This relaxation time is further reduced to T_1 = 1-3 s for ^{131}Xe in 8-12 mm diameter glass containers at the same pressure, ambient temperature, and 9.4 T field strength [24, 35]. Relaxation times of only a few seconds are problematic for the pumping process and subsequent transfer into the detection region.

Although the quadrupole moment of ^{83}Kr is about twice that of ^{131}Xe (See Table 1.1.), quadrupole interactions are usually smaller for krypton compared to xenon due to krypton's larger nuclear spin, smaller and less polarizable electron cloud, and smaller Sternheimer antishielding factor. The reduced quadrupolar interactions for krypton are reflected in the long T_1 of 470 s expected in the absence of container walls at 300 K, 100 kPa, and 2.1 T based on the work of Brinkmann and Kuhn [18]. Even in 10–12.5 mm

diameter and 4-5 cm long glass cylinders used in the currently discussed work, the T_1 times were found to be 90–150 s at 297 K, 100-200 kPa, and 9.4 T.

The setup used for ^{83}Kr optical pumping was similar to those used previsously for hp ^{129}Xe [9, 31, 36, 37]. In 'typical' xenon optical pumping, a low concentration of xenon (1–5%) in helium at 500–800 kPa is used to obtain spin polarizations up to 70% [31, 38, 39]. Because the hp ^{129}Xe signal intensity is a product of both concentration and spin polarization, a subsequent separation from helium via xenon freezing and sublimation is usually applied. The duration of this process ranges from minutes to tens of minutes and is possible because the long solid-state T_1 relaxation time of ^{129}Xe (~2 h) preserves spin polarization [40]. This separation is probably not possible for hp ^{83}Kr due to its short solid-state relaxation time of $T_1 < 10$ s [17] at liquid nitrogen temperatures. The problem was bypassed in this work by performing high density optical pumping [41]. Fig. 2.1 depicts the experimental setup and operational modes described in this chapter. Optical pumping takes place in a Pyrex cell at approximately 433 K under illumination by 30 or 60 W of circularly polarized 794.7 nm light. The gas mixture used for all experiments consisted of 95% natural abundance krypton (11.5% ^{83}Kr) and 5% N_2 (added for radiation quenching [42]).

Fig. 2.2A shows the first successful production of continuous-flow, hp ^{83}Kr where a 27-fold signal enhancement compared to thermally polarized ^{83}Kr at ambient pressure, room temperature, and 9.4 T was obtained. Laser intensity, pump cell temperature, and gas flow were held constant while the magnetic field generated by a Helmholtz coil pair was varied. As expected, nonequilibrium ^{83}Kr spin polarization was generated only in the presence of a magnetic field and inverted when the field was inverted. Note that the NMR

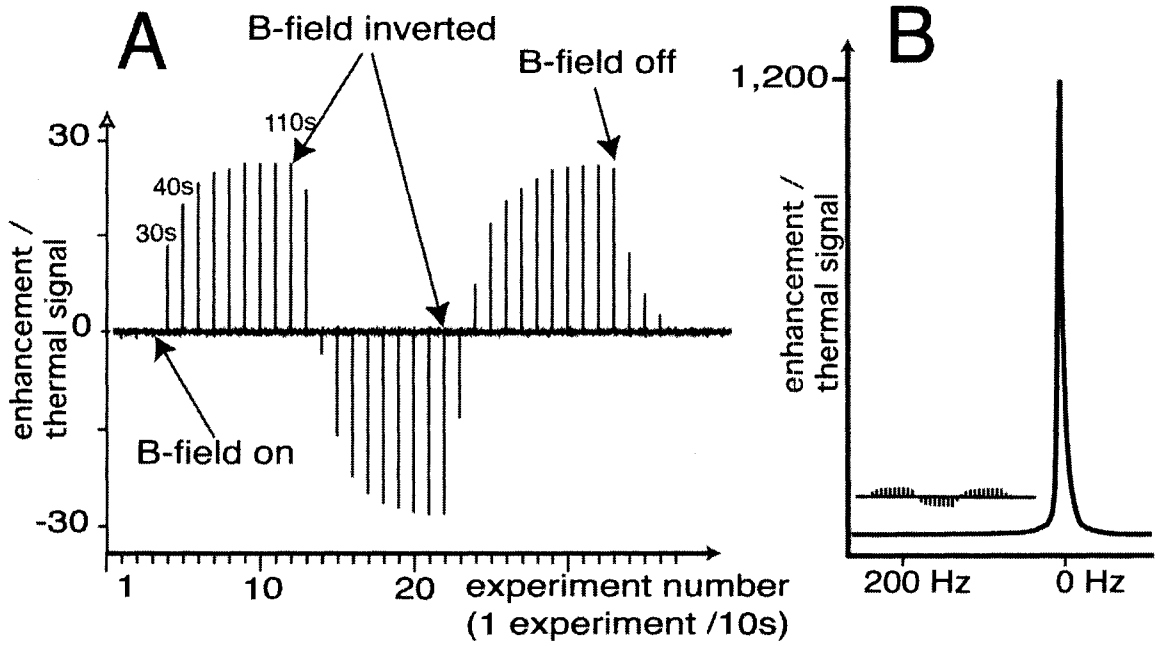

Figure 2.2: Enhancement of the ^{83}Kr NMR signal by spin exchange optical pumping. **(A)** Hp ^{83}Kr NMR spectrum recorded every 10 s under continuous-flow optical pumping conditions. The magnetic (B) field at the SEOP cell was switched on, twice inverted in direction, and finally switched off at the times indicated. The small signal at the beginning of the experiments arose from optical pumping in the arbitrarily aligned stray field from the superconducting NMR magnet. The effect on the NMR spectrum was time delayed, because the krypton flowed at a rate of 2.5 cm^3/s through approximately 3.5 m of PFA tubing into the high field detection region. The maximum enhancement factor was 27 times the thermal equilibrium signal at 9.4 T **(B)** Hp ^{83}Kr NMR signal obtained from a stopped-flow experiment with an enhancement factor of 1200 times the thermal signal at 9.4 T. The inset shows the spectrum from the continuous-flow experiment of Fig. 2.2A set to scale.

detection of these processes was delayed by the duration of gas transport into the detection cell.

Fig. 2.3 shows that, at a given pressure, the hp ^{83}Kr signal intensity was low at relatively low flow rates. As the flow rate was increased, the signal intensity increased to a maximum value before declining. This suggests that the signal observed under continuous flow conditions was influenced by two competing factors. Signal intensity was increased by longer residence times in the pump cell because greater initial polarization was achieved. Unfortunately, the low flow conditions that allowed for the longest residence times in the SEOP cell also increased the time needed for hp ^{83}Kr to reach the detection region. During this time, significant relaxation occurred as a result of interactions with the transfer tubing surface and lower the observed signal intensity.

Fig. 2.3 also displays a dependence of the observed signal intensity on the pressure. As the pressure was increased, the maximum signal intensity also increased. This is unsurprising because increasing the pressure increased the number density of the observed ^{83}Kr atoms. The influence of increased spin density was to some extent offset by lower non-equilibrium polarization that can be achieved at higher noble gas densities due to both reduced rubidium polarization and increased longitudinal relaxation. The data presented in Fig. 2.3 also seem to indicate that the maximum signal intensities are reached using higher flow rates at the higher gas pressures. This behavior likely results from increased relaxation experienced by ^{83}Kr at higher pressures (i.e. higher densities). The role of gas density on the longitudinal relaxation rate will be discussed in detail in Chapter 4.

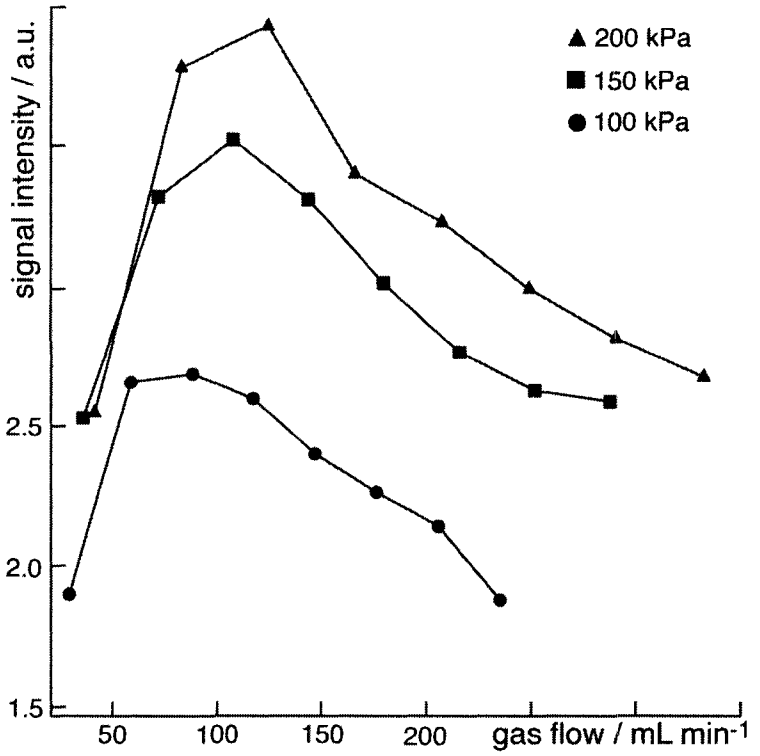

Figure 2.3: Hp ^{83}Kr signal intensity, in arbitrary units, produced under continuous-flow conditions as a function of gas flow rate. The experiments were performed at the three gas pressures indicated in the legend. The signal was obtained by averaging 16 individual scans to produce a single data point. Throughout the data collection, pump cell temperature was maintained at a nearly constant temperature of ~430 K.

A ^{83}Kr signal enhancement of less than 30 times that of thermal polarization at 9.4 T obtained under continuous-flow stands in stark contrast to enhancements of about 3 orders of magnitude reported for ^{129}Xe optical pumping under similar conditions [41]. Significant differences in the optimal optical pumping of the two noble gases are the need for a faster krypton gas flow of about 1.5–2.8 cm^3/s at a temperature of 433 K, while a gas flow of 1.0–1.5 cm^3/s at 395 K leads to optimization with ^{129}Xe. Higher flow rates appear to partially offset ^{83}Kr relaxation in the PFA transfer tubing. This idea is supported by signal enhancements up to 1200 times the thermal equilibrium value at 9.4 T obtained in the krypton shuttling experiments described in the Section 2.3.3.

2.3.2 Polarization Buildup of Hp ^{83}Kr in Batch-mode

The second optical pumping procedure (stopped-flow) led to signal enhancements that were 1200 times greater than the thermal signal at 9.4 T and 297 K (Fig. 2.2B). Following a SEOP period of many minutes, the hp ^{83}Kr was rapidly shuttled into the pre-evacuated detection cell by pressure equalization. This procedure is reminiscent of ^{3}He batch mode optical pumping where prolonged pumping times are needed, because the small rubidium–helium spin exchange cross-sections result in small spin exchange rates [3]. Long SEOP times are also required for ^{83}Kr optical pumping, because the relevant cross-sections for the rubidium–krypton system are about two order of magnitude smaller [3, 29] than those in the rubidium–xenon system [43] (See Table 1.2.). This is a particular problem for krypton in continuous-flow spin exchange experiments, which require high flow rates to reduce hp ^{83}Kr relaxation in the gas transfer tubing. However, high flow also prohibits prolonged pumping times and limits the polarization enhancement that can be achieved.

The 40-fold improvement in stopped-flow experiments over that observed in continuous-flow experiments thus resulted from both increased pumping times and reduced polarization losses during transfer between the optical pumping and detection cells.

The pumping time dependence of the hp ^{83}Kr signal enhancement in batch-mode experiments is shown in Fig. 2.4 for two different laser powers (30 and 60 W). In these experiments, the pump cell was maintained at 433 K under constant laser illumination with no magnetic field present (other than the stray field from the superconducting magnet) to obtain consistent initial thermal conditions with little or no spin polarization present (See Fig. 2.2A.). The magnetic field was then turned on for an optical pumping period, t_p, after which the hp ^{83}Kr was shuttled into the detection cell.

The dependence of the ^{83}Kr polarization $P(Kr)$ upon t_p is described by [36]

$$P_{Kr}(t_p) = \frac{\gamma_{se}}{\gamma_{se} + |\Gamma|} \cdot \frac{\gamma_{op(z)}}{\gamma_{op(z)} + \sum_i \kappa_{sd}^i [M_i]} \left(1 - e^{-(\gamma_{se}+\Gamma)t_p}\right). \qquad (2.3.1)$$

The ^{83}Kr self-relaxation rate, Γ, is caused primarily by quadrupolar interactions during interactions with pump cell walls, krypton atoms, or other gas-phase atoms and cannot be treated as negligible as is the case for ^{129}Xe optical pumping [36]. The Rb–Kr spin exchange rate, γ_{se}, in these high krypton density experiments was probably caused primarily by binary collision under these experimental conditions [29]. Note that γ_{se} is positive during optical pumping while Γ is negative. The ^{83}Kr quadrupolar self-relaxation thus limited the overall polarization produced during optical pumping and slowed the buildup rate. In Eq. 2.3.1, the destruction of Rb spin polarization by collisions with buffer gas atoms is

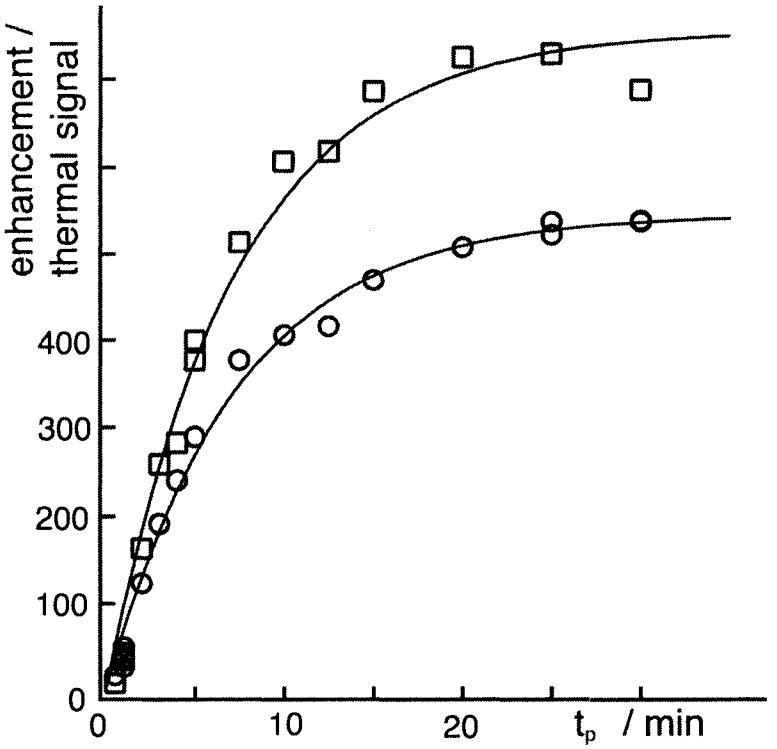

Figure 2.4: Enhancement over thermal signal of hp ^{83}Kr NMR as a function of polarization time. Data were collected using two different laser powers (60 W – open squares and 30 W – open circles). The curves were produced by fitting the data to a simplified form of Eq. 2.3.1, which used one pre-exponential fitting parameter (the maximum enhancement factor) and the exponential fitting parameter $(\gamma_{se} + \Gamma)$. The highest signal enhancement was about half that shown in Fig. 2.2B, because a slightly different experimental setup with a longer transfer tubing was used.

described by the sum of the products of the rate constants, κ_{sd}^{i}, with their corresponding gas atom number densities $[M_i]$.

The optical pumping rate per Rb atom, $\gamma_{op}(z)$, depends on position in the pump cell, z, due to reduced laser intensity along the optically thick beam path [44]. Because these measurements were performed in a cell with fixed dimensions, identical gas mixture, and constant temperature, all terms except $\gamma_{op}(z)$, which also depends on applied laser power, can be taken as constants. Thus, $\gamma_{op}(z)$ can be replaced by the mean optical pumping rate, $\bar{\gamma}_{op}$. The obtained signal enhancements as a function of t_p were fit to a simplified form of Eq. 2.3.1 using a single pre-exponential (i.e. the maximum hp ^{83}Kr intensity that would be obtained at infinitely long pumping times) and an single exponential fitting parameter. The pre-exponential factors for the two curves differed by about 40% for the two laser powers reflecting differences in optical pumping efficiencies. However, virtually identical exponential terms $(\gamma_{se}+\Gamma)$ = (2.2 ± 0.1) x10^{-3} s^{-1} and (2.3 ± 0.2) x10^{-3} s^{-1} were obtained for the 30 W and 60 W data respectively.

2.3.3 Field Dependence of ^{83}Kr Longitudinal Relaxation

Though the PFA transfer tubing's high internal surface-to-volume ratio (ID = 1.65 mm) favors quadrupolar relaxation, measurements at 9.4 T in materials with similar surface compositions and larger surface to volume ratios suggest that T_1 times of tens of seconds should be expected in the tubing [45] (See Chapter 3.). This relaxation is too slow to cause the depolarization observed during the 10 s or less needed for gas transfer under

continuous-flow conditions. However, little is known about ^{83}Kr quadrupolar T_1 relaxation on surfaces in low magnetic fields, and a significant portion of the transfer tubing, as well as the pump cell itself, was located in low field regions. Fig. 2.1B displays the experimental procedure for remotely detected NMR experiments that enabled ^{83}Kr relaxation measurements at a variety of field strengths. After optical pumping, hp ^{83}Kr was shuttled into the 12.5 mm ID Pyrex detection cell at 9.4 T. Signal from a small flip angle reference pulse, which destroyed a negligible amount of the nonequilibrium spin polarization, was acquired to correct for fluctuations in optical pumping efficiency. The detection cell was then physically moved into a position at known field strength for a period, τ_{relax}, before returning it to the 9.4 T region where signal was acquired from a final 90° pulse.

Fig. 2.5A displays the hp ^{83}Kr signal intensity as a function of τ_{relax} at various field strengths. The corresponding T_1 times obtained from mono-exponential fitting of these decay curves are summarized in Fig. 2.5B. The longitudinal relaxation times decrease by a factor of 2.3 if the field was lowered from 9.4 T to 0.15 T, which was the lowest field strength that could be studied using the setup shown in Fig. 2.1. As discussed in Chapter 1, the standard expressions for quadrupolar relaxation [45] are expected to become magnetic field independent at lower field strengths because the rapid narrowing condition is likely to be fulfilled, i.e. $\tau_c^2\omega_0^2 << 1$, where τ_c is approximately the mean ^{83}Kr surface adsorption time. If rapid narrowing condition were violated ($\tau_c^2\omega_0^2 \sim 1$), higher rank tensor elements or non-Bolzmann population distributions could have been created, and the mono-exponential relaxation would no longer be expected [17, 25, 46]. No evidence

for multi-exponential ^{83}Kr T_1 relaxation in glass containers at 297 K and high field strengths was found that would explain the observed field dependence in Fig. 2.5. However, field dependent surface relaxation has been observed at low fields in the case of hp ^{129}Xe [47], where the effect was attributed to dipole coupling to paramagnetic sites on the surface.

Another relaxation mechanism know to be strongly field dependent is caused by diffusion through inhomogeneous magnetic fields [48, 49]. However, this source can safely be excluded for hp ^{83}Kr relaxation reported in this work. The relaxation rate of hp gases in the presence of field inhomogeneities is given by

$$\frac{1}{T_1} = D \cdot \frac{\left|\vec{\nabla} B_x\right|^2 + \left|\vec{\nabla} B_y\right|^2}{B_z^2} \cdot \frac{1}{1+\omega_0^2 \tau_c^2}, \tag{2.3.2}$$

where D is the gas diffusion constant, B_z is the static magnetic field strength, $\left|\vec{\nabla} B_x\right|$ and $\left|\vec{\nabla} B_y\right|$ are the gradients of the x and y components of the magnetic field respectively. In Eq. 2.3.2, τ_c is approximately the time between gas-phase collisions. The expression $(1+\omega_0^2\tau_c^2)^{-1}$ can be neglected, because $\omega_0^2\tau_c^2 << 1$. Although the field gradient $\vec{\nabla} B_z$ in the stray field of a superconducting magnet is known to be large, the maximum $\left|\vec{\nabla} B_x\right|$ and $\left|\vec{\nabla} B_y\right|$ gradients examined in this study were found at the lowest magnetic field strength (B_z = 0.15 T) and were determined to be far less than 0.01 T/cm. Therefore the ^{83}Kr diffusion in the magnetic field gradient would have produced spin-lattice relaxation times of hundreds of seconds or more and should not have competed with quadrupolar relaxation.

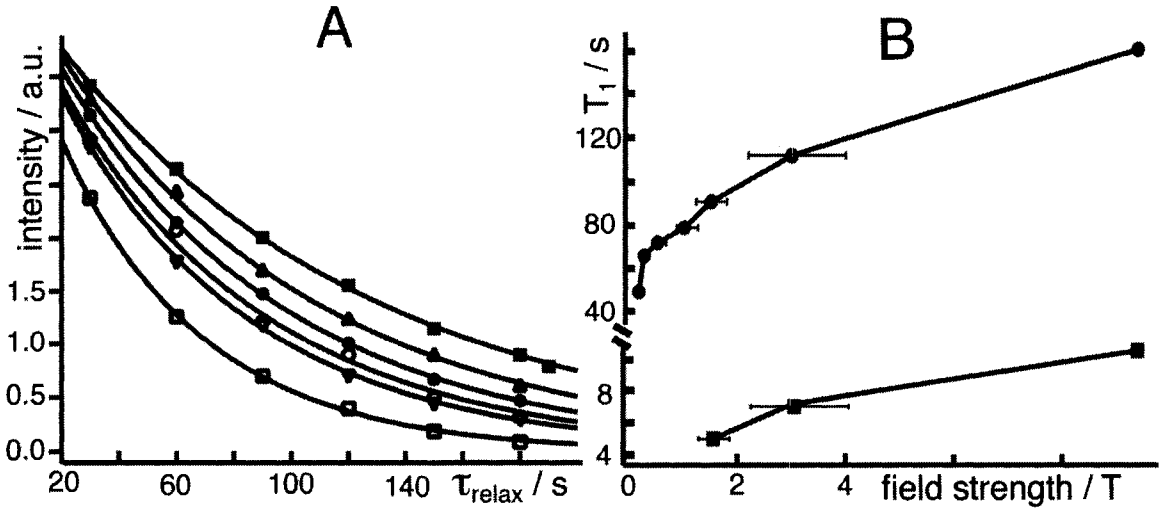

Figure 2.5: Field dependent longitudinal relaxation of hp ^{83}Kr. **(A)** Longitudinal relaxation decay curves. Data were collected a six different magnetic field strengths (3.0 T – closed squares, 1.5 T – closed triangles, 1.0 T – closed circles, 0.5 T – open circles, 0.25 T – open triangles, and 0.15 T – open squares). The reported intensities were obtained using the RF pulse sequence shown in Fig. 2.1B, and the curves are mono-exponential fittings of these data. The reported field strengths were at the center of the 40 mm sample region. **(B)** T_1 as a function of field strength in gas-phase (closed circles) and desiccated canine lung tissue (closed squares). All values, except the highest field strength (9.4 T) values, were calculated from mono-exponential fitting of longitudinal relaxation decay curves. The 9.4 T values were calculated by nonlinear least squares fitting of the ^{83}Kr signal as a function of time and number of applied medium flip angle (~12°) RF pulses. The horizontal bars represent the lower and upper limits of the field strength along B_z within the sample region (See Fig. 2.1A.). The lines in Fig. 2.5B are intended to guide the eye only.

A final source of the observed behavior could be that the standard expressions for relaxation no longer apply. An underlying assumption of relevant Redfield relaxation theory [50, 51] is that the interactions responsible for relaxation are small perturbations to the Zeeman Hamiltonian. The absolute value of the quadrupolar coupling for ^{83}Kr on Duran glass surfaces was previously found to be 5.6 MHz [21], while the ^{83}Kr Larmor frequency is 1.64 MHz/T. Clearly more theoretical and experimental work using more well defined magnetic fields is needed to quantitatively describe these observations.

The setup described here was also used to probe the feasibility of hp ^{83}Kr for pulmonary studies. Promising hp ^{83}Kr MRI studies of desiccated canine lung tissue at 9.4 T were reported elsewhere [52] (See Chapter 3.), and the relaxation time of krypton in this tissue at 9.4 T was found to be T_1 = 10.5 s. Using the setup described in Fig. 2.1B, relaxation times of T_1 = 7 s at 3 T and T_1 = 5 s at 1.5 T were found. These results are useful to assess the limitations of low field hp ^{83}Kr MRI. The increase in longitudinal relaxation rates with decreasing field strengths in lung tissue is similar to the trend found in the empty Pyrex cell despite the very different timescales of the relaxation. This further affirms that the spin-lattice relaxation is dominated by surface interactions rather than diffusion though magnetic field inhomogeneities, because the porous structure of the tissue would have restricted diffusive motion.

2.3.4 Temperature Dependent Relaxation Measured by Remote Detection

The experimental setup described Fig. 2.1C is reminiscent of remotely detected hp ^{129}Xe MRI reported by Pines and coworkers [10]. The hp ^{83}Kr was vacuum shuttled into a storage cell through valve C (Fig. 2.1A) and simultaneously into the detection cell where a

90° reference pulse was applied. After relaxation in a 24 mm ID and 53 mm long Pyrex storage cell during τ_{relax} and a second evacuation of the detection cell, the hp ^{83}Kr was again shuttled into the detection region, and signal was acquired from a second 90° pulse. Data collected using this technique are presented in Fig. 2.6. The longitudinal relaxation of T_1 = 85 s measured at 0.05 T and 297 K is relatively long given the general trend of Fig. 2.5B. However, the surface-to-volume ratio was about 2 times lower for the experiment shown in Fig. 2.6 compared to the one in Fig. 2.5B, and surface induced relaxation was thus decreased.

Except for the length and presence of rubidium, the storage and pump cells were identical, and at 433 K and 0.05 T (the SEOP cell operating conditions), a relaxation time of T_1 = 220 s ($\Gamma = -4.55\times10^{-3}$ s^{-1}) was found. From this rate and the value of $(\gamma_{se} + \Gamma)$, the spin exchange rate $\gamma_{se} \approx 6.8\times10^{-3}$ s^{-1} was calculated. This high value was possible only from the high rubidium number densities found at elevated temperatures [29, 41]. High temperatures are therefore required for krypton SEOP to reduce the quadrupolar relaxation on surfaces and increase the Rb-Kr spin exchange rate allowing for $\gamma_{se} > |\Gamma|$. The relaxation rate Γ will be reduced in pump cells with larger spatial dimensions and should allow for optical pumping at lower spin exchange rates and provide the improved optical pumping conditions generally found at lower temperatures. This temperature dependence further argues that field inhomogeneities are not the source of the T_1 field dependence, because Eq. 2.3.2 predicts a shorter T_1 at higher temperatures due to an increased diffusion constant.

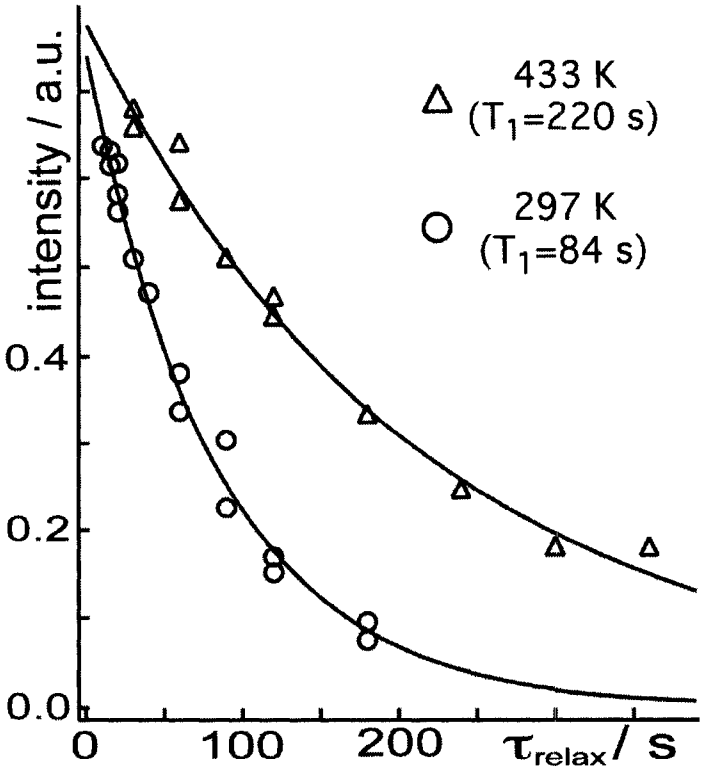

Figure 2.6: Remotely detected longitudinal relaxation decay curves at 0.05 T. The data were produced by the procedure described in Fig. 2.1C and were collected at two storage cell temperatures. The curves were produced by mono-exponential fitting of these data. T_1 times determined for each cell temperature are indicated in the legend.

2.4 Conclusions

A hyperpolarized noble gas with quadrupolar nuclei (hp ^{83}Kr) free from paramagnetic and highly reactive rubidium vapor was produced for the first time. Signal enhancements up to 1200 times that of thermally polarized ^{83}Kr were obtained using high density ^{83}Kr optical pumping that led to ^{83}Kr NMR signals strong enough for MRI applications. Further improvements may come from the use of laser line width narrowing external cavity devices [53], increased laser power [38], and isotopic enrichment. Improved ^{83}Kr optical pumping is also expected in light of the relaxation studies presented in this chapter, which may lead to improved SEOP and gas transfer system designs. For instance, an obvious improvement for ^{83}Kr SEOP would be the use of gas transport tubing with larger internal diameters. A strongly field dependent T_1 relaxation caused by surface interactions was observed by remotely detected NMR relaxometry with hp ^{83}Kr. Additionally, the T_1 of hp ^{83}Kr was shown to increase with increasing surface temperature due to reduced surface adsorption times. These results cannot be explained by relaxation caused by diffusion through inhomogeneous magnetic fields.

The results presented in this chapter are encouraging for further increasing the hp ^{83}Kr signal intensity and suggest that *in vivo* hp ^{83}Kr MRI at 1.5 T may be feasible. The experimental protocols are highly reproducible and will be useful for future quadrupolar relaxation studies of noble gases at a variety of magnetic field strengths. A potential future application of remotely detected hp ^{83}Kr relaxometry is surface investigation of electrically conducting materials that cannot be directly studied by conventional NMR.

References:

1. Raftery, D.; Long, H.; Meersmann, T.; Grandinetti, P. J.; Reven, L.; Pines, A., High-Field NMR of Adsorbed Xenon Polarized by Laser Pumping. *Physical Review Letters* **1991,** 66, (5), 584-587.

2. Goodson, B. M., Nuclear magnetic resonance of laser-polarized noble gases in molecules, materials, and organisms. *Journal of Magnetic Resonance* **2002,** 155, (2), 157-216.

3. Walker, T. G.; Happer, W., Spin-exchange optical pumping of noble-gas nuclei. *Review of Modern Physics* **1997,** 69, (2), 629-642.

4. Navon, G.; Song, Y. Q.; Room, T.; Appelt, S.; Taylor, R. E.; Pines, A., Enhancement of solution NMR and MRI with laser-polarized xenon. *Science* **1996,** 271, (5257), 1848-1851.

5. Raftery, D.; MacNamara, E.; Fisher, G.; Rice, C. V.; Smith, J., Optical pumping and magic angle spinning: Sensitivity and resolution enhancement for surface NMR obtained with laser-polarized xenon. *Journal of the American Chemical Society* **1997,** 119, (37), 8746-8747.

6. Haake, M.; Pines, A.; Reimer, J. A.; Seydoux, R., Surface-enhanced NMR using continuous-flow laser-polarized xenon. *Journal of the American Chemical Society* **1997,** 119, (48), 11711-11712.

7. Tseng, C. H.; Wong, G. P.; Pomeroy, V. R.; Mair, R. W.; Hinton, D. P.; Hoffmann, D.; Stoner, R. E.; Hersman, F. W.; Cory, D. G.; Walsworth, R. L., Low-field MRI of laser polarized noble gas. *Physical Review Letters* **1998,** 81, (17), 3785-3788.

8. Mair, R. W.; Wong, G. P.; Hoffmann, D.; Hurlimann, M. D.; Patz, S.; Schwartz, L. M.; Walsworth, R. L., Probing porous media with gas diffusion NMR. *Physical Review Letters* **1999,** 83, (16), 3324-3327.

9. Anala, S.; Pavlovskaya, G. E.; Pichumani, P.; Dieken, T. J.; Olsen, M. D.; Meersmann, T., In situ NMR spectroscopy of combustion. *Journal of the American Chemical Society* **2003,** 125, (43), 13298-13302.

10. Moule, A. J.; Spence, M. M.; Han, S. I.; Seeley, J. A.; Pierce, K. L.; Saxena, S.; Pines, A., Amplification of xenon NMR and MRI by remote detection. *Proceedings of the National Academy of Sciences of the United States of America* **2003,** 100, (16), 9122-9127.

11. Dubois, L.; Da Silva, P.; Landon, C.; Huber, J. G.; Ponchet, M.; Vovelle, F.; Berthault, P.; Desvaux, H., Probing the hydrophobic cavity of Lipid Transfer Protein from Nicotiana tabacum through xenon-based NMR spectroscopy. *Journal of the American Chemical Society* **2004,** 126, (48), 15738-15746.

12. Moudrakovski, I. L.; Wang, L. Q.; Baumann, T.; Satcher, J. H.; Exarhos, G. J.; Ratcliffe, C. I.; Ripmeester, J. A., Probing the geometry and interconnectivity of pores in organic aerogels using hyperpolarized Xe-129 NMR spectroscopy. *Journal of the American Chemical Society* **2004,** 126, (16), 5052-5053.

13. Jansch, H. J.; Gerhard, P.; Koch, M., Xe-129 on Ir(111): NMR study of xenon on a metal single crystal surface. *Proceedings of the National Academy of Sciences of the United States of America* **2004,** 101, (38), 13715-13719.

14. Lowery, T. J.; Doucleff, M.; Ruiz, E. J.; Rubin, S. M.; Pines, A.; Wemmer, D. E., Distinguishing multiple chemotaxis Y protein conformations with laser-polarized Xe-129 NMR. *Protein Science* **2005,** 14, (4), 848-855.

15. Appelt, S.; Hasing, F. W.; Kuhn, H.; Perlo, J.; Blumich, B., Mobile high resolution xenon nuclear magnetic resonance spectroscopy in the earth's magnetic field. *Physical Review Letters* **2005,** 94, (19), 197602.

16. Cowgill, D. F.; Norberg, R. E., Spin-Lattice Relaxation and Chemical-Shift of Kr-83 in Solid and Liquid Krypton. *Physical Review B* **1973,** 8, (11), 4966-4974.

17. Cowgill, D. F.; Norberg, R. E., Pulsed Nmr-Studies of Self-Diffusion and Defect Structure in Liquid and Solid Krypton. *Physical Review B* **1976,** 13, (7), 2773-2781.

18. Brinkmann, D.; Kuhn, D., Nuclear Magnetic-Relaxation of Kr-83 in Krypton Gas. *Physical Review A* **1980,** 21, (1), 163-167.

19. Wu, Z.; Schaefer, S.; Cates, G. D.; Happer, W., Coherent interactions of polarized nuclear spins of gaseous atoms with container walls. *Physical Review A* **1988,** 37, (4), 1161-1175.

20. Butscher, R.; Wäckerle, G.; Mehring, M., Nuclear quadrupole interaction of highly polarized gas phase 131Xe with a glass surface. *Journal of Chemical Physics* **1994,** 100, (9), 6923-6933.

21. Butscher, R.; Wäckerle, G.; Mehring, M., Nuclear quadrupole surface interaction of gas phase 83Kr: comparison with 131 Xe. *Chemical Physics Letters* **1996,** 249, 444-450.

22. Raftery, D.; Long, H. W.; Shykind, D.; Grandinetti, P. J.; Pines, A., Multiple-Pulse Nuclear-Magnetic-Resonance of Optically Pumped Xenon in a Low Magnetic-Field. *Physical Review A* **1994,** 50, (1), 567-574.

23. Jokisaari, J.; Ingman, P.; Lounila, J.; Pukkinen, O.; Diehl, P.; Muenster, O., Electric-Field Gradients Experienced by the Noble-Gas Isotopes Ne-21, Kr-83 and Xe-131 in Thermotropic Liquid-Crystals. *Molecular Physics* **1993,** 78, (1), 41-54.

24. Meersmann, T.; Smith, S. A.; Bodenhausen, G., Multiple-quantum filtered xenon-131 NMR as a surface probe. *Physical Review Letters* **1998,** 80, (7), 1398-1401.

25. Meersmann, T.; Deschamps, M.; Bodenhausen, G., Probing aerogels by multiple quantum filtered Xe-131 NMR spectroscopy. *Journal of the American Chemical Society* **2001,** 123, (5), 941-945.

26. Moudrakovski, I. L.; Ratcliffe, C. I.; Ripmeester, J. A., Xe-131, a new NMR probe of void space in solids. *Journal of the American Chemical Society* **2001,** 123, (9), 2066-2067.

27. Millot, Y.; Man, P. P.; Springuel-Huet, M. A.; Fraissard, J., Quantification of electric-field gradient in the supercage of Y zeolites with Xe-131 (I=3/2) NMR. *Comptes Rendus De L Academie Des Sciences Serie II Fascicule C-Chimie* **2001,** 4, (11), 815-818.

28. Horton-Garcia, C. F.; Pavlovskaya, G. E.; Meersmann, T., Introducing krypton NMR spectroscopy as a probe of void space in solids. *Journal of the American Chemical Society* **2005,** 127, (6), 1958-1962.

29. Schaefer, S. R.; Cates, G. D.; Happer, W., Determination of Spin-Exchange Parameters between Optically Pumped Rubidium and Kr-83. *Physical Review A* **1990,** 41, (11), 6063-6070.

30. Rosen, M. S.; Chupp, T. E.; Coulter, K. P.; Welsh, R. C.; Swanson, S. D., Polarized Xe-129 optical pumping/spin exchange and delivery system for magnetic resonance spectroscopy and imaging studies. *Review of Scientific Instruments* **1999,** 70, (2), 1546-1552.

31. Knagge, K.; Prange, J.; Raftery, D., A continuously recirculating optical pumping apparatus for high xenon polarization and surface NMR studies. *Chemical Physics Letters* **2004,** 397, (1-3), 11-16.

32. Moudrakovski, I. L.; Breeze, S. R.; Simard, B.; Ratcliffe, C. I.; Ripmeester, J. A.; Seideman, T.; Tse, J. S.; Santyr, G., Gas-phase nuclear magnetic relaxation in Xe-129 revisited. *Journal of Chemical Physics* **2001,** 114, (5), 2173-2181.

33. Brinkmann, D.; Brun, E.; Staub, H. H., Kernresonanz Im Gasformigen Xenon. *Helvetica Physica Acta* **1962,** 35, (6), 431-436.

34. Warren, W. W.; Norberg, R. E., Nuclear Quadrupole Relaxation and Chemical Shift of Xe131 in Liquid and Solid Xenon. *Physical Review* **1966,** 148, (1), 402-412.

35. Meersmann, T.; Haake, M., Magnetic field dependent xenon-131 quadrupolar splitting in gas and liquid phase NMR. *Physical Review Letters* **1998,** 81, (6), 1211-1214.

36. Dreihuys, B.; Cates, G. D.; Miron, E.; Sauer, K.; Walter, D. K.; Happer, W., *Applied Physics Letters* **1996,** 69, 1668.

37. Kneller, J. M.; Soto, R. J.; Surber, S. E.; Colomer, J. F.; Fonseca, A.; Nagy, J. B.; Pietrass, T., Continuous-flow optical pumping NMR in a closed circuit system. *Journal of Magnetic Resonance* **2000,** 147, (2), 261-265.

38. Zook, A. L.; Adhyaru, B. B.; Bowers, C. R., High capacity production of > 65% spin polarized xenon-129 for NMR spectroscopy and imaging. *Journal of Magnetic Resonance* **2002,** 159, (2), 175-182.

39. Ruset, I. C.; Ketel, S.; Hersman, F. W., Optical pumping system design for large production of hyperpolarized Xe-129. *Physical Review Letters* **2006,** 96, (5), 053002.

40. Kuzma, N. N.; Patton, B.; Raman, K.; Happer, W., Fast nuclear spin relaxation in hyperpolarized solid Xe-129. *Physical Review Letters* **2002,** 88, (14), 147602.

41. Mortuza, M. G.; Anala, S.; Pavlovskaya, G. E.; Dieken, T. J.; Meersmann, T., Spin-exchange optical pumping of high-density xenon-129. *Journal of Chemical Physics* **2003,** 118, (4), 1581-1584.

42. Happer, W., Optical-Pumping. *Reviews of Modern Physics* **1972,** 44, (2), 169-&.

43. Cates, G. D.; Fitzgerald, R. J.; Barton, A. S.; Bogorad, P.; Gatzke, M.; Newbury, N. R.; Saam, B., Rb Xe-129 Spin-Exchange Rates Due to Binary and 3-Body Collisions at High Xe Pressures. *Physical Review A* **1992,** 45, (7), 4631-4639.

44. Wagshul, M. E.; Chupp, T. E., Optical-Pumping of High-Density Rb with a Broad-Band Dye-Laser and Gaalas Diode-Laser Arrays - Application to He-3 Polarization. *Physical Review A* **1989,** 40, (8), 4447-4454.

45. Stupic, K. F.; Cleveland, Z. I.; Pavlovskaya, G. E.; Meersmann, T., Quadrupolar Relaxation of Hyperpolarized Krypton-83 as a Probe for Surfaces. *Solid State Nuclear Magnetic Resonance* **2006,** 29, 79-84.

46. Jaccard, G.; Wimperis, S.; Bodenhausen, G., multiple quantum NMR spectroscopy of S=3/2 spins in isotropic phase: A new probe for multiexponential relaxation. *Journal of Chemical Physics* **1986,** 85, (11), 6282-6293.

47. Driehuys, B.; Cates, G. D.; Happer, W., Surface Relaxation Mechanisms of Laser-Polarized Xe-129. *Physical Review Letters* **1995,** 74, (24), 4943-4946.

48. Schearer, L. D.; Walters, G. K., Nuclear Spin-Lattice Relaxation in Presence of Magnetic-Field Gradients. *Physical Review* **1965,** 139, (5A), 1398-1402.

49. Cates, G. D.; Schaefer, S. R.; Happer, W., Relaxation of Spins Due to Field Inhomogeneities in Gaseous Samples at Low Magnetic-Fields and Low-Pressures. *Physical Review A* **1988,** 37, (8), 2877-2885.

50. Abragam, A., *The Principles of Nuclear Magnetism.* Oxford University Press: Oxford, UK, 1961.

51. McConnell, J., *The theory of nuclear magnetic relaxation in liquids.* Cambridge Univeristy Press: Cambridge, UK, 1987.

52. Pavlovskaya, G. E.; Cleveland, Z. I.; Stupic, K. F.; Meersmann, T., Hyperpolarized Krypton-83 as a New Contrast Agent for Magnetic Resonance Imaging. *Proceedings of the National Academy of Sciences of the United States of America* **2005,** 102, 18275-18279.

53. Zerger, J. N.; Lim, M. J.; Coulter, K. P.; Chupp, T. E., Polarization of Xe-129 with high power external-cavity laser diode arrays. *Applied Physics Letters* **2000,** 76, (14), 1798-1800.

CHAPTER 3

HYPERPOLARIZED KRYPTON-83 AS A SURFACE SENSITIVE CONSTRAST AGENT

Most of the results presented in this chapter appear in the journal article: Galina E. Pavlovskaya, Zackary I. Cleveland, Karl F. Stupic, Randal J. Basaraba, and Thomas Meersmann, "Hyperpolarized Krypton-83 as a New Contrast Agent for Magnetic Resonance Imaging", *Proceedings of the National Academy of Sciences USA*. **2005,** 102 (51): 18275-18279. Data concerning hp ^{83}Kr relaxation in borosilicate beads were published in the article: Karl F. Stupic, Zackary I. Cleveland, Galina E. Pavlovskaya, and Thomas Meersmann, "Quadrupolar Relaxation of Hyperpolarized Krypton-83 as a Probe for Surfaces", *Solid State Nuclear Magnetic Resonance.* **2006,** 29 (1-3): 79-84.

Thomas Meersmann, Galina E. Pavlovskaya, Zackary I. Cleveland wrote the paper published in the *PNAS.* In that work, Galina E. Pavlovskaya performed the MR imaging and processed the image data. Zackary I. Cleveland produced the hp ^{83}Kr, designed the experimental apparatus, and prepared the studied samples. Randal J. Basaraba provided the lung tissue and performed the light microscopy on the tissue samples. Karl F. Stupic assisted in performing relaxation measurements and in delivery the hp gas to the sample region. Thomas Meersmann, Karl F. Stupic, and Zackary I. Cleveland wrote the paper published in *Solid State NMR.* Karl F. Stupic and Zackary I. Cleveland collected the relaxation data presented in this work. Galina E. Pavlovskaya provided technical advice and edited the manuscript.

3.1 Introduction

High nuclear spin polarization in noble gases can be generated through spin exchange optical pumping (SEOP) [1] and provides nuclear magnetic resonance (NMR) signal enhancements that are many orders of magnitude over the signal obtained at thermal equilibrium [2]. Hyperpolarized (hp) ^{3}He and hp ^{129}Xe (both I = 1/2) have both been used in a wide range of NMR and magnetic resonance imaging (MRI) experiments that would otherwise be impossible [3-15]. In particular hp ^{3}He has been applied for medical MRI diagnosis of pulmonary diseases [16-19]. One of the fundamental parameters with high diagnostic value for hp ^{3}He MRI is the spin density that results from the helium concentration in a particular volume. Spin density mapping of hp ^{3}He can be applied to visualize ventilation in lungs. Other useful parameters are ^{3}He diffusion that provides information about alveolar size distributions in lung tissue and hp ^{3}He relaxation that depends on oxygen partial pressure in lungs.

In vivo MRI of airways with hp ^{129}Xe as a contrast agent [19-21] suffers from a lower sensitivity compared to hp ^{3}He. However, ^{129}Xe adds an additional parameter not available from ^{3}He, namely the chemical shift that provides insights into the local environment of the xenon atoms [22-27]. The ^{129}Xe chemical shift has been used extensively for research in materials science and for xenon dissolved in a variety of liquids including human blood [3, 5, 6, 8, 9, 12, 28]. The chemical shift obtained from hp ^{129}Xe can be used to generate an *in vivo* MRI contrast that is a probe for gas perfusion in lungs (i.e. exchange of the gaseous xenon with the lung parenchyma) [29, 30].

^{3}He and ^{129}Xe are the only spin I = 1/2, stable noble gas isotopes, but there are three more NMR active isotopes in this group with a higher spin and nuclear electric

quadrupole moment. The three quadrupolar noble gas isotopes are ^{21}Ne (I= 3/2, natural abundance 0.27%), ^{83}Kr (I = 9/2, natural abundance 11.5%) and ^{131}Xe (I = 3/2, natural abundance 21%). Quadrupolar interactions in these noble gas atoms cause spin relaxation and coherent spin evolution that are probes for the shape, size, and symmetry of void spaces as well as the chemical composition of surfaces in porous media [31-36]. Thus the information provided is highly complementary to that obtained from ^{3}He and ^{129}Xe. For instance, thermally polarized liquid ^{131}Xe was used previously [37] to generate transverse relaxation weighted MRI contrast in aerogels that depended on the adsorption of water onto the surface.

Unfortunately, low thermal signals make conventional gas-phase MRI of the quadrupolar noble gases impractical. Although ^{83}Kr optical pumping has been explored in the past [38], the wealth of information provided by quadrupolar noble gas isotopes can only be used for *in vivo* MRI if SEOP, followed by the subsequent removal of the alkali metal vapor, is successful. As was shown in Chapter 2, this can be achieved for ^{83}Kr with enhancement factors of up to 1200 times that of the thermal equilibrium signal at 9.4 T. This chapter described the first report of alkali metal free hp ^{83}Kr used for void space imaging in porous materials and *in vitro* biological tissues.

3.2 Materials and Methods

3.2.1 NMR and MRI Instrumentation and Spin Exchange Optical Pumping

Experiments were performed on a Chemagnetics CMX II 400 MHz NMR spectrometer in a 9.4 T wide-bore (89 mm) superconducting magnet equipped with a Resonance Research imaging system consisting of triple axis gradient coils (100 G/cm

x,y-axes and 720 G/cm z-axis) and low noise linear gradient amplifiers. All NMR spectra and MRI images were obtained using a custom-built gas flow probe tuned to the ^{83}Kr frequency of 15.4 MHz. All images were acquired with a standard gradient–echo sequence. Continuous flow images were acquired in ~2 h using 32 phase encoding gradients. Stop flow images were acquired with 16 phase encoding gradients with 10-15 min polarization time between consecutive acquisitions. The subsequent image reconstruction was performed in MATLAB (version 14.2). The T_1 values were calculated by nonlinear least-squares fitting of the hp ^{83}Kr signal as a function of time and number of applied medium flip angle (~12°) RF pulses.

The production of rubidium free hp ^{83}Kr through SEOP of research grade krypton (99.995%, natural abundance; Airgas, Radnor, PA) was performed in a cylindrical Pyrex cell (length = 125 mm, ID = 24 mm). The gas mixture used in all experiments consisted of 95% krypton and 5% molecular nitrogen (N_2 was added for radiation quenching purposes [39]). The pump cell containing 2.5 to 5.0 g of rubidium (99.6%; Sigma-Aldrich, Milwaukee, WI) was housed in a quartz and aluminum oven to maintain even heating at ~433 K. Light (794.7 nm) from the 60 W Coherent FAP diode-array laser system (line width 2 nm) was directed through a circular polarizer onto the pump cell.

In continuous flow experiments, the pressure in the pump cell was kept above ambient (175 kPa) to avoid contamination by atmospheric oxygen and water vapor. The gas mixture was recirculated using a Watson-Marlow Bredel peristaltic pump, and the flow rate was monitored with a Gilmont direct-reading flow meter and converted for the applied gas mixture. As was discussed in Chapter 2, a 27-fold NMR signal enhancement

compared to thermally polarized ^{83}Kr at ambient temperature and 9.4 T was obtained under these conditions. Alternatively, a batch mode (i.e. stopped-flow) type of experiment was employed, which required a 10-15 min a SEOP period. Following SEOP, hp ^{83}Kr was released into a detection cell that had been evacuated to less than 0.1 kPa. During transfer the gas mixture passed through a glass wool filter to trap rubidium vapor. The technique produced signal enhancement of about 1200 times greater than the thermal signal. The 40 fold improvement of polarization in the batch mode experiment over the continuous flow experiment was a combined effect of prolonged SEOP and reduced relaxation during the transfer between the pump cell and the detection cell.

3.2.2 Sample Preparation

The 0.1 to 2.5 mm diameter borosilicate glass beads used in this work (Biospec Products, Inc., Bartlesville, OK) were degassed overnight at a pressure below 0.1 Pa and stored under dry nitrogen until use. Beads used as obtained from the supplier are referred to in this text as 'untreated'. Some untreated beads were washed for 15 min with a 1:1:5 solution of 30% v/v NH_4OH, 30% v/v H_2O_2, and distilled water while stirring vigorously. Following NH_4OH/H_2O_2 treatment, the beads were washed for 15 min at 358 K with a 1:1:5 solution of 30% v/v HCl, 30% v/v H_2O_2, and distilled water while stirring vigorously. The beads were then washed five times with distilled water and dried in a vacuum desiccator at 523 K for 1 h. These beads are referred to as 'basic peroxide/acidic peroxide' washed. 'Siliconized' beads were first subjected to the treatment described above and then reacted with a 1:10 mixture of SurfaSil (Pierce Biotechnology Inc., Rockford, IL) in acetone and washed with distilled water in accordance with the

manufacturer's instructions. 'Fluorosilane treated' beads were produced by reacting the washed beads with a 1:100 mixture of (3,3,3-Trifluoropropyl) tri-methoxyl silane (Gelest Inc., Morrisville, PA) in toluene with occasional stirring for 3 hours and then washing them with toluene 4 times followed by drying in a vacuum desiccator at 398 K overnight. The 70-250 μm porous polyethylene samples (Small Parts, Inc., Miami Lakes, FL) were degassed overnight at pressure of less than 0.1 Pa and stored under dry nitrogen until use.

The desiccated canine lung tissue was obtained after humane euthanization of the animal. The lung, heart, and mediastinal connective tissue were then removed *en bloc*, and the lungs were then separated, rinsed with tap water for 24 h via tracheal infusion and dried by tracheal insufflations with compressed air for 24 h. The tissue samples were then cut into cylinders, degassed overnight at less than 0.1 Pa, and stored under dry nitrogen until use. For the micrograph in Fig. 3.2A, desiccated lung tissue was routinely processed for histopathology. Briefly, the sample was rehydrated in 10% neutral buffered formalin, processed through a series of alcohol and xylene solutions, embedded in paraffin, serially sectioned at 4-6 μm, and stained with hematoxylin and eosin for histological examination.

3.3 Results and Discussion

3.3.1 Hp ^{83}Kr MR Imaging in Continuous Flow

Fig. 3.1A shows a continuous flow hp ^{83}Kr MR image of a glass phantom using krypton in bulk gas-phase located between glass structures. The hp ^{83}Kr was generated in continuous flow with polarization enhancement factors less than 30 times that of thermally polarized krypton (See Chapter 2 for additional details.). The obtained resolution was 270 × 270

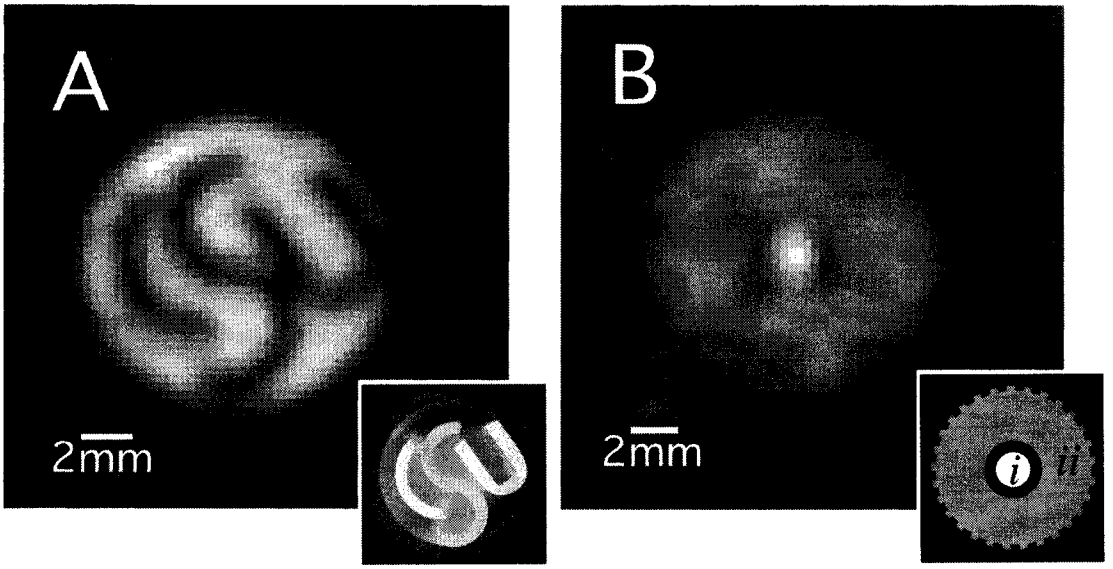

Figure 3.1. Hp ^{83}Kr MRI under continuous flow conditions **(A)** Hyperpolarized ^{83}Kr MRI of gas flowing around glass structures. The inset figure (lower right hand corner of Fig. 3.1A) is a photograph of the phantom used to produce the MRI. Gas flow was held constant at 125 cm^3/min. All figures are displayed after zero filling. **(B)** Hyperpolarized ^{83}Kr MRI of a porous polyethylene sample with 70 μm average pore size obtained under continuous flow at a rate of 100 cm^3/min. The inset sketch (lower right hand portion of Fig. 3.1B) is of the phantom used for the MRI. The center of the sample (*i*) is a 1.65 mm void space surrounded by a 0.76 mm PFA wall and an 11 mm wide area of a porous polymer (*ii*). The measurement at 9.4 T took about 2.1 h and led to a resolution of 650 x 650 μm (raw data).

mm after zero filling the data to 64 points in both dimensions. The overall duration of the MRI experiment was 1.7 h. The continuous flow type of experiment and the long experimental times are clearly prohibitive for medical applications but might be of use in materials science applications. The batch mode type of experiment will be required for medical MRI, but some of the findings of this section are also relevant for *in vivo* MRI.

Although the feasibility of void space imaging of bulk gas-phase was demonstrated in Fig. 3.1A, porous materials may have caused significant problems due to accelerated quadrupolar relaxation. For instance, the longitudinal relaxation time was found to be between 2.5 and 5.9 s in various porous polyethylene samples with average pore sizes ranging from 70 to 250 μm [40]. Even with relaxation times on the order of a few seconds, hp ^{83}Kr MRI is still possible. Fig. 3.1B shows a MR image of a phantom containing a porous polymer with a 70 μm average pore size that demonstrates the feasibility of hp ^{83}Kr MRI in materials with pore dimension below the alveolar size range.

3.3.2 Longitudinal Relaxation in Desiccated Canine Lung Tissue

For *in vivo* MRI studies of airways, the ^{83}Kr relaxation times in the lung tissue cannot be significantly shorter than the timescale of the gas transport into the lungs. To obtain a first estimate of pulmonary T_1 times, a desiccated canine lung tissue sample was prepared (See Section 3.2.2.) that should have been structurally similar to *in vivo* samples (See Fig. 3.2A.). The spin-lattice relaxation time of hp ^{83}Kr at 9.4 T and 289 K in this tissue was determined to be T_1 = 10.5 s. However, molecular oxygen will also be present in the hp ^{83}Kr mixtures for *in vivo* MRI applications. Because quadrupolar interactions

dominate the relaxation mechanism and also because of the low gyromagnetic ratio of krypton (See Chapter 5.), the T_1 relaxation time in the lung tissue was only mildly affected (T_1 = 8.6 s) by the presence of 20% oxygen. This is in clear contrast to ^{3}He and ^{129}Xe where the longitudinal relaxation times are entirely regulated by the oxygen partial pressure and can be lowered by orders of magnitude to T_1 = 10-20 s in lungs [19].

Although the ^{83}Kr relaxation times at 9.4 T are potentially long enough for practical MRI applications, the magnetic field strength dependence of the longitudinal relaxation rates discussed in Chapter 2 may be a concern. While the longitudinal relaxation times were reduced to 5 s at 1.5 T and T_1 = 7 s a 3 T, the relaxation times found in future *in vivo* work may be longer under physiological conditions due to increased temperature and the presence of surface water, which decreases ^{83}Kr relaxation rates. The effect of adsorbed surface water is the subject of Chapter 5. Of course only future studies in live animals will provide certainty about the relaxation behavior of ^{83}Kr *in vivo*, but the *in vitro* measurements in discussed here work provide a first insight into the general trends that are to be expected.

3.3.3 Hp ^{83}Kr MR Imaging of Desiccated Lung Tissue

The desiccated canine lung specimen examined in the work was also selected as a proof-of-concept sample for hp ^{83}Kr MRI. Although the surface chemistry of the desiccated tissue will be substantially different than will be found in a live lung, the pore structure was relatively unchanged (Fig. 3.2A.). Fig. 3.2C shows and MR image of hp ^{83}Kr in a 10 mm diameter, 2 cm long cylindrical sample of desiccated canine lung tissue obtained using small flip angle excitation FLASH sequence applied to a single bolus of hp

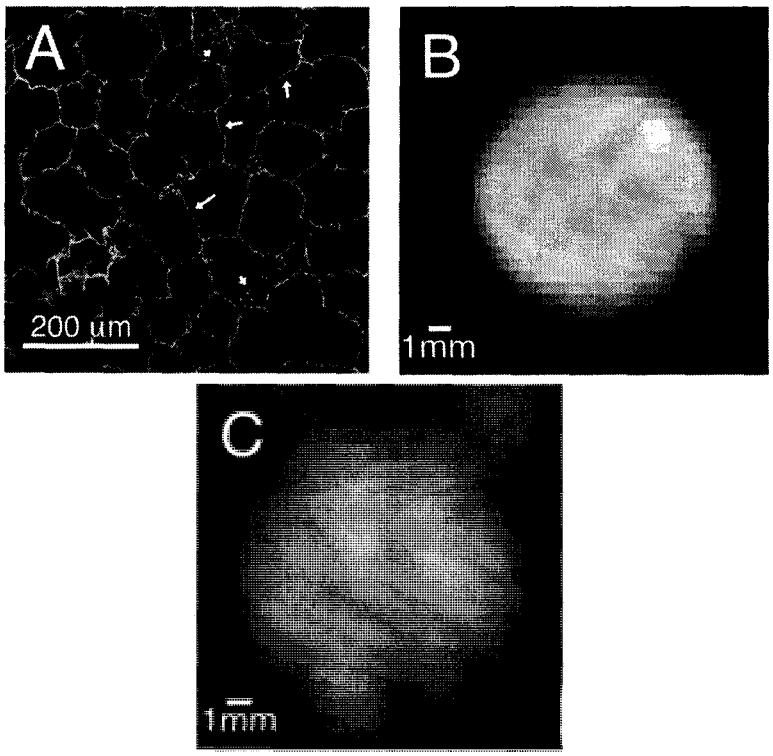

Figure 3.2: Hp ^{83}Kr MRI of canine lung tissue. **(A)** Lung tissue micrograph displaying intact alveolar septum walls (long arrows) and alveolar epithelium (short arrows). **(B)** Hp ^{83}Kr MRI obtained using repeated stopped-flow delivery. A 10 min SEOP period was required to produce the 16 boluses of hp ^{83}Kr, ~3 seconds were required for gas transfer, and 103 ms were needed for RF pulses, gradient pulses, and signal acquisition. The image resolution is 480 x 655 μm (raw data) with no slice selection applied. **(C)** FLASH MRI using one bolus of hp ^{83}Kr and sixteen 12° flip angle RF pulses. The measurement required 15 minutes for SEOP, 3 seconds for the gas transfer, and 0.46 s for the RF pulses, gradient pulses, and signal acquisition. The resolution is 1080 x 655 μm (raw data) with no slice selection.

^{83}Kr. The image was acquired in 46 ms after a 10 min of SEOP period. FLASH experiments were possible because of the large enhancement obtained from the stopped-flow experiment and because of the favorable porosity of lung tissue compared to the polymer sample. Note that only about 31% of the non-equilibrium spin polarization was used in this basic FLASH imaging experiment. Fig. 3.2B shows the hp ^{83}Kr MRI of a canine lung specimen obtained using multiple stopped-flow optical pumping cycles. The image was reconstructed from 16 individual stopped-flow experiments corresponding to 16 phase encoding field gradients. Comparing Fig. 3.2B and 3.2C clearly shows the improved signal-to-noise obtained using 90° flip angle pulses and one bolus of hp gas for each phase encoding gradient.

The MR images in Fig. 3.2 were obtained at 9.4 T, which was significantly higher than the 1.5 T commonly used for medical MRI, and the signal intensity is known to decrease linearly with decreasing magnetic field. This dependence is in contrast to thermally polarized samples in conventional MRI that approximately display an inverse square dependence on the external magnetic field [41, 42] and is a consequence of the non-equilibrium spin polarization generated by SEOP. The maximum spatial resolution in MRI is affected by the signal intensity that will be reduced by a factor of about 6 at 1.5 T compared to the MRI at 9.4 T. A more significant loss will occur because of the much larger detection coil dimensions in medical MRI. However, improved polarization of approximately 3 orders of magnitude is in principle possible. (See Chapter 7 for a more complete discussion of polarization and signal intensity.)

Nevertheless the sub-millimeter resolution obtained in this work will probably not be available using larger samples that require larger coil diameters. Clearly, hp ^{83}Kr MR

will be unable to compete in terms of resolution with hp ^{3}He MRI or even with ^{129}Xe MRI. However, the idea here is to introduce a novel contrast agent for MRI that is complementary to hp ^{3}He and hp ^{129}Xe. Thus reduction of spatial resolution may be acceptable provided that the technique provides meaningful biomedical data.

3.3.4 Surface Sensitive Relaxation in Hp ^{83}Kr

So far in this discussion, the relatively fast longitudinal relaxation of ^{83}Kr has been presented principally as an obstacle. However, useful information can also be obtained from the relaxation of hp ^{83}Kr, which is strongly influenced by surface interactions. To more fully assess the role of surface-to-volume ratio and surface chemistry in determining the observed ^{83}Kr T_1, a series of borosilicate glass bead samples with differing bead diameters and surface chemistry modifications were prepared (See Section 3.2.) These beads were approximately spherical and ranged from 0.1 to 2.5 mm in mean diameter. The total pore volume of a collection of equally sized spheres is approximately 26% that of the entire sample with the pores being the tetrahedral and octahedral holes expected from closest packing of spheres.

Fig. 3.3 depicts the ^{83}Kr relaxation rate as a function of inverse bead radii. The ^{83}Kr relaxation rates were found to increase with decreasing bead radius (i.e. pore size) for all surfaces studied. Because the bead diameter was not expected to influence the geometry of the pores (assuming perfectly spherical beads and closest packing), the effect must have been caused primarily by differences in the surface-to-volume ratio. The general dependence of relaxation on inverse radius is expected if the observed longitudinal relaxation rates are dominated by surface interactions.

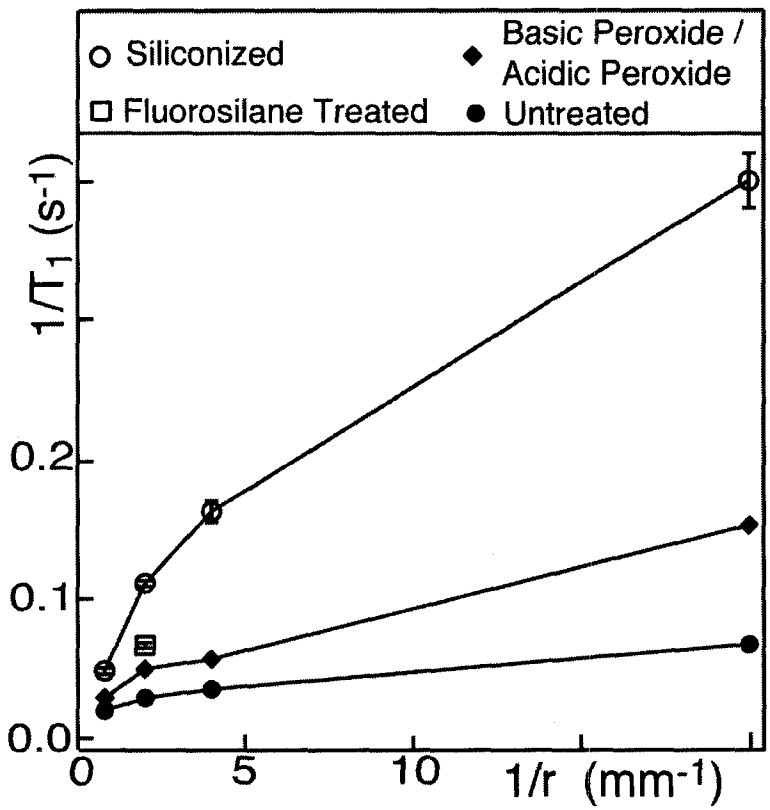

Figure 3.3: Hp ^{83}Kr longitudinal relaxation rates as a function of inverse borosilicate glass bead radii. The various bead surface chemistries are indicated in the legend. The error bars represent standard deviations resulting from at least four replicate measurements. The curves are intended only as a guide to the eye.

If quadrupolar interactions on the surface were the only source for the observed relaxation, a linear dependence of relaxation rates on the inverse radii would be expected. A clear deviation from linear behavior was observed but can probably be attributed to non-ideal bead packing and a range of bead surface topologies. Further, it is unlikely that the actual surface area can be calculated by simple geometric considerations alone as the surface areas of similarly sized E-glass (a commercially available, low alkali borosilicate glass) beads were found to deviate by more than a factor of two from the geometric value as measured by krypton BET adsorption isotherms [43].

The other important trend displayed in Fig. 3.3 is the effect of the surface chemistry on the observed relaxation rate. As the hydrophobicity of the surface increased, the relaxation rate also increased. The nonpolar, but highly polarizable, krypton electron cloud leads to higher surface adsorption energies for nonpolar, hydrophobic surfaces than for polar, hydrophilic surfaces. Quadrupolar interactions during longer krypton adsorption times on hydrophobic surfaces therefore induced faster longitudinal relaxation. Additionally, the strength of the quadrupolar interactions, and thus the longitudinal relaxation rate, may be affected by changes in surface chemistry.

In the highest surface-to-volume ratio samples (i.e. 0.1 mm mean diameter beads) the observed T_1 in the untreated sample is approximately six times that of the siliconized sample. Even in the 1.0 mm diameter bead samples, which had a substantially lower surface-to-volume ratio, the T_1 was decreased from 35.3 s to 9.0 s by siliconizing the untreated glass surface. The approximately four-fold difference in ^{83}Kr T_1 observed in the 1.0 mm beads was used to generate the strong T_1 contrast in MRI based on the surface chemistry that is discussed in Section 3.3.5. Of potential biomedical interest is the fact that

even stronger MRI contrast in hp ^{83}Kr MRI has been observed when tobacco smoke condensate, which contains a variety of hydrophobic substances, was deposited on glass surfaces [44]. The effect of tobacco smoke deposition on surfaces is the topic of Chapter 6.

A similar effect to that observed from hp ^{83}Kr interacting with surfaces has also been observed for hp ^{131}Xe (I = 3/2) on surface treated optical pumping cell walls [45]. The opposite effect on a much longer timescale has been observed with ^{129}Xe and ^{3}He NMR [46, 47], because the surface coating insulates the noble gas atoms from paramagnetic sites in the glass surface [48]. In the case of ^{83}Kr, the separation from paramagnetic sites in the glass surface is outweighed by quadrupolar relaxation on the high affinity, siliconized surface.

3.3.5 Surface Sensitive MRI Contrast through Quadrupolar Relaxation

The quadrupolar relaxation experienced by hp ^{83}Kr is a source of contrast that is not available with either hp ^{3}He or hp ^{129}Xe. In the following proof-of-concept demonstration, hp ^{83}Kr was generated via stopped-flow optical pumping and introduced into a sample that had been prepared from 1.0 mm diameter borosilicate glass beads. One sample region of the sample consisted of untreated hydrophilic glass beads, and the second region consisted of siliconized, hydrophilic beads. The sample was chosen for its simplicity and because void space dimensions, pore symmetry, pore shape, pore connectivity, and porosity should have been similar for the two regions. Furthermore, the void spaces in 1.0 mm beads, assuming closest packing, should have had sizes similar to human alveoli (i.e. the octahedral and tetrahedral holes can accommodate spheres with radii up to 414 μm and 223 μm respectively).

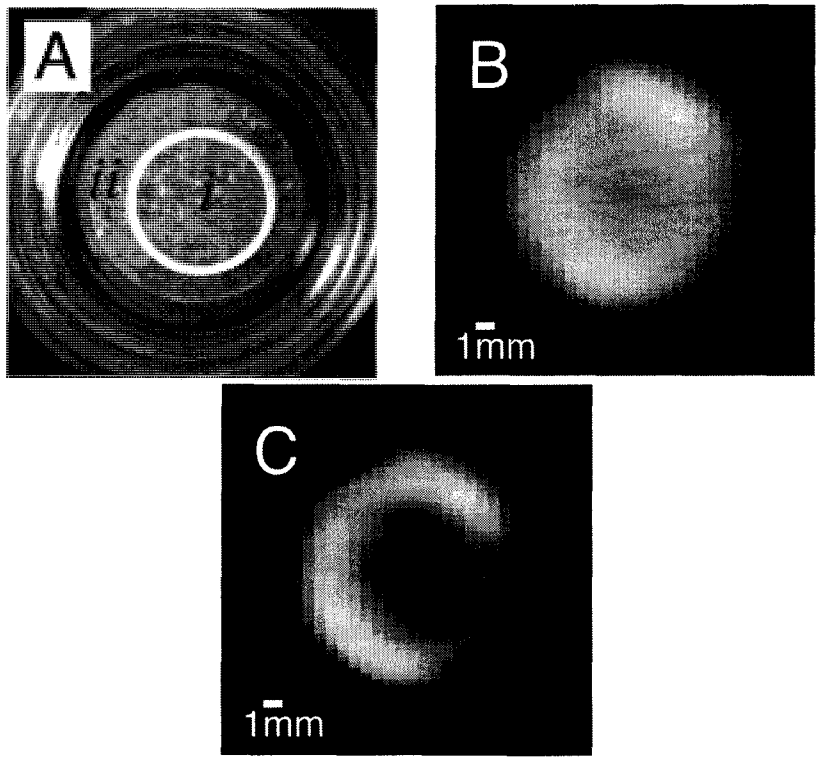

Figure 3.4 T_1 weighted MRI with hp ^{83}Kr. **(A)** Photograph of the MRI phantom. Siliconized 1.0 mm borosilicate glass beads (hydrophobic) were located within the center ring (*i*). The outer region (*ii*) contained untreated 1.0 mm beads (hydrophilic), and was separated from region *i* by an untreated glass tube (Seen as a white ring in the photograph due to illumination from below). The glass wall is not resolved because of the 424 x 864 μm image resolution. **(B)** ^{83}Kr MRI of the glass bead sample reconstructed from 16 boluses of hp ^{83}Kr. The MRI sequence was applied ~3 s after filling the sample leading to little MRI contrast between the two regions **(C)** Same as Fig. 3.4B except a 9 s delay was added. Clear contrast between region *i* (T_1 = 9 s) and region *ii* (T_1 = 35 s) can be seen. Increasing the delay would increase contrast but reduce the overall signal intensity.

Surface sensitive hp ^{83}Kr MR images are shown in Fig. 3.4B and 3.4C produced using the phantom shown in Fig. 3.4A, which contained the hydrophobic glass beads in the center (*i*) and hydrophilic glass beads in the outer region (*ii*). The sample was evacuated prior to the experiment, and the image was acquired ~3 s after the hp ^{83}Kr was transferred to the sample to allow the gas pressure to equilibrate. The image in Fig. 3.4B shows a weak contrast because the krypton in the sample center had already experienced moderate relaxation. The MR image in Fig. 3.4C was recorded under identical conditions except that a delay period of 9 s between gas transfer and signal acquisition was used. The contrast in Fig. 3.4C is clearly visible and demonstrates that hp ^{83}Kr MRI can be used to obtain information about the surface chemistry of porous media.

3.4. Conclusions

This chapter has described the first demonstration of MRI using a hyperpolarized noble gas with a nuclear spin $I > 1/2$ that had been separated from the rubidium vapor of the SEOP process. Hp ^{83}Kr MR images were obtained with sub-millimeter resolution at 9.4 T in porous media with pore sizes similar to alveolar dimensions and in desiccated canine lung tissue at ambient pressure. The ^{83}Kr spin-lattice relaxation times in the lung tissue were reasonably long and should allow for *in vivo* MRI even in the presence of 20% oxygen. It is shown that hp ^{83}Kr provides a source of contrast that can distinguish between different chemical compositions of surfaces in a simple test system. These results are of potential value for the development of novel *in vivo* MRI techniques for diagnosing of lung diseases where the surface chemistry is altered. An additional practical advantage of krypton is that, unlike xenon, it lacks significant anesthetic properties at near atmospheric

pressures [49] and should allows for prolonged exposure times and thus increased signal averaging. Further, hp ^{83}Kr NMR and MRI may be important in materials science for the studying of porous materials.

References:

1. Walker, T. G.; Happer, W., Spin-exchange optical pumping of noble-gas nuclei. *Review of Modern Physics* **1997,** 69, (2), 629-642.

2. Raftery, D.; Long, H.; Meersmann, T.; Grandinetti, P. J.; Reven, L.; Pines, A., High-Field NMR of Adsorbed Xenon Polarized by Laser Pumping. *Physical Review Letters* **1991,** 66, (5), 584-587.

3. Goodson, B. M., Nuclear magnetic resonance of laser-polarized noble gases in molecules, materials, and organisms. *Journal of Magnetic Resonance* **2002,** 155, (2), 157-216.

4. Navon, G.; Song, Y. Q.; Room, T.; Appelt, S.; Taylor, R. E.; Pines, A., Enhancement of solution NMR and MRI with laser-polarized xenon. *Science* **1996,** 271, (5257), 1848-1851.

5. Raftery, D.; MacNamara, E.; Fisher, G.; Rice, C. V.; Smith, J., Optical pumping and magic angle spinning: Sensitivity and resolution enhancement for surface NMR obtained with laser-polarized xenon. *Journal of the American Chemical Society* **1997,** 119, (37), 8746-8747.

6. Haake, M.; Pines, A.; Reimer, J. A.; Seydoux, R., Surface-enhanced NMR using continuous-flow laser-polarized xenon. *Journal of the American Chemical Society* **1997,** 119, (48), 11711-11712.

7. Tseng, C. H.; Wong, G. P.; Pomeroy, V. R.; Mair, R. W.; Hinton, D. P.; Hoffmann, D.; Stoner, R. E.; Hersman, F. W.; Cory, D. G.; Walsworth, R. L., Low-field MRI of laser polarized noble gas. *Physical Review Letters* **1998,** 81, (17), 3785-3788.

8. Mair, R. W.; Wong, G. P.; Hoffmann, D.; Hurlimann, M. D.; Patz, S.; Schwartz, L. M.; Walsworth, R. L., Probing porous media with gas diffusion NMR. *Physical Review Letters* **1999,** 83, (16), 3324-3327.

9. Anala, S.; Pavlovskaya, G. E.; Pichumani, P.; Dieken, T. J.; Olsen, M. D.; Meersmann, T., In situ NMR spectroscopy of combustion. *Journal of the American Chemical Society* **2003,** 125, (43), 13298-13302.

10. Moule, A. J.; Spence, M. M.; Han, S. I.; Seeley, J. A.; Pierce, K. L.; Saxena, S.; Pines, A., Amplification of xenon NMR and MRI by remote detection. *Proceedings of the National Academy of Sciences of the United States of America* **2003,** 100, (16), 9122-9127.

11. Dubois, L.; Da Silva, P.; Landon, C.; Huber, J. G.; Ponchet, M.; Vovelle, F.; Berthault, P.; Desvaux, H., Probing the hydrophobic cavity of Lipid Transfer Protein from Nicotiana tabacum through xenon-based NMR spectroscopy. *Journal of the American Chemical Society* **2004,** 126, (48), 15738-15746.

12. Moudrakovski, I. L.; Wang, L. Q.; Baumann, T.; Satcher, J. H.; Exarhos, G. J.; Ratcliffe, C. I.; Ripmeester, J. A., Probing the geometry and interconnectivity of pores in organic aerogels using hyperpolarized Xe-129 NMR spectroscopy. *Journal of the American Chemical Society* **2004,** 126, (16), 5052-5053.

13. Jansch, H. J.; Gerhard, P.; Koch, M., Xe-129 on Ir(111): NMR study of xenon on a metal single crystal surface. *Proceedings of the National Academy of Sciences of the United States of America* **2004,** 101, (38), 13715-13719.

14. Lowery, T. J.; Doucleff, M.; Ruiz, E. J.; Rubin, S. M.; Pines, A.; Wemmer, D. E., Distinguishing multiple chemotaxis Y protein conformations with laser-polarized Xe-129 NMR. *Protein Science* **2005,** 14, (4), 848-855.

15. Appelt, S.; Hasing, F. W.; Kuhn, H.; Perlo, J.; Blumich, B., Mobile high resolution xenon nuclear magnetic resonance spectroscopy in the earth's magnetic field. *Physical Review Letters* **2005,** 94, (19), 197602.

16. MacFall, J. R.; Charles, H. C.; Black, R. D.; Middleton, H.; Swartz, J. C.; Saam, B.; Driehuys, B.; Erickson, C.; Happer, W.; Cates, G. D.; Johnson, G. A.; Ravin, C. E., Human lung air spaces: Potential for MR imaging with hyperpolarized He-3. *Radiology* **1996,** 200, (2), 553-558.

17. Kauczor, H. U.; Hofmann, D.; Kreitner, K. F.; Nilgens, H.; Surkau, R.; Heil, W.; Potthast, A.; Knopp, M. V.; Otten, E. W.; Thelen, M., Normal and abnormal pulmonary ventilation: Visualization at hyperpolarized He-3 MR imaging. *Radiology* **1996,** 201, (2), 564-568.

18. Leawoods, J. C.; Yablonskiy, D. A.; Saam, B.; Gierada, D. S.; Conradi, M. S., Hyperpolarized He-3 gas production and MR imaging of the lung. *Concepts in Magnetic Resonance* **2001,** 13, (5), 277-293.

19. Moller, H. E.; Chen, X. J.; Saam, B.; Hagspiel, K. D.; Johnson, G. A.; Altes, T. A.; de Lange, E. E.; Kauczor, H. U., MRI of the lungs using hyperpolarized noble gases. *Magnetic Resonance in Medicine* **2002,** 47, (6), 1029-1051.

20. Albert, M. S.; Cates, G. D.; Driehuys, B.; Happer, W.; Saam, B.; Springer, C. S.; Wishnia, A., Biological Magnetic-Resonance-Imaging Using Laser Polarized Xe-129. *Nature* **1994,** 370, (6486), 199-201.

21. Mugler, J. P.; Driehuys, B.; Brookeman, J. R.; Cates, G. D.; Berr, S. S.; Bryant, R. G.; Daniel, T. M.; deLange, E. E.; Downs, J. H.; Erickson, C. J.; Happer, W.; Hinton, D. P.; Kassel, N. F.; Maier, T.; Phillips, C. D.; Saam, B. T.; Sauer, K. L.; Wagshul, M. E., MR imaging and spectroscopy using hyperpolarized Xe-129 gas: Preliminary human results. *Magnetic Resonance in Medicine* **1997,** 37, (6), 809-815.

22. Dybowski, C.; Bansal, N.; Duncan, T. M., Nmr-Spectroscopy of Xenon in Confined Spaces - Clathrates, Intercalates, and Zeolites. *Annual Review of Physical Chemistry* **1991,** 42, 433-464.

23. Barrie, P. J.; Klinowski, J., 129Xe NMR as a Probe for the study of microporous solids: a critical review. *Progress in NMR Spectroscopy* **1992,** 24, 91-108.

24. Raftery, D.; Chmelka, B. F., Xenon NMR Spectroscopy. *NMR Basic Principles and Progress* **1994,** 30, 111-158.

25. Springuel-Huet, M. A.; Bonardet, J. L.; Gedeon, A.; Fraissard, J., Xe-129 NMR overview of xenon physisorbed in porous solids. *Magnetic Resonance in Chemistry* **1999,** 37, S1-S13.

26. Ratcliffe, C. I., Xenon NMR. *Annual Reports on NMR Spectroscopy* **1998,** 36, 123-221.

27. Jameson, C. J., Xe chemical shift tensor in silicalite and SSZ-24. *Journal of the American Chemical Society* **2004,** 126, (33), 10450-10456.

28. Nossov, A.; Haddad, E.; Guenneau, F.; Gedeon, A., Application of continuously circulating flow of hyperpolarized (HP) Xe-129-NMR on mesoporous materials. *Physical Chemistry Chemical Physics* **2003,** 5, (20), 4473-4478.

29. Ruppert, K.; Mata, J. F.; Brookeman, J. R.; Hagspiel, K. D.; Mugler, J. P., Exploring lung function with hyperpolarized Xe-129 nuclear magnetic resonance. *Magnetic Resonance in Medicine* **2004,** 51, (4), 676-687.

30. Driehuys, B.; Cofer, G. P.; Pollaro, J.; Mackel, J. B.; Hedlund, L. W.; Johnson, G. A., Imaging alveolar-capillary gas transfer using hyperpolarized Xe-129 MRI. *Proceedings of the National Academy of Sciences of the United States of America* **2006,** 103, (48), 18278-18283.

31. Jokisaari, J.; Ingman, P.; Lounila, J.; Pukkinen, O.; Diehl, P.; Muenster, O., Electric-Field Gradients Experienced by the Noble-Gas Isotopes Ne-21, Kr-83 and Xe-131 in Thermotropic Liquid-Crystals. *Molecular Physics* **1993,** 78, (1), 41-54.

32. Meersmann, T.; Smith, S. A.; Bodenhausen, G., Multiple-quantum filtered xenon-131 NMR as a surface probe. *Physical Review Letters* **1998,** 80, (7), 1398-1401.

33. Meersmann, T.; Deschamps, M.; Bodenhausen, G., Probing aerogels by multiple quantum filtered Xe-131 NMR spectroscopy. *Journal of the American Chemical Society* **2001,** 123, (5), 941-945.

34. Moudrakovski, I. L.; Ratcliffe, C. I.; Ripmeester, J. A., Xe-131, a new NMR probe of void space in solids. *Journal of the American Chemical Society* **2001,** 123, (9), 2066-2067.

35. Millot, Y.; Man, P. P.; Springuel-Huet, M. A.; Fraissard, J., Quantification of electric-field gradient in the supercage of Y zeolites with Xe-131 (I=3/2) NMR. *Comptes Rendus De L Academie Des Sciences Serie II Fascicule C-Chimie* **2001,** 4, (11), 815-818.

36. Horton-Garcia, C. F.; Pavlovskaya, G. E.; Meersmann, T., Introducing krypton NMR spectroscopy as a probe of void space in solids. *Journal of the American Chemical Society* **2005,** 127, (6), 1958-1962.

37. Pavlovskaya, G.; Blue, A. K.; Gibbs, S. J.; Haake, M.; Cros, F.; Malier, L.; Meersmann, T., Xenon-131 surface sensitive imaging of aerogels in liquid xenon near the critical point. *Journal of Magnetic Resonance* **1999,** 137, (1), 258-264.

38. Schaefer, S. R.; Cates, G. D.; Happer, W., Determination of Spin-Exchange Parameters between Optically Pumped Rubidium and Kr-83. *Physical Review A* **1990,** 41, (11), 6063-6070.

39. Happer, W., Optical-Pumping. *Reviews of Modern Physics* **1972,** 44, (2), 169-&.

40. Stupic, K. F.; Cleveland, Z. I.; Pavlovskaya, G. E.; Meersmann, T., Quadrupolar Relaxation of Hyperpolarized Krypton-83 as a Probe for Surfaces. *Solid State Nuclear Magnetic Resonance* **2006,** 29, 79-84.

41. Chen, C. N.; Sank, V. J.; Cohen, S. M.; Hoult, D. I., The Field-Dependence of Nmr Imaging.1. Laboratory Assessment of Signal-to-Noise Ratio and Power Deposition. *Magnetic Resonance in Medicine* **1986,** 3, (5), 722-729.

42. Hoult, D. I.; Chen, C. N.; Sank, V. J., The Field-Dependence of Nmr Imaging.2. Arguments Concerning an Optimal Field-Strength. *Magnetic Resonance in Medicine* **1986,** 3, (5), 730-746.

43. Fuji, M.; Fujimori, H.; Takei, T.; Watanabe, T.; Chikazawa, M., Wettability of glass-bead surface modified by trimethylchlorosilane. *Journal of Physical Chemistry B* **1998,** 102, (51), 10498-10504.

44. Cleveland, Z. I.; Pavlovskaya, G. E.; Stupic, K. F.; Wooten, J. B.; Repine, J. E.; Meersmann, T., Detection of Tobacco Smoke Deposition by Hyperpolarized Krypton-83 MRI. *Magnetic Resonance Imaging* **2008,** 26, (270-278).

45. Wu, Z.; Happer, W.; Kitano, M.; Daniels, J., Experimental Studies of Wall Interactions of Adsorbed Spin-Polarized Xe-131 Nuclei. *Physical Review A* **1990,** 42, (5), 2774-2784.

46. Driehuys, B.; Cates, G. D.; Happer, W., Surface Relaxation Mechanisms of Laser-Polarized Xe-129. *Physical Review Letters* **1995,** 74, (24), 4943-4946.

47. Breeze, S. R.; Lang, S.; Moudrakovski, I.; Ratcliffe, C. I.; Ripmeester, J. A.; Santyr, G.; Simard, B.; Zuger, I., Coatings for optical pumping cells and short-term storage of hyperpolarized xenon. *Journal of Applied Physics* **2000,** 87, (11), 8013-8017.

48. Jacob, R. E.; Driehuys, B.; Saam, B., Fundamental mechanisms of He-3 relaxation on glass. *Chemical Physics Letters* **2003,** 370, (1-2), 261-267.

49. Cullen, S. C.; Gross, E. G., The Anesthetic Properties of Xenon in Animals and Human Beings, with Additional Observations on Krypton. *Science* **1951,** 113, (2942), 580-582.

CHAPTER 4

MECHANISMS OF GAS-PHASE LONGITUDINAL RELAXATION IN KRYPTON-83

The results presented in this chapter have been submitted for publication as two journal articles. The materials related to density dependent relaxation have been submitted as Zackary I. Cleveland and Thomas Meersmann, "Binary Collision Induced Longitudinal Relaxation in Gas-Phase ^{83}Kr", to the *Journal of Chemical Physics* (submitted 2008). The materials related to density independent relaxation due to both surface interactions and the formation of van der Waals molecules has been submitted as Zackary I. Cleveland and Thomas Meersmann, "Density Independent Contributions to Longitudinal Relaxation in ^{83}Kr" to *ChemPhysChem* (in press 2008).

For both works, Zackary I. Cleveland wrote the manuscripts, and Thomas Meersmann edited the manuscripts. Zackary I. Cleveland produced the hp ^{83}Kr, designed the experiments, built the experimental apparatus, and prepared the studied samples.

4.1 Introduction

The longitudinal relaxation rates of molecular gases have long been of interest because they are strongly influenced by intermolecular collisions [1, 2]. If the time between gas-phase collisions is significantly greater than the duration of the collisions, the molecules can be said to be in the binary collision limit. Within this limit, there exist well-defined relationships between gas density ρ and the average relative speed $\bar{v} = (8k_B T/\pi\mu)^{1/2}$ of the collision pair having reduced mass μ. In many cases, the relaxation rate can be attributed to a single mechanism such as spin rotation for nuclear spin I = 1/2 isotopes or quadrupolar interaction for spin I > 1/2 isotopes [3, 4]. Typically, molecules in the binary collision limit display an inverse dependence of the relaxation rate on the gas density, and the interactions can be characterized by a single effective collisional cross-section.

In principle, complementary information to that obtained from molecules should be available through studies of noble gas longitudinal relaxation. Although there are five stable, NMR active noble gas isotopes: ^{3}He, ^{129}Xe (both I = 1/2), ^{21}Ne, ^{131}Xe (both I = 3/2), and ^{83}Kr (I = 9/2), little work was been done concerning purely gas-phase relaxation of these atomic species. To date, the only rigorous studies of binary collision induced relaxation have been for ^{3}He [5], ^{129}Xe [6, 7] and ^{131}Xe [8] in pure xenon, ^{83}Kr in pure krypton [9], and ^{129}Xe and ^{3}He interacting with O_2 [10-12] and NO [13] both of which are paramagnetic. Presumably the lack of literature is due to the experimental difficulties associated with noble gas NMR studies, which include low intrinsic sensitivities for ^{21}Ne, ^{83}Kr, and ^{131}Xe, in addition to low natural abundance for ^{21}Ne.

Although the nuclear spin of the isotopes ^{3}He and ^{129}Xe can readily be hyperpolarized (hp) resulting in very high signal intensities [14], the extremely long T_1 times of hours for ^{129}Xe [15] and days for ^{3}He [16], which are beneficial for the generation of hyperpolarized spin systems, lead to prohibitively long experimental times. Similarly, the nuclear spin $I = 9/2$ noble gas isotope ^{83}Kr can also be hyperpolarized by spin exchange optical pumping (SEOP) [17, 18]. The longitudinal relaxation time is on the order of many minutes in the gas-phase and thus is long enough to allow separation of the rubidium vapor from the hp ^{83}Kr and transfer into a superconducting NMR magnet. Hp ^{83}Kr NMR signal intensities are three or more orders of magnitude greater than those obtained from thermally polarized krypton [19, 20] and provide sufficient signal intensities for relaxation measurements within a manageable experimental timeframe. This combination of relatively high signal intensities and favorable relaxation times makes ^{83}Kr possibly the best isotope for study gas-phase collisional processes in the noble gases.

In addition to being of value for the refinement of theory, the longitudinal relaxation of ^{83}Kr may be of practical importance as it has been shown to be a sensitive probe of surface-to-volume ratio [21], surface chemistry [21], surface hydration [20], and surface temperature [19] in porous materials and can yield strong surface sensitive contrast in T_1 weighted MR images [22, 23]. However, the maximum achievable polarization and the time needed to achieve this polarization are determined largely by relaxation during the SEOP process and subsequent gas transfer. Thus, a more detailed understanding of the factors that contribute to the longitudinal relaxation of ^{83}Kr could potentially lead to higher signal intensities and novel techniques for characterizing a number of important surface properties.

The T_1 times observed in this work ranged from 40 s to more than 400 s enabling relatively large numbers of measurements to be performed within a manageable experimental timeframe. In total, the work presented in this chapter comprises more than 700 individual relaxation measurements and represents the first systematic study of the longitudinal relaxation of ^{83}Kr in two-component gas mixtures and at low krypton densities of 0.1 to 10 amagat. (Note: An amagat is defined as the number of ideal gas molecules or atoms per unit volume at 101.325 kPa and 273.15 K and is equal to 2.6868×10^{25} m^{-3}). Additionally, ^{83}Kr longitudinal relaxation was studied in twelve different gas mixtures containing varying percentages of a buffer gas (either N_2 and He). By varying the composition of the gas mixtures, the contribution of each gas to the observed density dependent ^{83}Kr relaxation rate was determined. Finally, a relaxational efficiency is defined that depends on the details of binary krypton-collisions and that may be useful in refining intermolecular potentials.

The total ^{83}Kr relaxation rate was also found to be due to a density independent contribution. By varying the surface chemistry of the detection cell, it is shown that a portion of this density independent relaxation was due to surface interactions. However, the density independent relaxation was also influenced by the composition of the gas mixture indicating that another, surface independent contribution exists. By varying the composition of the gas mixture, in binary helium-krypton and nitrogen-krypton gas mixtures, it was determined that this second density dependent contribution resulted from the formation of relatively long-lived van der Waals molecules.

4.2 Materials and Methods

4.2.1 NMR Instrumentation and Methods

Experiments were performed on a Chemagnetics CMX II 400 NMR spectrometer in a 9.4 T wide-bore (89 mm) superconducting magnet using a custom-built probe tuned to the 15.4 MHz resonance frequency of ^{83}Kr. Relaxation was observed by acquiring spectra from sixteen, evenly spaced, constant flip angle (~12°) RF pulses applied to single boluses of hp gas. The relaxation rate was determined by normalizing the signal intensities to that of the spectrum resulting from the first RF pulse and fitting the data to

$$S_n(t) = \cos^n \theta \cdot e^{-t/T_1} = \cos^{t/\tau} \theta \cdot e^{-t/T_1}, \qquad (4.2.1)$$

where $S_n(t)$ is the normalized signal intensity, n is the number of pulses, t is the experimental time, τ is the delay between pulses, and θ is the flip angle. The second equality in Eq. 4.2.1 results from the even spacing between pulses and the pulse duration being negligible compared to τ. The flip angle was determined by varying the length of the RF pulse in a standard delay-pulse-acquire sequence with a 40-step array between 0° and 360° using hp ^{83}Kr (95% Kr, 5% N_2) produced under continuous flow conditions (~125 ml/min at 200 kPa) to allow signal averaging. Each increment in the array comprised 32 acquisitions and was acquired with phase cycling, and the delay between pulses was sufficient to replenish the hp ^{83}Kr within the detection region [19].

4.2.2 SEOP and Gas Delivery

Gas mixtures were produced from research grade krypton (99.995% purity, natural abundance), nitrogen (99.9997% purity), and helium (99.9999% purity) (Airgas, Radnor,

PA). Optical pumping was performed in cylindrical Pyrex cells (length = 125 mm, ID = 24 mm) containing ~1 g of rubidium (99.75%; Alfa Aesar, Ward Hill, MA), housed in a quartz and aluminum oven to maintain even heating (438 ± 5 K), and placed in the fringe field of the superconducting magnet (~0.05 T). The light (794.7 nm) from two, 30 W Coherent FAP diode-array laser systems (line width 2 nm) was directed via fiber optic coupling cables through a circular polarizer onto the pump cell. After the light passed through the fiber optics and the polarizer, the power was reduced to ~40 W.

Relaxation measurements were made in a single Pyrex detection cell (ID = 1.5 mm length = 65 mm: See Fig. 4.1) attached to a Pyrex transfer tube (ID = 3 mm, length = 0.6 m). Polarization was allowed to build for several minutes while evacuating the detection cell to less than 10 Pa. The hp gas was then transferred by pressure equalization from the SEOP cell to the detection cell through ~1 m of PFA tubing (ID = 1.7 mm: Swagelock, Solon, OH). Following gas transfer, a 90-150 s waiting period was applied before performing experiments to reduce temperature and pressure fluctuations. The pressure was monitored by a DTG-6000 digital pressure gauge (3D Instruments LLC, Anaheim, California), and gas densities were calculated assuming ideal gas behavior.

4.2.3 Detection Cell Preparation

Relaxation measurements were made for krypton mixtures in contact with two different of surface treatments. The initial measurements (i.e. approximately half of the total number of measurements) were performed in an untreated Pyrex detection cell, and the remaining measurements were made in the same detection cell after it had been siliconized. In both cases, the detection cell was evacuated overnight at a pressure of less

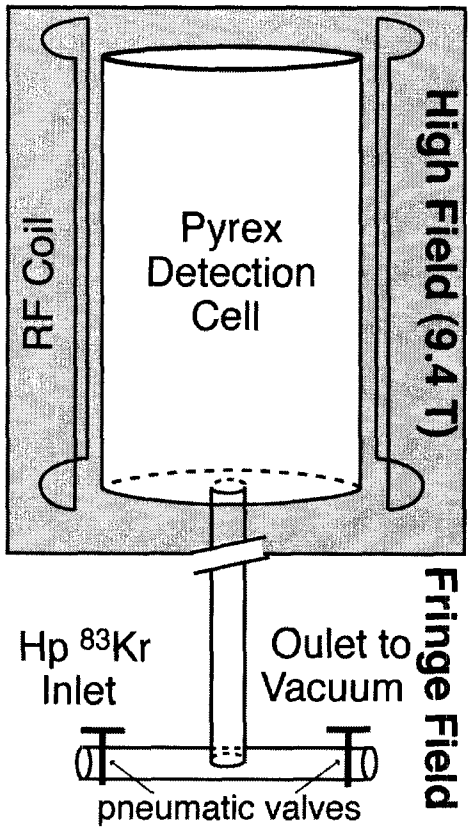

Figure 4.1: Hp ^{83}Kr Pyrex detection cell with an ID of 15 mm and a length of 66 mm located in the high field (9.4 T) region of the superconducting magnet. Attached to the cylinder was a Pyrex transfer tube with an ID of 3 mm and a length of 0.6 m. Prior to experiments, the cell was evacuated to a pressure of less than 10 Pa. The hp ^{83}Kr mixture was then transferred from the pump cell by pressure equalization, and a 90-150 s waiting period was applied to allow temperature and pressure fluctuations to subside. The gas flow was controlled by two pneumatically actuated values located in the fringe field of the superconducting magnet.

than 10 Pa to remove adsorbed atmospheric water vapor. Following evacuation, the cell was either kept under vacuum (during experiments only) or overpressure with a dry inert gas. Prior to siliconizing the detection cell, it was washed for 15 min with a 1:1:5 solution of 30% v/v NH_4OH, 30% v/v H_2O_2, and distilled water followed by a 15 min wash at 358 K with a 1:1:5 solution of 30% v/v HCl, 30% v/v H_2O_2, and distilled water. The cell was then washed five times with distilled water and dried by flowing N_2 gas over the surface for 45 min and then evacuating the cell at 4 Pa and 475 K for 1 h. The cell was then siliconized using a 1:15 mixture of SurfaSil (Pierce Biotechnology Inc., Rockford, IL) in toluene according to the manufacturer's instructions.

4.3 Density Dependent Longitudinal Relaxation

4.3.1 Relaxation Resulting from Binary Collisions

For molecular gases at moderate densities, the interactions responsible for longitudinal relaxation are always present. Binary collisions modulate these interactions, thus the collision rates cause the characteristic correlation times. As a result, the longitudinal relaxation rates typically decrease with increasing gas density due to decreasing correlation times. This often leads to a $1/\rho$ dependence of the relaxation rate for NMR transitions in gas-phase molecules [1]. In noble gas atoms, however, collisions are responsible for generating the interactions that cause relaxation, and the correlation times are dictated by the duration of these collision. Because the number of collisions increases linearly with density, the longitudinal relaxation rate for atomic species also increases linearly with the density. In an early theoretical treatment of gas-phase ^{129}Xe relaxation [24],

this linear dependence was attributed to the spin-rotation interaction during binary ^{129}Xe-Xe collisions. More recently, it was shown that these binary collisions also influence the relaxation through modulation of the chemical shift tensor [7] resulting in a dependence of the rate upon the square of the applied magnetic field strength.

The longitudinal relaxation rates of ^{131}Xe [8] and ^{83}Kr [9] also display a linear dependence on total gas density. Thus the ^{83}Kr relaxation rate can be expressed as

$$\frac{1}{T_1} = \left(\frac{1}{T_1\rho}\right)_{Kr} \rho_{Kr}. \tag{4.3.1}$$

In principle, the relaxation rates of $I > 1/2$ noble gases are affected by spin rotation, chemical shift anisotropy, and quadrupolar interactions, but quadrupolar contributions are expected to be dominant. A detailed theory of quadrupolar relaxation in ^{131}Xe was developed by Adrian [25] and extended to ^{83}Kr by Brinkmann and Kuhn [9]. (See Section 4.3.2.) The theory presented in these works provided better than order of magnitude agreement with the experimental data (See Table 4.1.) suggesting it captures the essential details of the underlying physical processes contributing to relaxation.

Rather than refining the assumptions or potential used in these earlier works, we will attempt to interpret our current experimental results in a manner that will be generally applicable for the spin $I > 1/2$ noble gas isotopes and that should be useful as a starting point for future theoretical development. This approach will be similar that that used by Jameson and co-workers to discuss the longitudinal relaxation of ^{129}Xe caused by dipolar coupling to gas-phase O_2 [10] and that was subsequently extended to ^{3}He interacting with O_2 [12] and NO [13]. For a noble gas relaxing due to intermolecular collisions, the relaxation rate is given by

$$\frac{1}{T_1} \approx \left|H^{(1)}\right|^2 \tau^2 Z_{eff}, \tag{4.3.2}$$

where $\left|H^{(1)}\right|$ is the magnitude of the interaction responsible for relaxation. In Eq. 4.3.2, $Z_{eff} = \rho \bar{v} \sigma_{eff}$ is the effective collision frequency with an effective collisional cross-section σ_{eff}, and $\tau = d/\bar{v}$ is the duration of the collision with d being the characteristic length of the interaction. Eq. 4.3.2 can be related to the geometric cross-section for hard sphere collisions by defining the collision efficiency

$$F(V,T) \equiv \sigma_{eff} / \sigma_{geom}, \tag{4.3.3}$$

where V is the interaction potential, T is the temperature, and $\sigma_{eff} \sim d^2 F(V,T)$.

The magnitude of the quadrupole interaction squared can be taken to be [25]

$$\left|H^{(1)}\right|^2 = \frac{3}{160} \frac{2I+3}{I^2(2I-1)} \left(\frac{eQq}{\hbar}\right)^2_{4p}, \tag{4.3.4}$$

where eQq/h is the nuclear electric quadrupole coupling constant. Using spectroscopic data of ref. [26], Brinkmann and Kuhn calculated the quadrupole coupling to a krypton 4p electron and determined that $(eQq/\hbar)^2_{4p}$ = 5.682 × 10^9 Hz . (Note that in the analogous expressions for ^{21}Ne and ^{131}Xe, the relevant quadrupole coupling terms would be $(eQq/\hbar)^2_{2p}$ and $(eQq/\hbar)^2_{5p}$ respectively.) Combining Eqs. 4.3.2 - 4.3.4 and the definition of τ yields

$$\frac{1}{T_1 \rho} = \frac{3}{160} \frac{2I+3}{I^2(2I-1)} \left(\frac{eQq}{\hbar}\right)^2_{4p} \frac{d^4}{\bar{v}} F(V,T). \tag{4.3.5}$$

Binary ^{83}Kr-buffer gas collisions are also expected to produce a relaxation rate that depends linearly buffer gas density. (Throughout this work, the subscript *bg* will be used

designate buffer gas specific quantities.) Thus, in a two-component gas mixture, Eq. 4.3.1 becomes

$$\frac{1}{T_1} = \left(\frac{1}{T_1\rho}\right)_{Kr} \rho_{Kr} + \left(\frac{1}{T_1\rho}\right)_{bg} \rho_{bg}, \tag{4.3.6}$$

where $(1/T_1\rho)_{bg}$ is specific to a given buffer gas and depends on the efficiency $F(V,T)_{bg}$. If the total gas density is varied in mixtures with fixed compositions, a ratio $r_{bg} \equiv \rho_{bg}/\rho_{Kr}$ can be defined, and Eq. 4.3.6 becomes

$$\frac{1}{T_1} = \left[\left(\frac{1}{T_1\rho}\right)_{Kr} + \left(\frac{1}{T_1\rho}\right)_{bg} \cdot r_{bg}\right]\rho_{Kr} = \left(\frac{1}{T_1\rho}\right)_{bc} \rho_{Kr}, \tag{4.3.7}$$

where $(1/T_1\rho)_{bc}$ will be the slope observed when plotting the relaxation rate versus krypton density. (Throughout the text, the subscript *bc* denotes that the parameter is determined by all types of binary collisions.)

4.3.2 Theoretical Treatments of Density Dependent Relaxation in the Nuclear Spin $I > 1/2$ Noble Gases

In its most general form, the theoretical expression for the binary collision induced relaxation rate of $I > 1/2$ noble gases given by Adrian [25] can be written as

$$\frac{1}{T_1} = \frac{3}{80}\frac{2I+3}{I^2(2I-1)}\left(\frac{eQq_d}{\hbar}\right)\int_0^\infty\int_0^\infty P_c(E,B)\times \left(\frac{1}{4}\sum_{\Delta J=0,\pm 2}\left(\frac{3}{2}\right)^{\frac{\Delta J}{2}}\left|\int_{-\infty}^{\infty} F(R)e^{i\omega(\Delta J)t}dt\right|^2\right)dEdB, \tag{4.3.8}$$

where eQq_d/h is the quadrupolar coupling constant at the collision diameter d, ΔJ is the change in rotational angular momentum of the collision pair, ω is the angular frequency

associated with the $\Delta J = 0,\pm 2$ transitions, and R is the interatomic separation with the distance of closest approach being denoted R_0. (Note that $F(R)$ in Eq. 4.3.8 should not be confused with $F(V,T)$ defined in Eq. 4.3.3.) The probability that an atom will undergo a collision characterized by an initial relative kinetic energy in the interval E to $E + dE$ and an impact factor in the interval B to $B + dB$ within the time interval Δt is given by $P_c(E,B)dEdB\Delta t$. The total quadrupole coupling constant is related to eQq_d/h by the equation $eQq/h = (eQq_d/h)F(R)$.

Brinkman and Kuhn [9] extended Eq. 4.3.8 to treat the longitudinal relaxation rate of ^{83}Kr, which was shown to take the form

$$\frac{1}{T_1} = \frac{3(2I+3)}{80I^2(2I-1)}\left[8.887\times 10^{-3}\left(\frac{eQq}{\hbar}\right)_{4p}\right]^2\left(\frac{\pi\mu d^2}{8\varepsilon}\right)^{1/2}\pi\rho d^3\sum_{\Delta J=0,\pm 2}\left(\frac{3}{2}\right)^{\frac{\Delta J}{2}} I(\Delta J,\overline{T}) \quad (4.3.9)$$

where $(eQq/\hbar)_{4p}$ is the quadrupole couple constant for a 4p electron in ^{83}Kr, ε is the well depth of the modified Buckingham potential assumed in the derivation, $\overline{T}$ is a reduced variable $\overline{T} = k_B T/\varepsilon$, and $I(\Delta J,\overline{T})$ is the integral

$$I(\Delta J,\overline{T}) = \frac{1}{2\pi\overline{T}^{\frac{3}{2}}}\int_0^\infty\int_0^\infty\left|\int_{-\infty}^{\infty}\left[F_{ex}(\overline{R}) - F_{vdw}(\overline{R})\right]\exp\left[i\frac{\overline{E}\overline{B}^2}{4\overline{R}_0^4}\Delta J\bar{t}\right]dt\right|^2 \times \overline{E}\exp\left(-\overline{E}/\overline{T}\right)d\overline{E}d\overline{B} \quad (4.3.10)$$

In Eq. 4.3.10, $\overline{R} = R/d$, $\overline{E} = E/\varepsilon$, $\overline{B} = B/d$, and $\bar{t} = t(8\varepsilon/\mu d^2)^{1/2}$ are reduced variables and $F_{ex}(\overline{R})$ and $F_{vdW}(\overline{R})$ are functions that describe the exchange interactions and van der Waals contributions to $F(\overline{R})$ respectively.

Collecting the terms that are not related to the impact factor or the interaction potential from Eq. 4.3.9 and factors of 1/2 and $(k_B T)^{-1/2}$ (from $1/\overline{T}^{3/2}$) from Eq. 4.3.10, yields the proportionality

$$\frac{1}{T_1} \propto \frac{3}{80} \frac{2I+3}{I^2(2I-1)} \left(\frac{eQq}{\hbar}\right)^2_{4p} \left(\frac{\pi\mu d^2}{8\varepsilon}\right)^{1/2} \rho d^3 \frac{1}{2(k_B T)^{1/2}}. \tag{4.3.11}$$

With slight rearrangement, Eq. 4.3.11 becomes

$$\frac{1}{T_1 \rho} \propto \frac{3}{160} \frac{2I+3}{I^2(2I-1)} \left(\frac{eQq}{\hbar}\right)^2_{4p} \frac{d^4}{v_{rms}}, \tag{4.3.12}$$

which contains all of the terms in Eq. 4.3.5 text except $F(V,T)$. Thus, the elements of Eqs. 4.3.9 and 4.3.10 that are not listed in Eq. 4.3.12 can be equated with $F(V,T)$, and the earlier theoretical treatments of relaxation in the spin $I > 1/2$ noble gases can essentially be viewed as a special case of Eq. 4.3.5 where a specific intermolecular potential was chosen.

4.3.3 Experimental Results in the Binary Collision Regime

In this work, the observed signal decay was in all cases well described by Eq. 4.2.1 as can be seen in Fig. 4.2, where Fig. 4.2A displays representative relaxation data from a 50% krypton, 50% N_2 gas mixture at total gas densities of approximately 2 and 10 amagat in contact with both detection cell surface chemistries. The relaxation rate was faster at higher total gas densities, as is expected from Eqs. 4.3.6 and 4.3.7, and also when in contact with the higher affinity, siliconized surface. This surface chemistry effect has been observed previously [21] (See Chapter 3.) and results from higher krypton affinity for the siliconized surface.

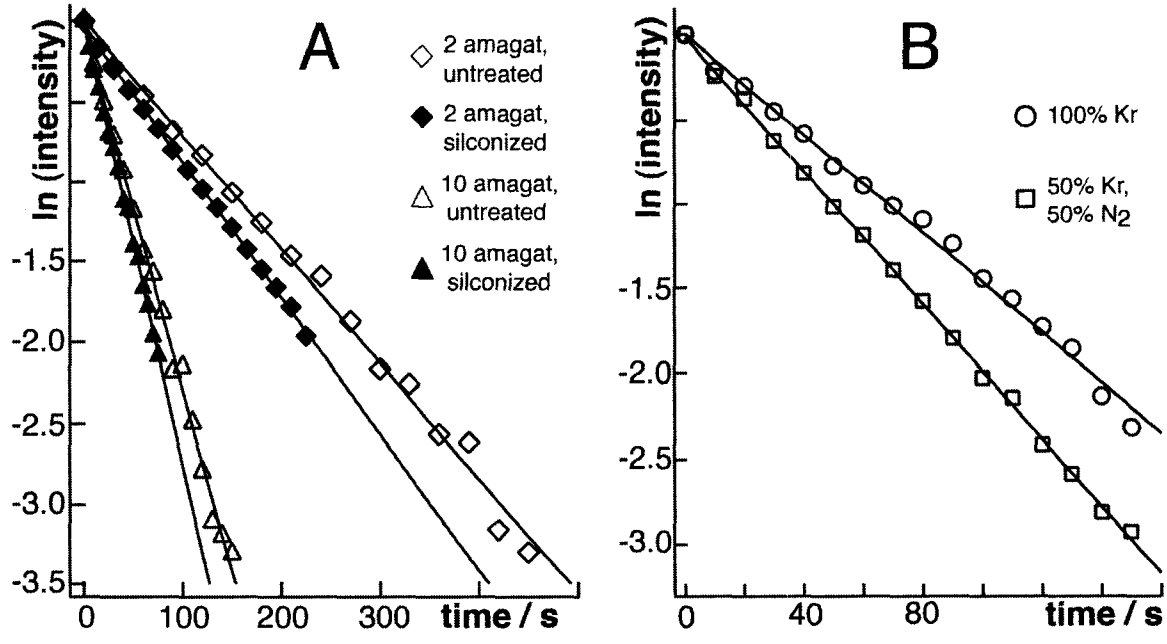

Figure 4.2: Representative signal intensity decay data from hp ^{83}Kr as a function of time. The y-axes represent the natural logarithm of the signal intensities measured from evenly spaced, medium angle (~12°) RF pulses applied to single boluses of hp gas. The intensities in each curve have been normalized to the intensity resulting from the first RF pulse. Lines are linear fits of the data. **(A)** Signal intensity decay in a 50% krypton, 50% N_2 gas mixture as function of time. The total gas density and the surface chemistry of the detection cell walls are indicated in the legend. Note that relaxation is influenced both by the surface chemistry and the total gas density. **(B)** Signal intensity decay data in pure krypton and in a 50% krypton, 50% N_2 mixture. Both sets of data were collected in the untreated detection cell at a krypton density of 3.8 amagat. The gas composition is indicated in the legend. The signal from the N_2 containing mixture decayed 42% more rapidly ($1/T_1 = 0.0182\ s^{-1}$) than did the signal from pure krypton ($1/T_1 = 0.0128\ s^{-1}$) partially due to binary, ^{83}Kr-N_2 collisions.

Fig. 4.3 displays representative ^{83}Kr relaxation rate data from the untreated detection cell as a function of density for 25% krypton mixtures containing either 75% N_2 or 75% helium. The resulting best-fit lines display pronounced non-zero y-intercepts. This density independent contribution is due to a combination of ^{83}Kr-surface interactions and the formation of ^{83}Kr-Kr van der Waals dimers, which also strongly influence ^{129}Xe relaxation [15,27]. Thus, all density dependent relaxation data in this work were fit to

$$\frac{1}{T_1} = \left(\frac{1}{T_1\rho}\right)_{bc} \rho_{Kr} + \frac{1}{T_{1i}}, \tag{4.3.13}$$

where $1/T_{1i}$ is the density independent, non-zero y-intercept. A more detailed treatment of $1/T_{1i}$ is given in Sections 4.4 to 4.6.

Fig. 4.4 shows the $(1/T_1\rho)_{bc}$ values obtained from the slopes of relaxation rate versus krypton density plots for the twelve different gas mixtures and both detection cell surface chemistries used in this work. For both the N_2 containing mixtures (squares) and the helium containing mixtures (circles), $(1/T_1\rho)_{bc}$ increases linearly with increasing r_{bg}, but the best-fit lines of these data have different slopes reflecting differences in the details of the ^{83}Kr-He and ^{83}Kr-N_2 collisions. However, both lines share a common y-intercept that is equal to $(1/T_1\rho)_{Kr}$ (i.e. the slope of relaxation rate versus krypton density plots generated from relaxation measurements with pure krypton gas). Within the scatter of the data, the $(1/T_1\rho)_{bc}$ data obtained from the untreated Pyrex detection cell and the siliconized Pyrex detection cell fall on the same line indicating that the surface contribution to ^{83}Kr longitudinal relaxation is indeed density independent. Table 4.1 lists the value of $(1/T_1\rho)_{Kr}$ obtained from the y-intercepts in Fig. 4.4 (See d and e in Table 4.1)

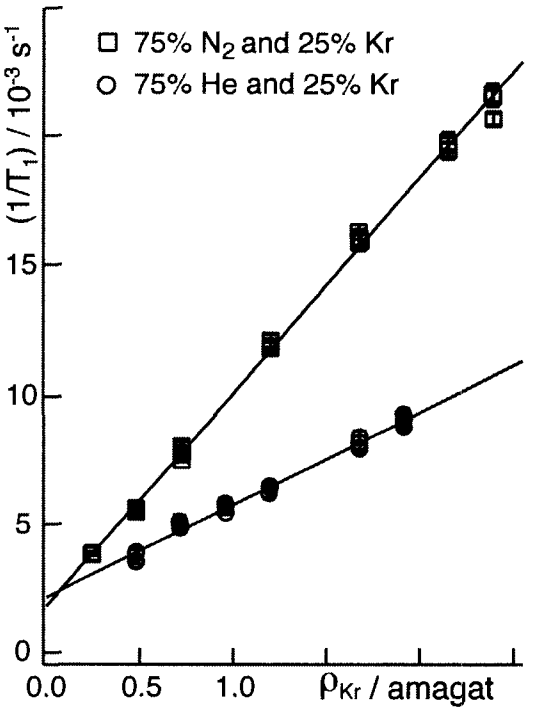

Figure 4.3: Longitudinal relaxation rates as a function of ρ_{Kr}. The data are from gas mixtures consisting of 25% Kr and either 75% N_2 or 75% He in the untreated detection cell. The gas mixture is indicated in the legend. The lines are fits of the data to Eq. 4.3.13. The error bars are the standard deviations in the residuals resulting from the fits of the signal decay to Eq. 4.2.1.

along with the values obtained from pure krypton relaxation data (b and c). The two different measures of $(1/T_1\rho)_{Kr}$ are in good agreement. Also listed in Table 4.1 are the values of $(1/T_1\rho)_{bg}$ calculated for both helium and N_2.

4.3.4 Comparison of Density Dependent Relaxation with Earlier Work

The value of $(1/T_1\rho)_{Kr}$ in this work differs from that of Brinkman and Kuhn [9] by about 35%. Our work was conducted at 9.4 T, while the earlier work was conducted at 2.1 T, but field strength is not expected to influence gas-phase quadrupolar relaxation [25, 28]. Although previous work showed that the relaxation hp ^{83}Kr rate increased with decreasing field strength [19], this dependence is likely due to surface interactions as has been observed for hp ^{129}Xe [29].

Therefore the source of the discrepancy likely lies with the data interpretation by Brinkman and Kuhn, who worked krypton densities between 25 and 156 amagat in sealed Pyrex bulbs. These densities were assumed to be high enough for surface contributions to be negligible, and the relaxation data were fit to a straight line through the origin. However, the density independent contribution (i.e. from relaxation due to surface interactions and van der Waals complex formation) to the rate observed in the current work from pure krypton in the untreated detection cell was 6.6×10^{-3} s^{-1}. Extrapolating our results to 25 and 156 amagat suggests that density independent processes would be responsible for at least 15% and 3% of the total relaxation rate at each of these densities respectively. Further, the samples used by Brinkman and Kuhn had volumes ranging from 0.4 to 2.8 cm^3 resulting in larger surface-to-volume ratios and thus larger values of surface

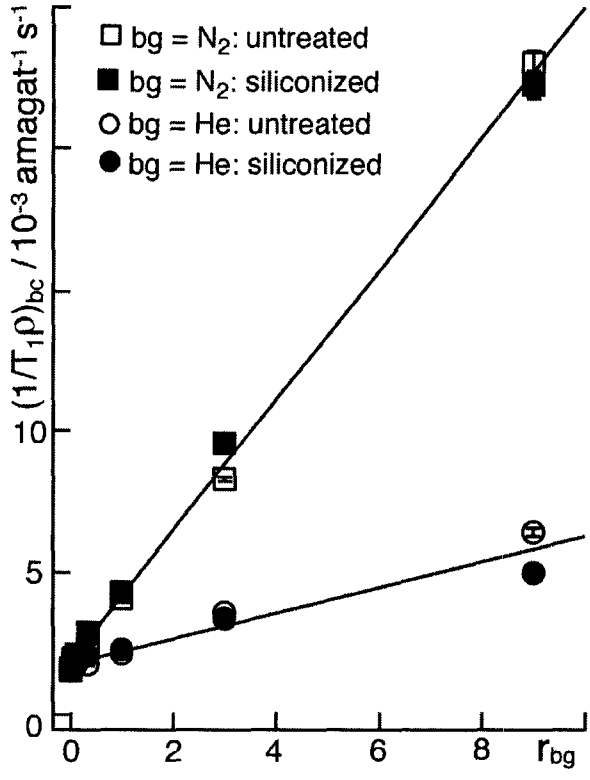

Figure 4.4: The slopes of the various density dependent curves, $(1/T_1\rho)_{bc}$, plotted against $r_{bg} \equiv \rho_{bg}/\rho_{Kr}$. The buffer gas and the surface chemistry of the detection cell walls are indicated in the legend. The lines are fits of the data with slopes of $(1/T_1\rho)_{bg}$ and the intercepts of $(1/T_1\rho)_{Kr}$ (see Table 4.2.). The error bars are the standard deviations in the residuals resulting from fitting density dependent data to Eq. 4.3.13.

relaxation than was present in our work. Therefore, Brinkman and Kuhn may have overestimated the contribution of the gas-phase relaxation.

Table 4.1: Binary collision data for ^{83}Kr longitudinal relaxation.

Collision Pair	$(1/T_1\rho)$ amagat^{-1} s^{-1}	$\bar{v}$ m s^{-1}	d [a] Å	σ_{geom} [a] Å^2	$F(V,T)$
^{83}Kr-Kr	$1.58\pm0.03\times10^{-3}$ [b] $1.67\pm0.05\times10^{-3}$ [c] $1.8\pm0.1\times10^{-3}$ [d] $1.7\pm0.1\times10^{-3}$ [e]	382	3.581	40.29	3.1×10^{-5} [f]
^{83}Kr-N_2	$2.31\pm0.03\times10^{-3}$	540	3.639	41.60	5.9×10^{-5}
^{83}Kr-He	$4.5\pm0.3\times10^{-4}$	1270	3.288	33.96	4.1×10^{-5}
^{83}Kr-Kr	$2.13\pm0.05\times10^{-3}$ [g] 5.87×10^{-3} [h]	--	--	--	--
^{131}Xe-Xe	3.92×10^{-2} [i] 4.61×10^{-2} [j]	311	3.917	48.20	7.7×10^{-5} [k]

[a] Geometric cross-sections ($\sigma_{geom} = \pi d^2$) and d from ref. [30] (Table A3.2).
[b] $(1/T_1\rho)_{Kr}$ from the untreated detection cell.
[c] $(1/T_1\rho)_{Kr}$ from the siliconized detection cell.
[d] Y-intercept from N_2-Kr mixtures (see Fig. 4.4 squares).
[e] Y-intercept from He-Kr mixtures (see Fig. 4.4 circles).
[f] Calculated using the average $(1/T_1\rho)_{Kr}$ from both the siliconized and untreated cell.
[g] Experimental value from ref [9].
[h] Theoretical value from ref. [9].
[i] Experimental value from ref. [8].
[j] Theoretical value from ref [25].
[k] Calculated using $(eQq/\hbar)_{5p} = 3.173\times10^9$ Hz (ref. [25]).

4.3.5 General Trends in Relaxation Parameters

Using the data presented in Table 4.1, the $(1/T_1\rho)$ values determined in this work can be ranked with respect to the collision partner in the order

$$(1/T_1\rho)_{N_2} > (1/T_1\rho)_{Kr} > (1/T_1\rho)_{He}.$$

The relationship $(1/T_1\rho)_{Kr} > (1/T_1\rho)_{He}$ results largely from the smaller collision diameter and greater relative speed of a krypton-helium compared to a krypton-krypton pair. While a krypton-nitrogen pair also has greater relative velocity than a krypton-krypton pair, the relationship $(1/T_1\rho)_{N_2} > (1/T_1\rho)_{Kr}$ is observed, and the relationship must result from a higher efficiency for ^{83}Kr-N_2 collisions.

Using Eqs. 4.3.5 and 4.3.7, the $F(V,T)$ values were calculated from $(1/T_1\rho)$ data of all collision pairs studied in this work (See Table 4.1) and can be ranked in the order

$$F(V,T)_{N_2} > F(V,T)_{He} > F(V,T)_{Kr}.$$

In general, the collision efficiencies shown in Table 4.1 are quite small, but this is to be expected for an isotope that has T_1 times on the order of tens of seconds at densities of a few amagat. The nature of the trend in $F(V,T)$ is not intuitively obvious, but the data in Table 4.1 suggest a complex interplay of attractive van der Waals and repulsive exchange interactions.

4.3.6 Implications for Hp ^{83}Kr Production and Storage

Although $F(V,T)$ may be of interest for refining intermolecular potentials, $(1/T_1\rho)$ ultimately determines the observed relaxation rate. Relaxation rates are the limiting factor in achieving high non-equilibrium ^{83}Kr polarization and limit the lifetime of the hp state. Therefore the $(1/T_1\rho)$ values reported in this work are of practical interest. Neglecting the contribution of van der Waals molecules and surface interactions, the relaxation time expected for pure krypton at ambient pressures (~1 amagat) is T_1 = 615 s. The T_1 times

observed in this work ranged from about 40 s at the highest total gas densities to slightly over 400 s in the 90% helium mixture at gas densities of less than 2 amagat suggesting that T_1 times in excess of ten minutes should be achievable using dilute gas mixtures in containers with smaller surface-to-volume ratios. These longer T_1 times should be achievable without sacrificing signal intensity because the decreased ^{83}Kr spin density in low percentage krypton mixtures should be offset by improved polarization efficiency and reduced relaxational losses [20]. Although no attempt was made to rigorously compare the hp ^{83}Kr signal intensities from the various gas mixtures, little qualitative difference was observed for a give buffer throughout the total range of compositions and densities.

The observation $(1/T_1\rho)_{N_2} > (1/T_1\rho)_{Kr}$ suggests that removing N_2 from the optical pumping gas mixture entirely might be beneficial. However, N_2 serves to non-radiatively quench the excited state of the rubidium vapor during SEOP [14], and, as a result of improved SEOP efficiency, a 95% krypton and 5% N_2 mixture yields about twice the signal intensity as does pure krypton at the same total gas density. By measuring the density dependent relaxation of ^{83}Kr in the presence of other gases such as H_2, it may be possible it identify alternate quenching gases that have lower $(1/T_1\rho)_{bg}$ values and thus lead to improved signal intensities. In the absence of such data, the N_2 concentration should be kept as low as possible without compromising radiation quenching. By using IR measurements during ^{129}Xe SEOP, a concentration of 10-30 kPa was previously found to be sufficient for this purpose [31].

4.3.7 Additional Comments on the Experimental Approach

The methods used in this work should be fairly robust and provide information about interactions between ^{83}Kr and most non-reactive buffer gases (e.g. H_2, alkanes, fluorinated molecules, and other noble gases). In addition to having more convenient T_1 times, ^{83}Kr has two further fundamental advantages for studying noble gas-molecule interactions compared to ^{129}Xe. The density dependence of the ^{83}Kr relaxation rate is linear with density even at krypton densities of less than one amagat. In sharp contrast to this simple behavior, the relaxation rate ^{129}Xe goes through a minimum at ~3 amagat [7, 32], which may complicate the identification of the contribution from binary collisions. Finally, ^{129}Xe relaxes by two mechanisms (i.e. spin rotation and chemical shift anisotropy), which are of comparable magnitudes at the magnetic field strengths in common use [7]. Therefore, a single effective collisional cross-section, and thus relaxation efficiency, cannot be defined. Although a similar approach to that used in this work may be possible for ^{131}Xe, which will relax even more quickly than ^{83}Kr, its low-density relaxation behavior is currently unknown.

A limitation of the technique used in this work is that the hp ^{83}Kr residing in the transfer tube was not subject to the small flip angle RF pulse (See Fig. 4.1.) but was subject to more pronounced surface relaxation. Diffusion from this region could have caused the relaxation rate to be either underestimated or overestimated slightly. A more serious concern is the uncertainty in the temperature of the gas mixtures. The ambient bore temperature of the magnet was ~290 K, but the temperature inside the detection cell could not be measured. However, the 90-150 s (~1 T_1) waiting period between the gas transfer and the experiments should have allowed substantial thermal equalization. More

importantly, the value of $F(V,T)$ is expected increase with increasing temperature [25], but $1/\bar{v}$ decreases with increasing temperature. Thus the two effects should be offsetting, and it is unlikely that the uncertainties in temperature caused substantial artifacts.

4.4 Surface Induced Density Independent Relaxation

4.4.1 Influence of Surface Chemistry

Fig. 4.5 displays the relaxation rate as a function of ρ_{Kr} in pure krypton and in a 50% krypton, 50% N_2 mixture. Linear fits of these data display pronounced non-zero y-intercepts indicating that a density independent component, $1/T_{1i}$, strongly influences the relaxation rate. Density independent relaxation was observed for all krypton mixtures examined in this work suggesting Eq. 4.3.13 is valid for all gas mixtures studied. Also presented in Fig. 4.5 are data from krypton mixtures in contact with two different surface chemistries. The intercept $1/T_{1i}$ in pure krypton was found to be increased by 13% to 7.49×10^{-3} s^{-1} in the cell with the siliconized surface compared to the untreated Pyrex cell. This surface effect was even more apparent in 10% krypton mixtures where 390% and 320% increases for the siliconized surface were observed for N_2 and He containing mixtures respectively. Because these measurements were performed in a single detections cell with a constant surface-to-volume ratio, the differences must have been caused by the altered surface chemistry.

4.4.2 Phenomenological Description of Surface Induced Relaxation

While the details of noble gas surface relaxation are thoroughly understood only for ^{3}He [33-36], a qualitative description can be developed for hp ^{83}Kr. The surface dominated T_1 relaxation is consider to be 'surface limited' when the overall relaxation rate is substantially slower than the time scale of the gas diffusion through the sample (i.e. when surface relaxation is the rate limiting step). Under these conditions, diffusion is rapid enough to eliminate any spatial dependence in the relaxation (i.e. there is no distance dependence in the gas-phase relaxation rate in relation to the surfaces), and the observed rate is expected to be monoexponential [37, 38] assuming that the relaxation of the adsorbed species while on the surface is itself monoexponential. Although multiexponential surface relaxation is in principle possible for $I > 1/2$ nuclei [39, 40], the relaxation behavior was observed in this work appeared to be clearly monoexponential (See Fig. 4.2.). Thus, the surface induced contribution to the overall relaxation, $1/T_{1s}$, depends only on the relaxation rate experienced while adsorbed on the surface, $1/T_{1a}$, and the fraction of adsorbed atoms. Under these conditions, $1/T_{1s}$ can be expressed as [41]

$$\frac{1}{T_{1s}} = \frac{1}{T_{1a} + \tau_a} \frac{n_a}{n_a + n_g} \tag{4.4.1}$$

where n_a is the number of adsorbed atoms, n_g is the number of bulk gas-phase atoms, and $\tau_a = \tau_0 \exp(E/k_B T)$ is the average adsorption time with τ_0 being the inverse of the desorption attempt rate and E being the desorption activation energy. Taking E to be 0.095 eV for krypton adsorbed on borosilicate glass [18] and assuming $\tau_0 = 10^{-12}$ s, at 300 K τ_a is approximately 4×10^{-11} s suggesting that $T_{1a} >> \tau_a$.

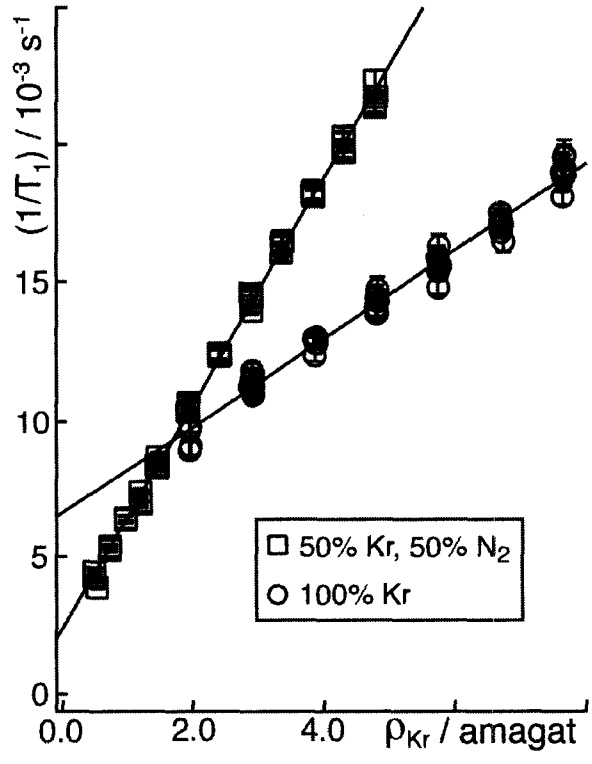

Figure 4.5: Longitudinal relaxation rate as a function of krypton density in the untreated Pyrex detection cell. The data were obtained from pure krypton and a 50% krypton, 50% N_2 mixture. The gas composition of the mixture is indicated in the legend. The lines are linear fits of the relaxation data as a function of density. The errors are the standard deviations in the residuals resulting from nonlinear least squares fitting of relaxation decay data. At higher total gas densities, the N_2 containing mixture relaxes more quickly than does pure krypton. At lower densities, the pure krypton mixture relaxes faster indicating that a mechanism exists which, to some extent, compensates for relaxation due to binary, ^{83}Kr-N_2 collisions. Note that the presence of N_2 alters the value of the y-intercept of the fits (i.e. $1/T_{1i}$).

At moderate temperatures and pressures it is expected that $n_g >> n_a$, and Eq. 4.4.1 simplifies to

$$\frac{1}{T_{1s}} = \frac{n_a}{T_{1a} \cdot n_g}. \tag{4.4.2}$$

The value of n_a is determined by the surface coverage, θ, and is given by $n_a = A \cdot \theta$, where A is the surface area. Using the relationship $n_g = V \cdot \rho_{Kr}$, the surface induced relaxation rate becomes

$$\frac{1}{T_{1s}} = \frac{A\theta}{T_{1a} V \rho_{Kr}}, \tag{4.4.3}$$

where θ is expected to be linearly dependent on gas density at moderate pressures and temperatures [42]. In the simplest case, the coverage is the product of the surface collision rate and τ_a. Thus, $\theta = (\rho_{Kr} v/4)\tau_a$, where $v = (8k_B T/\pi m)^{1/2}$ is the average speed with mass m, and Eq. 4.4.3 becomes

$$\frac{1}{T_{1s}} = \frac{A}{V}\frac{\tau_a}{T_{1a}}\frac{v}{4}. \tag{4.4.4}$$

Thus at the temperatures and densities used in this work (i.e. under conditions of low surface coverage), $1/T_{1s}$ is expected to be density independent.

For ^{83}Kr, quadrupolar interactions will dominate the relaxation on the surface suggesting [28]

$$\frac{1}{T_{1a}} \propto \frac{2I+3}{I^2(21-1)}\left(\frac{eQq}{\hbar}\right)^2 \tau_c, \tag{4.4.5}$$

where eQq/h is the quadrupole coupling constant and $\tau_c \approx \tau_a$ is the correlation time. Together Eqs. 4.4.4 and 4.4.5 lead to the relationship $1/T_{1s} \propto \tau_a^2$, thus explaining the strong

influence of surface chemistry and surface temperature observed in Chapters 2 and 3, both of which affect τ_a, on the observed relaxation rate. The actual relaxation time of surface-adsorbed ^{83}Kr is currently unknown, but work in zeolites suggests that T_{1a} is on the order of a millisecond [43]. Taking T_{1a} to be 1 ms, A/V to be the geometric surface-to-volume ratio of the detection cell (~360 m^{-1}), v to be 275 m/s, and τ_a to be 4×10^{-11} s, the surface contribution to the overall rate is expected to be $1/T_{1s}\sim1\times10^{-3}$ s^{-1}, which is of the correct order of magnitude to contribute to $1/T_{1i}$. However, Eq. 4.4.4 is not a function of gas composition, and therefore surface relaxation cannot explain the dependence on r_{bg} observed in Figs. 4.5 and 4.6 indicating that another mechanism must also contribute to $1/T_{1i}$.

4.5 Relaxation due to van der Waals Molecule Formation

The $1/T_{1i}$ intercepts from experiments with various gas compositions and two different container surfaces are presented in Figure 4.6 as a function of the ratio of buffer gas density, ρ_{bg}, to krypton density, $r_{bg} \equiv \rho_{bg}/\rho_{Kr}$. In both N_2 and helium containing mixtures, $1/T_{1i}$ decreased with increasing r_{bg}. For pure krypton (r_{bg} = 0) in the untreated Pyrex cell, the intercept is $1/T_{1i} = 6.63\times10^{-3}$ s^{-1}, but in a 10% krypton mixtures (r_{bg} = 9), $1/T_{1i}$ was reduced by more than an order of magnitude to 5.85×10^{-4} s^{-1} and 6.27×10^{-4} s^{-1} in the N_2 and helium containing mixtures respectively.

For ^{129}Xe, in addition to surface interactions [29] and binary ^{129}Xe-Xe collisions [6, 7], relatively long-lived ^{129}Xe-Xe van der Waals dimers also contribute to relaxation [27]. This van der Waals mediated mechanism is density dependent at high magnetic field strengths

[15], but density independent at low fields (i.e. at low resonance frequencies) [27] and is strongly influenced by gas composition suggesting dimer formation may contribute to $1/T_{1i}$ in ^{83}Kr. The fraction of krypton atoms in van der Waals dimers should to be small compared to the number of free krypton atoms and is therefore given by

$$\frac{2\rho_{Kr2}}{(\rho_{Kr}+2\rho_{Kr_2})} \approx 2\mathrm{K}\rho_{Kr}, \tag{4.5.1}$$

where $\mathrm{K} = \rho_{Kr_2}/\rho_{Kr}^2$ is the chemical equilibrium constant for Kr_2 formation. For ^{129}Xe, chemical shift anisotropy and spin rotation interactions contribute to the ^{129}Xe molecular relaxation [15], but for ^{83}Kr quadrupolar interactions will also contribute. The longitudinal relaxation rate can therefore be written as

$$\frac{1}{T_{1vdw}} = 2\mathrm{K}\rho_{Kr}\left(M^{sr}+M^{csa}+M^{q}\right)\left(\frac{\tau_c}{1+\omega_0^2\tau_c^2}\right), \tag{4.5.2}$$

where ω_0 is the ^{83}Kr Larmor frequency, τ_c is the correlation time, and M^{sr}, M^{csa}, M^{q} describe the relaxation due to spin-rotation, chemical shift anisotropy, and quadrupole interactions respectively. In the absence of paramagnetic species, quadrupole interactions typically dominate relaxation for spin $I > 1/2$ nuclei [28] suggesting

$$M^{sr}+M^{csa}+M^{q} \approx M^{q}, \tag{4.5.3}$$

where the quadrupolar term in a linear molecule is given by [3]

$$M^{q} = \frac{3(2I+3)}{160I^2(2I-1)}\left(\frac{eQq}{\hbar}\right)^2. \tag{4.5.4}$$

Krypton dimers are weakly bound with ε/k_B = 201.2 K [44], where ε is the well depth of the interaction potential. At 300 K, gas-phase collisions should be energetic

enough to break up the van der Waals molecules making τ_c approximately equal to the lifetime of the Kr_2 dimer. The inverse correlation time is thus

$$1/\tau_c = \sigma\bar{v}\rho_{Kr} = k_{Kr}\rho_{Kr}, \tag{4.5.5}$$

where k_{Kr} is the rate constant for dimer breakup, σ is the effective collisional cross-section, and $\bar{v} = (8kT/\pi\mu)^{1/2}$ is the average relative speed of the collision complex having reduced mass μ. The collisional cross-section can be approximated as the geometric cross-section $\sigma_{geom} = 2\pi R_e^2$, where R_e= 4.008 Å is the krypton-krypton equilibrium internuclear separation in a van der Waals dimer [44]. At 1 amagat, the correlation time is expected to be $\tau_c = 1.1\times10^{-10}$ s, and at field strength of 9.4 T, $\omega_0^2\tau_c^2 = 3\times10^{-6} << 1$.

Thus, relaxation due to Kr_2 dimers is expected to be density independent even at the high magnetic field strength of 9.4 T for all gas densities used in this work. In gas mixtures, van der Waals dimers can also be broken apart by collisions with the buffer gas, and for a two-component gas mixture

$$1/\tau_c = k_{Kr}\rho_{Kr} + k_{bg}\rho_{bg} = \left(k_{Kr} + r_{bg}k_{bg}\right)\rho_{Kr}, \tag{4.5.6}$$

where k_{bg} is the rate constant for ^{83}Kr-Kr dimer break

up due to collisions with the buffer gas. Because $\omega_0^2\tau_c^2 << 1$, the longitudinal relaxation rate due to the formation of van der Waals molecules becomes

$$\frac{1}{T_{1vdw}} = \frac{3(2I+3)}{80I^2(2I-1)}\left(\frac{eQq}{\hbar}\right)^2 \frac{K}{\left(k_{Kr} + r_{bg}k_{bg}\right)}. \tag{4.5.7}$$

The functional form of Eq. 4.5.7 predicts decreasing values of $1/T_{1vdW}$, and thus $1/T_{1i}$, with increasing r_{bg}, which is in agreement with the behavior observed in this work.

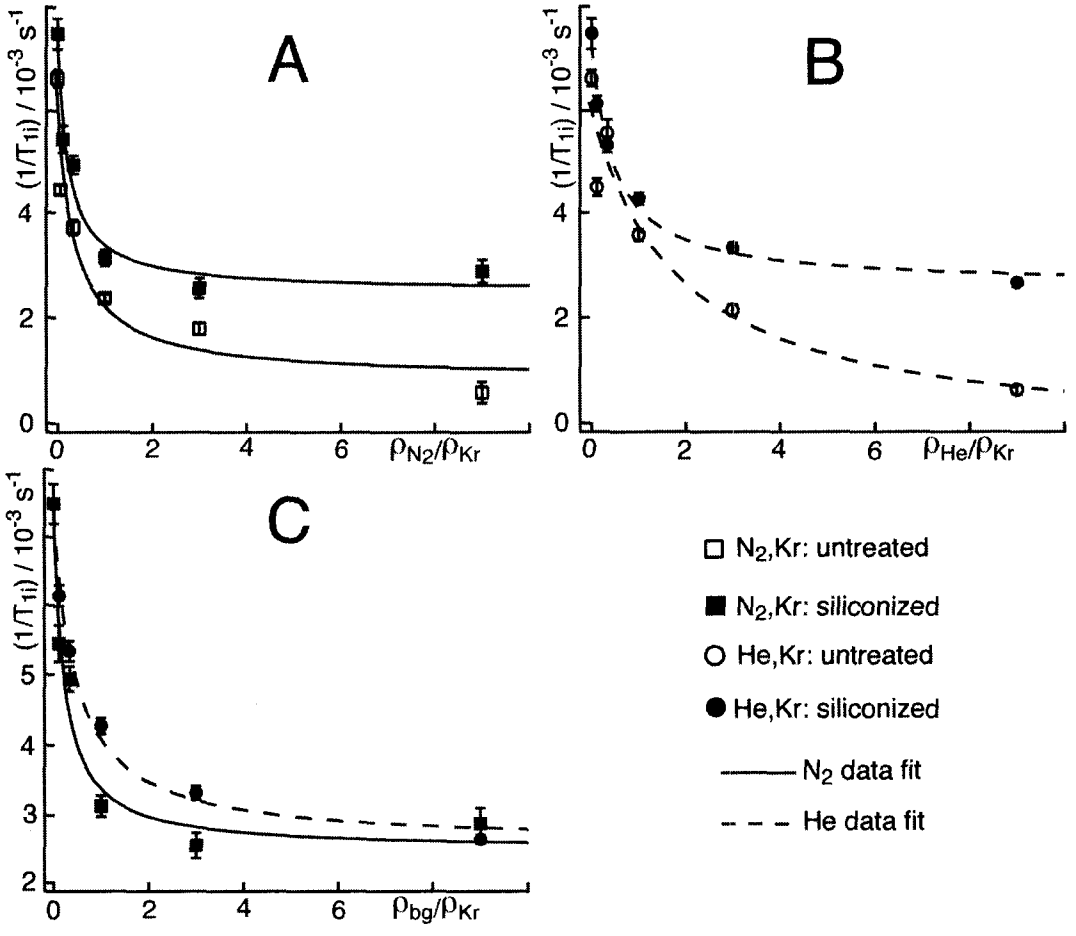

Figure 4.6: Density independent longitudinal relaxation. The data are plotted as a function of the ratio of buffer gas to krypton density, $r_{bg} \equiv \rho_{bg} / \rho_{Kr}$. The nature of the buffer gas and detection cell surface chemistry are indicated in the legend. The cures are fits of the data to Eq. 4.6.2. The error bars are statistical errors resulting from fitting density dependent relaxation rate data to Eq. 4.3.13. **(A)** Nitrogen containing mixtures in contact with both surface chemistries. **(B)** Helium containing mixtures in contact with both surface chemistries. **(C)** Nitrogen and helium containing mixtures in contact with the siliconized surface only.

To our knowledge, the value of the quadrupole coupling constant, eQq/h, for a ^{83}Kr-Kr dimer has never been reported. However, the quadrupole coupling constant can be determined from the rotational spectra of van der Waals molecules that posses a permanent dipole moments. The quadrupole coupling for ^{83}Kr in numerous krypton van der Waals dimers has been studied by microwave spectroscopy[45-47]. The eQq/h values for ^{83}Kr and ^{131}Xe (spin I = 3/2) bound to various partners that lack a permanent dipole moment are presented in Table 4.2. Together, these data strongly suggest that $|eQq/h|$ for ^{83}Kr in a Kr_2 dimer is on the order of a MHz.

Table 4.2: Quadrupole coupling constants in noble gas dimers

Isotope	Dimer	eQq/h MHz [a]	Ref.
^{83}Kr	^{20}Ne-^{83}Kr	-0.5205(23)	47
	^{40}Ar-^{83}Kr	-0.8529(14)	47
	$^{15}N_2$-^{83}Kr	0.5 [b]	46
^{131}Xe	^{20}Ne-^{131}Xe	0.3878(9)	45
	^{40}Ar-^{131}Xe	0.7228(36)	45
	^{84}Kr-^{131}Xe	0.7079(86)	45

[a] Parenthesis indicated the reported experimental error.
[b] The sign was not determined in the original work.

To estimate $1/T_{1vdW}$, the chemical equilibrium constant for Kr_2 formation must also be known. From the theory due to Bernardes and Primakoff[48], K can be expressed as

$$K \approx s^3 \frac{\left(2\pi^3 k_B T/\varepsilon\right)^{1/2}}{6\xi} \frac{(\xi\varepsilon/k_B T)^2}{1+(\xi\varepsilon/k_B T)^2} e^{\xi\varepsilon/k_B T}, \tag{4.5.8}$$

where ε is the well depth of the interaction potential, s is the range of the interatomic force, and

$$\xi = 1 - \frac{3}{2^{1/6}}\left(\frac{\hbar^2}{2\mu\varepsilon s^2}\right)^{1/2}. \tag{4.5.9}$$

Taking s to be equilibrium internuclear separation R_e= 4.008 Å [44], the equilibrium constant at 300 K becomes K = 60 Å^{-3}. For pure krypton at a density of 1 amagat, this corresponds to ~0.3% of krypton atoms residing in van der Waals dimers. Using Eq. 4.5.6 and assuming $|eQq/h|$ = 1 MHz, K= 60 Å^{-3}, and the collisional cross-section to be σ_{geom}, the ^{83}Kr relaxation rate due to Kr_2 van der Waals dimers is calculated to be $1/T_{1vdW}$~ 5×10^{-4} s^{-1}. As can be seen in Figure 4.7, the above discussion underestimates of $1/T_{1vdW}$. However, the large uncertainties in the quadrupole coupling constant, which is squared in Eq. 4.5.4, the collisional cross-section, and the equilibrium constant, $1/T_{1vdW}$ likely contributed to the lack of agreement.

4.6 Total Density Independent Relaxation in Krypton-83

Assuming that relaxation mechanisms other than quadrupolar interactions are negligible, the total pressure independent relaxation rate for ^{83}Kr is expected to be

$$\frac{1}{T_{1i}} = \frac{A}{V}\frac{\tau_a}{T_{1a}}\frac{\nu}{4} + \frac{3(2I+3)}{80I^2(2I-1)}\left(\frac{eQq}{\hbar}\right)^2 \frac{K}{\left(k_{Kr} + r_{bg}k_{bg}\right)}. \tag{4.6.1}$$

Additionally, as was done in work with ^{129}Xe-Xe van der Waals molecules [15, 27], the possible contribution from bound ^{83}Kr-buffer gas dimers has been neglected. If these dimers form, they would also contribute to $1/T_{1i}$. Unfortunately, Eq. 4.6.1 contains too many parameters to adequately fit the data in Figure 4.6, so the expression

$$1/T_{1i} = 1/T_{1s} + \Gamma/(1 + r_{bg}\kappa), \tag{4.6.2}$$

with fitting parameters $\Gamma = M^q \mathrm{K}/k_{Kr}$, $\kappa = k_{bg}/k_{Kr}$, and $1/T_{1i}$ was used allowing qualitative conclusions to be drawn. Fig. 4.6C displays $1/T_{1i}$ data from both helium and N_2 containing mixtures in the siliconized detection cell. At a given krypton density, the N_2 containing mixtures display lower $1/T_{1i}$ values than do the helium containing mixtures suggesting that N_2 is more efficient at breaking up Kr_2 than is helium (i.e. $k_{N2} > k_{He}$). This trend was also seen in the untreated detection cell and is consistent with results for Xe_2 dimers, where k_{N2} was about four times larger than k_{He} [27].

In previous work with ^{129}Xe [15, 27], the van der Waals contribution to the relaxation was isolated by preparing detection cells that produced extremely slow surface relaxation. The analogous approach is not possible for ^{83}Kr, because is it unlikely that surface induced quadrupolar relaxation can be suppressed. However, the functional form of Eq. 4.6.1 suggests a method by which surface and van der Waals relaxation can be disentangled. Increasing r_{bg} will reduce $1/T_{1vdW}$, and $1/T_{1i}$ should therefore asymptotically approach $1/T_{1s}$ at high values of r_{bg}. By obtaining these asymptotic values in a series of detection cells with varying A/V it should be possible to obtain τ_a/T_{1a} and thus calculate $1/T_{1s}$. This approach will require detection cells with well-defined surface-to-volume ratios and uniform surface chemistries. Also, it may be necessary to use more dilute krypton mixtures to completely suppress $1/T_{1vdW}$. Very dilute mixtures may be problematic because of the currently limited hp ^{83}Kr polarization. However, signal intensity improvements of an order of magnitude or more are expected through a isotopic enrichment and improved SEOP [49, 50] allowing experiments at low ρ_{Kr}.

4.7 Conclusions

This work demonstrates that the longitudinal relaxation of ^{83}Kr, unlike that of ^{129}Xe, is a linear function of density even at low noble gas densities. By studying the relaxation in a single sample cell with two different surface treatments, the density dependent relaxation was shown to be independent of surface contributions. The previous study of gas-phase ^{83}Kr relaxation published in 1980 [9] may have overestimated the density dependence of the longitudinal relaxation by ignoring these density independent contributions. Additionally, the first investigation of ^{83}Kr relaxation in the presence of buffer gases has been reported in this work. The density dependent relaxation of ^{83}Kr represents a novel and possibly unique probe of noble gas-molecular interactions. The technique promises to be quite robust and should allow studies with a multitude of different buffer gases. With relatively minor modifications, the experimental procedure used in this work should be suitable for obtaining temperature dependent relaxation data. This temperature dependent data, coupled with the definition of collision efficiency discussed in this work will be useful in evaluating intermolecular potentials from the perspective for the noble gas atom, and provide complementary data to that obtained from the gas-phase longitudinal relaxation in molecules.

Additionally the relaxation rate displays a pronounced density independent component. Varying the surface chemistry of the detection cell demonstrated that part of this relaxation originated from surface interactions. By varying the gas composition it was shown that $1/T_{1i}$ was reduced in dilute krypton mixtures. This compositional dependence cannot be attributed to surface interactions but is consistent with relaxation caused by the

formation of van der Waals dimers. Relaxation due to gas-phase van der Waals molecules was previously observed only in ^{129}Xe suggesting that dimer mediated longitudinal relaxation is a general feature of the heavy nobles gas isotopes. At the 9.4 T field strength used in this work, the relaxation of ^{129}Xe due to van der Waals dimer formation is expected to be density dependent. The density independence of van der Waals mediated relaxation observed in this work is due to the much lower gyromagnetic ratio, and thus resonance frequency, of ^{83}Kr.

For ^{83}Kr, the values of $1/T_{1s}$ and $1/T_{1vdW}$ are similar making them difficult to quantitatively separate. However, in future work, it should be possible to decouple the two contributions by varying the surface-to-volume ratio of the detection cell. Finally, the T_1 times observed in this work ranged tens to hundreds of seconds, which are substantially shorter than those of ^{129}Xe or ^{3}He. Thus ^{83}Kr may be a superior choice for studying fundamental longitudinal relaxation mechanisms than are the spin $I = 1/2$ noble gases, because large ^{83}Kr data sets can be collected in a comparatively short amounts of time. Lastly, the presented relaxation data will help to modify the SEOP conditions and may allow for improved ^{83}Kr hyperpolarization.

References:

1. Armstrong, R. L., Nuclear magnetic relaxation effects in polyatomic gases. *Magnetic Resonance Review* **1987,** 12, 91-135.

2. Jameson, C. J., Gas-Phase Nmr-Spectroscopy. *Chemical Reviews* **1991,** 91, (7), 1375-1395.

3. Gordon, R. G., Kinetic Theory of Nuclear Spin Relaxation in Gases. *Journal of Chemical Physics* **1966,** 44, (1), 228-234.

4. Gordon, R. G., Semiclassical Theory of Spectra and Relaxation in Molecular Gases. *Journal of Chemical Physics* **1966,** 45, (5), 1649-1655.

5. Newbury, N. R.; Barton, A. S.; Cates, G. D.; Happer, W.; Middleton, H., Gaseous He-3 He-3 Magnetic Dipolar Spin Relaxation. *Physical Review A* **1993,** 48, (6), 4411-4420.

6. Hunt, E. R.; Carr, H. Y., Nuclear Magnetic Resonance of Xe129 in Natural Xenon. *Physical Review* **1963,** 130, (6), 2302-2305.

7. Moudrakovski, I. L.; Breeze, S. R.; Simard, B.; Ratcliffe, C. I.; Ripmeester, J. A.; Seideman, T.; Tse, J. S.; Santyr, G., Gas-phase nuclear magnetic relaxation in Xe-129 revisited. *Journal of Chemical Physics* **2001,** 114, (5), 2173-2181.

8. Brinkmann, D.; Brun, E.; Staub, H. H., Kernresonanz Im Gasformigen Xenon. *Helvetica Physica Acta* **1962,** 35, (6), 431-436.

9. Brinkmann, D.; Kuhn, D., Nuclear Magnetic-Relaxation of Kr-83 in Krypton Gas. *Physical Review A* **1980,** 21, (1), 163-167.

10. Jameson, C. J.; Jameson, A. K.; Hwang, J. K., *JCP* **1988,** 89, 4074-4081.

11. Karra, J. S.; Kemmerer, G. E., Density-Dependence of Diffusion Constant and Nuclear Spin Lattice Relaxation Rate of He-3 Gas. *Physics Letters A* **1970,** A 33, (2), 105-106.

12. Saam, B.; Happer, W.; Middleton, H., Nuclear-Relaxation of He-3 in the Presence of O-2. *Physical Review A* **1995,** 52, (1), 862-865.

13. Archibald, G.; Brief, E.; Lei, C.; Pausak, T.; Hayden, M. E., Nuclear relaxation of He-3 in the presence of NO. *Physical Review A* **2006,** 73, (2), 022721.

14. Walker, T. G.; Happer, W., Spin-exchange optical pumping of noble-gas nuclei. *Review of Modern Physics* **1997,** 69, (2), 629-642.

15. Berry-Pusey, B. N.; Anger, B. C.; Laicher, G.; Saam, B., Nuclear spin relaxation of Xe-129 due to persistent xenon dimers. *Physical Review A* **2006,** 74, (6), 063408.

16. Babcock, E.; Chann, B.; Walker, T. G.; Chen, W. C.; Gentile, T. R., Limits to the polarization for spin-exchange optical pumping of He-3. *Physical Review Letters* **2006,** 96, (8), 083003.

17. Schaefer, S. R.; Cates, G. D.; Happer, W., Determination of Spin-Exchange Parameters between Optically Pumped Rubidium and Kr-83. *Physical Review A* **1990,** 41, (11), 6063-6070.

18. Butscher, R.; Wäckerle, G.; Mehring, M., Nuclear quadrupole surface interaction of gas phase 83Kr: comparison with 131 Xe. *Chemical Physics Letters* **1996,** 249, 444-450.

19. Cleveland, Z. I.; Pavlovskaya, G. E.; Stupic, K. F.; LeNoir, C. F.; Meersmann, T., Exploring hyperpolarized 83Kr by remotely detected NMR relaxometry. *Journal of Chemical Physics* **2006,** 124, 044312.

20. Cleveland, Z. I.; Stupic, K. F.; Pavlovskaya, G. E.; Repine, J. E.; Wooten, J. B.; Meersmann, T., Hyperpolarized ^{83}Kr and ^{129}Xe NMR Relaxation Measurements of Hydrated Surfaces: Implications for Materials Science and Pulmonary Diagnostics. *Journal of the American Chemical Society* **2007,** 129, (6), 1784-1792.

21. Stupic, K. F.; Cleveland, Z. I.; Pavlovskaya, G. E.; Meersmann, T., Quadrupolar Relaxation of Hyperpolarized Krypton-83 as a Probe for Surfaces. *Solid State Nuclear Magnetic Resonance* **2006,** 29, 79-84.

22. Pavlovskaya, G. E.; Cleveland, Z. I.; Stupic, K. F.; Meersmann, T., Hyperpolarized Krypton-83 as a New Contrast Agent for Magnetic Resonance Imaging. *Proceedings of the National Academy of Sciences of the United States of America* **2005,** 102, 18275-18279.

23. Cleveland, Z. I.; Pavlovskaya, G. E.; Stupic, K. F.; Wooten, J. B.; Repine, J. E.; Meersmann, T., Detection of Tobacco Smoke Deposition by Hyperpolarized Krypton-83 MRI. *Magnetic Resonance Imaging* **2008,** 26, (270-278).

24. Torrey, H. C., Chemical Shift and Relaxation of Xe129 in Xenon Gas. *Physical Review* **1963,** 130, (6), 2306-2312.

25. Adrian, F. J., Quadrupolar Relaxation of Xe131 in Xenon Gas. *Physical Review* **1965,** 138, (2A), A403-409.

26. Faust, W. L.; Chiu, L. Y. C., Hyperfine Structure of Metastable (4P)5(5S) 3P2 State of 36Kr83. *Physical Review* **1963,** 1, (3), 1214-1220.

27. Chann, B.; Nelson, I. A.; Anderson, L. W.; Driehuys, B.; Walker, T. G., Xe-129-Xe molecular spin relaxation. *Physical Review Letters* **2002,** 88, (11), 113201.

28. Abragam, A., *The Principles of Nuclear Magnetism.* Oxford University Press: Oxford, UK, 1961.

29. Driehuys, B.; Cates, G. D.; Happer, W., Surface Relaxation Mechanisms of Laser-Polarized Xe-129. *Physical Review Letters* **1995,** 74, (24), 4943-4946.

30. Maitland, G. C.; Rigby, M.; Smith, E. B.; Wakeham, W. A., *Intermolecular Forces, Their Origin and Determination.* Oxford Univeristy Press: Oxford, UK, 1981.

31. Mortuza, M. G.; Anala, S.; Pavlovskaya, G. E.; Dieken, T. J.; Meersmann, T., Spin-exchange optical pumping of high-density xenon-129. *Journal of Chemical Physics* **2003,** 118, (4), 1581-1584.

32. Breeze, S. R.; Lang, S.; Moudrakovski, I.; Ratcliffe, C. I.; Ripmeester, J. A.; Santyr, G.; Simard, B.; Zuger, I., Coatings for optical pumping cells and short-term storage of hyperpolarized xenon. *Journal of Applied Physics* **2000,** 87, (11), 8013-8017.

33. Jacob, R. E.; Driehuys, B.; Saam, B., Fundamental mechanisms of He-3 relaxation on glass. *Chemical Physics Letters* **2003,** 370, (1-2), 261-267.

34. Schmiedeskamp, J.; Heil, W.; Otten, E. W.; Kremer, R. K.; Simon, A.; Zimmer, J., Paramagnetic relaxation of spin polarized He-3 at bare glass surfaces Part I. *European Physical Journal D* **2006,** 38, (3), 427-438.

35. Deninger, A.; Heil, W.; Otten, E. W.; Wolf, M.; Kremer, R. K.; Simon, A., Paramagnetic relaxation of spin polarized He-3 at coated glass walls Part II. *European Physical Journal D* **2006,** 38, (3), 439-443.

36. Schmiedeskamp, J.; Elmers, H. J.; Heil, W.; Otten, E. W.; Sobolev, Y.; Kilian, W.; Rinneberg, H.; Sander-Thommes, T.; Seifert, F.; Zimmer, J., Relaxation of spin polarized

He-3 by magnetized ferromagnetic contaminants Part III. *European Physical Journal D* **2006,** 38, (3), 445-454.

37. Cohen, M. H.; Mendelson, K. S., Nuclear Magnetic-Relaxation and the Internal Geometry of Sedimentary-Rocks. *Journal of Applied Physics* **1982,** 53, (2), 1127-1135.

38. Wilkinson, D. J.; Johnson, D. L.; Schwartz, L. M., Nuclear Magnetic-Relaxation in Porous-Media - the Role of the Mean Lifetime Tau(Rho,D). *Physical Review B* **1991,** 44, (10), 4960-4971.

39. Jaccard, G.; Wimperis, S.; Bodenhausen, G., multiple quantum NMR spectroscopy of S=3/2 spins in isotropic phase: A new probe for multiexponential relaxation. *Journal of Chemical Physics* **1986,** 85, (11), 6282-6293.

40. Meersmann, T.; Smith, S. A.; Bodenhausen, G., Multiple-quantum filtered xenon-131 NMR as a surface probe. *Physical Review Letters* **1998,** 80, (7), 1398-1401.

41. Fitzsimmons, W. A.; Tankersley, L. L.; Walters, G. K., Nature of Surface-Induced Nuclear-Spin Relaxation of Gaseous He3. *Physical Review* **1969,** 179, (1), 156-165.

42. Jaroniec, M.; Madey, R., *Physical Adsorption on Heterogeneous Solids.* Elsevier Science Publishing Company Inc.: Amsterdam, The Netherlands, 1988; Vol. 59.

43. Horton-Garcia, C. F.; Pavlovskaya, G. E.; Meersmann, T., Introducing krypton NMR spectroscopy as a probe of void space in solids. *Journal of the American Chemical Society* **2005,** 127, (6), 1958-1962.

44. Aziz, R. A.; Slaman, M. J., The Argon and Krypton Interatomic Potentials Revisited. *Molecular Physics* **1986,** 58, (4), 679-697.

45. Jager, W.; Xu, Y. J.; Gerry, M. C. L., Pure Rotational Spectra of the Mixed Rare-Gas Van-Der-Waals Complexes Ne-Xe, Ar-Xe, and Kr-Xe. *Journal of Chemical Physics* **1993,** 99, (2), 919-927.

46. Jager, W.; Xu, Y. J.; Heineking, N.; Gerry, M. C. L., The Microwave Rotational Spectrum of the Van-Der-Waals Complex Kr-N2. *Journal of Chemical Physics* **1993,** 99, (10), 7510-7520.

47. Xu, Y. J.; Jager, W.; Djauhari, J.; Gerry, M. C. L., Rotational Spectra of the Mixed Rare-Gas Dimers Ne-Kr and Ar-Kr. *Journal of Chemical Physics* **1995,** 103, (8), 2827-2833.

48. Bernardes, N.; Primakoff, H., Molecule Formation in the Inert Gases. *Journal of Chemical Physics* **1959,** 30, (3), 691-694.

49. Knagge, K.; Prange, J.; Raftery, D., A continuously recirculating optical pumping apparatus for high xenon polarization and surface NMR studies. *Chemical Physics Letters* **2004,** 397, (1-3), 11-16.

50. Ruset, I. C.; Ketel, S.; Hersman, F. W., Optical pumping system design for large production of hyperpolarized Xe-129. *Physical Review Letters* **2006,** 96, (5), 053002.

CHAPTER 5

LONGITUDINAL RELAXATION OF HYPERPOLARIZED KRYPTON-83 AS A PROBE FOR HYDRATED SURFACES

The results presented in this dissertation chapter appear in the journal article: Zackary I. Cleveland, Karl F. Stupic, Galina E. Pavlovskaya, John E. Repine, Jan B. Wooten, and Thomas Meersmann, "Hyperpolarized ^{83}Kr and ^{129}Xe NMR Relaxation Measurements of Hydrated Surfaces: Implications for Materials Science and Pulmonary Diagnostics", *Journal of the American Chemical Society.* **2007,** 129 (6): 1784-1792.

Zackary I. Cleveland and Thomas Meersmann wrote the paper mentioned above. Karl F. Stupic performed some of the ^{129}Xe relaxation measurements. John E. Repine and Jan B. Wooten edited the manuscripts and provided expertise concerning the aspects of the work that were of potential biomedical interest. John E. Repine also provided the lung surfactant extract used in this work. Zackary I. Cleveland produced the hp ^{83}Kr, participated in the design of the experiments, built the experimental apparatus, and prepared the studied samples. Galina E. Pavlovskaya built the ^{129}Xe and ^{83}Kr NMR probes.

5.1 Introduction

In situ and *in vivo* measurements of surface properties under ambient conditions impose serious experimental challenges, particularly when porous materials and surfaces within opaque media are of interest. Nuclear magnetic resonance (NMR) spectroscopy and magnetic resonance imaging (MRI) require transparence only within the radio frequency regime and can therefore probe surfaces that are obstructed from direct optical or other types of examination. This chapter describes the use of hyperpolarized (hp) ^{83}Kr and hp ^{129}Xe longitudinal relaxation time (T_1) measurements to probe hydrated surfaces under near atmospheric conditions.

In the past, several NMR studies of thermally polarized krypton in materials have made use of the high nuclear spin (I = 9/2) and the nuclear quadrupole moment (See Table 1.1.) of the ^{83}Kr isotope. The ^{83}Kr NMR spectrum shows distinct splitting in liquid crystalline phase caused by anisotropy in the environment of the dissolved krypton atoms [1, 2]. The NMR line shape of ^{83}Kr obtained in zeolites is sensitive to pore dimensions, pore geometry, counter-cation charge, and, potentially, to long range disorder in the nanoporous materials [3]. The coherent evolution and relaxation behavior of ^{83}Kr (15.4 MHz resonance frequency at 9.4 T) in these materials are dominated by quadrupolar interactions and can therefore provide valuable information that is complementary to that obtained from the chemical shift observed in NMR spectroscopy with ^{129}Xe (110.6 MHz resonance frequency at 9.4 T and I = 1/2) [4-6].

The nuclear spin polarization of ^{129}Xe can be increased (i.e. hyperpolarized) through rubidium vapor spin exchange optical pumping (SEOP) [7] by many orders of magnitude over the Boltzmann equilibrium value of thermally polarized ^{129}Xe at ambient

temperature and high magnetic field strengths. Since its introduction [8], hp ^{129}Xe NMR has proved to be a powerful spectroscopic tool and is increasingly used to study porous materials, gas-surface interactions, surface chemistry, biomolecules, chemical reactors, and gas dynamics. Hp ^{129}Xe and hp ^{3}He have also led to exciting advances in the MR imaging of airways and materials (See [9-11] for reviews.).

The hyperpolarization of the ^{83}Kr nuclear spin is also possible through SEOP [12-14], but the separation of hp ^{83}Kr from paramagnetic and highly reactive rubidium vapor was not reported until the recent introduction of hp ^{83}Kr NMR spectroscopy and MRI, which was described in the earlier chapters. The T_1 time of hp ^{83}Kr is sensitive to the surfaces of materials in contact with the hp gas and yields information about the surface-to-volume ratio [15], chemical composition [15], and temperature [16] of the material-gas interface. The potential of hp ^{83}Kr to serve as a surface chemistry sensitive MRI contrast agent has also been demonstrated using siliconized (hydrophobic) and untreated (hydrophilic) glass surfaces [17].

This chapter demonstrates that water adsorption on surfaces dramatically alters ^{83}Kr relaxation times. This effect is reversible with water desorption and is observed even for hydrophobic surfaces suggesting that hp ^{83}Kr longitudinal relaxation is potentially a powerful probe of surface hydration over a wide range of surface chemistries. To test the feasibility of *in vivo* applications, the commercially available pulmonary surfactant extract Survanta was applied to some of the hydrated surfaces, and its influence on the ^{83}Kr T_1 time as investigated. Additionally, information about the presence of paramagnetic surface sites was obtained by comparing hp ^{83}Kr and hp ^{129}Xe NMR relaxation times.

5.2 Materials and Methods

5.2.1 NMR Measurements and Instrumentation

Experiments were performed on a Chemagnetics CMX II 400 MHz NMR spectrometer in a 9.4 T wide-bore (89 mm) superconducting magnet. All NMR data were obtained using custom-built, gas-flow probes tuned to the frequency of either ^{83}Kr (15.4 MHz) or ^{129}Xe (110.6 MHz). T_1 values from hp gases were calculated by nonlinear least squares fitting of the NMR signal as a function of time as described in Chapter 4. The 90° pulses for ^{83}Kr (63 μs) and ^{129}Xe (47 μs) were determined under continuous-flow optical pumping conditions similar to those used in earlier work [16, 18]. All T_1 values reported are the averages of four to eight replicate measurements and, unless otherwise indicated, are conducted at 85.0 ± 0.5 kPa (i.e. ambient pressure at the laboratory elevation of 1500 m). The errors reported are the standard deviations resulting from those replicate measurements. The stated signal enhancements reported for hp ^{83}Kr are relative to the thermal signal obtained from a sample containing 500 kPa natural abundance krypton and 100 kPa O_2.

5.2.2 Optical Pumping of ^{83}Kr and ^{129}Xe

All gas mixtures in this work were produced from research grade krypton (99.995%, natural abundance), xenon (99.995%, natural abundance), nitrogen (99.9997%), and helium (99.9999%) (Airgas, Radnor, PA). SEOP was performed in a cylindrical Pyrex cell (length = 125 mm, ID = 24 mm). The gas mixtures consisted of 95% Kr and 5% N_2 (mixture-I); 25% Kr, 5% N_2, and 70% He (mixture-II); or 20% Xe, 5% N_2,

and 75% He. N_2 was added to the mixtures for radiation quenching purposes [19]. The pump cell, containing approximately 1 g of rubidium (99.75%; Alfa Aesar, Ward Hill, MA), was housed in a quartz and aluminum oven to maintain even heating (438 ± 5 K for ^{83}Kr and 393 ± 5 K for ^{129}Xe). The pump cell was maintained above ambient pressure (150-200 kPa) to avoid pump cell contamination. Light (794.7 nm) from a 30 W Coherent FAP diode-array laser system (line width 2 nm) was directed via fiber optic coupling cables through a circular polarizer onto the pump cell. After the light passed through the fiber optics and the polarizer, the power was reduced to approximately 20 W. The magnetic field needed for SEOP was provided by the fringe field of the superconducting magnet (0.05 T). Rb vapor was separated from the hp gas mixtures by an air-cooled trap at the outlet to the pump cell and a glass wool filter placed directly before the sample region.

5.2.3 Delivery of Optically Pumped Gases

In the stopped-flow experiments used to measure T_1 values in the dehydrated samples, polarization was allowed to build several minutes in the pump cell while the detection cell (length = 50 mm, ID 12 = mm) was evacuated to a pressure of less than 0.1 kPa. Following SEOP, the hp gas was rapidly transferred from the pump cell to the detection cell by pressure equalization. In the injection delivery method (See Fig. 5.1.), polarization was also allowed to build for several minutes and then the hp gas mixture was transferred by pressure equalization into an evacuated Pyrex storage cell (length = 80mm, ID = 24 mm). From the storage cell, the hp gas mixture was transferred to a Pyrex injection cell (length = 150mm, ID = 24 mm) containing distilled water and a thermally

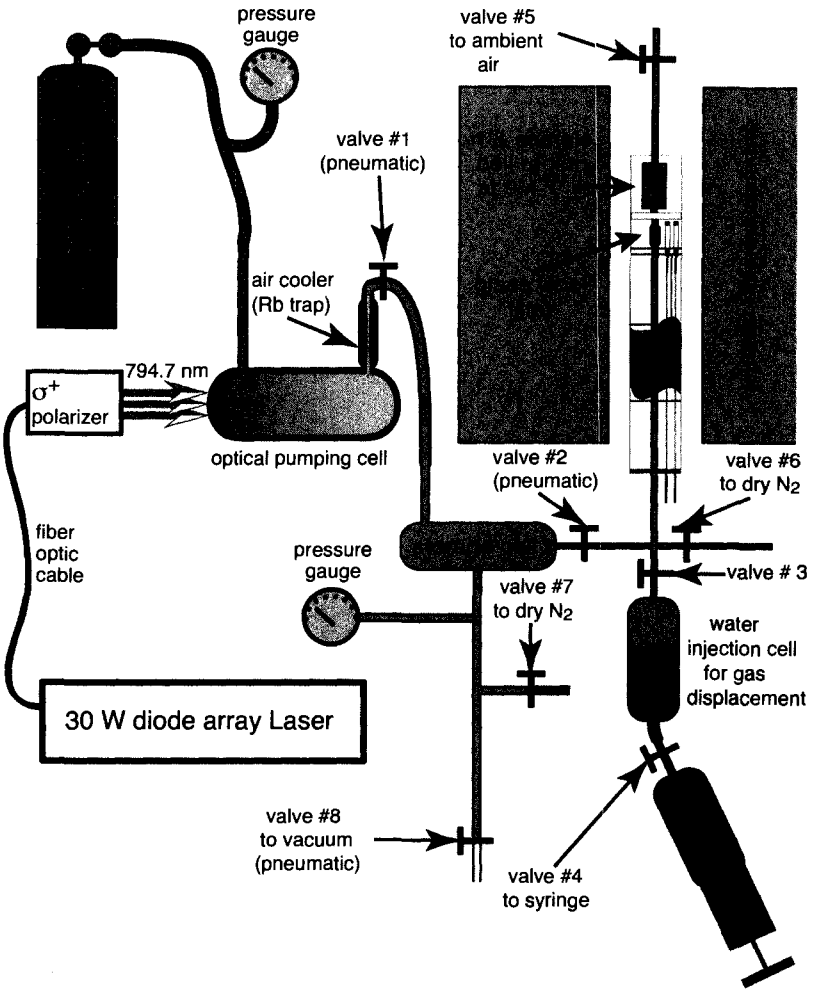

Figure 5.1: Apparatus for injection delivery of hp gases. Following SEOP, hp gas was transferred by pressure equalization to the storage cell (Valve 1 was open; valves 2, 7, and 8 were closed). Next, hp gas was transferred to the injection cell by displacing distilled water into the syringe (Valves 2, 3, and 4 were open; valves 1, 5, 6, 7, and 8 were closed.). Finally, the hp gas was injected into the detection region by forcing the distilled water into the injection cell (Valves 3, 4, and 5 were open; valves 2 and 6 were closed.). During signal acquisition, valves 2, 3, 5, and 6 were closed to ensure constant pressure in the detection region and prevent contamination by atmospheric oxygen.

polarized gas mixture having the same composition as the hp gas. During transfer from the storage cell, approximately 50 mL of distilled water was displaced into the attached syringe. The syringe then forced the distilled water back into the injection cell and, thus, the hp gas mixture into the sample region for detection.

To limit the exposure of hp gases to oxygen, helium was bubbled through the water in the injection cell for several minutes prior to conducting injection delivery experiments. The apparatus was then thoroughly flushed with nitrogen gas prior to filling the injection and detection cells with the thermally polarized noble gas mixture. Between experiments, the storage cell was repeatedly filled with dry nitrogen and evacuated to reduce pump cell contamination by water vapor.

5.2.4 Preparation of Borosilicate Glass Beads

Untreated, 1.0 mm diameter, borosilicate glass beads (Biospec Products, Inc., Bartlesville, OK) were degassed overnight at a temperature of 473 K and a pressure of below 0.1 Pa and then stored under dry nitrogen until use (for stopped-flow delivery) or stored overnight in a saturated water vapor (for injection delivery). Siliconized beads were prepared as described in Chapter 3. Following surface treatment, the siliconized beads were hydrated or dehydrated using the same procedure as was used for the untreated beads.

5.2.5 Storage and Application of Lung Surfactant

A 4 mL vial of Survanta (Ross Products Division, Abbott Laboratories, Columbus, OH), a suspension of bovine pulmonary surfactant extract, was stored under refrigerated

conditions in accordance with the manufactures instructions prior to use. The chemical composition of Survanta (as stated by the manufacturer) was primarily that of natural bovine lung extract and comprised phospholipids (25 mg/mL), triglycerides (0.5-1.75 mg/mL), free fatty acids (1.4-3.5mg/mL), and surfactant associated proteins (> 1 mg/mL) suspended in a 0.9% aqueous NaCl solution. Before applying the suspension to the various bead samples, Survanta was removed from refrigeration and warmed to room temperature. A sterile syringe was then used to remove a portion of the suspension through a rubber septum. The beads were coated with approximately 0.3 mL Survanta by gently rolling the beads in a few droplets of surfactant mixture until the glass surface was visibly covered. For one sample, the surfactant extract was diluted 1:2 with distilled water but, otherwise, treated identically. For the dehydrated lung surfactant sample, untreated beads were coated as described above, transferred to the detection cell, and dried overnight at room temperature under a 0.1 Pa vacuum.

5.3 Results

5.3.1 Probing Surfaces under Near Atmospheric Conditions

As described previously, the ^{83}Kr signal can be enhanced by more than three orders of magnitude at 9.4 T field strength using SEOP. To obtain this level of enhancement, vacuum shuttling rather than the relatively slow flow often used to deliver hp ^{129}Xe is necessary due to fast quadrupolar relaxation during gas transfer [16]. However, an evacuation of the sample region may alter surface hydration and is ill suited for *in situ* or *in vivo* biomedical applications. Additionally, surface hydration changes may be

introduced by the hp noble gas mixtures themselves, which are devoid of water vapor due to reaction with rubidium during the optical pumping process.

Fig. 5.1 shows the experimental apparatus used to simultaneously solve both of these problems. The hp gas was vacuum shuttled through pneumatic valves from the pump cell to a storage cell. Subsequently, the gas at 150-200 kPa was released into a water-filled glass container where it displaced water into an attached syringe. The gas, which became least partially saturated with water vapor, lost trace amounts of rubidium vapor carried over from SEOP. Finally, the hp gas was injected into the sample cell through operation of the syringe (See Section 5.2.3.). Using this procedure, the sample region was only gently ventilated by the gas flow with minimal influence on surface hydration. Further, this procedure produced an acceptable hp ^{83}Kr polarization loss of at most 50% compared to one-step vacuum shuttling.

Of great importance for practical MR studies using hp ^{83}Kr is the magnitude of the signal intensity resulting from SEOP. For gas mixture-I (95% Kr and 5% N_2), the ^{83}Kr polarization was typically enhanced by a factor of ~1000 times that of thermal equilibrium at 9.4 T field strength, a value consistent with prior work using this gas composition [16, 17]. Optical pumping of mixture-II (25% Kr, 70% He, and 5% N_2) produced polarization enhancements up to 4500 times that of thermal equilibrium, which is the highest ^{83}Kr polarization enhancement reported. The higher polarization achieved using mixture-II was probably due to reduced rubidium electron spin relaxation and slower ^{83}Kr self-relaxation during the SEOP process. This is demonstrated in Fig. 5.2 where the hp ^{83}Kr NMR spectra obtained from gas mixture-I and II at constant overall gas pressure yielded similar integrated signal intensities.

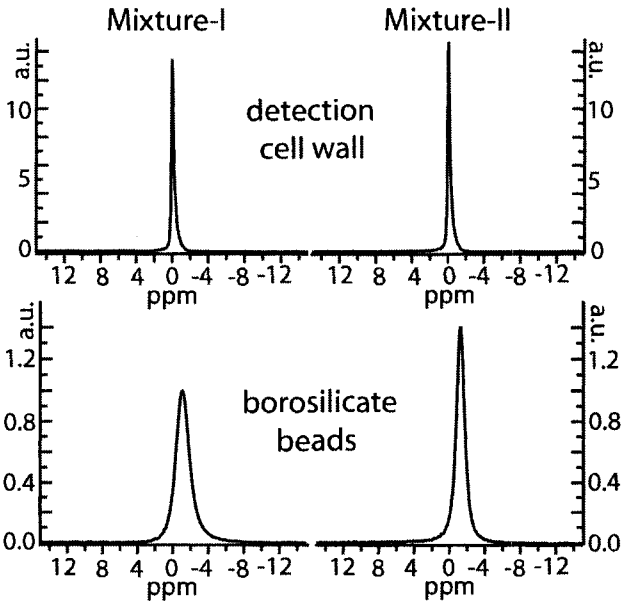

Figure 5.2: Hp ^{83}Kr spectra at ambient pressure. The upper two spectra were obtained from hp ^{83}Kr in contact with the detection cell wall only (without beads), and the lower spectra were obtained from hp ^{83}Kr in the cell filled with 1 mm diameter, dehydrated borosilicate glass beads. The two spectra on the left hand side of the figure are of hp ^{83}Kr from gas mixture-I (95% Kr), and the two on the right are from gas mixture-II (25% Kr). All four spectra are plotted on the same arbitrary scale (a.u.) of peak height. The peak position of mixture-I in the absence of borosilicate beads was used as the zero ppm reference.

The integrated signal intensity changed with the sample porosity and was reduced in a glass bead sample by approximately 70% compared to the detection cell without glass beads. This value corresponds well to the 74% filling factor expected for closest packed solid spheres. Bulk magnetic susceptibility of the material was responsible for the -1.1 ppm peak shift observed for the materials-phase (borosilicate beads) peaks compared to the peaks observed from hp ^{83}Kr in contact with the detection cell walls only. The line width was broadened from 4.5 Hz for the bulk gas-phase in the cell lacking any bead sample to 24 Hz (gas mixture-I) or 16 Hz (gas mixture-II) in the void spaces of the glass bead sample. The mixture dependent line width can be caused by transverse relaxational processes or coherent quadrupolar interactions on the surface [12, 14, 20-26], and the magnetic susceptibility of the material may lead to additional line broadening.

5.3.2 Studies of Hydrated and Dehydrated Surfaces

In hp ^{83}Kr magnetic resonance, the detected signal originates from gas-phase krypton but not from the adsorbed phase. However, a significant and often dominating contribution to the longitudinal relaxation of ^{83}Kr is caused by quadrupolar interactions during brief periods of surface adsorption. The more negative the krypton surface adsorption enthalpy, the more rapid will be the resulting surface induced relaxation. As a test system where gas-phase relaxation due to binary collisions plays an insignificant role due to high surface-to-volume ratio, sample tubes were filled with 1 mm diameter borosilicate glass beads that allowed for the study of both surface treatment and hydration levels.

The data shown in Table 5.1 show how strongly the water adsorption on glass surfaces influenced krypton relaxation times. At ambient pressure (85.0 kPa) and 289 K, the ^{83}Kr relaxation from gas mixture-I in untreated borosilicate glass beads was prolonged by 184% from T_1 = 22.1 s for the dehydrated surface to T_1 = 62.8 s when the glass was hydrated by overnight exposure to a saturated water vapor. Similarly, a T_1 increase of 173% was observed upon hydration is with mixture-II. An increase in the longitudinal relaxation time also occurred upon hydration of a highly hydrophobic siliconized glass surface. After overnight hydration of the siliconized beads, the krypton longitudinal relaxation times experienced 102% or 114% increases for mixture-I and II respectively.

Table 5.1: T_1 values for hp ^{83}Kr in contact with hydrated and dehydrated surfaces.

Gas Mixture	Dehydrated Detection Cell [a,b]	Hydrated Detection Cell [a,c]	Dehydrated Untreated Beads [b]	Hydrated Untreated Beads [c]	Dehydrated Siliconized Beads [b]	Hydrated Siliconized Beads [c]
I 95% Kr	104.3 ± 3.3 s	129.3 ± 2.8 s	22.1 ± 1.3 s	62.8 ± 3.3 s	6.1 ± 0.4 s	12.3 ± 0.5 s
I 95% Kr (P = 0) [d]	124.0 ± 3.6 s	161.1 ± 3.2 s	22.9 ± 1.3 s	69.5 ± 3.4 s	6.2 ± 0.4 s	12.5 ± 0.5 s
II 25% Kr	165.5 ± 3.7 s	202.3 ± 9.0 s	36.0 ± 5.5 s	98.4 ± 9.3 s	8.3 ± 0.8 s	17.8 ± 0.3 s
II 25% Kr (P = 0) [d]	223.4 ± 5.0 s	296.1 ± 13.5 s	38.2 ± 5.8 s	116.3 ± 10.1 s	8.4 ± 0.8 s	18.3 ± 0.3 s

a) No bead sample present.
b) Stopped-flow delivery.
c) Injection delivery.
d) T_1 extrapolated to zero pressure.

The hp ^{83}Kr relaxation times in both the untreated and siliconized beads showed little variation between identically treated replicate samples. In fact, bead samples (both untreated and siliconized) could be thoroughly dehydrated (See Section 5.2.3.), subsequently placed overnight in a saturated water vapor, and then dehydrated a second time. At each stage, the resulting T_1 values were identical within experimental error to those reported Table 5.1.

However, the data shown in Table 5.1 display only qualitative agreement with earlier work involving similarly treated dehydrated samples [15], and the values reported in this chapter are systematically lower by about 30%. The source of this variation was not investigated, but a probable explanation is differences in average bead surface areas in the two studies. The glass beads used in both studied were selected for their ability to undergo various surface modifying reactions not bead-to-bead uniformity in size and shape. Although the beads are described as 1 mm diameter spheres, a distribution in the size, shape, and in surface features such as corrugation and cracks were observed.

Table 5.2: T_1 values for hp ^{83}Kr in contact with bovine lung surfactant.

Gas Mixture	Hydrated (Trial 1) [a]	Hydrated (Trail 2) [a]	1:2 Dilution (Surfactant: Water) [a]	Dehydrated [b]	Hydrated (Siliconized Support) [a]
I 95% Kr	15.7 ± 0.5 s	16.2 ± 1.1 s	20.8 ± 2.1 s	19.3 ± 0.2 s	12.9 ± 0.9 s
I 95% Kr (P = 0) [c]	16.1 ± 0.5 s	16.4 ± 1.1 s	21.7 ± 2.1 s	19.9 ± 0.3 s	13.2 ± 0.9 s

a) Injection delivery.
b) Stopped-flow delivery.
c) T_1 extrapolated to zero pressure.

5.3.3 Bovine Lung Surfactant Experiments

The ^{83}Kr longitudinal relaxation times shown in Table 5.2 range between approximately $T_1 = 13$ s and $T_1 = 22$ s depending on two parameters: the type of support surface used for the Survanta and the amount of water present. The label 'hydrated surfactant' describes glass beads coated that were with undiluted Survanta without subsequent dehydration. To examine the reproducibility of the data, two trials comprising four replicate T_1 measurements were performed and yield essentially identical results of $T_1 \approx 16$ s. Diluting the Survanta 1:2 with distilled water prolonged the T_1 to 21 s. Dehydration of the Survanta coated beads under vacuum conditions also prolonged the T_1 to 19 s compared to the hydrated surfactant. Accelerated relaxation times, insignificantly different from hp ^{83}Kr in contact with the siliconized support surface without surfactant, occurred when using a siliconized support surface.

5.3.4 Hyperpolarized ^{129}Xe Relaxation Measurements

When xenon was exposed to a glass surface, the ^{129}Xe longitudinal relaxation rate can be accelerated due to the presence of paramagnetic surface impurities. This is seen in Table 5.3 for dehydrated glass beads with $T_1 = 43$ s, a relaxation time that is quite short for gas-phase ^{129}Xe, which in macroscopic glass containers, at near ambient pressures, and 1.5 T can be as long as 13,200 s in pure xenon [27]. Hydrating the beads either obstructed xenon contact with paramagnetic sites or reduced the xenon surface coverage, prolonging the relaxation time to $T_1 = 103$ s. Siliconizing the surface [28-30] dramatically increased the ^{129}Xe T_1 in sharp contrast to the effect seen with ^{83}Kr [17]. A similar effect was seen with

lung surfactant coated beads, indicating that this treatment too obstructed a contact with paramagnetic surface sites.

Table 5.3: Hp ^{129}Xe [a] T_1 in contact with borosilicate glass beads.

Dehydrated Untreated Beads [b]	Hydrated Untreated Beads [c]	Surfactant Coated Beads [c]	Dehydrated Siliconized Beads [b]
43 ± 3 s	103 ± 8 s	420 ± 27 s	773 ± 9 s

a) 20% xenon, 5% N_2, and 70% He.
b) Stopped-flow delivery.
c) Injection delivery.

In addition to the observed T_1 times, Tables 5.1 and 5.2 list the expected relaxation times for krypton gas mixtures extrapolated to zero pressure. At densities low enough for the Ideal Gas Law to apply, a linear dependence of relaxation rate upon gas pressure is expected. However, surface interactions and the formation of van der Waals molecules also contribute the overall relaxation (See Chapter 4.). Thus the relaxation rate for ^{83}Kr can be written as

$$\frac{1}{T_1} = \frac{1}{T_{1\,vdW}} + \frac{1}{T_{1\,s}} + \frac{1}{T_{1\,bc}}, \tag{5.3.1}$$

where $1/T_{1vdw}$ is the pressure independent van der Waals molecule induced relaxation rate, $1/T_{1s}$ is the pressure independent surface induced relaxation rate, and $1/T_{1bc}$ is the pressure dependent gas-phase relaxation rate caused by binary collisions.

Figure 5.3 shows the pressure dependence of the ^{83}Kr longitudinal relaxation rate when in contact with detection cell walls only. Both mixtures display the expected linear pressure dependence and non-zero y-intercepts corresponding to the sum of $1/T_{1vdw}$ and $1/T_{1s}$. Eqs. 5.3.2 and 5.3.3 represent linear least square fits of the relaxation rates as a

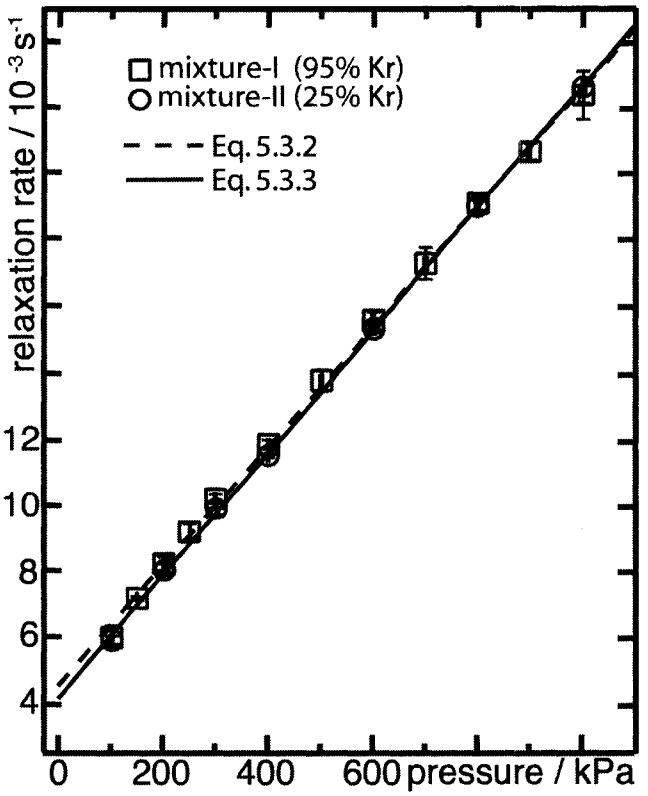

Figure 5.3: Pressure dependence of hp ^{83}Kr longitudinal relaxation rates. X-axis error bars represent the total pressure range contributing to each data point. The linear fits of the data and the accompanying fitting errors are presented as Eq. 5.3.2 (mixture-I) and Eq. 5.3.3 (mixture-II) in the text.

function of pressure, P, (in kPa) for gas mixture-I (95% Kr) and mixture-II (25% Kr) respectively.

$$\frac{1}{T_1} = [(1.79 \pm 0.02) \times 10^{-5} s^{-1} kPa^{-1}] \times P + (4.5 \pm 0.1) \times 10^{-3} s^{-1} \quad (5.3.2)$$

$$\frac{1}{T_1} = [(1.84 \pm 0.01) \times 10^{-5} s^{-1} kPa^{-1}] \times P + (4.17 \pm 0.08) \times 10^{-3} s^{-1} \quad (5.3.3)$$

The slopes of the lines depend only on the gas composition and are therefore expected to be sample independent. Thus, the value of $1/T_{1bc}$ can be calculated and then subtracted from the observed relaxation rate. The pressure independent (P = 0) T_1 values in Tables 5.1 and 5.2 were calculated using the slopes from Eqs. 5.3.2 and 5.3.3 and exclude contributions originating from binary gas-phase collisions. In the hydrated samples a small amount of water vapor was also present in the gas mixture, but its influence on the pressure dependent relaxation can be assumed to be negligible.

Because the surface coverage of noble gases at room temperature and near atmospheric pressure is low, the ratio of surface adsorbed to gas-phase krypton atoms stays constant as the pressure is moderately altered. The contribution to the relaxation arising from the surface is therefore also constant. For the surface-to-volume ratios in the studied borosilicate bead samples, surfaces processes largely dominated the ^{83}Kr relaxation, and the data do not deviate significantly from the extrapolated zero pressure values.

Of course, the pressure independent relaxation contains contributions due to krypton van der Waals molecules as can be seen by comparing the P = 0 T_1 values in Table 5.1 for the dehydrated, untreated beads. Due to the presence of helium the buffer

gas in the 25% krypton mixture (mixture-II), the pressure independent T_1 time was prolonged by about 60% compared to the mixture-I. In principle, the existence of this second density independent relaxation mechanism could obscure the effect of surface relaxation in these materials. In the strongly relaxing siliconized beads where T_1 times of less than 10 s are observed, the relaxation is clearly dominated by surface interactions. However, the P = 0 data shown in Table 5.1 for the dehydrated bead samples seems displays a dependence upon gas composition. The origin of this behavior is has not been investigated and requires additional study.

5.4 Discussion

5.4.1 Paramagnetic Relaxation of ^{83}Kr: Comparison with Hp ^{129}Xe

Fig. 5.4 provides a comparison of the experimental T_1 data for hp ^{83}Kr (Tables 5.1 and 5.2) and hp ^{129}Xe (Table 5.3). The ^{83}Kr relaxation times from the 25% krypton gas mixture in contact with untreated bead samples are identical, within experimental error, to those obtained from hp ^{129}Xe for both the dehydrated and hydrated glass surfaces. The similarity of these values is coincidental and resulted from a combined effect of the surface chemistry, void-space geometry, and gas composition. In the presence of paramagnetic surface sites, the ^{129}Xe relaxation is dominated by paramagnetic relaxation, and shielding the ^{129}Xe from these sites by siliconizing the surface increases the T_1. In contrast, the ^{83}Kr relaxation is dominated by quadrupolar contributions that increase in the presence of the nonpolar siliconized surface.

Further, the ^{83}Kr relaxation is much less affected by paramagnetic sites than the ^{129}Xe relaxation due to the 7.2 times smaller gyro-magnetic ratio, γ, of the ^{83}Kr nucleus, because paramagnetic relaxation follows a $T_1 \propto \gamma^{-2}$ dependence [31]. The 1.9 Å van der Waals radius of krypton is only slightly smaller than the 2.2 Å radius of xenon and cannot offset the effect caused by the small γ despite the $T_1 \propto r^6$ dependence on distance, r, for paramagnetic driven relaxation. In addition, the smaller krypton electron cloud will lead to decreased surface affinity and, therefore, to reduced contact time with the paramagnetic sites. Similar arguments explain why the presence of 20% paramagnetic gas-phase oxygen reduced the ^{83}Kr T_1 time in a desiccated canine lung specimen by only 20% [17]. The low ^{83}Kr gyromagnetic ratio, because of its inherent insensitivity to paramagnetic relaxation, can actually be advantageous for some applications of this gas, provided sufficiently high signal intensity is generated through the SEOP process.

5.4.2 Effects of Krypton Concentration on T_1 Relaxation

An important point for practical MR studies with hp ^{83}Kr is that the relaxation time in porous structures can be adjusted by changing the composition of the krypton gas mixture. Even though the binary collision induced relaxation is negligible in these materials, diluting the krypton prolongs relaxation times by suppressing contributions from van der Waals molecules. The ^{83}Kr relaxation in porous materials is, however, relatively insensitive to changes in the total gas pressure if the surface-to-volume ratio is large enough to be the dominant source of relaxation. In addition to the influence of the krypton concentration on relaxation reported here, it was previously shown that lower

magnetic field strengths lead to increased ^{83}Kr relaxation rates [16]. The capability to adjust the relaxation rate by manipulating various physical interactions provides experimental adaptability for practical requirements such as future *in vivo* hp ^{83}Kr MRI for pulmonary diagnostics. Relaxation times substantially below 3 s would be problematic because of the duration of the inhalation process. Relaxation times in excess of 30 s would probably not allow for sufficient contrast because of limitations in breath holding by patients and because of competing relaxation caused by paramagnetic oxygen at prolonged timescales.

5.4.3 Effects of Surface Hydration

The effect of surface hydration on the ^{83}Kr longitudinal relaxation time is reminiscent of previous work with liquefied, thermally polarized ^{131}Xe (spin I = 3/2) in aerogels where the observed relaxation times were T_1 = 11.2 ms (hydrated) and 3.6 ms (dehydrated) [26, 32]. Due to the fractal geometry of the aerogels in the 10 to 50 nm regime and the large water uptake (up to 30% of the aerogel dry weight) a substantial change in the surface morphology was the likely cause for the observed changes that also included alterations in the NMR line width and multiple quantum filtered ^{131}Xe NMR spectra.

The effect reported in this chapter was observed with gas-phase hp ^{83}Kr on glass bead surfaces with surface-to-volume ratios that were orders of magnitude smaller than that of aerogels. The ^{83}Kr relaxation time was even sensitive to water uptake on the surface of detection cell wall (13.5 mm ID) in the absence of a glass beads sample (See Table 5.1), which has a surface-to-volume ratio approximately two orders of magnitude lower than the bead sample. Owing to this much smaller surface-to-volume ratio, binary collision induced gas-phase relaxation noticeably contributed to the overall relaxation

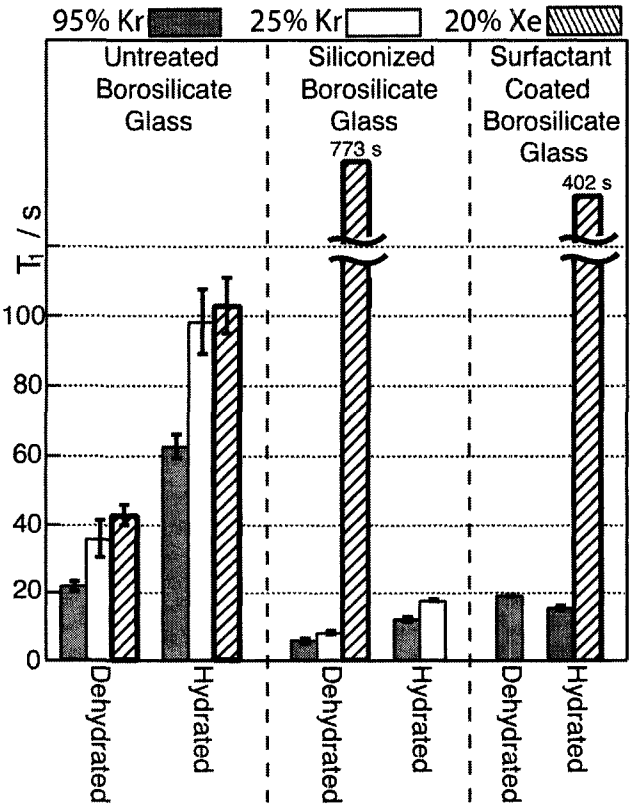

Figure 5.4: T_1 values of hp ^{83}Kr and ^{129}Xe in contact with 1 mm diameter borosilicate glass bead samples. The error bars are omitted from data for hp ^{129}Xe in contact with siliconized and surfactant coated surfaces but are reported in Table 5.3.

time. A ^{83}Kr T_1 of 165.5 s was observed for gas mixture-II at ambient pressure when located within the dehydrated detection cell and was prolonged by 22% to 202.3 s within hydrated detection cell. Interpolated to zero pressure, the relaxation times are $T_1 = 223.4$ s and $T_1 = 269.1$ s for the dehydrated and hydrated container walls respectively. A similar trend was also observed for gas mixture-I.

The sensitivity of hp ^{83}Kr relaxation to adsorbed surface water allowed for measurements of surface hydration in dilute gas-phase at various concentrations. It also allowed for measurements in systems with a wide range of low surface-to-volume ratios and small overall surface areas. A crucial result is the strong effect of water vapor on ^{83}Kr relaxation caused by siliconized (hydrophobic) surfaces. It is possible that the siliconizing of the surface was incomplete and that some untreated glass was still exposed to the gas-phase. However, the long ^{129}Xe T_1 in the siliconized beads indicated that the overall glass surface exposed to the noble gases was small and that the adsorption affinity of the surface upon hydration plays an important role in extending the ^{83}Kr relaxation time.

In principle, gas-phase water molecules could serve to beak up krypton van der Waals molecules and thus reduce the observed relaxation rate. However, even at saturation, water molecules are expected to contribute only a few percent to the total gas number density. In the experiments discussed in Chapter 4, the density independent relaxation was reduced by only 33% in going from the pure krypton to the 95% krypton 5% N_2 gas mixture. Thus it is unlikely that the small partial pressure of water present in these experiments could produce the dramatic effects seen in Table 5.1. Additionally, the influence of van der Waals mediated relaxation should be significantly suppressed in the 25% krypton mixture, but the effect of water vapor was observed to be quite strong even

in this gas mixture. Finally, van der Waals molecule formation in ^{129}Xe leads to T_1 times of many hours [33] and cannot contribute significantly to the 43 s T_1 observed in the dehydrated, untreated beads (See Table 5.2.). However, upon surface hydration, the ^{129}Xe T_1 time more than doubled. Thus competitive adsorption must play a dominant role in extending the relaxation times of hp noble gases in these porous materials.

5.4.4 Lung Surfactant Studies

In vivo NMR spectroscopy and MR imaging for pulmonary diagnostics are potential applications for hp ^{83}Kr because of the sensitivity of ^{83}Kr relaxation to surface chemistry in porous materials. As a model *in vitro* system that should be chemically similar to the interior of the mammalian pulmonary system, the commercially available bovine pulmonary extract Survanta was selected. Survanta is used to treat premature infants with Respiratory Distress Syndrome (RDS) by lowering the surface tension on alveolar surfaces and, thus, stabilizing the alveoli against collapse. A parameter of potential importance for *in vivo* and *in situ* lung studies is the relative humidity of the gas mixture introduced. Under normal circumstances, the relative humidity inside the mammalian lung approaches 100% [34]. Even for *in vitro* experiments, the relative humidity is potentially important as it has been shown to influence lung surfactant adsorption kinetics at the air-water interface [35]. To minimize perturbations caused by the addition of the hp gas mixtures, the injection delivery method was used for all relaxation measurements involving hydrated lung surfactant.

As a support for the bovine lung extract, 1 mm untreated and siliconized borosilicate glass beads were again selected because the void spaces formed by tightly

packing the beads are similar in size to mammalian alveoli (i.e. around 200 microns in human lungs [36]). Hydrated surfactant (i.e. Survanta used as supplied by the manufacturer) appeared to completely coat the glass beads and therefore strongly prolongs ^{129}Xe relaxation times (See Figure 5.4 and Table 5.3.). The ^{83}Kr longitudinal relaxation time of T_1 = 16 s observed for krypton in the surfactant coated beads was significantly shorter than the T_1 = 62.8 s (mixture-I) observed in untreated, hydrated glass beads. The observation of relaxation times on the order of 15 s is an important result because it suggests that similar relaxation times may be observed *in vivo*. Diluting the surfactant with distilled water (1:2) produced prolonged relaxation times of around T_1 = 20 s, perhaps due to a decreased concentration of the non-polar surfactant components. (Note that dehydration produces a similar effect as is shown in Table 5.2.).

The ^{83}Kr relaxation in *in vivo* pulmonary studies will also depend on changes in the surface-to-volume ratios because the surfactant concentration also determines the alveolar dimensions. This sensitivity to surface chemistry could be valuable for understanding certain pulmonary diseases, particularly if used in conjunction with techniques such as apparent diffusion constant weighted (ADC) hp ^{3}He MRI that can provide independent information about alveolar size [37].

5.5 Conclusions

The work discussed in this chapter provided the first direct comparisons of ^{129}Xe and ^{83}Kr longitudinal relaxation in porous materials. In stark contrast to ^{129}Xe, the relaxation of ^{83}Kr was largely unaffected by small amounts of paramagnetic impurities. The longitudinal relaxation of hp ^{83}Kr was presented as a sensor for water adsorption on

untreated, hydrophilic and siliconized, strongly hydrophobic glass surfaces. The method does not require vacuum conditions or optical transparency and allows for measurements under near atmospheric conditions in systems with low surface-to-volume ratios.

Surfaces coated with bovine pulmonary extract produced ^{83}Kr T_1 times that were of reasonable lengths for medical applications and sensitive to changes in the chemical composition of the surfactant. The results are promising for future *in vivo* hp ^{83}Kr MRI diagnosis of various forms of Acute Lung Injury (ALI), including the most severe form, Acute Respiratory Distress Syndrome (ARDS) [38], which are characterized by alteration in the lipid and protein composition of the pulmonary surfactant system [39, 40], alveolar fluid levels [41], and alveolar size [42]. The longitudinal relaxation of hp ^{83}Kr is, in principle, sensitive to all of these changes and, in concert with biochemical and biophysical markers [43], could provide a powerful tool for early diagnosis of ALI in at risk individuals, monitoring the effectiveness of ALI therapies, and developing improved surfactant therapies [44].

Future work will need to focus on the quantifying water uptake on various materials, comparing krypton relaxation data with more traditional measures of macroscopic surface wettability [45, 46] such as contact angle measurements with sessile water droplets, and examining the influence of alternate adsorbate molecules (e.g. short chain alcohols) on relaxation. Potential applications of this technique are water content analysis of solid chemicals, pharmaceutical products, and food materials that otherwise rely on Karl Fischer water titrations that can be complicated by side reactions and reagent instability [47]. *In situ* hp ^{83}Kr MR imaging could potentially monitor the water distribution

in porous fuel cell cathodes that require careful engineering of composite hydrophobic and hydrophilic surface sites to allow optimized water transport without flooding [48].

As a final point, it is also demonstrated that the hp ^{83}Kr relaxation in porous materials is dependent on the krypton concentration in the gas mixtures used. This may allow for optimizing the range of the relaxation times for particular applications. For a reasonably broad range of gas compositions, this ability to tune the relaxational properties of the gas mixture can be achieved without sacrificing signal intensity.

References:

1. Ingman, P.; Jokisaari, J.; Diehl, P., Kr-83 and Xe-131-Nmr of the Noble-Gases Dissolved in Nematic Liquid-Crystals - Determination of Quadrupole Couplings and Electric-Field Gradients. *Journal of Magnetic Resonance* **1991,** 92, (1), 163-169.

2. Jokisaari, J.; Ingman, P.; Lounila, J.; Pukkinen, O.; Diehl, P.; Muenster, O., Electric-Field Gradients Experienced by the Noble-Gas Isotopes Ne-21, Kr-83 and Xe-131 in Thermotropic Liquid-Crystals. *Molecular Physics* **1993,** 78, (1), 41-54.

3. Horton-Garcia, C. F.; Pavlovskaya, G. E.; Meersmann, T., Introducing krypton NMR spectroscopy as a probe of void space in solids. *Journal of the American Chemical Society* **2005,** 127, (6), 1958-1962.

4. Ito, T.; Fraissard, J., Xe-129 NMR-Study of Xenon Adsorbed on Y Zeolites. *Journal of Chemical Physics* **1982,** 76, (11), 5225-5229.

5. Ratcliffe, C. I., Xenon NMR. *Annual Reports on NMR Spectroscopy* **1998,** 36, 123-221.

6. Springuel-Huet, M. A.; Bonardet, J. L.; Gedeon, A.; Fraissard, J., Xe-129 NMR overview of xenon physisorbed in porous solids. *Magnetic Resonance in Chemistry* **1999,** 37, S1-S13.

7. Walker, T. G.; Happer, W., Spin-exchange optical pumping of noble-gas nuclei. *Review of Modern Physics* **1997,** 69, (2), 629-642.

8. Raftery, D.; Long, H.; Meersmann, T.; Grandinetti, P. J.; Reven, L.; Pines, A., High-Field NMR of Adsorbed Xenon Polarized by Laser Pumping. *Physical Review Letters* **1991,** 66, (5), 584-587.

9. Goodson, B. M., Nuclear magnetic resonance of laser-polarized noble gases in molecules, materials, and organisms. *Journal of Magnetic Resonance* **2002,** 155, (2), 157-216.

10. Stapf, S.; Han, S. I., *Nuclear Magnetic Resonance Imaging in Chemical Engineering*. Wiley-VCH: Weinheim, Germany, 2005.

11. Raftery, D., Xenon NMR Spectroscopy. *Annual Reports on NMR Spectroscopy* **2006,** 57, 205-271.

12. Volk, C. H.; Mark, J. G.; Grover, B. C., Spin Dephasing of Kr-83. *Physical Review A* **1979,** 20, (6), 2381-2388.

13. Schaefer, S. R.; Cates, G. D.; Happer, W., Determination of Spin-Exchange Parameters between Optically Pumped Rubidium and Kr-83. *Physical Review A* **1990,** 41, (11), 6063-6070.

14. Butscher, R.; Wäckerle, G.; Mehring, M., Nuclear quadrupole surface interaction of gas phase 83Kr: comparison with 131 Xe. *Chemical Physics Letters* **1996,** 249, 444-450.

15. Stupic, K. F.; Cleveland, Z. I.; Pavlovskaya, G. E.; Meersmann, T., Quadrupolar Relaxation of Hyperpolarized Krypton-83 as a Probe for Surfaces. *Solid State Nuclear Magnetic Resonance* **2006,** 29, 79-84.

16. Cleveland, Z. I.; Pavlovskaya, G. E.; Stupic, K. F.; LeNoir, C. F.; Meersmann, T., Exploring hyperpolarized 83Kr by remotely detected NMR relaxometry. *Journal of Chemical Physics* **2006,** 124, 044312.

17. Pavlovskaya, G. E.; Cleveland, Z. I.; Stupic, K. F.; Meersmann, T., Hyperpolarized Krypton-83 as a New Contrast Agent for Magnetic Resonance Imaging.

Proceedings of the National Academy of Sciences of the United States of America **2005,** 102, 18275-18279.

18. Mortuza, M. G.; Anala, S.; Pavlovskaya, G. E.; Dieken, T. J.; Meersmann, T., Spin-exchange optical pumping of high-density xenon-129. *Journal of Chemical Physics* **2003,** 118, (4), 1581-1584.

19. Happer, W., Optical-Pumping. *Reviews of Modern Physics* **1972,** 44, (2), 169-&.

20. Kwon, T. M.; Mark, J. G.; Volk, C. H., Quadrupole Nuclear-Spin Relaxation of Xe-131 in the Presence of Rubidium Vapor. *Physical Review A* **1981,** 24, (4), 1894-1903.

21. Raftery, D.; Long, H. W.; Shykind, D.; Grandinetti, P. J.; Pines, A., Multiple-Pulse Nuclear-Magnetic-Resonance of Optically Pumped Xenon in a Low Magnetic-Field. *Physical Review A* **1994,** 50, (1), 567-574.

22. Meersmann, T.; Smith, S. A.; Bodenhausen, G., Multiple-quantum filtered xenon-131 NMR as a surface probe. *Physical Review Letters* **1998,** 80, (7), 1398-1401.

23. Deschamps, M.; Burghardt, I.; Derouet, C.; Bodenhausen, G.; Belkic, D., Nuclear magnetic resonance study of xenon-131 interacting with surfaces: Effective Liouvillian and spectral analysis. *Journal of Chemical Physics* **2000,** 113, (4), 1630-1640.

24. Moudrakovski, I. L.; Ratcliffe, C. I.; Ripmeester, J. A., Xe-131, a new NMR probe of void space in solids. *Journal of the American Chemical Society* **2001,** 123, (9), 2066-2067.

25. Millot, Y.; Man, P. P.; Springuel-Huet, M. A.; Fraissard, J., Quantification of electric-field gradient in the supercage of Y zeolites by comparing the chemicl shifts of Xe-131 (I=3/2) NMR. *Studies in Surface Sciences and Catalysis* **2001,** 135.

26. Meersmann, T.; Deschamps, M.; Bodenhausen, G., Probing aerogels by multiple quantum filtered Xe-131 NMR spectroscopy. *Journal of the American Chemical Society* **2001,** 123, (5), 941-945.

27. Pfeffer, M.; Lutz, O., Xe-129 Gas Nmr-Spectroscopy and Imaging with a Whole-Body Imager. *Journal of Magnetic Resonance Series A* **1994,** 108, (1), 106-109.

28. Driehuys, B.; Cates, G. D.; Happer, W., Surface Relaxation Mechanisms of Laser-Polarized Xe-129. *Physical Review Letters* **1995,** 74, (24), 4943-4946.

29. Breeze, S. R.; Lang, S.; Moudrakovski, I.; Ratcliffe, C. I.; Ripmeester, J. A.; Santyr, G.; Simard, B.; Zuger, I., Coatings for optical pumping cells and short-term storage of hyperpolarized xenon. *Journal of Applied Physics* **2000,** 87, (11), 8013-8017.

30. Jacob, R. E.; Driehuys, B.; Saam, B., Fundamental mechanisms of He-3 relaxation on glass. *Chemical Physics Letters* **2003,** 370, (1-2), 261-267.

31. Abragam, A., *The Principles of Nuclear Magnetism.* Oxford University Press: Oxford, UK, 1961.

32. Pavlovskaya, G.; Blue, A. K.; Gibbs, S. J.; Haake, M.; Cros, F.; Malier, L.; Meersmann, T., Xenon-131 surface sensitive imaging of aerogels in liquid xenon near the critical point. *Journal of Magnetic Resonance* **1999,** 137, (1), 258-264.

33. Berry-Pusey, B. N.; Anger, B. C.; Laicher, G.; Saam, B., Nuclear spin relaxation of Xe-129 due to persistent xenon dimers. *Physical Review A* **2006,** 74, (6), 063408.

34. Schmidt-Nielsen, K., *Animal Physiology: Adaptation and Environment.* 5th ed.; Cambridge University Press: Cambridge, UK, 1997.

35. Zuo, Y. Y.; Gitiafroz, R.; Acosta, E.; Policova, Z.; Cox, P. N.; Hair, M. L.; Neumann, A. W., Effect of humidity on the adsorption kinetics of lung surfactant at air-water interfaces. *Langmuir* **2005,** 21, (23), 10593-10601.

36. Ochs, M.; Nyengaard, L. R.; Jung, A.; Knudsen, L.; Voigt, M.; Wahlers, T.; Richter, J.; Gundersen, H. J. G., The number of alveoli in the human lung. *American Journal of Respiratory and Critical Care Medicine* **2004,** 169, (1), 120-124.

37. Yablonskiy, D. A.; Sukstanskii, A. L.; Leawoods, J. C.; Gierada, D. S.; Bretthorst, G. L.; Lefrak, S. S.; Cooper, J. D.; Conradi, M. S., Quantitative in vivo assessment of lung microstructure at the alveolar level with hyperpolarized He-3 diffusion MRI. *Proceedings of the National Academy of Sciences of the United States of America* **2002,** 99, (5), 3111-3116.

38. Repine, J. E., Scientific Perspectives on Adult Respiratory-Distress Syndrome. *Lancet* **1992,** 339, (8791), 466-469.

39. Schmidt, R.; Meier, U.; Yabut-Perez, M.; Walmrath, D.; Grimminger, F.; Seeger, W.; Gunther, A., Alteration of fatty acid profiles in different pulmonary surfactant phospholipids in acute respiratory distress syndrome and severe pneumonia. *American Journal of Respiratory and Critical Care Medicine* **2001,** 163, (1), 95-100.

40. Cochrane, C. G., Pulmonary surfactant in allergic inflammation: new insights into the molecular mechanisms of surfactant function. *American Journal of Physiology-Lung Cellular and Molecular Physiology* **2005,** 288, (4), L608-L609.

41. Guidot, D. M.; Folkesson, H. G.; Jain, L.; Sznajder, J. I.; Pittet, J.-F.; Matthay, M. A., Integrating acute lung injury and regulation of alveolar fluid clearance. *American Journal of Physiology-Lung Cellular and Molecular Physiology* **2006,** 291, L301-L306.

42. Schiller, H. J.; McCann, U. G.; Carney, D. E.; Gatto, L. A.; Steinberg, J. M.; Nieman, G. F., Altered alveolar mechanics in the acutely injured lung. *Critical Care Medicine* **2001,** 29, (5), 1049-1055.

43. Connelly, K. G.; Repine, J. E., Markers for predicting the development of acute respiratory distress syndrome. *Annual Review of Medicine* **1997,** 48, 429-445.

44. Cochrane, C. G.; Revak, S. D., Surfactant lavage treatment in a model of respiratory distress syndrome. *Chest* **1999,** 116, (1), 85S-86S.

45. Adamson, A. W.; Gast, A. P., *Physical Chemistry of Surfaces*. John Wiley & Sons, Inc.: New York, 1997.

46. Fuji, M.; Fujimori, H.; Takei, T.; Watanabe, T.; Chikazawa, M., Wettability of glass-bead surface modified by trimethylchlorosilane. *Journal of Physical Chemistry B* **1998,** 102, (51), 10498-10504.

47. Grunke, S., Main and side reactions in the Karl Fischer solution. *Food Control* **2001,** 12, (7), 419-426.

48. Zhang, F. Y.; Yang, X. G.; Wang, C. Y., Liquid water removal from a polymer electrolyte fuel cell. *Journal of the Electrochemical Society* **2006,** 153, (2), A225-A232.

CHAPTER 6

DETECTING TOBACCO SMOKE DEPOSITION WITH HYPERPOLARIZED KRYPTON-83 MRI

The results presented in this dissertation chapter appear in the journal article: Zackary I. Cleveland, Galina E. Pavlovskaya, Karl F. Stupic, Jan B. Wooten, John E. Repine, and Thomas Meersmann, "Detecting Tobacco Smoke Deposition by Hyperpolarized ^{83}Kr MRI", *Magnetic Resonance Imaging* **2008,** 26 (2): 270-278.

Zackary I. Cleveland and Thomas Meersmann wrote the paper mentioned above. Karl F. Stupic performed some of the ^{129}Xe relaxation measurements. John E. Repine provided the lung surfactant extract and edited the manuscript, and provided expertise concerning the aspects of the work that were of biomedical interest. Jan B. Wooten edited the manuscript and provided the reference cigarettes used in this work. Zackary I. Cleveland produced the hp ^{83}Kr, participated in the design of the experiments, built the experimental apparatus, and prepared the studied samples. Galina E. Pavlovskaya built the ^{83}Kr imaging probe used in this work, performed the MR imaging, and processed the image data.

6.1 Introduction

Exposure to tobacco smoke is known to cause emphysema [1], lung cancer, [2] and cardiovascular disease [3] in cigarette smokers. A growing body of work suggests that both the location and type of smoking related cancers are influenced by the manner in which cigarettes are smoked [4, 5]. This dependence presumably results from differences in smoke particulate deposition within the respiratory tract. Because of the deleterious impacts on human health, the deposition of tobacco smoke constituents in the human respiratory tract has been the subject of a great deal of biomedical research [6, 7]. Unfortunately, mapping the regions of cigarette smoke particulate deposition within the lung remains problematic.

Extrapolating particulate deposition based on computational fluid dynamic (CFD) simulations is hindered by the precision with which airway geometry and dimensions can be measured [8]. Further, neither in-vitro models nor animal models, which often inhale differently than do humans, can fully reflect particle deposition in humans. Direct measurement of the differences between inhaled and exhaled smoke particulate matter [6, 9] can provide information about the amount of material deposited in the respiratory tract but does not address medically important issues such the location of deposited materials or the rate at which the body removes these materials from the lungs. Studies using radioactively labeled tracer compounds have attempted to evaluate regional smoke particulate deposition and clearance, but have led to conflicting results [7]. Mathematical models of particulate deposition [10, 11] in the respiratory tract have attempted to resolve these issues but currently lack experimental validation. In general, the current understanding of the

diseases caused by smoking could be improved by developing techniques to visualize the deposition and clearance of tobacco smoke condensate from the respiratory tract.

As discussed in Chapter 3, hyperpolarized (hp) ^{83}Kr can serve as a surface sensitive MRI contrast agent that allows investigations of surfaces under near-ambient pressure and temperature conditions [12]. The longitudinal (T_1) relaxation observed in magnetic resonance experiments with the stable krypton isotope ^{83}Kr (nuclear spin I = 9/2) was shown to be highly dependent upon the nature of the surfaces in contact with the krypton gas. The ^{83}Kr T_1 relaxation yields information about the surface-to-volume ratio [13] in porous host materials and the chemistry [13], temperature [14], and degree of hydration [15] at the gas-surface interface. In hp krypton MR, the ^{83}Kr isotope is both the contrast agent and the NMR active spin that can yield high signal intensities despite its low resonance frequency of 15.4 MHz at 9.4 T field strength. Through rubidium vapor spin exchange optical pumping [16] (SEOP), signal enhancements of more than three orders of magnitude greater than thermally polarized ^{83}Kr at 9.4 T field strength and ambient temperature were produced and were found to be sufficient allow hp ^{83}Kr MRI applications including images with surface chemistry sensitive T_1 [12].

The signal intensity obtained from hp ^{83}Kr is currently less than that of the more widely used spin I = 1/2 hp noble gas isotopes ^{129}Xe and ^{3}He (See [17-21] for recent reviews.). Additionally, ^{83}Kr lacks the tissue solubility and the relatively long dissolved-phase T_1 times of hp ^{129}Xe that allow MRI studies of pulmonary gas exchange and lung physiology [22-24]. Although the ^{129}Xe chemical shift interactions are sensitive probes of the local environment when xenon is dissolved in solution or contained in nanoporous materials such as zeolites, surface dependent chemical shifts cannot be observed when

xenon is contained in macroscopic pores where the ^{129}Xe spectrum is indistinguishable from the bulk gas-phase signal. The ^{83}Kr nuclear quadrupolar interactions, however, are sensitive to surface temperature and surface chemistry even when surface-to-volume ratios are as small as 0.1 cm^{-1}. Therefore, hp ^{83}Kr has the ability to probe the surface molecular layers exposed to the gas-phase even in media with relatively large pore dimensions such as lungs. Hence, hp ^{83}Kr is of interest because of its potential ability to serve as a surface sensitive contrast agent.

In this work, we demonstrate that the longitudinal relaxation of hp ^{83}Kr is strongly accelerated by the presence of tobacco smoke deposited on model glass surfaces. The resulting T_1 variations have been exploited to produce contrast in MR images that not only indicate the presence or absence of tobacco smoke deposited on surfaces but also, to some extent, the level of smoke deposition. Of potential biomedical interest is the observation that decreased hp ^{83}Kr T_1 times are also produced after tobacco smoke is deposited on pulmonary surfactant extract coated surfaces.

6.2 Materials and Methods

6.2.1 MR Instrumentation

All MR experiments were performed on a Chemagnetics CMX II 400 MHz NMR spectrometer in a 9.4 T wide-bore (89 mm) superconducting magnet equipped with an imaging system (Resonance Research, Billerica, MA) consisting of triple axis gradient coils (100 G/cm x,y axes and 720 G/cm z axis) and low-noise linear gradient amplifiers. All MR data were obtained using custom-built, gas-flow probes tuned to either the ^{83}Kr frequency of 15.4 MHz or the ^{129}Xe frequency of 110.6 MHz. The non-selective, 90°

pulse widths were 220 μs for ^{83}Kr and 47 μs for ^{129}Xe. The receiver gain was adjusted such that no signal clipping was observed and was kept constant for all experiments.

6.2.2 Spin Exchange Optical Pumping of ^{83}Kr and ^{129}Xe

SEOP was performed in cylindrical Pyrex cells (length = 125 mm, ID = 24 mm) housed in a quartz and aluminum oven to maintain even heating (438 ± 5 K for ^{83}Kr and 393 ± 5 K for ^{129}Xe) and containing ~1 g of rubidium (99.75%; Alfa Aesar, Ward Hill, MA). The pump cell was maintained above ambient pressure (150 - 200 kPa) to decrease contamination by atmospheric oxygen and water vapor. Light (794.7 nm) from two 30 W Coherent FAP diode-array lasers (Coherent Inc., Santa Clara, CA) with a line width of approximately 2 nm was directed via fiber optic coupling cables through a circular polarizer onto the pump cell. After passing through the fiber optics and polarizer, the laser power was reduced to approximately 40 W. SEOP occurred in the fringe field of the superconducting magnet at a field strength of approximately 0.05 T. Rubidium vapor was separated from the hp gas mixtures by means of an air-cooled trap at the outlet to the pump cell and a glass wool filter placed directly before the sample region. All gas mixtures were produced from natural abundance, research grade krypton (99.995% pure), xenon (99.995% pure), nitrogen (99.9997% pure), and helium (99.9999% pure) (Airgas, Radnor, PA). Gas mixtures consisted of 95% Kr and 5% N_2; 25% Kr, 5% N_2, and 70% He; or 20% Xe, 5% N_2, and 75% He. In both gas mixtures, the N_2 gas was added to the mixtures for radiation quenching purposes [25].

6.2.3 Hp Gas Delivery

An experimental apparatus was described in Chapter 5 that exposed samples to hp gases with minimal disturbance to surface hydration while maintaining reasonably high nonequilibrium spin polarization [15]. After a SEOP period of several minutes, the hp gas was vacuum shuttled from the pump cell to an intermediate storage cell. Subsequently, the gas at 150 - 200 kPa was released into a water-filled glass container displacing water into an attached syringe. The hp gas was then injected into the sample cell. In the current work, the same setup was used to deliver hp ^{83}Kr and hp ^{129}Xe to a series of 1 mm diameter borosilicate glass beads samples (See section 6.2.4.) for longitudinal relaxation measurements. These T_1 measurements were performed only on the borosilicate gas beads samples at an ambient pressure of approximately 85 kPa.

MR imaging experiments were conducted at 150 kPa to provide higher hp ^{83}Kr density to the sample region thus increasing the observed signal intensity. The hp gas was delivered by a stopped-flow [12-14] method, in which polarization was allowed to build for 10 minutes while evacuating the sample region to less than 10 Pa. Following SEOP, the hp gas was transferred from the pump cell to the sample by pressure equalization over the course of approximately 3 s.

6.2.4 Sample Preparation

Tobacco smoke was produced by combusting 2R4F cigarettes, which are standard reference cigarettes with tobacco blend composition, cigarette design, and smoke chemistry that are representative of domestic cigarettes manufactured by major US cigarette companies [26]. In experiments involving the combustion of one or more full

cigarettes, smoke was drawn from the cigarette through an intact cigarette filter at approximately 250 mL/min using a peristaltic pump (Watson-Marlow Bredel Inc., Wilmington, MA). Samples were located in line between the cigarette filter and the pump. For experiments in which less than one full cigarette was combusted, smoke was deposited by pulling 60 mL of air through a lit cigarette in 4 s with a 10 s waiting period between pulls. In the text, one such deposition is referred to as one "puff". Note that neither of these smoking conditions conform to the Federal Trade Commission (FTC) smoking standard and were chosen simply to generate varying amounts of cigarette smoke for smoke deposition experiments.

As a model system to study the influence of tobacco smoke deposition on the observed ^{83}Kr T_1, untreated, 1.0 mm diameter, borosilicate glass beads (Biospec Products, Inc., Bartlesville, OK) were selected. Because water vapor from the combustion of organic materials may adsorb onto the glass surfaces, and surface hydration alters the T_1 of ^{83}Kr [15], the beads were stored overnight in a saturated water vapor to hydrate the surface and provide consistent initial conditions for deposition experiments. For the experiments involving bovine pulmonary surfactant extract (Survanta, Ross Products Division, Abbott Laboratories, Columbus, OH), a 4 mL vial of surfactant was applied to the beads as described in Chapter 5. Following application of the surfactant, the beads were exposed to cigarette smoke with the same technique as was used for the non-surfactant coated beads.

Although the borosilicate glass beads provided simple and fairly reproducible samples for T_1 measurements, they were not suitable for FLASH imaging. Assuming hard sphere packing, the sample void-space would comprise only 26% of the sample volume.

Consequently, an alternate model system (i.e. soda lime glass capillaries) that provided a higher gas filling factor, and thus higher ^{83}Kr density, was selected. The phantom used to produce the images (See Fig. 5.3A.) comprised three Pyrex tubes (length = 60 mm, OD = 10.0 mm, and ID = 7.8 mm). These tubes were formed from three individual pieces: the top cap (length = 5 mm), the main body (length = 50 mm), and the top portion of the gas delivery tubing (length = 5 mm). Contained within each tube were 16 soda lime glass capillaries (length = 59 mm, OD = 1.5 mm, and ID = 1.1 mm). The hp ^{83}Kr mixture was supplied to each tube from a common source through 1 mm wide holes at the bottom of each tube. This ensured that equal gas pressure was reached in each tube while limiting gas exchange between the tubes during the experiments. One tube was not exposed to cigarette smoke, one was exposed to the smoke of one cigarette, and one was exposed to the smoke of three cigarettes. Following smoke application, the three portions of the Pyrex sample tubes were sealed together using LOCITE 409 Superbond Instant Adhesive (Locite Corp., Kartford, CT). The adhesive was allowed to set for 30 minutes prior to the first experiment to allow a gas-tight seal to form.

To assess the amount of tobacco smoke condensate deposited on the phantom surface, six 10 mm ID Pyrex tubes containing soda lime capillaries identical to those used in the imaging experiments were constructed. The mass of each tube was determined prior to smoke exposure. Three tubes were then exposed to the smoke of one cigarette, and three tubes were exposed to the smoke of three cigarettes. For the tubes exposed to the smoke of one cigarette, the mass was found to increase in each case by only 0.1 mg (the sensitivity limit of the analytical balance used). For the heavily smoked tubes (three cigarettes) the mass increased by 0.2, 0.3, or 0.6 mg. From these results, it was concluded

that no substantial changes in the gas volume of the samples occurred upon smoke deposition.

6.2.5 MR Data Analysis

All T_1 values reported in this work were obtained by nonlinear least squares fitting of the signal intensities resulting from sixteen, 12° pulses applied to single boluses of hp gas as was described in Chapter 4. The delays between pulses were varied between sample types and were selected so that no more that 10% of the initial signal intensity that resulted from the first RF pulse was acquired from the final pulse. The reported values are the averages of four to eight replicate measurements conducted at ambient pressure (~85 kPa) and 290 K. The errors reported are the standard deviations resulting from those replicate measurements.

Compared to MRI of thermally polarized systems, the application of FLASH imaging sequences [27] is less straightforward for hyperpolarized nuclei, in particular when the signal intensity is a limiting factor. A variation on FLASH [28] replaces the small but constant flip angle of typical sequences with progressively increasing flip angles according to the relation

$$\theta_n = \tan^{-1}\left(\frac{1}{\sqrt{N-n}}\right) \tag{6.2.1}$$

where n is the acquisition increment, N is the total number of RF pulses applied, and θ_n is the flip angle of the n^{th} RF pulse. Note that the final RF pulse ($n = N$) corresponds to 90°. Incrementing the pulse lengths in this manner produces identical signal intensities from each excitation, assuming negligible T_1 relaxation during image acquisition, and will

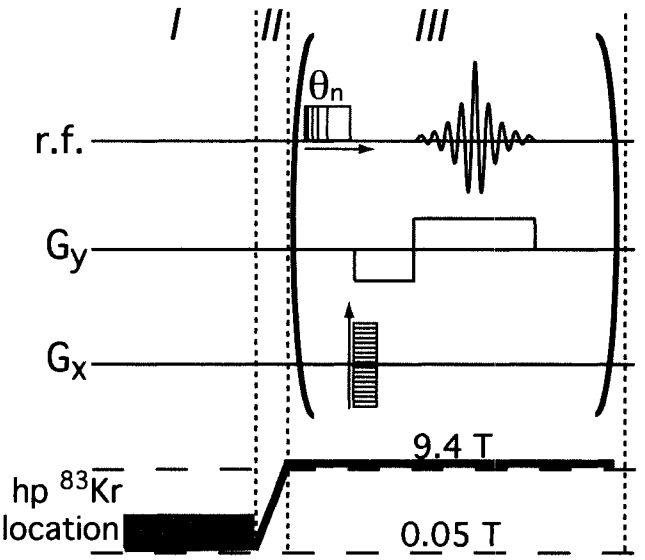

Figure 6.1: Timing diagram including the pulse sequence, SEOP, and hp ^{83}Kr shuttling scheme used in imaging experiments. The vertical dashed lines separate events (labeled *I*, *II*, and *III*) occurring on different time scales. Event *I* represents the optical pumping period of approximately 10 min. Event *II* represents the 3 s period during which the hp ^{83}Kr was transferred from the pump cell (0.05 T) to the detection cell (9.4 T). The thick line follows the location of hp ^{83}Kr in the magnetic field. Event *III* represents the timing diagram of the imaging sequence. The brackets indicate that the 32 phase-encoding steps of the variable flip angle matrix were recorded from a single delivery of hp ^{83}Kr. Each acquisition was obtained using an RF pulse, θ_n, with a 0.1 s spacing added after each individual data increment was stored. The value of θ_n was varied according to Eq. 6.2.1 with values of n ranging from 1 to 32. Note that for n = 32, θ_n = 90° (220 μs). Thus, the final pulse destroyed all of the remaining nonequilibrium magnetization. The horizontal arrow indicates increasing values of θ_n, and the vertical arrow indicates increasing values of the phase encoding gradient.

utilize all of the non-equilibrium spin polarization. Although this technique was originally designed with hp ^{129}Xe and hp ^{3}He in mind, it is particularly valuable for hp ^{83}Kr MRI because of the limited krypton spin polarization. A diagram showing the pulse sequence used to obtain the images and the timing of the relevant SEOP and gas shuttling procedures is shown in Fig. 6.1.

This sequence, applied to individual stopped-flow deliveries of hp ^{83}Kr, was used to obtain the hp ^{83}Kr MR images depicted in Figs. 6.3 and 6.4. The image in Fig. 3B was produced by averaging three variable flip angle FLASH sequences, each comprising 32 phase-encoding steps, with no slice selection. The above acquisition scheme resulted in $980\mu m \times 980\mu m$ image resolution. The acquisition matrix was processed with zero filling to 64 points in each dimension and using no apodization. Each of the images displayed in Fig. 6.4A-C resulted from a single variable flip angle FLASH sequence, each with 32 phase-encoding steps, with no slice selection applied. Acquisition matrices were zero filled to 64 points in both dimensions and apodized once using sine bell squared function. Image processing was performed in MATLAB R2006a (Version 14.2; Mathworks, Natick, MA).

6.3 Results and Discussion

6.3.1 Longitudinal Relaxation Measurements

The results of the hp ^{83}Kr and hp ^{129}Xe T_1 measurements are summarized in Table 6.1 and Fig. 6.2. In prior work with untreated glass bead samples under similar surface hydration conditions [15], the T_1 of ^{83}Kr (95% Kr and 5% N_2 gas mixture) was found to be 62.8 s and was shown to be dominated by surface induced quadrupolar relaxation. For the

two hydrated bead samples treated with the smoke of one full cigarette, the T_1 values were reduced by a factor of approximately 20 to 3.35 ± 0.26 s and 2.81 ± 0.42 s. Even when the beads were exposed to only five puffs of smoke, the hp ^{83}Kr experienced a 60% T_1 reduction compared to the untreated beads.

Like all isotopes with nuclear spin $I > 1/2$, the ^{83}Kr nucleus possesses a nonzero nuclear electric quadrupole moment making it extremely sensitive to anisotropy in its surrounding electronic environment [29]. In the presence of surfaces the krypton atoms experience brief periods of adsorption that distort the noble gas electron cloud. The resulting electronic anisotropy produces electric field gradients (EFGs) at timescales (i.e. adsorption times) that result in fast quadrupolar driven relaxation.

Table 6.1: Hp ^{83}Kr [a] and ^{129}Xe [b] T_1 times in contact with 1 mm dia. borosilicate glass beads

Kr untreated surface [c]	Kr full cigarette trial 1	Kr full cigarette trial 2	Kr 5 cigarette puffs	Kr + lung surfactant [c]	Kr full cigarette + lung surfactant
62.8 ± 3.3 s	3.3 ± 0.3 s	2.8 ± 0.4 s	24.4 ± 0.8 s	16.1 ± 0.5 s	10.6 ± 1.2 s

Xe untreated surface [c]	Xe full cigarette	Xe + lung surfactant [c]	Xe full cigarette + lung surfactant
103.0 ± 8.2 s	120.1 ± 4.9 s	420.1 ± 27.4 s	346.4 ± 11.1 s

All T_1 values are the averages resulting from 4-8 replicate measurements, and the reported errors are the standard deviations resulting from those measurements.
a) 95 % Kr + 5% N_2
b) 20% Xe + 5% N_2 +75% He
c) previously reported in ref. [15]

Although the relaxation times of surface-adsorbed ^{83}Kr are currently unknown, work in zeolites suggest that the T_1 times are in the millisecond regime or faster [30]. The relaxation measured in NMR experiments is the average between surface induced

relaxation and the relaxation occurring during the long bulk gas-phase residence time [31, 32]. The resulting T_1 times typically range between a few seconds and a few tens of seconds when the gas is contained in desiccated lung tissue or materials with similar surface-to-volume ratios. Under these conditions, moderate fluctuations in gas-phase temperature and pressure have little influence on ^{83}Kr relaxation. However, changes in the surface-to-volume ratio, surface temperature, and surface composition, or the co-adsorption of molecules on the surface can dramatically alter the ^{83}Kr relaxation rates.

Hydrophobic surfaces lead to a higher krypton surface adsorption affinity and therefore cause faster relaxation rates relative to hydrophilic surfaces for which krypton has lower affinity. For instance, a 95% Kr and 5% N_2 mixture in contact with 1 mm borosilicate glass beads treated with the siliconizing agent SurfaSil experienced a 75 – 80 % T_1 reduction [13, 15] compared to untreated beads. Many of the components comprising deposited tobacco smoke are highly nonpolar, and thus hydrophobic, in nature [33]. It is therefore reasonable to assume that these substances were responsible for the rapid T_1 relaxation of hp ^{83}Kr in the samples exposed to tobacco smoke.

6.3.2 Effects of Paramagnetic Species in Smoke Deposits

An alternative explanation for the observed ^{83}Kr T_1 decrease could potentially be relaxation caused by trace levels of paramagnetic metal ions or long-lived radicals [34] in the tobacco smoke. However, the ^{129}Xe data presented in Table 6.1 and Fig. 6.2B suggest that this not the case. The T_1 relaxation of ^{129}Xe is much more sensitive to the presence of paramagnetic compounds than that of ^{83}Kr due to the smaller gyromagnetic ratio of the ^{83}Kr nucleus $\left(\gamma_{129Xe}/\gamma_{83Kr} \approx 50\right)$ [12, 15]. Given the same surface residence time and proximity

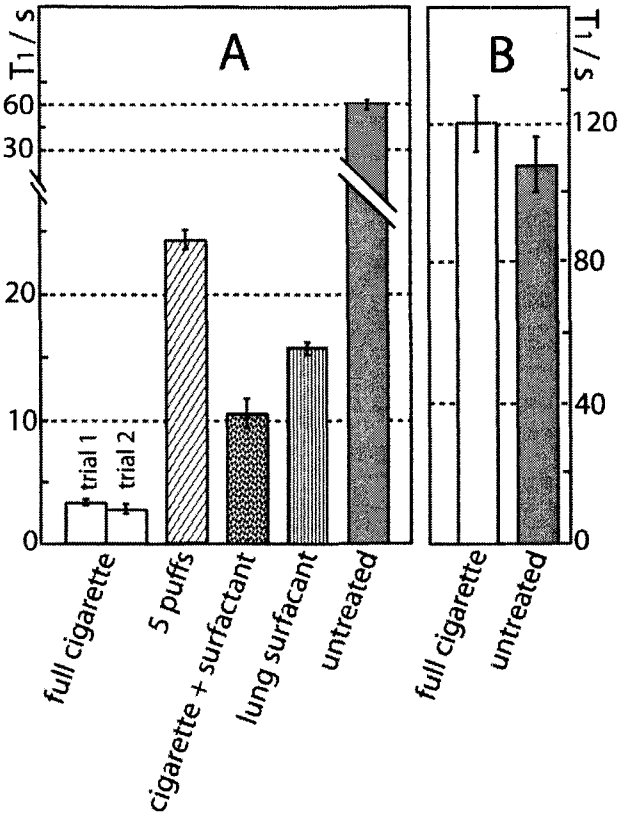

Figure 6.2: T_1 values of hp ^{83}Kr and ^{129}Xe in contact with surface treated, 1 mm diameter borosilicate glass beads (See Table 6.1.). The data for surfaces without deposited tobacco smoke were previously reported in Chapter 5. **(A)** T_1 values for a 95% Kr and 5% N_2 gas mixture. **(B)** T_1 values for a 20% Xe, 75 % He, and 5% N_2 gas mixture.

to the paramagnetic surface sites, this smaller gyromagnetic ratio leads to a ~50 fold lower sensitivity of the ^{83}Kr longitudinal relaxation to paramagnetic species compared to that of ^{129}Xe. Additionally, the smaller and thus less polarizable krypton electron cloud leads to a decreased surface affinity for krypton compared to xenon and, therefore, to reduced contact time with the paramagnetic surface sites. Thus, the ^{129}Xe longitudinal relaxation is a much more sensitive probe for the presence of paramagnetic species than is the ^{83}Kr T_1 relaxation [15].

The data in Table 6.1 and Fig. 6.2 show that, other than a perhaps a slightly prolonged T_1 value, the ^{129}Xe longitudinal relaxation was little affected by the presence of tobacco smoke deposits. The 103 ± 8 s T_1 time of ^{129}Xe in a 20% xenon mixture exposed to hydrated, 1 mm borosilicate glass beads was somewhat less than the 120.1 ± 4.9 s observed for the same gas mixture in a similar bead sample that had been exposed the smoke of one full cigarette. This finding suggests that the paramagnetic species present in cigarette smoke condensate, such as trace levels of transition metal ions and persistent semiquinone radicals [35], contribute no more to the ^{129}Xe T_1 times than do the paramagnetic impurities in the borosilicate glass surface.

The opposite effect, a shortening of the ^{129}Xe T_1 times upon smoke deposition, did occur when the glass beads were pre-coated with lung surfactant. The ^{129}Xe relaxation time of T_1 = 420 s for lung surfactant coated glass beads was decreased to T_1 = 346 s after smoke deposition on the lung surfactant. It is possible that, at this longer time scale, paramagnetic species in the smoke condensate might cause accelerated longitudinal relaxation. However, it is unlikely that this acceleration could be observed by *in vivo* ^{129}Xe MRI of lungs where the presence of molecular oxygen typically leads to ^{129}Xe

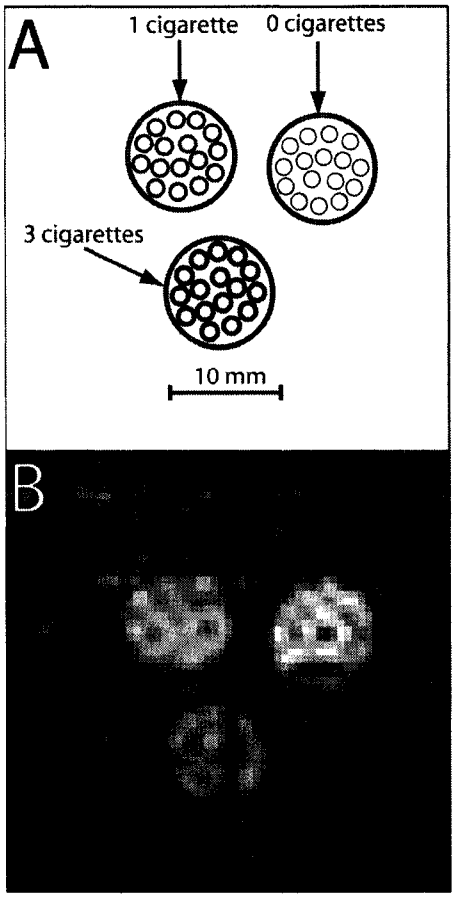

Figure 6.3: Hp ^{83}Kr FLASH image of glass capillaries exposed to cigarette smoke. **(A)** Sketch of the phantom used to produce the image. The large circles represent the 10 mm OD and 7.8 mm ID Pyrex tubes, and the smaller circles represent the 1.5 mm OD and 1.1 mm ID glass capillaries. The tube contents were exposed smoke from 0 (upper right), 1 (upper left), or 3 (bottom) cigarettes. The thickness of the smaller circles is intended to indicate the level of smoke deposition not changes in surface-to-volume ratio. **(B)** Variable flip angle FLASH image acquired immediately after stopped-flow transfer of the hp ^{83}Kr to the phantom. Three FLASH images were superimposed to provide an improved signal-to-noise ratio.

relaxation times of T_1 = 10 - 20 s [36]. Because of the low sensitivity of the ^{83}Kr nucleus to paramagnetic relaxation it can be concluded that the 38% reduction in the ^{83}Kr T_1 time after smoke deposition on surfactant coated surfaces was not caused by paramagnetic surface sites, in particular if one considers the short ^{83}Kr T_1 time scales (i.e. the T_1 was reduced from 16 s to 10 s). The ^{129}Xe relaxation data therefore strongly argue that relaxation caused by paramagnetic species within the deposited tobacco smoke plays an insignificant role in the hp ^{83}Kr longitudinal relaxation processes.

6.3.3 T_1 Weighted FLASH MR Imaging

Fig. 6.3B displays a variable flip angle FLASH image acquired immediately after stopped-flow transfer of the hp ^{83}Kr to the phantom, which displays several noteworthy features. Within the images from each of the three Pyrex tubes are alternating regions of higher and lower signal intensity. The approximately 1 mm diameter of these higher intensity regions corresponds well with the 1.1 mm ID of the glass capillaries in the samples suggesting that the image resolution is sufficient to partially resolve the interior structure of the phantom. Three FLASH images have been superimposed to provide an improved signal-to-noise ratio.

It should also be noted that, while all three Pyrex tubes are clearly visible in Fig. 6.3B, there are differences in the observed signal-to-noise ratio observed from each tube. The signal-to-noise ratio was similar for the tube exposed to no cigarette smoke (S/N = 21) and the tube exposed to the smoke of one cigarette (S/N = 17) but was significantly lower (S/N = 9) for the tube with the greatest smoke exposure (3 cigarettes). The smoke of three cigarettes leads to a smoke condensate deposition on the exposed surfaces of less

than 1 mg (See Section 6.2.4.). This level of surface deposition will not significantly alter the surface-to-volume ratio of the sample and thus cannot account for the observed decreased in hp ^{83}Kr signal intensity (and thus S/N). Additionally, the sample was constructed to provide equal gas pressure and thus equal krypton number densities to each tube. Therefore, the lower intensity observed from the tube with the greatest exposure to cigarette smoke must result from the loss of nonequilibrium ^{83}Kr spin polarization to T_1 relaxation during time needed to obtain complete pressure equalization and the time needed for image acquisition.

At longer waiting times, the effect of the cigarette smoke becomes even more pronounced as can be seen in Fig. 6.4. The internal structure of each tube phantom is unresolved because apodization was applied in both dimensions to achieve a satisfactory signal-to-noise ratio after data processing. The effect of the cigarette smoke deposition, however, is readily observed. When a 5 s period elapsed between the end of the stopped-flow transfer and the beginning of the image acquisition (See Fig. 6.4B.), the intensity of the hp ^{83}Kr in the tube containing untreated capillaries experienced only minor signal decay. At the same time the signal intensity from the tube exposed to the smoke of one cigarette visually decreased, and the intensity from the tube exposed to three cigarettes experienced an even more dramatic reduction. After a 10 s waiting period (See Fig. 6.4C.), moderate signal intensity loss was observed from the unexposed tube as is expected from the slower T_1 relaxation experienced by the hp ^{83}Kr in contact with untreated glass surfaces. The signal intensity from the two other tubes, however, has either decayed substantially (1 cigarette) or is not observed in the image at all above the level of the noise (3 cigarettes). The rapid decay in ^{83}Kr polarization seen in the tube exposed to

the smoke of three cigarettes displays the strong sensitivity of hp ^{83}Kr longitudinal relaxation to the more heavily "smoked" surfaces.

Because of the limited nonequilibrium ^{83}Kr nuclear spin polarization that can currently be generated, reasonable signal-to-noise ratios can be achieved only if the imaging sequence comprises a limited number of RF excitations. However, substantial signal intensity gains are expected in the near future using a combination of isotopic enrichment, better gas deliver systems [14], improved pump cell designs [37], higher laser power [14, 38], and line-narrowed laser sources [39, 40]. Together these improvements will lead to additional signal enhancements of an order of magnitude or more and allow for FLASH sequences with a higher number of excitations.

Unfortunately, increasing the number of phase-encoding steps may introduce an additional complication in T_1 weighted hp ^{83}Kr FLASH imaging. In the time required to apply one hundred or more pulses with pulse delays of milliseconds or tens of milliseconds, T_1 relaxation could occur during the image acquisition. Such polarization losses during image acquisition are known to introduce experimental artifacts [28]. If the sample being imaged possesses T_1 homogeneity, these losses can be accounted for by appropriately altering the pulse lengths in a variable flip angle pulse sequence. This trivial correction cannot be made if the sample possesses T_1 inhomogeneity or if the T_1 time is unknown. In this work, we have attempted to approximate an upper limit of these future difficulties by intentionally selecting a 0.1 s time delay between RF pulses resulting in total image acquisition times of 3.5 s.

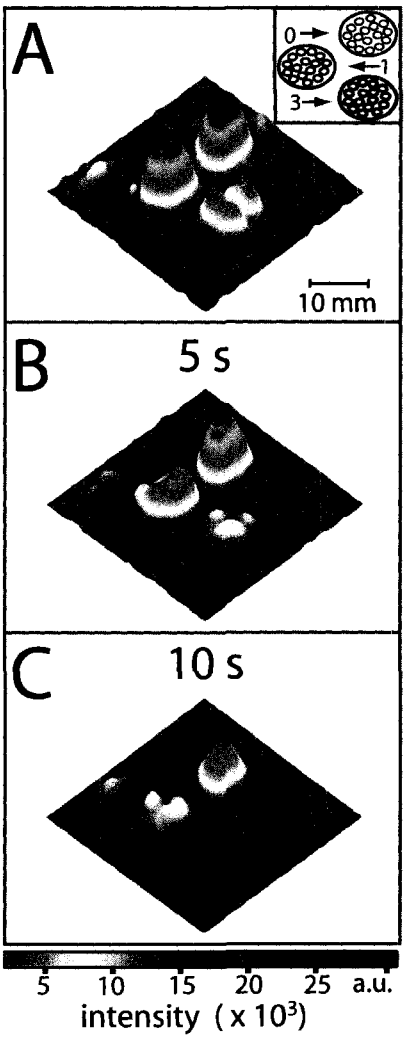

Figure 6.4: T_1 weighted hp ^{83}Kr MR FLASH images. Each image was produced from a single, variable angle FLASH sequence. In these images, internal structure is not observed due to the lower signal-to-noise ratio compared to that of Fig. 6.3B. The scale at the bottom of the figure indicates the signal intensity in arbitrary units. **(A)** Image acquired immediately after stopped-flow transfer of the hp ^{83}Kr. The inset in the top right is a sketch of the phantom used to produce the images. The labels 1-3 indicate the number of cigarettes combusted to supply smoke to a given tube. The image scale is indicated in the lower right. **(B)** Image acquired 5 s after hp ^{83}Kr transfer. **(C)** Image acquired 10 s after hp ^{83}Kr transfer.

6.4 Conclusions

The T_1 relaxation of hyperpolarized ^{83}Kr was found to accelerate by at least a factor of twenty in the presence of tobacco smoke deposits on glass surfaces. The T_1 differences were sufficient to produce meaningful T_1 contrast in hp ^{83}Kr MR images of model samples with different levels of smoke deposition. The experimental evidence presented in this work strongly supports the hypothesis that the contrast was caused by quadrupolar relaxation during brief surface adsorption periods of the krypton atoms and can therefore not be observed in MRI using the spin $I = 1/2$ noble gas isotopes ^{129}Xe or ^{3}He. An accelerated ^{83}Kr T_1 relaxation was also found when surfaces coated with a pulmonary lung surfactant extract were exposed to tobacco smoke suggesting that the ^{83}Kr specific contrast may potentially be obtained *in vivo* and enhance the current understanding of the pathology of smoking related respiratory diseases. Of course other factors such as the bronchopulmonary inflammation that commonly occurs in smokers may also play a role in future *in vivo* work. Comparisons with ^{129}Xe T_1 data indicate that the observed acceleration was not due to the presence of paramagnetic species in the deposited cigarette smoke. It is also concluded that cigarette smoke is unlikely to directly produce useful longitudinal relaxation contrast in *in vivo* hp ^{129}Xe MRI of airways.

References:

1. Viegi, G.; Scognamiglio, A.; Baldacci, S.; Pistelli, F.; Carrozzi, L., Epidemiology of Chronic Obstructive Pulmonary Disease (COPD). *Respiration* **2001,** 68, (1), 4-19.

2. Hecht, S. S., Tobacco carcinogens, their biomarkers and tobacco-induced cancer. *Nature Reviews Cancer* **2003,** 3, (10), 733-744.

3. Ambrose, J. A.; Barua, R. S., The pathophysiology of cigarette C-V smoking and cardiovascular disease - An update. *Journal of the American College of Cardiology* **2004,** 43, (10), 1731-1737.

4. Wynder, E. L.; Muscat, J. E., The changing epidemiology of smoking and lung cancer histology. *Environmental Health Perspectives* **1995,** 103, 143-148.

5. Janssen-Heijnen, M. L. G.; Coebergh, J. W. W., The changing epidemiology of lung cancer in Europe. *Lung Cancer* **2003,** 41, (3), 245-258.

6. Bernstein, D. M., A review of the influence of particle size, puff volume, and inhalation pattern on the deposition of cigarette smoke particles in the respiratory tract. *Inhalation Toxicology* **2004,** 16, (10), 675-689.

7. Baker, R. R.; Dixon, M., The retention of tobacco smoke constituents in the human respiratory tract. *Inhalation Toxicology* **2006,** 18, (4), 255-294.

8. Minard, K. R.; Einstein, D. R.; Jacob, R. E.; Kabilan, S.; Kuprat, A. P.; Timchalk, C. A.; Trease, L. L.; Corley, R. A., Application of magnetic resonance (MR) imaging for the development and validation of computational fluid dynamic (CFD) models of the rat respiratory system. *Inhalation Toxicology* **2006,** 18, (10), 787-794.

9. Morawska, L.; Hofmann, W.; Hitchins-Loveday, J.; Swanson, C.; Mengersen, K., Experimental study of the deposition of combustion aerosols in the human respiratory tract. *Journal of Aerosol Science* **2005,** 36, (8), 939-957.

10. Nazaroff, W. W.; Hung, W. Y.; Sasse, A. G. B. M.; Gadgil, A. J., Predicting Regional Lung Deposition of Environmental Tobacco-Smoke Particles. *Aerosol Science and Technology* **1993,** 19, (3), 243-254.

11. Yeh, H. C.; Schum, G. M., Models of Human-Lung Airways and Their Application to Inhaled Particle Deposition. *Bulletin of Mathematical Biology* **1980,** 42, (3), 461-480.

12. Pavlovskaya, G. E.; Cleveland, Z. I.; Stupic, K. F.; Meersmann, T., Hyperpolarized Krypton-83 as a New Contrast Agent for Magnetic Resonance Imaging. *Proceedings of the National Academy of Sciences of the United States of America* **2005,** 102, 18275-18279.

13. Stupic, K. F.; Cleveland, Z. I.; Pavlovskaya, G. E.; Meersmann, T., Quadrupolar Relaxation of Hyperpolarized Krypton-83 as a Probe for Surfaces. *Solid State Nuclear Magnetic Resonance* **2006,** 29, 79-84.

14. Cleveland, Z. I.; Pavlovskaya, G. E.; Stupic, K. F.; LeNoir, C. F.; Meersmann, T., Exploring hyperpolarized 83Kr by remotely detected NMR relaxometry. *Journal of Chemical Physics* **2006,** 124, 044312.

15. Cleveland, Z. I.; Stupic, K. F.; Pavlovskaya, G. E.; Repine, J. E.; Wooten, J. B.; Meersmann, T., Hyperpolarized ^{83}Kr and ^{129}Xe NMR Relaxation Measurements of Hydrated Surfaces: Implications for Materials Science and Pulmonary Diagnostics. *Journal of the American Chemical Society* **2007,** 129, (6), 1784-1792.

16. Walker, T. G.; Happer, W., Spin-exchange optical pumping of noble-gas nuclei. *Review of Modern Physics* **1997,** 69, (2), 629-642.

17. Goodson, B. M., Nuclear magnetic resonance of laser-polarized noble gases in molecules, materials, and organisms. *Journal of Magnetic Resonance* **2002,** 155, (2), 157-216.

18. Raftery, D., Xenon NMR Spectroscopy. *Annual Reports on NMR Spectroscopy* **2006,** 57, 205-271.

19. van Beek, E. J. R.; Wild, J. M.; Kauczor, H. U.; Schreiber, W.; Mugler, J. P.; de Lange, E. E., Functional MRI of the lung using hyperpolarized 3-helium gas. *Journal of Magnetic Resonance Imaging* **2004,** 20, (4), 540-554.

20. Kadlecek, S. J.; Emami, K.; Fischer, M. C.; Ishii, M.; Yu, J. S.; Woodburn, J. M.; NikKhah, M.; Vahdat, V.; Lipson, D. A.; Baumgardner, J. E.; Rizi, R. R., Imaging physiological parameters with hyperpolarized gas MRI. *Progress in Nuclear Magnetic Resonance Spectroscopy* **2005,** 47, (3-4), 187-212.

21. Conradi, M. S.; Saam, B. T.; Yablonskiy, D. A.; Woods, J. C., Hyperpolarized He-3 and perfluorocarbon gas diffusion MRI of lungs. *Progress in Nuclear Magnetic Resonance Spectroscopy* **2006,** 48, (1), 63-83.

22. Ruppert, K.; Brookeman, J. R.; Hagspiel, K. D.; Mugler, J. P., Probing lung physiology with xenon polarization transfer contrast (XTC). *Magnetic Resonance in Medicine* **2000,** 44, (3), 349-357.

23. Ruppert, K.; Mata, J. F.; Brookeman, J. R.; Hagspiel, K. D.; Mugler, J. P., Exploring lung function with hyperpolarized Xe-129 nuclear magnetic resonance. *Magnetic Resonance in Medicine* **2004,** 51, (4), 676-687.

24. Driehuys, B.; Cofer, G. P.; Pollaro, J.; Mackel, J. B.; Hedlund, L. W.; Johnson, G. A., Imaging alveolar-capillary gas transfer using hyperpolarized Xe-129 MRI. *Proceedings of the National Academy of Sciences of the United States of America* **2006,** 103, (48), 18278-18283.

25. Mortuza, M. G.; Anala, S.; Pavlovskaya, G. E.; Dieken, T. J.; Meersmann, T., Spin-exchange optical pumping of high-density xenon-129. *Journal of Chemical Physics* **2003,** 118, (4), 1581-1584.

26. Chen, P. X.; Moldoveanu, S. C., Mainstream Smoke Chemical Analyses for 2R4F Kentucky Reference Cigarette. *Beiträge zur Tabakforschung* **2003,** 20, (7), 448-458.

27. Haase, A.; Frahm, J.; Matthaei, D.; Hanicke, W.; Merboldt, K. D., Flash Imaging - Rapid Nmr Imaging Using Low Flip-Angle Pulses. *Journal of Magnetic Resonance* **1986,** 67, (2), 258-266.

28. Zhao, L.; Mulkern, R.; Tseng, C. H.; Williamson, D.; Patz, S.; Kraft, R.; Walsworth, R. L.; Jolesz, F. A.; Albert, M. S., Gradient-echo imaging considerations for hyperpolarized Xe-129 MR. *Journal of Magnetic Resonance Series B* **1996,** 113, (2), 179-183.

29. Abragam, A., *The Principles of Nuclear Magnetism.* Oxford University Press: Oxford, UK, 1961.

30. Horton-Garcia, C. F.; Pavlovskaya, G. E.; Meersmann, T., Introducing krypton NMR spectroscopy as a probe of void space in solids. *Journal of the American Chemical Society* **2005,** 127, (6), 1958-1962.

31. Butscher, R.; Wäckerle, G.; Mehring, M., Nuclear quadrupole interaction of highly polarized gas phase 131Xe with a glass surface. *Journal of Chemical Physics* **1994,** 100, (9), 6923-6933.

32. Butscher, R.; Wäckerle, G.; Mehring, M., Nuclear quadrupole surface interaction of gas phase 83Kr: comparison with 131 Xe. *Chemical Physics Letters* **1996,** 249, 444-450.

33. Hoffmann, D.; Hoffmann, I.; El-Bayoumy, K., The less harmful cigarette: A controversial issue. A tribute to Ernst L. Wynder. *Chemical Research in Toxicology* **2001,** 14, (7), 767-790.

34. Pryor, W. A.; Hales, B. J.; Premovic, P. I.; Church, D. F., The Radicals in Cigarette Tar - Their Nature and Suggested Physiological Implications. *Science* **1983,** 220, (4595), 425-427.

35. Wooten, J. B.; Chouchane, S.; McGrath, T. E., Tobacco Smoke Constituents Affecting Oxidative Stress. In *Cigarette Smoke and Oxidative Stress*, Halliwell, B. B.; Poulsen, H. E., Eds. Springer Verlag: Berlin, 2006; pp 5-46.

36. Moller, H. E.; Chen, X. J.; Saam, B.; Hagspiel, K. D.; Johnson, G. A.; Altes, T. A.; de Lange, E. E.; Kauczor, H. U., MRI of the lungs using hyperpolarized noble gases. *Magnetic Resonance in Medicine* **2002,** 47, (6), 1029-1051.

37. Ruset, I. C.; Ketel, S.; Hersman, F. W., Optical pumping system design for large production of hyperpolarized Xe-129. *Physical Review Letters* **2006,** 96, (5), 053002.

38. Zook, A. L.; Adhyaru, B. B.; Bowers, C. R., High capacity production of > 65% spin polarized xenon-129 for NMR spectroscopy and imaging. *Journal of Magnetic Resonance* **2002,** 159, (2), 175-182.

39. Zerger, J. N.; Lim, M. J.; Coulter, K. P.; Chupp, T. E., Polarization of Xe-129 with high power external-cavity laser diode arrays. *Applied Physics Letters* **2000,** 76, (14), 1798-1800.

40. Mair, R. W.; Barlow, M. J.; Rosen, M. S.; Walsworth, R. L., Improved noble gas polarization production for porous and granular media studies using narrowed-line VBG laser sources. *Journal of Magnetic Resonance* **2007,** 25, (4), 549

CHAPTER 7

HYPERPOLARIZED KRYPTON-83 MAGNETIC RESONANCE IMAGING OF LUNGS

The results presented in this chapter have been submitted for publication as the journal article: Zackary I. Cleveland, Galina E. Pavlovskaya, Nancy D. Elkins, Karl F. Stupic, John E. Repine, and Thomas Meersmann, "Hyperpolarized ^{83}Kr MRI of Lungs" to *Journal of Magnetic Resonance* (accepted 2008).

Zackary I. Cleveland and Thomas Meersmann wrote the paper mentioned above. Karl F. Stupic assisted in conducting the imaging experiments and the relaxation measurements. John E. Repine provided the lungs using the work and edited the manuscript. Nancy D. Elkins performed the lung excision and prepared the lungs for experiments. Zackary I. Cleveland produced the hp ^{83}Kr, participated in the design of the experiments and built the experimental setup. Galina E. Pavlovskaya performed the MR imaging and processed the image data.

7.1 Introduction

Hyperpolarized (hp) noble gases [1, 2] display dramatically increased signal intensities in nuclear magnetic resonance (NMR) spectroscopy and magnetic resonance imaging (MRI) enabling a wide range of novel applications [3-5]. Biomedical interest in hp gases began in the mid-1990's with proof-of-principle reports of hp ^{129}Xe [6] and hp ^{3}He [7] lung MRI. Hp ^{3}He has proven particularly valuable for studying lung ventilation distribution [8], alveolar size [9, 10], and O_2 partial pressure [11]. Recently, pulmonary ^{3}He MRI was also demonstrated in very weak magnetic fields that produced ^{3}He resonance frequencies of around 200 kHz [12]. Hp ^{129}Xe yields lower signal intensities than hp ^{3}He, but through its high tissue solubility and 300 ppm chemical shift range [3] provides additional information about structure and gas dynamics in lungs [13-15], displays tissue specific chemical shifts [16] and, in conjunction with functionalized xenon biosensors, can be used for molecular imaging [17, 18].

However, neither hp ^{3}He, hp ^{129}Xe, nor alternative techniques using thermally polarized fluorinated gas species [19, 20] can deliver information about lung surface chemistry, which is intimately linked to certain lung diseases. For instance, acute lung injury (ALI), including its most severe form acute respiratory distress syndrome (ARDS) [21], is characterized by changes in the lipid and protein composition of the pulmonary surfactant system. Additionally, disease inducing aerosols such as tobacco smoke and mineral dusts can both transiently and chronically alter the lung surface chemistry [22, 23]. Thus, there is a pressing need to develop non-invasive, spatially resolved techniques that provide information about pulmonary surface chemistry.

Recently, the development of hp ^{83}Kr NMR and MRI was reported [24, 25]. Like ^{129}Xe and ^{3}He (both nuclear spin I =1/2), ^{83}Kr (I = 9/2) can be hyperpolarized by spin exchange optical pumping (SEOP) [26, 27], and its relatively long gas-phase T_1 [28] allows the gas to be separated from the reactive alkali metal vapor without extensive depolarization [24]. Unlike hp ^{129}Xe or hp ^{3}He, hp ^{83}Kr provides MRI contrast that is highly sensitive to a number of surface properties including surface-to-volume ratio [29], surface chemistry [29, 30], surface hydration [31], and surface temperature [24] even in relatively low surface-to-volume ratio environments. This sensitivity is caused by quadrupolar interactions that strongly influence the longitudinal relaxation rate when krypton is in contact with surfaces.

For instance, the T_1 of hp ^{83}Kr was shown to increase by up to a factor of twenty if tobacco smoke condensate, which contains numerous hydrophobic constituents [22], was deposited on model surfaces [30]. These large relaxational differences enabled T_1 contrast weighted FLASH MR imaging that provided spatially resolved information about both the location and amount of tobacco smoke deposited on surfaces. The sensitivity hp ^{83}Kr displays to surface-to-volume ratio within porous materials may also be of diagnostic value. Increased alveolar size due to both natural aging [10] and chronic obstructive pulmonary disease (COPD) progression [20] has been observed using hp ^{3}He apparent diffusion coefficient (ADC) measurements, while other disorders, such as ALI, are associated with alveolar collapse and thus increased surface-to-volume ratios.

Although hp ^{83}Kr has been explored as a surface sensitive contrast agent in model systems (See Chapters 3 and 6.), the feasibility of hp ^{83}Kr lung MRI must still be demonstrated. Fast T_1 relaxation during inhalation and when inside the alveolar regions could potentially depolarize hp ^{83}Kr to unobservable levels. Previous studies with

desiccated canine lung tissue showed promising T_1 times of about 10 s [25], but the surface chemistry and microscopic surface morphology found *in vivo* will be substantially different than those of desiccated tissue. Also, these earlier experiments were performed by rapidly shuttling hp ^{83}Kr into a pre-evacuated sample to reduce T_1 relaxation during transfer, but this technique is obviously unsuitable for *in vivo* work or *ex vivo* studies of intact lungs. In this chapter, we report the first hp ^{83}Kr NMR spectra, T_1 data, and hp ^{83}Kr MRI from freshly excised, but otherwise intact, rat lungs obtained with natural abundance krypton gas (11.5% ^{83}Kr) using a novel device for ventilating excised lungs. Additionally, a discussion of the maximum future improvements to the hp ^{83}Kr signal intensity is presented.

7.2 Materials and Methods

7.2.1 NMR Spectroscopy and MR Imaging

Experiments were performed on a Chemagnetics CMX II 400 MHz NMR spectrometer in a 9.4 T, wide-bore (89 mm) superconducting magnet equipped with an imaging system (Resonance Research, Billerica, MA) consisting of triple axis gradient coils (100 G/cm x,y axes and 720 G/cm z axis) and low-noise linear gradient amplifiers. Spectra and images were obtained using a custom-built probe tuned to the 15.4 MHz ^{83}Kr frequency. A 10-15 min SEOP period was applied between consecutive hp gas deliveries to replenish the nonequilibrium ^{83}Kr polarization. T_1 values were calculated by nonlinear least squares fitting of the hp ^{83}Kr signal as a function of time and number 24° RF pulses (See Chapter 4.). The image was produced from a series of 16 traces acquired using a nonselective, gradient–echo sequence with phase encoding gradients incremented in each

hp gas delivery. To reconstruct the image, acquisition matrices were zero filled to 32 points in both dimensions and apodized using a sine bell squared function before Fourier transformation in each dimension. Image processing was performed in MATLAB R2006a (Version 14.2; Math-works, Natick, MA).

7.2.2 Spin Exchange Optical Pumping

^{83}Kr SEOP was performed in untreated, cylindrical Pyrex cells (length = 125 mm, ID = 24 mm). The krypton mixture was produced from research grade gases (Airgas, Radnor, PA) and contained 25% krypton (natural abundance, 99.995% pure), 5% N_2 (99.9997% pure), and 70% helium (99.9999% pure). Pump cells containing ~1 g of rubidium (99.75%; Alfa Aesar, Ward Hill, MA) were housed in a quartz and aluminum oven to maintain even heating (438 ± 5 K) and maintained above ambient pressure (~120 kPa) to avoid atmospheric contamination. Light (794.7 nm) from two 30 W Coherent FAP diode-array lasers (line width ~2 nm) was directed via fiber optic coupling cables through a circular polarizer onto the pump cell. SEOP occurred in the fringe field of the superconducting magnet at approximately 0.05 T. Rubidium vapor was separated from the hp gas mixtures by an air-cooled trap at the outlet of the pump cell.

7.2.3 Animal Care and Usage

The Institutional Animal Care and Use Committee of the University of Colorado at Denver and Health Sciences Center approved the protocol used in this work. Seven healthy, male Sprague-Dawley rats (Charles River Laboratories, Inc., Wilmington, MA) were acclimated to altitude (~1600 m) for at least 14 days while being fed a normal diet

and weighed 193-266 g at the time of lung excision. The rats were anesthetized with ketamine (80 mg/kg) and xylazine (16mg/kg) (MWT Veterinary Supply) delivered intraperitoneally. The trachea was clamped at time of inhalation to avoid collapsing the airways while removing the heart and lungs from chest cavity. The right ventricle was injected with 100 USP units heparin (American Pharmaceutical Partners, Inc., Schaumburg, IL) and allowed to circulate for 10-15 s before the heart and lungs were excised. The trachea was then cannulated with an indwelling 16-gauge stub adapter tube positioned 5 mm above the bifurcation of the lungs.

7.2.4 Lung Ventilation

Following excision, the lungs were placed in a Pyrex ventilation chamber (ID = 24 mm and height = 100 mm; See Fig. 7.1A) and immersed in isotonic saline solution (0.9% NaCl, pH 5.5; Baxter Heathcare Corporation, Deerfield, IL). The lungs were then inflated with 4-5 ml of air and transported at 277 K to the imaging facility. To prevent flooding of the airways and hp ^{83}Kr from escaping before entering the lung, the trachea was tightly sutured to the stub adapter tube affixed to the bottom of the inflation chamber. Upon inflation, experiments were performed only if no gas bubbling was observed either at the location of the sutures or from the lungs themselves indicating that the gas entered and remained within the lungs. Consequently, three of the seven sets of lungs were not used for experiments.

Hp ^{83}Kr needed to reach the lungs quickly enough to avoid substantial T_1 relaxation during transfer while maintaining at most a slight overpressure to prevent lung damage. Therefore, the hp ^{83}Kr was transferred (See Fig. 7.1B.) by pressure equalization

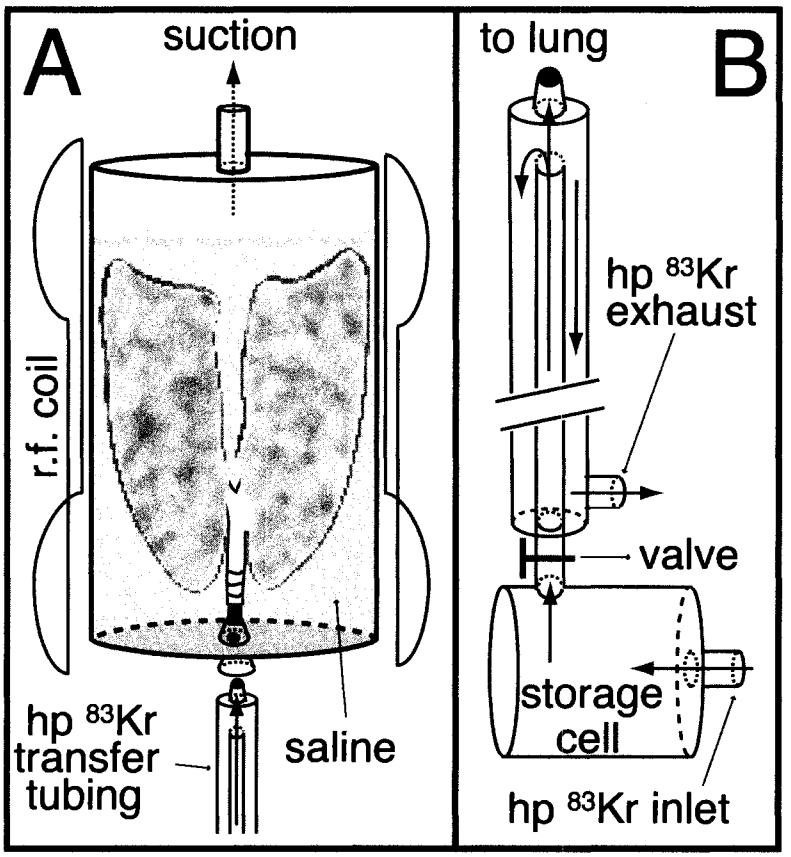

Figure 7.1: Apparatus for delivering hp ^{83}Kr to lungs. The thick, solid arrows indicate the direction of hp ^{83}Kr flow. **(A)** *Ex vivo* lung ventilation chamber. The lungs were inverted (trachea pointing down) and completely immersed in a physiological saline solution. The lungs were then inflated with 6 ml of hp gas mixture by applying a slight suction and deflated by applying slight overpressure. Hp ^{83}Kr flowed past the entrance to the lungs and was pulled into the lungs during inflation. **(B)** Hp ^{83}Kr transfer system. The storage cell was evacuated to less than 10 Pa, and hp ^{83}Kr was transferred from the SEOP cell by pressure equalization (final pressure ~110 kPa). The valve was then opened, and gas flowed from the storage cell, through the inner tube, and past the entrance to the lung. Hp ^{83}Kr was either pulled into the lung during inflation or flowed through the outer tube to the ambient air.

from the SEOP cell to a pre-evacuated (pressure <10 Pa) Pyrex storage cell (length = 80 mm, ID = 24 mm). After the pressure equalized, the valve separating the storage cell from the Pyrex transfer tubing was opened, and the hp gas flowed from the storage cell through the inner tube (ID = 2 mm) and past the entrance of the lung. The lungs were inflated by applying a slight suction above the saline solution and deflated by applying a slight overpressure. In doing so, the lungs were ventilated with 6 ml of hp gas, as monitored by saline solution displacement. Prior to experiments, the lungs were repeatedly ventilated with nitrogen gas to remove residual air.

7.3 Results and Discussion

7.3.1 NMR Spectroscopy and MR Imaging of Lungs

Fig. 7.2A displays a representative hp ^{83}Kr NMR spectrum from excised rat lungs following a 90° RF pulse. The hp ^{83}Kr signal previously obtained from the 25% krypton mixture used in this work was enhanced 4500 times over that of thermally polarized krypton at 9.4 T corresponding to a spin polarization of about 1% [31]. However, this intensity was only observed by vacuum shuttling hp ^{83}Kr into the detection region. The signal enhancement from lungs in the current work was probably reduced about 50% by relaxation during the relatively slow hp gas transfer from the pump cell [31] and further reduced during the brief (~1 s) residence time in the lung prior to the application of RF pulses. Despite polarization losses, the spectra displayed acceptable signal-to-noise ratios of 50 to 60 depending on SEOP efficiency and possibly individual-to-individual differences in the lungs.

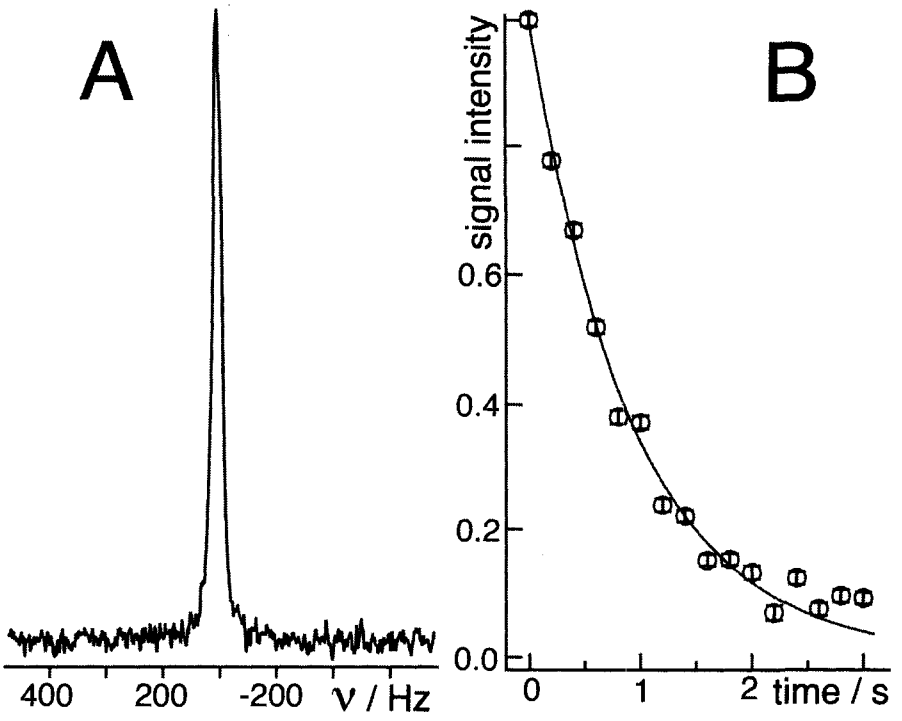

Figure 7.2: Hp ^{83}Kr NMR spectroscopy. **(A)** Typical hp ^{83}Kr spectrum from excised rat lungs at 9.4 T. **(B)** T_1 decay curve of hp ^{83}K in rat lungs. Data points are signal intensities of the hp ^{83}Kr spectra obtained from a series of 24° RF pulses normalized to the signal intensity resulting from the first pulse. The error bars are the standard deviations in the baseline noise.

To qualitatively assess if hp ^{83}Kr reached beyond the finer airways and into the alveoli without depolarization, the signal from the lungs was compared to that arising from 6 ml of hp krypton mixture in a balloon with no internal structure that had been inflated using the same ventilation system. The ^{83}Kr T_1 inside the balloon exceeded 40 s when fully inflated, so the signal intensity was not substantially affected by relaxation. The signals from the lungs were found to be around 30-50% of that observed from the inflated balloon. These intensities are substantially greater than would be expected from ^{83}Kr confined to the anatomical dead space (i.e. the volume of the conducting airways) alone, which typically constitutes less than 5% of the total lung volume [32, 33]. Therefore, a substantial fraction of ^{83}Kr lung signal intensity must have originated from the alveolar region.

Fig. 7.3 shows an MR image (x,y projection with no slice selection) of hp ^{83}Kr in an excised rat lung with 2.3 × 2.3 mm image resolution (raw data) that was obtained from 16 single acquisitions with incremented gradients. The dashed, white line surrounding the image indicates the location of the inner wall of the ventilation chamber. Several morphological features are readily observed in the image. The separation between the right and left lung is easily seen, as is a dark area between these two high signal intensity regions. This dark region corresponds to the location of the heart, which contained no hp ^{83}Kr. When the lungs were inflated to 6 ml outside the superconducting magnet, the sides of the lung were observed to touch the inner inflation chamber wall. From the image, it is clear that substantial signal intensity extends to the chamber wall and was not merely confined to the major airways.

7.3.2 Longitudinal Relaxation in Lungs

Fig. 7.2B shows a typical hp ^{83}Kr T_1 decay curve in an excised rat lung. The data points are hp ^{83}Kr signal intensities obtained from a series of 24° RF pulses. These relatively long pulses were necessitated by the modest hp ^{83}Kr signal intensity and were found to be a reasonable compromise between obtaining acceptable signal-to-noise ratios and maintaining nonequilibrium polarization long enough to adequately observe T_1 decay. The T_1 values were typically several seconds and were reproducible for a given lung for several hours after excision, but a T_1 range 0.7 to 3.7 s was observed in various lungs (See Table 7.1.). T_1 times of this length are promising and should allow *in vivo* hp ^{83}Kr MRI in rats, which breath 1-5 times per second.

Table 7.1: T_1 data from individual rats [a].

Mass of Rats [b] (g)	Hp ^{83}Kr T_1 (s) [c]
245	3.74 ± 0.41
	3.66 ± 0.39
210	2.43 ± 0.13
	2.33 ± 0.20
210	1.55 ± 0.11
193	0.67 ± 0.04
	0.64 ± 0.01
	0.65 ± 0.01

[a] Three lungs were not used for experiments because of damage during transport.
[b] Mass of rat prior to lung excision.
[c] Errors are ± one standard deviation in the residuals resulting from the fit.

Due to of the small gyro-magnetic ratio of ^{83}Kr (4% of ^{1}H) compared to ^{3}He (76% of ^{1}H) and ^{129}Xe (28% of ^{1}H), the presence of 20% O_2 was previously found to reduce the ^{83}Kr T_1 time in desiccated canine lung tissue by only 18% from 10.5 s to 8.6 s [25]. In

comparison, the ^{3}He T_1 time is reduced from hundreds of hours in the absence of paramagnetic species [34, 35] to 10-20 s in lungs containing a breathable oxygen mixture [36]. The T_1 of ^{83}Kr was also shown to be much less affected by paramagnetic surface impurities than that of ^{129}Xe [30, 31]. Thus paramagnetic species in the lung will be unlikely to prevent surface sensitive T_1 contrast in hp ^{83}Kr MRI. Additionally, the T_1 time of hp ^{83}Kr has been shown to increase with increasing surface temperatures [24] suggesting that physiologically relevant temperatures will result in slower relaxation. Longer T_1 times are also to be expected in larger animals due to larger alveoli that presumably lead to decreased surface-to-volume ratios. For instance, the average alveolar diameter is about 225 μm in adult human lungs but only 94 μm and 58 μm in rats and mice respectively [37].

7.3.3 Signal-to-Noise in Lungs

Like early hp ^{129}Xe lung MRI [6], hp ^{83}Kr MRI will require significant improvements in signal intensity to be biomedically useful. However, isotopically enriched krypton mixtures have yet to be exploited and would immediately improve the observed signal-to-noise ratio by nearly an order of magnitude. Even larger enhancements may be gained from improved ^{83}Kr SEOP that currently generates only about 0.3% spin polarization in a mixture of 95% krypton and 5% nitrogen. Although a higher spin polarization was obtained with more dilute krypton mixtures (i.e. ~1% polarization with 25% krypton mixtures), improved signal intensity was not achieved because no method currently exists to concentrate hp krypton without depolarization.

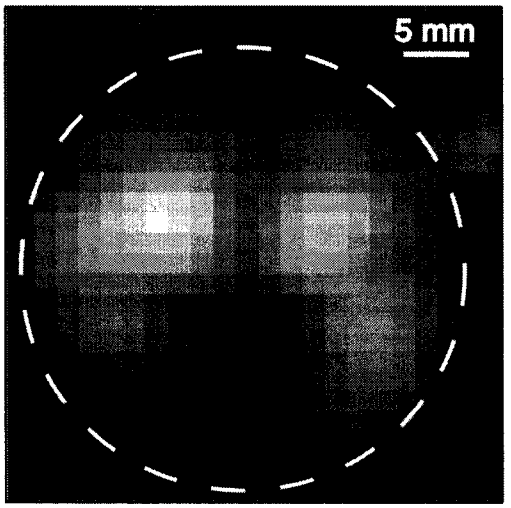

Figure 7.3: *Ex vivo* hp ^{83}Kr MR image of a rat lung. The image was reconstructed from 16 individual SEOP/gas delivery cycles. Each phase encoding step in the x,y lung image was acquired from a single hp ^{83}Kr delivery using no slice selection and resulted in 2.3 × 2.3 mm resolution (raw data). The image scale is displayed in the upper right hand corner, and the white, dashed ring indicates the location of the inner wall of the ventilation chamber.

However, improvement in gas delivery methods [38], better pump cell designs [39], higher laser powers [40], and line-narrowed laser sources [41] have vastly increased the hp ^{3}He and ^{129}Xe NMR signal intensities and production rates. Similar improvements should also advance work with hp ^{83}Kr, and, together with isotopic enrichment, lead to signal enhancements high enough for *in vivo* applications, at least for small animal studies. Assuming SEOP sufficiently overcomes the poor sensitivity arising from the small ^{83}Kr gyromagnetic ratio, the associated low resonance frequency (i.e. 15.4 MHz at 9.4 T) will be advantageous due to reduced inductive losses [42].

7.3.4 Hyperpolarization in Spin $I > 1/2$ Nuclei

Fully assessing the feasibility of hp ^{83}Kr lung MR requires a discussion of the fundamental limits to hyperpolarization. For the general case of spin $I \geq 1/2$ nuclei with a Boltzmann population distribution, it is possible to define a spin polarization, P, as

$$P = \frac{\gamma}{|\gamma|} \frac{\sum_{m=-I}^{m=(I-1)} \left(e^{-(m+1)\gamma\hbar B_0 / k_B T} - e^{-m\gamma\hbar B_0 / k_B T} \right)}{\sum_{m=-I}^{I} e^{-\gamma m\hbar B_0 / k_B T}}, \tag{7.3.1}$$

where $m = -I, -I+1, ..., I-1, I$ is the z-quantization number of spin I, B_0 is magnetic field strength, γ is the gyromagnetic ratio of the nucleus, and $\gamma/|\gamma|$ accommodates the sign of γ. All of the population terms other than those of the highest and lowest energy states cancel, and Eq. 7.3.1 simplifies to

$$P = \frac{\gamma}{|\gamma|} \frac{e^{m\gamma\hbar B_0 / k_B T} - e^{-\gamma m\hbar B_0 / k_B T}}{\sum_{m=-I}^{I} e^{-\gamma m\hbar B_0 / k_B T}}. \tag{7.3.2}$$

For the thermal equilibrium at high temperatures (i.e. $T >> |\gamma|\hbar B_0 / k_B$), Eq. 7.3.2 further simplifies to

$$P = \frac{2I}{2I+1}\frac{|\gamma|\hbar B_0}{k_B T} \tag{7.3.3}$$

in general, which leads to the familiar

$$P = \frac{|\gamma|\hbar B_0}{2k_B T} \tag{7.3.4}$$

for spin I = 1/2 systems. For spin I > 1/2 systems, non-Boltzmann population distributions are in principle possible, but the thermal equilibrium (Boltzmann) polarization, P_{tp}, can be calculated through Eq. 7.3.2 at any temperature or Eq. 7.3.3 at high T. The hyperpolarization, P_{hp}, can be related to P_{tp} by defining an enhancement factor,

$$f_{hp}^{B_0,T} = S_{hp}^{B_0} / S_{tp}^{B_0,T}, \tag{7.3.5}$$

where $S_{hp}^{B_0}$ is the hp signal measured at the magnetic field B_0 and $S_{tp}^{B_0}$ is the thermally polarized signal obtained at the same magnetic field and at a temperature T. Defining

$$P_{hp} = P_{tp}^{B_0,T} \cdot f_{hp}^{B_0,T}, \tag{7.3.6}$$

the previously observed hp ^{83}Kr enhancement of 1200 over the thermal signal obtained for 95% krypton mixtures at 9.4 T and 300 K corresponds to $P_{hp}^{9.4T,300K}$ = 0.28%. Thus a further polarization improvement of more than 350 times is theoretically possible.

However, the concept of polarization is problematic for hp spin I > 1/2 systems, which may not possess Boltzmann-like population distributions. For spin I > 1 systems, the use of P may also be misleading when discussing the maximum hp signal intensity

even if a nonequilibrium, but Boltzmann-like, population distribution is generated. For a general spin I system at any temperature, the signal intensity can be expressed as

$$S = A\frac{\gamma^3}{|\gamma|}B_0\frac{\sum_{m=-I}^{m=(I-1)} C_{I,m}^2\left(e^{-(m+1)\gamma\hbar B_0/k_BT} - e^{-m\gamma\hbar B_0/k_BT}\right)}{\sum_{m=-I}^{I} e^{-\gamma m\hbar B_0/k_BT}}. \tag{7.3.7}$$

where A is a constant containing all contributions to the signal intensity other than γ, B_0, and the populations of the various quantum states. In Eq. 7.3.7, the transition matrix element $C_{I,m}^2$ is obtained from the expression

$$C_{I,m}^2 = \left|\langle I,m+1|\hat{I}_+|I,m\rangle\right|^2 \tag{7.3.8}$$

using the angular momentum raising

$$\hat{I}_+|I,m\rangle = \hbar\sqrt{I(I+1)-m(m+1)}|I,m\rangle. \tag{7.3.9}$$

In the high temperature limit to Eq. 7.3.3 simplifies

$$S = \frac{2}{3}\frac{A|\gamma^3|\hbar B_0{}^2}{k_BT}\cdot I(I+1), \tag{7.3.10}$$

Using Eq. 7.3.3 for the polarization at high temperatures, Eq. 7.3.7 can be rewritten as

$$S = A\gamma^2 B_0\frac{(2I+1)(I+1)}{3}P. \tag{7.3.11}$$

However, the relation $S \propto P$ of Eq. 7.3.11 fails at high P (i.e. low spin temperature). Thus, feasibility of hp ^{83}Kr lung MRI is better discussed in relation to the maximum possible thermal signal $S_{tp}^{B_0,T\to 0K}$ that would be observed at a given field strength and at 0 K. This signal maximum is given by

$$S_{tp}^{B_0,T\to 0K} = A\gamma^2 C_{I,m=-I}^2 = A\gamma^2 2I, \tag{7.3.12}$$

and the maximum enhancement factor becomes

$$f_{\max}^{B_0,T} = S_{tp}^{B_0,T\to 0K} / S_{tp}^{B_0,T}. \tag{7.3.13}$$

At high temperatures (i.e. $T >> |\gamma|\hbar B_0/k_B$), the maximum possible enhancement factor is

$$f_{\max}^{B_0,T} = \frac{3k_B T}{|\gamma|\hbar B_0(I+1)}, \tag{7.3.14}$$

and specifically for ^{83}Kr at 300 K and 9.4 T, the enhancement limit is $f_{\max}^{9.4T,300K} = 2.2\times 10^5$. Thus the 1200 fold ^{83}Kr signal enhancement obtained for 95% krypton mixtures can be further improved by ~180 times before the absolute maximum is reached. Unlike spin I = 1/2 systems, the signal enhancement factors for ^{83}Kr is not directly proportional to the maximum polarization. However, there is still significant room for improving the currently obtained hp ^{83}Kr signal used in this study. Note that for the simplest case of an I = 1/2 system, Eq. 7.3.13 reduced to $f_{\max}^{B_0,T} = P^{-1}$ at all temperatures and field strengths.

7.4 Conclusions

This work demonstrates that hp ^{83}Kr MRI of intact, excised lungs is possible with natural abundance krypton gas. An improvement of up to 180 times the currently obtained signal is theoretically possible, leaving significant room for improvements through the advancement of SEOP technology. An additional increase in the signal-to-noise ratio of almost an order of magnitude is possible using isotopically enriched krypton. The ^{83}Kr T_1 time found in lungs was up to several seconds and should be long enough for *in vivo* work with small animals. The ^{83}Kr T_1 relaxation is expected to be insensitive to the presence of paramagnetic species such as oxygen and therefore capable of providing surface sensitive

MRI contrast. Although no attempts have been made to observe a pathology specific contrast in lungs, the experiments presented here are a necessary step in developing hp ^{83}Kr NMR and MRI into useful biomedical tools. Although earlier work focused on the T_1 of hp ^{83}Kr, MRI contrast could also be obtained by exploiting T_2 as was done in work with thermally polarized ^{131}Xe (I = 3/2) in aerogels [43]. Additional sources of contrast with hp ^{83}Kr may be $T_{1\rho}$, quadrupolar evolution under spin-lock conditions [44, 45], and multiple quantum filtering [46-48].

References:

1. Walker, T. G.; Happer, W., Spin-exchange optical pumping of noble-gas nuclei. *Review of Modern Physics* **1997,** 69, (2), 629-642.

2. Gentile, T. R.; Jones, G. L.; Thompson, A. K.; Rizi, R. R.; Roberts, D. A.; Dimitrov, I. E.; Reddy, R.; Lipson, D. A.; Gefter, W.; Schnall, M. D.; Leigh, J. S., Demonstration of a compact compressor for application of metastability-exchange optical pumping of He-3 to human lung imaging. *Magnetic Resonance in Medicine* **2000,** 43, (2), 290-294.

3. Goodson, B. M., Nuclear magnetic resonance of laser-polarized noble gases in molecules, materials, and organisms. *Journal of Magnetic Resonance* **2002,** 155, (2), 157-216.

4. Cherubini, A.; Bifone, A., Hyperpolarised xenon in biology. *Progress in Nuclear Magnetic Resonance Spectroscopy* **2003,** 42, (1-2), 1-30.

5. van Beek, E. J. R.; Wild, J. M.; Kauczor, H. U.; Schreiber, W.; Mugler, J. P.; de Lange, E. E., Functional MRI of the lung using hyperpolarized 3-helium gas. *Journal of Magnetic Resonance Imaging* **2004,** 20, (4), 540-554.

6. Albert, M. S.; Cates, G. D.; Driehuys, B.; Happer, W.; Saam, B.; Springer, C. S.; Wishnia, A., Biological Magnetic-Resonance-Imaging Using Laser Polarized Xe-129. *Nature* **1994,** 370, (6486), 199-201.

7. Middlleton, H.; Black, R. D.; Saam, B.; G.D.Cates; Cofer, G. P.; Guenther, R.; Happer, W.; Hedlund, L. W.; Johnson, G. A.; Shattuck, M. D.; Schwartz, J. C., *Magnetic Resonance in Medicine* **1995,** 33, 271-275.

8. Spector, Z. Z.; Emami, K.; Fischer, M. C.; Zhu, J.; Ishii, M.; Yu, J.; Kadlecek, S.; Driehuys, B.; Panettieri, R. A.; Lipson, D. A.; Gefter, W.; Shrager, J.; Rizi, R. R., A small animal model of regional alveolar ventilation using (HPHe)-He-3 MRI. *Academic Radiology* **2004,** 11, (10), 1171-1179.

9. Woods, J. C.; Choong, C. K.; Yablonskiy, D. A.; Bentley, J.; Wong, J.; Pierce, J. A.; Cooper, J. D.; Macklem, P. T.; Conradi, M. S.; Hogg, J. C., Hyperpolarized He-3 diffusion MRI and histology in pulmonary emphysema. *Magnetic Resonance in Medicine* **2006,** 56, (6), 1293-1300.

10. Altes, T. A.; Mata, J.; de Lange, E. E.; Brookeman, J. R.; Mugler, J. P., Assessment of lung development using hyperpolarized helium-3 diffusion MR imaging. *Journal of Magnetic Resonance Imaging* **2006,** 24, (6), 1277-1283.

11. Fischer, M. C.; Kadlecek, S.; Yu, J. S.; Ishii, M.; Emami, K.; Vahdat, V.; Lipson, D. A.; Rizi, R. R., Measurements of regional alveolar oxygen pressure using hyperpolarized He-3 MRI. *Academic Radiology* **2005,** 12, (11), 1430-1439.

12. Mair, R. W.; Hrovat, M. I.; Patz, S.; Rosen, M. S.; Ruset, I. C.; Topulos, G. P.; Tsai, L. L.; Butler, J. P.; Hersman, F. W.; Walsworth, R. L., He-3 lung imaging in an open access, very-low-field human magnetic resonance imaging system. *Magnetic Resonance in Medicine* **2005,** 53, (4), 745-749.

13. Ruppert, K.; Brookeman, J. R.; Hagspiel, K. D.; Mugler, J. P., Probing lung physiology with xenon polarization transfer contrast (XTC). *Magnetic Resonance in Medicine* **2000,** 44, (3), 349-357.

14. Ruppert, K.; Mata, J. F.; Brookeman, J. R.; Hagspiel, K. D.; Mugler, J. P., Exploring lung function with hyperpolarized Xe-129 nuclear magnetic resonance. *Magnetic Resonance in Medicine* **2004,** 51, (4), 676-687.

15. Driehuys, B.; Cofer, G. P.; Pollaro, J.; Mackel, J. B.; Hedlund, L. W.; Johnson, G. A., Imaging alveolar-capillary gas transfer using hyperpolarized Xe-129 MRI. *Proceedings of the National Academy of Sciences of the United States of America* **2006,** 103, (48), 18278-18283.

16. Kershaw, J.; Nakamura, K.; Kondoh, Y.; Wakai, A.; Suzuki, N.; Kanno, I., Confirming the existence of five peaks in Xe-129 rat head spectra. *Magnetic Resonance in Medicine* **2007,** 57, (4), 791-797.

17. Hilty, C.; Lowery, T. J.; Wemmer, D. E.; Pines, A., Spectrally resolved magnetic resonance imaging of a xenon biosensor. *Angewandte Chemie-International Edition* **2006,** 45, (1), 70-73.

18. Schroder, L.; Lowery, T. J.; Hilty, C.; Wemmer, D. E.; Pines, A., Molecular imaging using a targeted magnetic resonance hyperpolarized biosensor. *Science* **2006,** 314, (5798), 446-449.

19. Kuethe, D. O.; Caprihan, A.; Fukushima, E.; Waggoner, R. A., Imaging lungs using inert fluorinated gases. *Magnetic Resonance in Medicine* **1998,** 39, (1), 85-88.

20. Jacob, R. E.; Chang, Y. V.; Choong, C. K.; Bierhals, A.; Hu, D. Z.; Zheng, J.; Yablonskiy, D. A.; Woods, J. C.; Gierada, D. S.; Conradi, M. S., F-19 MR imaging of ventilation and diffusion in excised lungs. *Magnetic Resonance in Medicine* **2005,** 54, (3), 577-585.

21. Repine, J. E., Scientific Perspectives on Adult Respiratory-Distress Syndrome. *Lancet* **1992,** 339, (8791), 466-469.

22. Baker, R. R.; Dixon, M., The retention of tobacco smoke constituents in the human respiratory tract. *Inhalation Toxicology* **2006,** 18, (4), 255-294.

23. Fubini, B.; Arean, C. O., Chemical aspects of the toxicity of inhaled mineral dusts. *Chemical Society Reviews* **1999,** 28, (6), 373-381.

24. Cleveland, Z. I.; Pavlovskaya, G. E.; Stupic, K. F.; LeNoir, C. F.; Meersmann, T., Exploring hyperpolarized 83Kr by remotely detected NMR relaxometry. *Journal of Chemical Physics* **2006,** 124, 044312.

25. Pavlovskaya, G. E.; Cleveland, Z. I.; Stupic, K. F.; Meersmann, T., Hyperpolarized Krypton-83 as a New Contrast Agent for Magnetic Resonance Imaging. *Proceedings of the National Academy of Sciences of the United States of America* **2005,** 102, 18275-18279.

26. Schaefer, S. R.; Cates, G. D.; Happer, W., Determination of Spin-Exchange Parameters between Optically Pumped Rubidium and Kr-83. *Physical Review A* **1990,** 41, (11), 6063-6070.

27. Butscher, R.; Wäckerle, G.; Mehring, M., Nuclear quadrupole surface interaction of gas phase 83Kr: comparison with 131 Xe. *Chemical Physics Letters* **1996,** 249, 444-450.

28. Brinkmann, D.; Kuhn, D., Nuclear Magnetic-Relaxation of Kr-83 in Krypton Gas. *Physical Review A* **1980,** 21, (1), 163-167.

29. Stupic, K. F.; Cleveland, Z. I.; Pavlovskaya, G. E.; Meersmann, T., Quadrupolar Relaxation of Hyperpolarized Krypton-83 as a Probe for Surfaces. *Solid State Nuclear Magnetic Resonance* **2006,** 29, 79-84.

30. Cleveland, Z. I.; Pavlovskaya, G. E.; Stupic, K. F.; Wooten, J. B.; Repine, J. E.; Meersmann, T., Detection of Tobacco Smoke Deposition by Hyperpolarized Krypton-83 MRI. *Magnetic Resonance Imaging* **2008,** 26, (270-278).

31. Cleveland, Z. I.; Stupic, K. F.; Pavlovskaya, G. E.; Repine, J. E.; Wooten, J. B.; Meersmann, T., Hyperpolarized ^{83}Kr and ^{129}Xe NMR Relaxation Measurements of Hydrated Surfaces: Implications for Materials Science and Pulmonary Diagnostics. *Journal of the American Chemical Society* **2007,** 129, (6), 1784-1792.

32. Fowler, W. S., Lung Function Studies.2. the Respiratory Dead Space. *Americam Journal of Physiology* **1948,** 154, (3), 405-416.

33. Heller, H.; Konen-Bergmann, M.; Schuster, K. D., An algebraic solution to dead space determination according to Fowler's graphical method. *Computers and Biomedical Research* **1999,** 32, (2), 161-167.

34. Hsu, M. F.; Cates, G. D.; Kominis, I.; Aksay, I. A.; Dabbs, D. M., Sol-gel coated glass cells for spin-exchange polarized He-3. *Applied Physics Letters* **2000,** 77, (13), 2069-2071.

35. Babcock, E.; Chann, B.; Walker, T. G.; Chen, W. C.; Gentile, T. R., Limits to the polarization for spin-exchange optical pumping of He-3. *Physical Review Letters* **2006,** 96, (8), 083003.

36. Moller, H. E.; Chen, X. J.; Saam, B.; Hagspiel, K. D.; Johnson, G. A.; Altes, T. A.; de Lange, E. E.; Kauczor, H. U., MRI of the lungs using hyperpolarized noble gases. *Magnetic Resonance in Medicine* **2002,** 47, (6), 1029-1051.

37. Mercer, R. R.; Russell, M. L.; Crapo, J. D., Alveolar Septal Structure in Different Species. *Journal of Applied Physiology* **1994,** 77, (3), 1060-1066.

38. Knagge, K.; Prange, J.; Raftery, D., A continuously recirculating optical pumping apparatus for high xenon polarization and surface NMR studies. *Chemical Physics Letters* **2004,** 397, (1-3), 11-16.

39. Ruset, I. C.; Ketel, S.; Hersman, F. W., Optical pumping system design for large production of hyperpolarized Xe-129. *Physical Review Letters* **2006,** 96, (5), 053002.

40. Zook, A. L.; Adhyaru, B. B.; Bowers, C. R., High capacity production of > 65% spin polarized xenon-129 for NMR spectroscopy and imaging. *Journal of Magnetic Resonance* **2002,** 159, (2), 175-182.

41. Zerger, J. N.; Lim, M. J.; Coulter, K. P.; Chupp, T. E., Polarization of Xe-129 with high power external-cavity laser diode arrays. *Applied Physics Letters* **2000,** 76, (14), 1798-1800.

42. Hoult, D. I.; Chen, C. N.; Sank, V. J., The Field-Dependence of Nmr Imaging.2. Arguments Concerning an Optimal Field-Strength. *Magnetic Resonance in Medicine* **1986,** 3, (5), 730-746.

43. Pavlovskaya, G.; Blue, A. K.; Gibbs, S. J.; Haake, M.; Cros, F.; Malier, L.; Meersmann, T., Xenon-131 surface sensitive imaging of aerogels in liquid xenon near the critical point. *Journal of Magnetic Resonance* **1999,** 137, (1), 258-264.

44. Hancu, I.; van der Maarel, J. R. C.; Boada, F. E., Detection of sodium ions in anisotropic environments through spin-lock NMR. *Magnetic Resonance in Medicine* **2002,** 47, (1), 68-74.

45. van der Maarel, J. R. C., Thermal relaxation and coherence dynamics of spin 3/2. II. Strong radio-frequency field. *Concepts in Magnetic Resonance Part A* **2003,** 19A, (2), 117-133.

46. Jaccard, G.; Wimperis, S.; Bodenhausen, G., multiple quantum NMR spectroscopy of S=3/2 spins in isotropic phase: A new probe for multiexponential relaxation. *Journal of Chemical Physics* **1986,** 85, (11), 6282-6293.

47. Meersmann, T.; Smith, S. A.; Bodenhausen, G., Multiple-quantum filtered xenon-131 NMR as a surface probe. *Physical Review Letters* **1998,** 80, (7), 1398-1401.

48. Meersmann, T.; Deschamps, M.; Bodenhausen, G., Probing aerogels by multiple quantum filtered Xe-131 NMR spectroscopy. *Journal of the American Chemical Society* **2001,** 123, (5), 941-945.

APPENDIX

Published Works Related to This Dissertation

Peer Reviewed Publications:

Galina E. Pavlovskaya, Zackary I. Cleveland, Karl F. Stupic, Randal J. Basaraba, and Thomas Meersmann, "Hyperpolarized Krypton-83 as a New Contrast Agent for Magnetic Resonance Imaging", *Proceedings of the National Academy of Sciences USA*. **2005,** 102 (51): 18275-18279.

Zackary I. Cleveland, Galina E. Pavlovskaya, Karl F. Stupic, Catherine F. LeNoir, and Thomas Meersmann, "Exploring Hyperpolarized Krypton-83 by Remotely Detected NMR Relaxometry", *Journal of Chemical Physics.* **2006,** 124 (4): 044312.

Karl F. Stupic, Zackary I. Cleveland, Galina E. Pavlovskaya, and Thomas Meersmann, "Quadrupolar Relaxation of Hyperpolarized Krypton-83 as a Probe for Surfaces", *Solid State Nuclear Magnetic Resonance.* **2006,** 29 (1-3): 79-84.

Zackary I. Cleveland, Karl F. Stupic, Galina E. Pavlovskaya, John E. Repine, Jan B. Wooten, and Thomas Meersmann, "Hyperpolarized 83Kr and 129Xe NMR Relaxation Measurements of Hydrated Surfaces: Implications for Materials Science and Pulmonary Diagnostics", *Journal of the American Chemical Society.* **2007,** 129 (6): 1784-1792.

Zackary I. Cleveland and Thomas Meersmann, "Studying Porous Materials with Krypton-83 NMR Spectroscopy", *Magnetic Resonance in Chemistry* **2007,** 45 (S1): S12-S23.

Zackary I. Cleveland, Galina E. Pavlovskaya, Karl F. Stupic, Jan B. Wooten, John E. Repine, and Thomas Meersmann, "Detecting Tobacco Smoke Deposition by Hyperpolarized 83Kr MRI", *Magnetic Resonance Imaging* **2008,** 26 (2): 270-278.

Zackary I. Cleveland, Galina E. Pavlovskaya, Nancy D. Elkins, Karl F. Stupic, John E. Repine, and Thomas Meersmann, "Hyperpolarized 83Kr MRI of Lungs", *Journal of Magnetic Resonance.* **2008,** accepted.

Zackary I. Cleveland and Thomas Meersmann, "Density Independent Contributions to Longitudinal Relaxation in ^{83}Kr", *ChemPhysChem.* **2008,** accepted.

Works Submitted for Peer Review:

Zackary I. Cleveland and Thomas Meersmann, "Binary Collision Induced Longitudinal Relaxation in Gas-Phase 83Kr", *Journal of Chemical Physics.* submitted.

Works to be Submitted for Peer Review:

Karl F. Stupic, Galina E. Pavlovskaya, Zackary I. Cleveland, and Thomas Meersmann, "NMR Investigations of Hyperpolarized 131-Xenon", in preparation.

Zackary I. Cleveland and Thomas Meersmann, "Probing Surfaces with Spin I>1/2 Noble Gas NMR Spectroscopy and MRI", *Progress in Nuclear Magnetic Resonance Spectroscopy.* **invited review**, in preparation.

Zackary I. Cleveland, Karl F. Stupic, and Thomas Meersmann, "Longitudinal Relaxation of Xenon-129 in Materials with Macroscopic Pores", in preparation.

Patent:

Thomas Meersmann, Galina E. Pavlovskaya, Zackary I. Cleveland, Karl F. Stupic, and "Nuclear Electric Quadrupolar Properties of Hyperpolarized Noble Gases to Probe Surfaces and Interfaces", US patent pending.